

Evidence for Electroweak Top Quark Production in
Proton-Antiproton Collisions at $\sqrt{s} = 1.96$ TeV

Thomas Gadfort

A dissertation submitted in partial fulfillment of
the requirements for the degree of

Doctor of Philosophy

University of Washington

2007

Program Authorized to Offer Degree: Physics

University of Washington
Graduate School

This is to certify that I have examined this copy of a doctoral dissertation by

Thomas Gadfort

and have found that it is complete and satisfactory in all respects,
and that any and all revisions required by the final
examining committee have been made.

Chair of the Supervisory Committee:

Gordon Watts

Reading Committee:

Gordon Watts

Peter Doe

Henry Lubatti

Date:

In presenting this dissertation in partial fulfillment of the requirements for the doctoral degree at the University of Washington, I agree that the Library shall make its copies freely available for inspection. I further agree that extensive copying of this dissertation is allowable only for scholarly purposes, consistent with "fair use" as prescribed in the U.S. Copyright Law. Requests for copying or reproduction of this dissertation may be referred to Proquest Information and Learning, 300 North Zeeb Road, Ann Arbor, MI 48106-1346, 1-800-521-0600, to whom the author has granted "the right to reproduce and sell (a) copies of the manuscript in microform and/or (b) printed copies of the manuscript made from microform."

Signature_____

Date_____

University of Washington

Abstract

Evidence for Electroweak Top Quark Production in Proton-Antiproton Collisions at
 $\sqrt{s} = 1.96$ TeV

Thomas Gadfort

Chair of the Supervisory Committee:
Professor Gordon Watts
Physics

We present the first evidence for electroweak single top quark production using nearly 1 fb^{-1} of Tevatron Run II data at $\sqrt{s} = 1.96$ TeV. We select single-top-like data events in the lepton+jets decay channel and separate them from backgrounds using the matrix element analysis method. This technique uses leading order matrix elements to compute an event probability for both signal and background hypotheses. Using the expected signal acceptance, background, and observed data we measure the single top quark cross section:

$$\sigma(p\bar{p} \rightarrow tb + tqb + X) = 4.6_{-1.5}^{+1.8} \text{ pb}$$

The probability for the background to have fluctuated up to give at least the cross section measured in this analysis is 0.21%, which corresponds to a Gaussian equivalent significance of 2.9σ .

TABLE OF CONTENTS

	Page
List of Figures	iii
List of Tables	xi
Chapter 1: Introduction	1
Chapter 2: Theory	4
2.1 Standard Model: Matter Particles	4
2.2 Standard Model: Particle Interactions	4
2.3 The Top Quark	8
2.4 Electroweak Top Quark Production	9
Chapter 3: Experimental Apparatus	18
3.1 Fermilab Accelerator Complex	18
3.2 $p\bar{p}$ Collisions	22
3.3 Coordinate System and Units Convention	23
3.4 DØ Detector	24
Chapter 4: Event Reconstruction And Simulation	40
4.1 Object Reconstruction	40
4.2 Monte Carlo Generation and Detector Simulation	54
4.3 Trigger Simulation	56
4.4 Monte Carlo Corrections	57
Chapter 5: The Single Top Quark Dataset	69
5.1 Previous Single Top Searches	69
5.2 Analysis Measurement Strategy	70
5.3 Triggers for Single Top Quark Events	71
5.4 Reconstructed Object Selection	75

Chapter 6:	Background Estimation	81
6.1	Background Modeling	81
6.2	Background Normalization	88
6.3	Background Yields	92
6.4	Comparison of Data with Expectation	95
Chapter 7:	Matrix Element Analysis Method	100
7.1	Motivation and Introduction to the Matrix Element Method	100
7.2	Event Probability Density, $P_{S B}(\vec{x})$	102
7.3	Single Top Discriminant Performance	115
7.4	Cross-Check Samples	126
7.5	Matrix Element Discriminants	131
Chapter 8:	Cross Section Determination Method	135
8.1	Bayesian Posterior Density Function	135
8.2	Systematic Uncertainties	142
8.3	Ensemble Testing	148
8.4	Expected Results	151
Chapter 9:	Results With Data	154
9.1	Measured Cross Section	154
9.2	Signal Significance and Standard Model Compatibility	156
Chapter 10:	Conclusion and Discussion	160
Bibliography	163
Appendix A:	Differential Cross Section Derivation	170
A.1	Probability Calculation	170
A.2	Integration Variable Remapping	176
Appendix B:	Discriminant Output Plots	186
Appendix C:	Luminosity Calculation	194
Appendix D:	Ensemble Generation Technique	195
Appendix E:	Analysis Channel Systematics Uncertainties	197

LIST OF FIGURES

Figure Number	Page
1.1 Aerial view of the Fermilab accelerator complex.	2
2.1 The Higgs "wine-bottle" potential [11].	6
2.2 Main leading order $t\bar{t}$ pair production Feynman diagrams [67].	9
2.3 The leading order Feynman diagram for the s -channel single top production mode [67].	10
2.4 The leading order (left) and an important next-to-leading order (right) Feynman diagrams for the t -channel single top production mode [67].	10
2.5 The leading order Feynman diagrams for the s -channel like process involving a W' boson [67].	13
2.6 A leading order Feynman diagram for a t -channel-like process produced through FCNC [67].	13
2.7 CTEQ 6M parton distribution functions for the gluon and all quark flavors for a small momentum transfer (left) and large momentum transfer (right). The x -axis is the proton momentum fraction of the parton and the y -axis is the parton density [82].	15
2.8 p_T (left) and η (right) distributions of final state particles in s -channel events [67].	16
2.9 p_T (left) and η (right) distributions of final state particles in s -channel events [67].	17
3.1 Schematic of the Fermilab accelerator complex [63].	19
3.2 Cartoon example of the linear accelerator's alternating series of gaps and drift tubes [2].	20
3.3 $D\bar{O}$ coordinate system with respect to the Tevatron ring [86].	23
3.4 Schematic side-view of the $D\bar{O}$ detector [21].	25
3.5 Schematic of the two tracking detectors (SMT and CFT) as well as the superconducting solenoid magnet [21].	26
3.6 Schematic of the silicon microstrip tracker sub-detector [21].	27
3.7 Schematic endview of the central fiber tracker with corresponding waveguides [21].	28
3.8 3D view of the $D\bar{O}$ calorimeter [21].	29

3.9	Initial stages of an electromagnetic shower caused by a photon interacting with an absorber material. The radiation length x_0 is the typical distance a photon will travel before producing an e^+e^- pair or the distance before an electron will radiate a photon [9].	30
3.10	Example of a typical calorimeter cell of alternating absorber and active material. Particles traverse the calorimeter cell from left to right in this diagram [21].	31
3.11	Octant of the DØ calorimeter. The fine segmentation of the calorimeter is clearly seen in this diagram [21]. The alternating dark and light blocks represent cells in different calorimeter towers.	32
3.12	Schematic of the DØ luminosity monitor shown in relation to the beam pipe, SMT, and endcap calorimeter [21].	33
3.13	3D view of the DØ muon detector [21].	35
3.14	Cartoon drawing of the DØ trigger system [21].	36
3.15	Experimental setup of the level 3 trigger and data acquisition system (left) and the flow of data through the system (right).	38
4.1	This histogramming track finding technique shown for an example of a single 1.5 GeV track of 5 hits. (a) The family of trajectories containing a given hit. (b) The geometric place of all trajectories containing a given hit in parameters space. (c) Curves from different hits intersect at one point corresponding to the track parameters. (d) The point of intersection can be seen as a peak in the (ρ, ϕ) histogram [69].	43
4.2	Minimum bias probability for the hard scatter vertex (left) and inelastic $p\bar{p}$ vertices (right). The vertex in the event with the lowest minimum bias probability is selected as the hard scatter vertex [33].	45
4.3	Offset energy correction for jets with a cone radius of 0.5 as a function of η^{det} [4].	49
4.4	Missing E_T (E_T imbalance) projection fraction method cartoon [4].	50
4.5	The relative energy correction for jets with a cone radius of 0.5 as a function of η^{det} (right) [4].	50
4.6	Absolute energy response of jets in the calorimeter for several η regions [4].	51
4.7	Showering correction for jets as a function of E_T for jets in three different η regions [4].	52
4.8	Peak instantaneous luminosity as a function of time [10].	55
4.9	An example electron turn-on curve measured as a function of the electron p_T (left) and an example muon turn-on curve measured as a function of η (right). The points are trigger efficiencies derived from data in that bin (with uncertainty bars) [56].	58

4.10	Muon reconstruction efficiency as measured in $Z \rightarrow \mu\mu$ data events (left) and the Monte Carlo correction factor as a function of muon η (right) [59].	60
4.11	Muon track match efficiency as measured in $Z \rightarrow \mu\mu$ data events (left) and the Monte Carlo correction factor as a function of track η (right) [59].	60
4.12	Muon isolation efficiency as measured in $Z \rightarrow \mu\mu$ data events for various regions of primary vertex z position (left) and Monte Carlo correction factor as a function of the number of reconstructed jets. The isolation used in the single top quark analysis is labeled TopScaledLoose and corresponds to the blue triangle curve [59].	61
4.13	Electron reconstruction efficiency as measured in $Z \rightarrow ee$ data (red) and Monte Carlo (blue) events (left) and Monte Carlo correction factor as a function of electron p_T (right) [57].	62
4.14	Electron reconstruction efficiency as measured in $Z \rightarrow ee$ data (red) and Monte Carlo (blue) events (left) and Monte Carlo correction factor as a function of electron p_T (right) [57].	62
4.15	Primary vertex reconstruction as measured on $Z \rightarrow ee$ data events. The efficiencies are shown as a function of the longitudinal primary vertex position [33].	63
4.16	p_T imbalance (ΔS) distribution before (left) and after (right) jet smearing and removal are applied for two photon p_T regions: $23 < p_T^\gamma < 26$ (top) and $75 < p_T^\gamma < 80$ (bottom). The data is shown in blue and the Monte Carlo is shown in red [8].	65
4.17	Neural network B -jet tagger efficiency (green line) and 1σ error bands (dashed lines) jet p_T and B -jets (left) and charm-jets (right) [80].	67
4.18	The impact parameter significance for B -jets and light jets. The IP significance is defined as the signed scalar product of the jet-axis and vector defined by the tracks of the displaced vertex divided by the error on that measurement [7].	68
5.1	Muon p_T (left) and η (right) distributions for s -channel (red) and t -channel (blue) single top. Muons are required to have $p_T > 18$ GeV and $ \eta < 2$	76
5.2	Leading jet p_T (left) and η (right) distributions for s -channel (red) and t -channel (blue) single top. The leading jet is required to have $p_T > 25$ GeV and $ \eta < 2.5$	76
5.3	Second leading jet p_T (left) and η (right) distributions for s -channel (red) and t -channel (blue) single top. The second leading jet is required to have $p_T > 20$ GeV and $ \eta < 3.4$	77
5.4	Missing E_T distribution for s -channel (red) and t -channel (blue) single top. The missing E_T is required to larger than 15 GeV.	77

5.5	Longitudinal location of the primary interaction vertex for s -channel (red) and t -channel (blue) single top. The primary interaction vertex is required to be located within 60 cm of the detector origin.	78
5.6	Example triangle cut between a muon and the missing E_T for mis-measured events (left) and s -channel single top events (right). The colors indicate the density of events. The brighter colors indicate more densely populated regions. Events which fall inside the triangles are removed from the final data sample. The black line at $ME_T = 15$ GeV indicates the standard missing E_T selection [58].	80
6.1	Example leading order Feynman diagram for a “ W +jets” event. This particular diagram represents the production of a W boson, and two b quarks and an associated gluon [5].	82
6.2	Example Feynman diagram for a $t\bar{t} \rightarrow \ell + jets$ event [5].	83
6.3	Example Feynman diagram for a multijet event [5].	83
6.4	α values with errors for the eight zero B -tagged jet samples and the linear fit with error to the values [56].	93
6.5	Color convention used in all histograms.	95
6.6	Leading jet p_T distributions. Upper row: events with 2 jets, Middle row: events with 3 jets, Lower row: events with 4 jets. Left column: events before B -tagging, Middle row: events with one selected B -jet, Right column: events with two selected B -jets [56].	96
6.7	Second leading jet p_T distributions. Upper row: events with 2 jets, Middle row: events with 3 jets, Lower row: events with 4 jets. Left column: events before B -tagging, Middle row: events with one selected B -jet, Right column: events with two selected B -jets [56].	97
6.8	Lepton p_T distributions. Upper row: events with 2 jets, Middle row: events with 3 jets, Lower row: events with 4 jets. Left column: events before B -tagging, Middle row: events with one selected B -jet, Right column: events with two selected B -jets [56].	98
6.9	Missing E_T distributions. Upper row: events with 2 jets, Middle row: events with 3 jets, Lower row: events with 4 jets. Left column: events before B -tagging, Middle row: events with one selected B -jet, Right column: events with two selected B -jets [56].	99
7.1	Comparison of the lepton charge multiplied by the forward un-tagged jet η ($q_\ell \times \eta$) for t -channel single top (blue) and $Wb\bar{b}$ Monte Carlo events.	101
7.2	Representative Feynman diagrams corresponding to the leading-order matrix elements used for event probability calculation for events with exactly two jets. Upper row are signals: $ud \rightarrow tb$ and $ub \rightarrow td$; lower row are backgrounds: $ud \rightarrow Wbb$, $sg \rightarrow Wcg$, and $ud \rightarrow Wgg$	104

7.3	Representative Feynman diagrams corresponding to the leading-order matrix elements used for event probability calculation for events with exactly three jets. Left two plots: signals, $ud \rightarrow tbg$, $ug \rightarrow tbd$; right plot: background, $ud \rightarrow Wbbg$.	104
7.4	Energy difference between a reconstructed jet and its matched parton for three types of jets for all eta regions and all jet energies.	106
7.5	Discriminant plots and efficiency curves for: first row, s -channel vs. Wbb and second row, t -channel vs. Wbb . The numbers in the efficiency curves (right column) represent the fraction of signal or background the remains after a discriminant cut of 0.8.	117
7.6	Discriminant plots and efficiency curves for: first row, s -channel vs. Wcc and second row, t -channel vs. Wcc . The numbers in the efficiency curves (right column) represent the fraction of signal or background the remains after a discriminant cut of 0.8.	118
7.7	Discriminant plots and efficiency curves for: first row, s -channel vs. Wjj and second row, t -channel vs. Wjj . The numbers in the efficiency curves (right column) represent the fraction of signal or background the remains after a discriminant cut of 0.8.	119
7.8	Discriminant plots and efficiency curves for: first row, s -channel vs. Multijets and second row, t -channel vs. Multijets. The numbers in the efficiency curves (right column) represent the fraction of signal or background the remains after a discriminant cut of 0.8.	120
7.9	Discriminant plots and efficiency curves for: first row, s -channel vs. $t\bar{t} \rightarrow \ell\ell$ and second row, t -channel vs. $t\bar{t} \rightarrow \ell\ell$. The numbers in the efficiency curves (right column) represent the fraction of signal or background the remains after a discriminant cut of 0.8.	121
7.10	Discriminant plots and efficiency curves for: first row, s -channel vs. $t\bar{t} \rightarrow \ell + jets$ and second row, t -channel vs. $t\bar{t} \rightarrow \ell + jets$. The numbers in the efficiency curves (right column) represent the fraction of signal or background the remains after a discriminant cut of 0.8.	122
7.11	2D-discriminant templates for: left, s -channel, and right, t -channel Monte Carlo events.	123
7.12	2D-discriminant templates for: top-left, Wbb , top-right, Wcc , and bottom-left, Wjj Monte Carlo events.	124
7.13	2D-discriminant templates for: top-left, multijets events, top-right, $t\bar{t} \rightarrow \ell\ell$, and bottom-right, $t\bar{t} \rightarrow \ell + jets$ Monte Carlo events.	125
7.14	“Soft W +jets” cross-check plots in two-jet events for the s -channel discriminant (upper row) and the t -channel discriminant (lower row). The left column shows the full discriminant region while the right column shows the high discriminant region above 0.7.	127

7.15	“Soft W +jets” cross-check plots in three-jet events for the s -channel discriminant (upper row) and the t -channel discriminant (lower row). The left column shows the full discriminant region while the right column shows the high discriminant region above 0.7.	128
7.16	“Hard W +jets” cross-check plots in two-jet events for the s -channel discriminant (upper row) and the t -channel discriminant (lower row). The left column shows the full discriminant region while the right column shows the high discriminant region above 0.7.	129
7.17	“Hard W +jets” cross-check plots in three-jet events for the s -channel discriminant (upper row) and the t -channel discriminant (lower row). The left column shows the full discriminant region while the right column shows the high discriminant region above 0.7.	130
7.18	Discriminant plots for the $e+\mu$ channel with two jets and ≥ 1 B tag. Upper row: s -channel discriminant; lower row: tq discriminant. Left column: full output range; right column: close-up of the high end of the distributions. . .	131
7.19	Discriminant plots for the $e+\mu$ channel with three jets and ≥ 1 b tag. Upper row: s -channel discriminant; lower row: tq discriminant. Left column: full output range; right column: close-up of the high end of the distributions. . .	132
7.20	Invariant mass of the lepton, neutrino, and tagged jet for all events (upper left plot), for events with $D < 0.4$ (upper right plot), and events with $D > 0.7$ (bottom left plot).	133
7.21	Lepton charge multiplied by the pseudorapidity of the untagged jet for all events (upper left plot), for events with $D < 0.4$ (upper right plot), and events with $D > 0.7$ (bottom left plot). The number of observed events is different from the b -tagged top mass plot because this variable is only defined for events with at least one untagged jet.	134
8.1	Example cross section measurement (solid blue line) with $\pm 1\sigma$ error band (dashed blue lines).	139
8.2	Example of the 95% CL upper cross section limit. The value of the upper limit is shown by the blue curve. For this posterior the cross section limit is 8.4 pb.	140
8.3	Example of the Bayes ratio defined as the maximum of the posterior (top blue line) over the posterior at zero cross section (lower blue line). The Bayes ratio for this curve is 5.0.	141
8.4	Electron p_T in weighted $t\bar{t} \rightarrow \ell\ell$ Monte Carlo events. The three curves represent the estimated yield in each p_T bin for the case of $+1\sigma$ trigger weights (red), nominal trigger weights (black), and -1σ trigger weights (blue).	144

8.5	1σ uncertainties from each of the jet energy scale components as a function of jet p_T for jets with $\eta = 0.0$. The total uncertainty is shown by the black line.	145
8.6	Neural network B -jet tagger efficiency (green line) and 1σ error bands (dashed lines) jet p_T and η for B -jets (upper row) and charm-jets (lower row). The red lines represent the efficiency of the B -tagging algorithm when applied directly to the Monte Carlo.	147
8.7	Observed cross section for a set of 2,000 pseudo-datasets for the five ensembles: $\sigma_{s+t} = 2.0$ pb (upper left), $\sigma_{s+t} = 2.9$ pb (upper right), $\sigma_{s+t} = 4.0$ pb (middle left), $\sigma_{s+t} = 6.0$ pb (middle right), and $\sigma_{s+t} = 8.0$ pb (bottom middle)	149
8.8	Response of the five generated ensemble sets versus input cross section. The response is measured as the mean value of the histogram for each ensemble.	150
8.9	Expected 1D posterior plots for the combined $e+\mu \geq 1$ B -tag channel in two-jet events, with statistical uncertainties only (left plot) and including also systematic uncertainties (right plot).	151
8.10	Expected 1D posterior plots for the combined $e+\mu \geq 1$ b -tag channel in three-jet events, with statistical uncertainties only (left plot) and including also systematic uncertainties (right plot).	152
8.11	Expected 1D posterior plots for the combination of all channels, with statistical uncertainties only (left plot) and including also systematic uncertainties (right plot).	152
9.1	Measured 1D posterior plots for the combined $e+\mu \geq 1$ B -tag channel with statistical uncertainties only (left plot) and with systematic uncertainties as well (right plot).	154
9.2	Summary plot of the measured single top quark cross sections showing the individual measurements and their combination.	157
9.3	Distribution of expected (left) and measured (right) cross sections from a zero-signal ensemble with full systematics included. The probability that the background alone could have a measured cross section above 4.6 pb or above is 0.21% leading to a Gaussian equivalent signal significance of 2.9σ	158
9.4	Distribution of measured cross sections from a Standard Model ensemble with full systematics included. The probability that a Standard Model signal could have a measured cross section of 4.6 pb or above is 20.5%.	159
10.1	Results from the three single top quark analyses and the combined analysis compared with two NLO cross section calculations [54].	161
B.1	Discriminant plots for the electron channel with one b tag and two jets. Upper row: tb discriminant, lower row: tq discriminant. Left column, full discriminant range, right column, close-up of the high end of the distribution.	186

- B.2 Discriminant plots for the electron channel with two b tags and two jets.
Upper row: tb discriminant, lower row: tq discriminant. Left column, full discriminant range, right column, close-up of the high end of the distribution. 187
- B.3 Discriminant plots for the muon channel with one b tag and two jets. Upper row: tb discriminant, lower row: tq discriminant. Left column, full discriminant range, right column, close-up of the high end of the distribution. . . . 188
- B.4 Discriminant plots for the muon channel with two b tags and two jets. Upper row: tb discriminant, lower row: tq discriminant. Left column, full discriminant range, right column, close-up of the high end of the distribution. . . . 189
- B.5 Discriminant plots for the electron channel with one b tag and three jets.
Upper row: tb discriminant, lower row: tq discriminant. Left column, full discriminant range, right column, close-up of the high end of the distribution. 190
- B.6 Discriminant plots for the electron channel with two b tags and three jets.
Upper row: tb discriminant, lower row: tq discriminant. Left column, full discriminant range, right column, close-up of the high end of the distribution. 191
- B.7 Discriminant plots for the muon channel with one b tag and three jets. Upper row: tb discriminant, lower row: tq discriminant. Left column, full discriminant range, right column, close-up of the high end of the distribution. . . . 192
- B.8 Discriminant plots for the muon channel with two b tags and three jets.
Upper row: tb discriminant, lower row: tq discriminant. Left column, full discriminant range, right column, close-up of the high end of the distribution. 193

LIST OF TABLES

Table Number	Page	
2.1	Properties of the fundamental spin- $\frac{1}{2}$ fermions in the Standard Model [91].	5
2.2	Properties of the fundamental spin-1 gauge bosons in the Standard Model [91].	7
2.3	Total cross sections for single top quark production at $\sqrt{s} = 1.96$ TeV with $m_t = 175$ GeV.	11
4.1	Variables used in the neural networks training. The variables are listed in order of relative importance as determined in the training [80].	54
4.2	Muon smearing parameters for the function $(A + \frac{B}{p_T})$ for two different run periods.	59
5.1	Summary of limits on s -channel, t -channel, and combined $s+t$ -channel single top quark production from the DØ and CDF collaborations.	70
5.2	Integrated luminosities by trigger version for the triggers used to record electron single top quark events. The total integrated luminosity is shown in bold.	73
5.3	Integrated luminosities by trigger version for the triggers used to record muon single top quark events. The total integrated luminosity is shown in bold.	75
5.4	Single acceptances after selection cuts, one, and two B -tags. The branching ratio for $W \rightarrow \ell\nu$ is included in the acceptance.	80
6.1	Absolute weights for W +light parton ALPGEN Monte Carlo events.	86
6.2	Absolute weights for $W+c\bar{c}$ +light parton ALPGEN Monte Carlo events.	86
6.3	Absolute weights for $W+b\bar{b}$ +light parton ALPGEN Monte Carlo events.	87
6.4	Absolute weights for $t\bar{t} \rightarrow \ell + jets$ +light parton ALPGEN Monte Carlo events.	87
6.5	Absolute weights for $t\bar{t} \rightarrow \ell\ell$ +light parton ALPGEN Monte Carlo events.	88
6.6	Number of loose and tight data events after all selection cuts (top two rows) along with the expected number W +jets and multijet events in the tight sample (bottom two rows).	90
6.7	Average multijet efficiency: $\varepsilon_{\text{Multijet}}$	91
6.8	Average W +jets efficiency: ε_{W+jets}	91

6.9	Scale factor α for the $Wb\bar{b}$ and $Wc\bar{c}$ yields to match the data in each jet bin, for zero B -tags, 1 B -tag, and two B -tags samples. The uncertainties are statistical only.	92
6.10	Event yields after selection and before B tagging.	93
6.11	Event yields after selection and one selected B -jet.	94
6.12	Event yields after selection and two selected B -jets.	94
7.1	Light jet transfer function parameters.	107
7.2	B jet transfer function parameters.	107
7.3	B w/ μ jet transfer function parameters.	107
7.4	Electron transfer function parameters.	108
7.5	Muon transfer function parameters (Eq. 7.11) for muons with and without SMT hits.	109
7.6	Cross section times branching fraction for each analysis channel. All cross sections are given in units of femtobarns (fb).	113
7.7	Weights for the event differential cross section depending on the B -jet tagging status of the jet and jet-parton assignment.	114
7.8	Background fractions chosen for each analysis channel in two-jet events.	116
8.1	A summary of the relative systematic uncertainties for each of the applied corrections and efficiencies. The uncertainty shown is the error on the correction or the efficiency, before it has been applied to the MC or data samples.	142
8.2	$\varepsilon_{\text{Multijet}}$ for electrons as a function of the trigger period and jet multiplicity, and $\varepsilon_{\text{Multijet}}$ for muons averaged over η . The definition of the trigger periods is found in Chapter 5.	146
8.3	Expected $tb+qb$ cross sections, without and with systematic uncertainties, for many combinations of the analysis channels. The final expected result of this analysis are shown in the lower right hand corner in bold type.	153
8.4	Relative uncertainties on the expected $tb+qb$ cross section, without and with systematic uncertainties, for many combinations of the analysis channels. The best value from all channels combined, with systematics, is shown in bold type.	153
9.1	Measured $tb+qb$ cross sections, without and with systematic uncertainties, for many combinations of the analysis channels. The final result of this analysis is shown in the lower right hand corner in bold type.	155
9.2	Relative uncertainties on the measured $tb+qb$ cross section, without and with systematic uncertainties, for many combinations of the analysis channels. The best value from all channels combined, with systematics, is shown in bold type.	155

9.3	Contribution of each systematic uncertainty to the total systematic uncertainty on the $tb+tb$ cross section.	156
E.1	Electron channel uncertainties, requiring exactly one tag and exactly two jets.	198
E.2	Electron channel uncertainties, requiring exactly one tag and exactly three jets.	199
E.3	Muon channel uncertainties, requiring exactly one tag and exactly two jets. .	200
E.4	Muon channel uncertainties, requiring exactly one tag and exactly three jets.	201
E.5	Electron channel uncertainties, requiring exactly two tags and exactly two jets.	202
E.6	Electron channel uncertainties, requiring exactly two tags and exactly three jets.	203
E.7	Muon channel uncertainties, requiring exactly two tags and exactly two jets. .	204
E.8	Muon channel uncertainties, requiring exactly two tags and exactly three jets.	205

Chapter 1

INTRODUCTION

The field of high energy physics is the study of all fundamental particles and their interactions at extremely short distances, which are described by a quantum field theory known as the Standard Model of particle physics. The Standard Model is an extremely successful framework which predicts and calculates quantities that can be measured in high energy physics experiments. Perhaps one of the most notable predictions of the Standard Model is that of the top quark. This particle was predicted long before it was discovered in 1995 because the Standard Model required a particle with its charge and intrinsic spin to conserve several of the fundamental symmetries built into the model.

The top quark is unique because of its large mass, which is nearly that of a gold atom. Because of its large mass, creating top quarks requires a tremendously energetic particle accelerator. Such an accelerator exists, called the Tevatron, located at the Fermi National Laboratory, which collides protons (p) and antiprotons (\bar{p}) at a center of mass energy of 1.96 TeV. An aerial view of the accelerator facility is shown in Figure 1.1. At the Tevatron the top quark is primarily studied when a top (t) and antitop (\bar{t}) quark are produced together; this process occurs for roughly one out of every five billion $p\bar{p}$ collisions. The Standard Model also predicts that the top quark can be produced singly at the Tevatron; however, it is expected to occur at half the rate of top-antitop production, or in nearly one out of every ten billion collisions.

Measuring single top quark production is interesting for several reasons, but perhaps the most compelling reason is that one can test the unitarity of the matrix (V_{CKM}) that governs how quarks mix. If unitarity is violated (i.e. $VV^\dagger \neq I$) it would provide clear evidence for physics beyond the Standard Model such as a possible fourth quark generation. Models which predict new processes that are not allowed by the Standard Model can also

be tested by measuring the single top production rate. For instance, many theories beyond the Standard Model predict a large “flavor changing neutral current” rate which could enhance the single top production rate by one order of magnitude. Finally, single top is important to measure because it represents one of the largest irreducible backgrounds for Higgs production at the Tevatron. The Higgs particle is predicted by the theory that explains why fundamental particles have mass and remains the only Standard Model particle not to have been found by high energy experiments.



Figure 1.1: Aerial view of the Fermilab accelerator complex.

An outline of this thesis is as follows. Chapter 2 of this thesis gives an introduction to the Standard Model of particle physics. Also described in this chapter is the motivation for measuring properties of the top quark along with a detailed description of single top quark production. Chapter 3 describes the Tevatron particle accelerator at Fermilab used to create $p\bar{p}$ collisions at $\sqrt{s}=1.96$ TeV. The decay products of the proton-antiproton collisions are measured using the DØ detector, which is also described in this chapter. Chapter 4 explains how signals in the DØ detector are used to reconstruct the collision to determine if it is consistent with single top quark production.

Chapter 5 describes the Tevatron Run II dataset used to search for single top quark

production. Because single top quark production is rare and its signature is common to many other physics processes a proper modeling of the background is crucial to the analysis. Chapter 6 describes the main sources of background to single top quark production as well as how they are modeled.

To better identify the single top signal contribution in the dataset a technique known as the matrix element method is employed. This technique uses leading order matrix elements to create an event probability for both signal and background hypotheses. These probabilities are combined to form a variable for each event which is designed to peak near one for signal-like events or near zero for background-like events. This technique and its application is described in chapter 7.

Chapter 8 describes the sophisticated Bayesian statistical analysis used to extract the single top quark cross section in the dataset. A detailed discussion of the systematic errors in the signal and background modeling is also provided here. Chapter 9 shows the results of the single top quark analysis including the measured cross section and signal significance. Finally, chapter 10 concludes the thesis with a few remarks on future improvements to the analysis technique as well as possible measurements with an increased dataset.

Chapter 2

THEORY

All particles and their interactions at short distances are described by a quantum field theory known as the Standard Model. In the Standard Model there are two fundamental divisions of particles: matter particles (Section 2.1) and particles which facilitate interactions between the matter particles (Section 2.2). The heaviest matter particle in the Standard Model is the top quark and its properties and production via the strong interaction are discussed in Section 2.3. Finally, Section 2.4 explains how the top quark is singly produced via an electroweak interaction.

2.1 Standard Model: Matter Particles

All matter particles in the Standard Model can be categorized either as quarks or leptons. Quarks are spin- $\frac{1}{2}$ particles that are grouped into three generations. Each generation contains two quarks: one with fractional electric charge $+\frac{2}{3}e$ (commonly called up type) and one with charge $-\frac{1}{3}e$ (commonly called down type). Leptons are also spin- $\frac{1}{2}$ particles that are grouped into three generations. In the lepton generation, one particle has unit charge ($\pm 1e$) and the other has no charge and essentially no mass. The lightest particles in both the quark and lepton generations are found in the first generation while the heaviest are found in the third generation. Table 2.1 summarizes the spin- $\frac{1}{2}$ matter particles in the Standard Model.

2.2 Standard Model: Particle Interactions

There are three fundamental interactions described by the Standard Model. The first is the electromagnetic interaction between any objects that carry electric charge such as the electron or proton. The second is the weak interaction which, at low energies, is responsible for nuclear beta decay (e.g. $\text{neutron} \rightarrow \text{proton} + \text{electron} + \text{neutrino}$). The third interaction

Table 2.1: Properties of the fundamental spin- $\frac{1}{2}$ fermions in the Standard Model [91].

Gen.	<u>Quarks</u>			<u>Leptons</u>		
	Flavor	Charge	Mass [MeV]	Flavor	Charge	Mass [MeV]
I	Up (u)	$+\frac{2}{3}e$	1.5 to 3.0	Electron (e)	-e	0.511
	Down (d)	$-\frac{1}{3}e$	3 to 7	(e) neutrino (ν_e)	0	$< 2.2 \times 10^{-6}$
II	Charm (c)	$+\frac{2}{3}e$	1.25×10^3	Muon (μ)	-e	105.7
	Strange (s)	$-\frac{1}{3}e$	80-130	(μ) neutrino (ν_μ)	0	$< 1.7 \times 10^{-4}$
III	Top (t)	$+\frac{2}{3}e$	171.4×10^3	Tau (τ)	-e	1777
	Bottom (b)	$-\frac{1}{3}e$	4.7×10^3	(τ) neutrino (ν_τ)	0	< 15.5

described by the Standard Model is the strong interaction, which binds protons and neutrons together in the atomic nucleus.

The electromagnetic and weak interactions are unified in the Standard Model in an $SU(2)_L \otimes U(1)_Y$ gauge theory. This theory predicts four force carriers: two neutral (B and W^0) and two charged (W^\pm). These particles are required to explain neutral and charged current interactions, however the theory does not explain why three of these particles are observed to be massive and one is massless. To allow for massive force carriers, a neutral scalar particle ($\phi = [\phi_1 \ \phi_2]^T$) is added to the theory, with a potential shown in Fig. 2.1. The addition of this particle and its potential breaks the $SU(2)_L \otimes U(1)_Y$ gauge symmetry. This new term gives mass to the two charged force carriers (W^\pm) and mixes the two neutral particles such that one acquires mass (Z^0) and the other remains massless (γ). While this theory is very elegant, its prediction of a neutral scalar particle has yet to be verified experimentally. The search for this particle, known as the Higgs boson, is one of the foremost challenges in high energy physics.

The strong interaction is an $SU(3)$ gauge theory mediated by eight massless gauge bosons called gluons. The gluons interact with any particle that carries color charge, which in the Standard Model are quarks and the gluons themselves. The strong interaction exhibits an interesting property that the strength of the interaction decreases as the energy of the

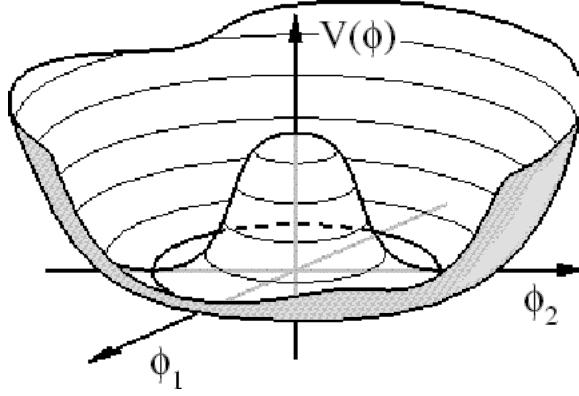


Figure 2.1: The Higgs "wine-bottle" potential [11].

processes increases. Eq. 2.1 shows the strong coupling parameter (α_S) dependence on the energy of the process.

$$\alpha_S(E) = \frac{12\pi}{33 - 2n_f \ln \left[\left(\frac{E}{\Lambda} \right)^2 \right]} \quad (2.1)$$

n_f is the number of active¹ quark flavors and Λ is the natural scale of the strong interaction ($\Lambda \sim 200$ MeV). The decreased coupling strength at energies greater than Λ allows quarks to break their confined states and travel as bare color charges. As the quark begins to propagate however, it polarizes the vacuum between itself and its color partner until it becomes energetically favorable to create a new quark-antiquark pair. This process can repeat itself many times with a net effect of creating of a large number of strongly interacting particles traveling in the same direction as the originating colored particle.

A summary of the gauge bosons which mediate interactions in the Standard Model is given in Table 2.2.

¹The number of active quark flavors depends on the energy of the process. At energies of ~ 100 MeV, there are three quark flavors (u,d,s). At higher energies of ~ 10 GeV, there are five quark flavors (u,d,s,c,b).

Table 2.2: Properties of the fundamental spin-1 gauge bosons in the Standard Model [91].

Interaction	Gauge Boson	Electric Charge	Mass [GeV]
Strong	Gluon (g)	0	0
Weak	W	$\pm 1e$	80.4
Weak	Z	0	91.2
Electromagnetic	Photon (γ)	0	0

2.2.1 Cabibbo-Kobayashi-Maskawa Quark Mixing Matrix

It has been observed that the quantum states that describe a quark when produced via the strong interaction (e.g. $g \rightarrow b\bar{b}$) are not the same as the states used to describe the quark under a flavor changing weak transition (e.g. $W \rightarrow t\bar{b}$). The relationship between the strong and weak basis states is summarized by the Cabibbo-Kobayashi-Maskawa (CKM) unitary quark mixing matrix, shown in Eq. 2.2.

$$\begin{bmatrix} d' \\ s' \\ b' \end{bmatrix} = \begin{bmatrix} V_{ud} & V_{us} & V_{ub} \\ V_{cd} & V_{cs} & V_{cb} \\ V_{td} & V_{ts} & V_{tb} \end{bmatrix} \begin{bmatrix} d \\ s \\ b \end{bmatrix} \quad (2.2)$$

where $[d' \ s' \ b']^T$ are the weak eigenstates and $[d \ s \ b]^T$ are the strong eigenstates.

The CKM matrix contains the probabilities for charged current transitions of one quark to another within the same generation or between generations. For example, V_{ud} is the probability for a down quark to transition to an up quark in a flavor changing weak decay. The experimentally determined values for the CKM matrix elements are shown in Eq. 2.3 [91]. As seen from this matrix transitions within the same generation are preferred over transitions between generations.

$$\begin{bmatrix} 0.97383_{-0.00023}^{+0.00024} & 0.2272_{-0.0010}^{+0.0010} & 3.96_{-0.09}^{+0.09} \times 10^{-3} \\ 0.2271_{-0.0010}^{+0.0010} & 0.97296_{-0.00024}^{+0.00024} & 42.21_{-0.80}^{+0.10} \times 10^{-3} \\ 8.14_{-0.64}^{+0.32} \times 10^{-3} & 41.61_{-0.78}^{+0.12} \times 10^{-3} & 0.999100_{-0.000004}^{+0.000034} \end{bmatrix} \quad (2.3)$$

Of particular interest for this thesis is the V_{tb} matrix element. This matrix element has never been directly measured although it is heavily constrained once the unitarity of the matrix is imposed. A direct measurement of this quantity is possible through an observation of electroweak top quark production. The measurement of this process in $p\bar{p}$ collisions at the Tevatron is the subject of this thesis.

2.3 The Top Quark

In the Standard Model all quarks exist in left-handed isospin doublets. Thus when the bottom quark was discovered in 1977, a new left-handed isospin partner quark was required to exist. The long predicted top quark was finally discovered in $p\bar{p}$ collisions at the Tevatron in 1995 by the DØ and CDF collaborations [23, 12]. The top quark is unique from previously measured quarks because its mass is nearly forty times larger than the next heaviest quark with a mass of $171.4 \pm 2.1 \text{ GeV}/c^2$ [41].

Due to its very large mass the top quark has an relatively large decay width. The width of the top quark can be calculated within the framework of the Standard Model and is shown in Eq. 2.4². The top quark width is estimated to be 1.53 GeV, which can be converted to a lifetime of 0.4×10^{-24} sec. This lifetime is almost one order of magnitude smaller than the typical time scale for all strong interactions ($1/\Lambda \sim 10^{-23}$ s) and leads to the property that the top quark does not form strong bound states [36].

$$\Gamma(t \rightarrow Wb) = \frac{G_F m_t^3 |V_{tb}|^2}{8\pi\sqrt{2}} \left[1 - \frac{m_W^2}{m_t^2} \right] \left[1 + 2\frac{m_W^2}{m_t^2} \right] \left[1 - \frac{2\alpha_s(4\pi - 15)}{18\pi} \right] \quad (2.4)$$

At the Tevatron the top quark is primarily produced through pair production via the strong interaction. The cross section for this process has been calculated as 6.77 ± 0.42 pb for a top mass at 175 GeV [71]. The $t\bar{t}$ system has been extensively studied at the Tevatron and the measured cross section in all decay channels agrees well with theory [19, 14, 16, 15, 25, 26, 27, 24, 31, 30]. The leading order Feynman diagrams for $t\bar{t}$ production are shown in Fig. 2.2.

²In Eq. 2.4, G_F is the Fermi constant, m_t is the top quark mass, m_W is the W boson mass, and α_s is the strong coupling constant.

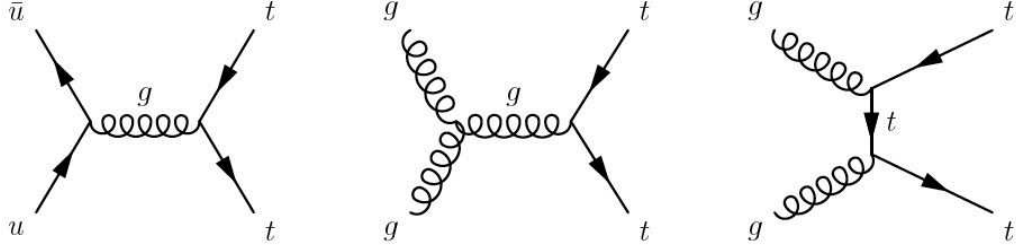


Figure 2.2: Main leading order $t\bar{t}$ pair production Feynman diagrams [67].

2.4 Electroweak Top Quark Production

Top quarks can also be produced via an electroweak interaction commonly called single top because only one top quark is produced in the event. At the Tevatron there are two dominant modes of single top production. The first is the s -channel process defined by a virtual time-like ($Q_W^2 > 0$) W boson formed from a $q\bar{q}'$ annihilation and decaying to a top and bottom quark. The second is the t -channel process defined by a virtual space-like ($Q_W^2 < 0$) W boson produced by a light and bottom quark exchange and producing a forward scattered light quark and a top quark. There is a third mode of production where the top quark is created in association with an on-shell ($Q_W^2 = M_W^2$) W boson; however, the cross section for this production mode is negligible at the Tevatron. Feynman diagrams for the s -channel and t -channel production modes are shown in Figs. 2.3 and 2.4. The s -channel and t -channel cross sections have been calculated in [85, 65, 87, 64, 88, 45, 44, 70] with the cross sections used in the data analysis shown in Table 2.3.

As stated earlier in this chapter, the top quark prefers to decay to a W boson and a b quark. The common decay mode to detect single top events is when the W boson either decays to an electron or muon and an associated neutrino³. For the s -channel, the final state particles for the leading order process are (1) lepton, (1) neutrino, and (2) b quarks. The t -channel final state is characterized by (1) lepton, (1) neutrino, (1) light quark, and at least one (1) b quark. The s -channel and t -channel processes are sometimes referred to

³The $W \rightarrow \tau\nu_\tau$ and $W \rightarrow q\bar{q}'$ channels are not considered in this thesis due to the large expected background rate.

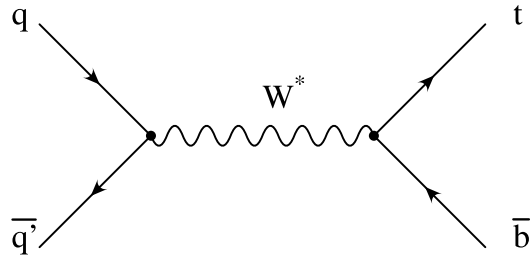


Figure 2.3: The leading order Feynman diagram for the s -channel single top production mode [67].

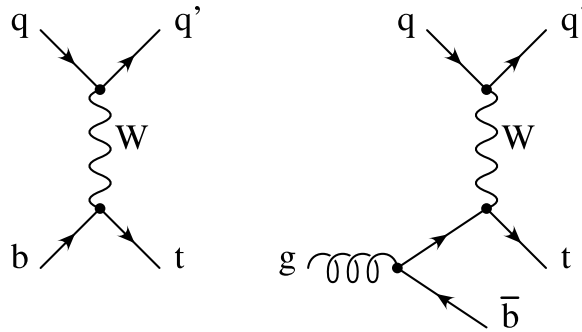


Figure 2.4: The leading order (left) and an important next-to-leading order (right) Feynman diagrams for the t -channel single top production mode [67].

as tb and tqb , respectively.

Table 2.3: Total cross sections for single top quark production at $\sqrt{s} = 1.96$ TeV with $m_t = 175$ GeV.

Process	Cross Section [pb]
s -channel (tb)	0.88 ± 0.11
t -channel (tqb)	1.98 ± 0.25
$s + t$	2.86 ± 0.27

2.4.1 Motivation for Single Top

Measuring the single top quark production cross section (σ) and the angular differential cross section ($\frac{d\sigma}{d\Omega}$) is interesting as a test of the Standard Model as well as a probe for new physics beyond the Standard Model. Perhaps the most interesting product of a single top quark cross section measurement is a direct determination of the CKM matrix element $|V_{tb}|$ since the cross section is proportional to the square of this quantity ($\sigma \propto |V_{tb}|^2$). If one assumes a unitary 3x3 CKM matrix then by measuring $|V_{ub}|$ and $|V_{cb}|$, $|V_{tb}|$ is required to be within the following range:

$$0.9991 < |V_{tb}| < 0.9994 \quad (2.5)$$

By relaxing the assumption on a unitary 3x3 CKM matrix [89], $|V_{tb}|$ is allowed in the following range:

$$0.06 < |V_{tb}| < 0.9994 \quad (2.6)$$

A measurement of $|V_{tb}|$ that differed significantly from the range shown in Eq. 2.5 would be clear evidence for physics beyond the Standard Model such as a fourth generation of quarks.

Another interesting test of the Standard Model that can be made as a result of measuring single top is to probe the structure of the Wtb vertex. In the Standard Model all single

top quarks are produced via the left-handed electroweak interaction. If one were to boost into the top quark rest frame and know the four momenta of the decay products, then the angular decay distribution for the charged lepton from the W boson decay would follow the distribution shown in Eq. 2.7 where the angle θ_l is calculated with respect the top quark spin vector.

$$\frac{1}{\sigma} \frac{d\sigma}{d(\cos(\theta_l))} = \frac{1}{2} [1 + \cos(\theta_l)] \quad (2.7)$$

In practice, boosting into the correct top quark frame does not always result in 100% left handed polarized ($\hat{s} \bullet \hat{p} = -1$) top quarks [77]. For the s -channel process there an ambiguity resulting from the possibility of the up-type quark originating from the proton and the down-type quark origination from anti-proton and the reverse case. By boosting into the top quark frame and choosing the spin of the top quark along the direction of the anti-proton, one can expect to measure 98% polarization of top quarks. For the t -channel, the addition of higher order diagrams reduces the fraction of polarized top quarks. By boosting into the top frame and choosing the spin of the top quark along the direction of the forward down-type quark as seen in Fig. 2.4, one expects to measure 96% of top quarks to be polarized. By measuring the degree to which top quarks are polarized one can test the left-handed structure of the Wtb vertex.

Finally, the s and t -channel cross sections are sensitive to new particles predicted by theories beyond the Standard Model [89]. The Standard Model s -channel amplitude will interfere with any other diagram that includes a charged vector boson as the interaction mediator. One example of such a boson is the W' which results from an additional SU(2) group structure in the electroweak Lagrangian. The leading order Feynman diagrams for the W' boson production is shown in Fig. 2.5.

The Standard Model t -channel diagram will interfere primarily with new diagrams that involve flavor changing neutral currents (FCNC) including the top quark, which are predicted by models such as supersymmetry and technicolor [89]. A leading order Feynman diagram for this process is shown in Fig. 2.6.

Thus, by measuring each production cross section to high accuracy, one can test the

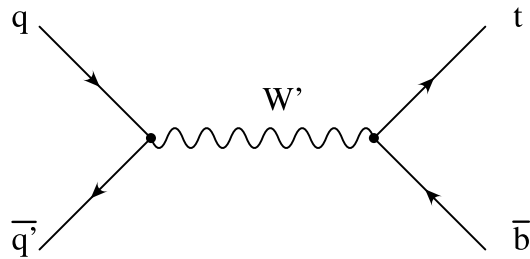


Figure 2.5: The leading order Feynman diagrams for the s -channel like process involving a W' boson [67].

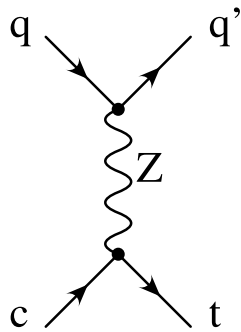


Figure 2.6: A leading order Feynman diagram for a t -channel-like process produced through FCNC [67].

validity of new physics models.

2.4.2 Signal Event Generation

An important part of a physics analysis is to have a determination of the kinematic distributions of signal events along with a cross section estimate to provide a normalization for the number of events to expect from the $p\bar{p}$ collisions. Both of these tasks can be accomplished by Monte Carlo generators. Monte Carlo generators use a set of random numbers to sample the N-dimensional phase space defined by the number of initial and final state particles in the event. The trial event is given a weight determined by the differential cross section, shown in Eq. 2.8, and is selected as a signal event if the weight is greater than a new random number sampled from the properly normalized differential cross section distribution. This method allows for more events to be selected from a region in phase space where the differential cross section is large and few events are selected from regions of low differential cross section. The final step of the Monte Carlo simulation is to hadronize⁴ and shower⁵ the final state partons and allow for additional energy in the event resulting from the breakup of the two protons in the collision. This final step is performed using the Pythia [84] Monte Carlo generator.

$$\frac{\partial\sigma(\vec{y})}{\partial\vec{y}} = \sum_{i,j} f_i(Q^2, x_1) f_j(Q^2, x_2) \times \frac{\partial\sigma_{hs,ij}(\vec{y})}{\partial\vec{y}} \quad (2.8)$$

In Eq. 2.8, $\frac{\partial\sigma_{hs,ij}(\vec{y})}{\partial\vec{y}}$ is the differential cross section for the parton-parton⁶ collision and $f_i(x_1, Q^2)$ and $f_j(x_2, Q^2)$ are the parton distribution functions (PDFs) that describe the number density of partons i and j inside the proton. The two parameters in these functions are the proton momentum fraction ($x = p_{\text{parton}}/p_{\text{proton}}$) and the energy scale (factorization scale) at which the two partons collide (Q). A plot of the parton density functions from the CTEQ [82] collaboration is shown in Fig. 2.7 for two distinct momentum transfers.

⁴Hadronization is the process of forming bound states (hadrons) between two or three quarks. A bound state of two quarks is called a meson and a three quark bound state is called a baryon.

⁵A shower, or parton shower, is the result of multiple gluon emission from final state particles.

⁶A parton is a constituent particle within the proton.

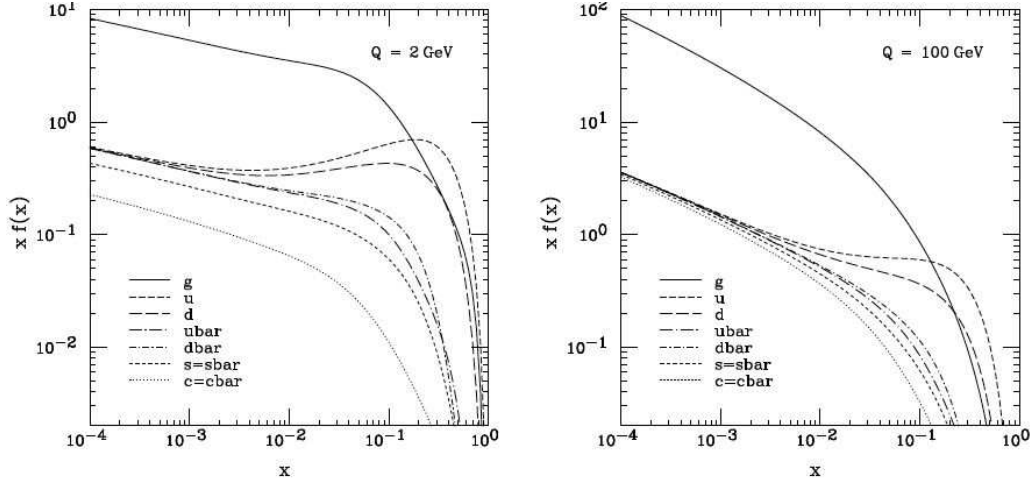


Figure 2.7: CTEQ 6M parton distribution functions for the gluon and all quark flavors for a small momentum transfer (left) and large momentum transfer (right). The x -axis is the proton momentum fraction of the parton and the y -axis is the parton density [82].

Single top signal events are generated using the CompHEP based SingleTop [38] Monte Carlo generator. The following two sections describe the generation of s -channel and t -channel production. All events were generated using CTEQ6L1 PDFs. The s -channel events were generated with $Q^2 = m_t^2$ and t -channel events were generated with $Q^2 = (m_t/2)^2$.

s-channel Generation Using CompHEP

It has been shown in [88] that s -channel kinematic distributions between leading order (LO) and next-to-leading order (NLO) in α_s are the same up to an overall normalization. The ratio of NLO to LO events, called a k -factor, is 1.3 for the s -channel production mode. Fig. 2.8 shows the transverse momentum (p_T) and pseudorapidity⁷(η) distributions for s -channel events generated by SingleTop.

⁷The pseudorapidity is related to the polar angle θ . More discussion of this variable is given in Chapter 3.

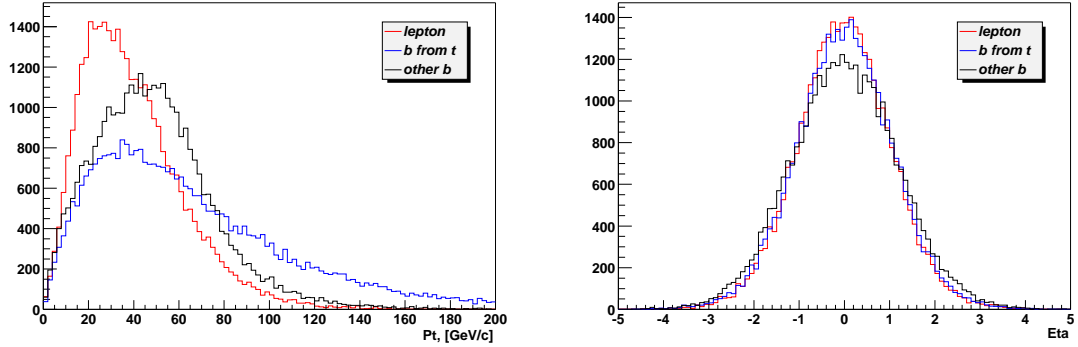


Figure 2.8: p_T (left) and η (right) distributions of final state particles in s -channel events [67].

t-channel Generation Using CompHEP and Pythia

Generating t -channel Monte Carlo events is slightly more difficult than s -channel events because the effective cross section of higher order Feynman diagrams ($qg \rightarrow q'tb$), shown in Fig. 2.4, is of the same order as the leading order diagram ($qb \rightarrow tq'$). A proper treatment of the combination is required to avoid double counting regions of phase space where the two matrix elements overlap. The SingleTop generator avoids double counting by defining two distinct regions of phase space where the different processes are the dominant contribution to the total t -channel cross section. The first region of phase space is defined by $p_T(b) < 10$ GeV. In this region the final state b quark is produced by Pythia through initial state radiation (ISR). The second phase space region is defined by $p_T(b) > 10$ GeV. In this region the b quark is produced by the next-to-leading order Feynman diagram shown in Fig 2.4. To ensure a smooth transition from low to high b quark p_T , the weight for the low p_T region is multiplied by a k -factor to make the leading order Pythia generated b quark p_T match the next-to-leading order b quark p_T distribution. The k -factor used at the Tevatron is 1.21 and the effective NLO cross section used in the SingleTop generator is shown in Eq. 2.9.

$$\sigma_{\text{NLO}} = K\sigma_{\text{Pythia}}|_{p_T(b)<10} + \sigma_{\text{CompHEP-SingleTop}}|_{p_T(b)>10} \quad (2.9)$$

The result of the b quark p_T splicing is an almost exact reproduction of many NLO dif-

ferential distributions. Fig. 2.9 shows p_T and η distributions for t -channel events generated by SingleTop.

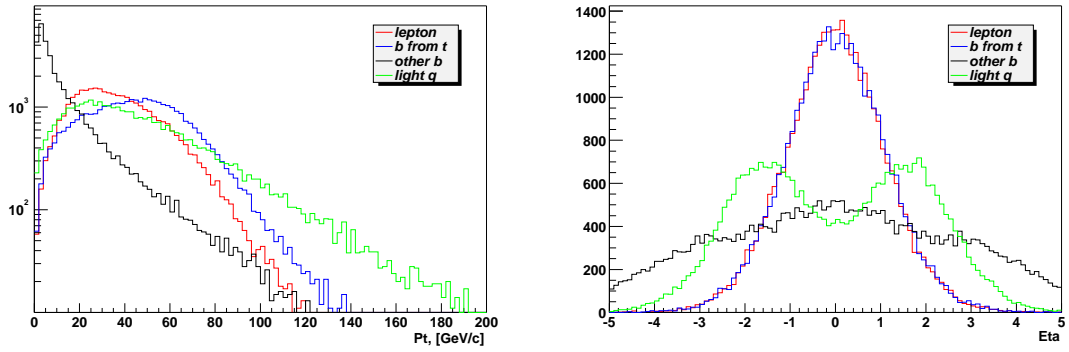


Figure 2.9: p_T (left) and η (right) distributions of final state particles in s -channel events [67].

Chapter 3

EXPERIMENTAL APPARATUS

All data used in the single top quark analysis was produced by high energy $p\bar{p}$ collisions at the Tevatron accelerator and recorded by the DØ detector. The Tevatron is currently the only collider with enough center of mass energy to directly produce top quarks in relative abundance. Section 3.1 describes how protons are accelerated to an energy of 980 GeV as well as how antiprotons are created to produce $p\bar{p}$ collisions at $\sqrt{s} = 1.96$ TeV. Sections 3.2 and 3.3 give an introduction to $p\bar{p}$ collisions at the Tevatron and explain several useful quantities which described particles produced in the collisions. Finally, Section 3.4 describes the DØ detector that is used to collection information about the particles produced in the $p\bar{p}$ collisions.

3.1 Fermilab Accelerator Complex

The Fermilab accelerator complex is a chain of accelerators designed to produce and collide two circulating beams of protons and antiprotons each with an energy of 980 GeV. Fermilab employs five unique accelerators to create and accelerate protons and antiprotons: the Cockcroft-Walton, the LINAC, the Booster, the Main Injector, and the Tevatron. Fig. 3.1 shows a schematic of these accelerators.

3.1.1 Cockcroft-Walton

The first accelerator in the chain is the Crockroft-Walton. In this accelerator a hydrogen gas is heated which allows an additional electron to bond with the hydrogen atom producing a net negative charge. The Crockroft-Walton is a DC voltage ladder that produces a voltage difference of 750 kV across which the newly negatively hydrogen ions are accelerated.

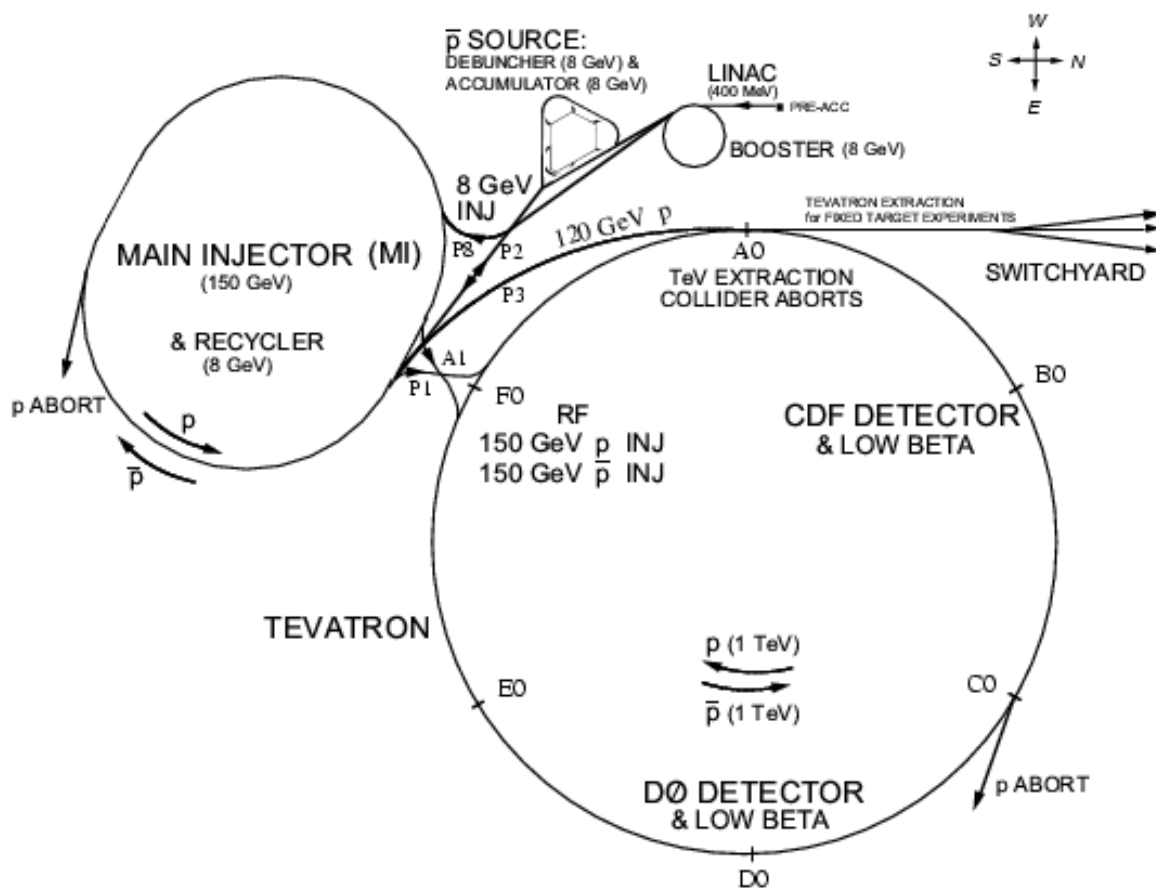


Figure 3.1: Schematic of the Fermilab accelerator complex [63].

3.1.2 LINAC

After the negatively charged hydrogen ions have been accelerated to an energy of 750keV, they are further accelerated by the LINAC (LINear ACcelerator). The LINAC is a 130-m long set of metallic drift tubes separated by vacuum gaps. An alternating electric field produced by a radio frequency (RF) power source accelerates the negatively charged hydrogen ions across the gap while the electric field is parallel with the ion direction of motion. When the field direction reverses the ions are shielded by the metallic drift tubes. As the ions increase their speed the gap length and drift tube length increases as shown in Fig. 3.2. Because the LINAC uses an alternating electric field the continuous ion beam produced by the Cockroft-Walton is altered such that the protons are concentrated or “bunched” together. By the end of the acceleration the proton bunches are separated by 5 ns and have an energy of 400 MeV. Finally, the orbital electrons are removed by passing the ions through a carbon foil leaving behind the positively charged protons.

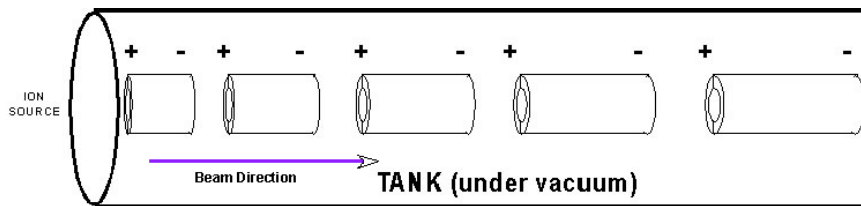


Figure 3.2: Cartoon example of the linear accelerator’s alternating series of gaps and drift tubes [2].

3.1.3 Booster

The next accelerator in the chain is the Booster, which is a circular synchrotron accelerator 475-m in circumference. The Booster consists of RF cavities that accelerate the 400 MeV proton bunches to an energy of 8 GeV. The proton bunches circulate the Booster 16,000 times and the entire acceleration process takes 33 ms.

3.1.4 Main Injector

The Main Injector is the next accelerator in the chain after the Booster. This accelerator uses RF cavities to accelerate the proton bunches to an energy of 120 GeV and employs strong magnets to keep the protons moving along a circular path. After the acceleration there are two possible paths for the protons: \bar{p} production or continued acceleration. The protons that will eventually circulate in the Tevatron ring are further accelerated to an energy of 150 GeV and then continue to circulate the Main Injector ring until needed [2]. The remaining protons are used to create antiprotons that will also eventually circulate in the Tevatron ring. Antiprotons are created when 120 GeV protons from the Main Injector strike a fixed 7 cm thick nickel target producing a spray of short lived particles and anti-particles. From this spray roughly 20 antiprotons are produced for every million protons used [1]. All particles produced from the collision are focused and collimated by a lithium lens. A bending magnetic is employed to separate the negatively charged antiprotons from all positively charged particles. To remove the remnant bunch structure the antiprotons are passed through a debuncher, which separates the antiprotons in space-time as well as reducing their energy spread. A process known as stochastic cooling is applied to further reduce the energy spread. This process uses ultra-cold electronics (-269° C) to detect and alter the particles trajectories to make their orbits and thereby their energies more uniform. Because each $p\bar{p}$ collision requires $\sim 10^{10}$ antiprotons the final stage for \bar{p} production is to collect and store large quantities of antiprotons. This is done with the accumulator, which allows for many circulating beams of antiprotons to be kept for many hours. Once enough antiprotons have been collected they are sent to the Main Injector where they are accelerated to a final energy of 150 GeV.

3.1.5 Tevatron

The Tevatron is the final acceleration stage for the protons and antiprotons, which reach an energy of 980 GeV using RF cavities in the same manner as the Booster and the Main Injector [3]. The Tevatron uses nearly 1,000 superconducting magnets running at 4.3° K with a magnetic field strength of 4.2 T to bend the two circulating beams around the nearly

6 $\frac{1}{2}$ km circumference ring. At an energy of 980 GeV the bunches circulate the Tevatron ring nearly 57,000 times per second crossing one-another every 396 ns. The two circulating beams are separated in the ring to avoid direct collisions unless they are further focused. In the Tevatron ring there are two places where the beams are focused, which correspond to the two large experiments: DØ and CDF.

3.2 $p\bar{p}$ Collisions

When the two circulating beams at the Tevatron are brought into focus, an enormous range of kinematically allowed processes and final state decays are possible. While the outcome of a particular $p\bar{p}$ collision is random, the rate at which certain processes occur can be calculated within the Standard Model framework. The most common type of collision is an inelastic $p\bar{p}$ collision which produces one or more particles scattered at low angles with respect to the beam axis. These processes usually do not involve much energy transfer between the colliding particles and are therefore called low- p_T events. More rare processes, such as top quark or W boson production, require much more energy to be transferred between colliding particles. These processes occur when one of the constituent quarks or gluons inside the proton collide with another quark or gluon from the antiproton. This process is referred to as the hard scatter process. The hard scatter process can produce on-shell resonances ($Q^2 = M^2$) of heavy particles such as a W Boson or sometimes it can produce very short lived virtual particles ($Q^2 \neq M^2$) such as the case with s -channel single top quark production where a W boson is produced with $Q^2 > M_W^2$.

The heavy particles produced in the hard scatter collision will decay into more stable particles as governed by the interactions allowed in the Standard Model. For very heavy particles with short lifetimes the decay occurs in a space much smaller than the resolution of any detector. For instance, the top quark lifetime is $\sim 10^{-24}$ s which is more than nine orders of magnitude smaller than the fastest detector electronics. In fact almost all short-lived particles produced in the hard scatter can not be measured directly, but instead their presence is inferred from precise measurements of the their decay products.

The remainder of this chapter is dedicated to describing the DØ detector and how it makes the measurements required to infer the presence of heavy resonances such as the

top quark. Section 3.3 gives a short introduction to the coordinate system convention used throughout the rest of the chapter as well as introduces several new units typically used in high energy physics. Section 3.4 describes the DØ detector and explains how it is used to measure the particles resulting from the $p\bar{p}$ collisions at the Tevatron.

3.3 Coordinate System and Units Convention

The DØ detector is typically referenced using a spherical coordinate system (r, θ, ϕ) with an origin located at the center of the detector. The polar angle θ is defined with respect to the beam axis where 0° is aligned with the proton direction and 180° is aligned with the antiproton direction. The azimuthal angle ϕ is defined with respect to the x -axis as shown in Fig. 3.3. The z -axis is defined to be parallel with the beam axis with the positive direction corresponding to $\theta = 0^\circ$ and the negative direction corresponding to $\theta = 180^\circ$.

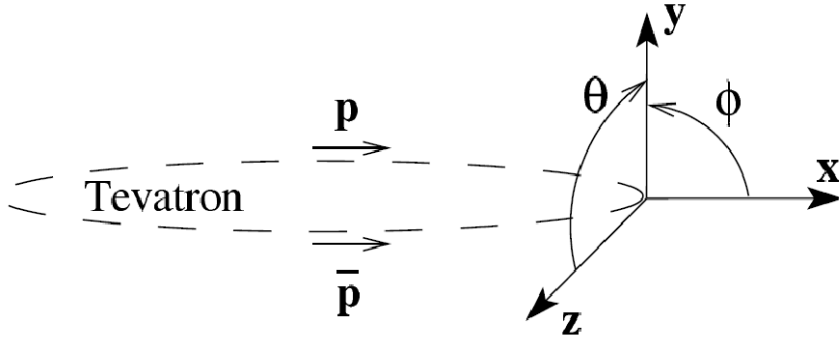


Figure 3.3: DØ coordinate system with respect to the Tevatron ring [86].

It is often convenient to convert the angle θ to a quantity called pseudorapidity η defined in Eq. 3.1.

$$\eta = -\ln \left[\tan \left(\frac{\theta}{2} \right) \right] \quad (3.1)$$

This quantity is identical, in the limit of massless particles, to the true rapidity y , shown in Eq. 3.2, which is invariant under a Lorentz boost along the z -direction. This is useful

because $p\bar{p}$ collisions at the Tevatron usually occur with such a boost. The pseudorapidity is 0 for a particle with $\theta = 90^\circ$ and approaches ∞ as $\theta \rightarrow 0^\circ$.

$$y = \frac{1}{2} \log \left[\frac{E + p_z}{E - p_z} \right] \quad (3.2)$$

Another quantity used when describing the relationship between two objects or the size of an object in the DØ detector is the solid angle ΔR defined in terms of $\Delta\phi = \phi_1 - \phi_2$ and $\Delta\eta = \eta_1 - \eta_2$.

$$\Delta R = \sqrt{(\Delta\phi)^2 + (\Delta\eta)^2} \quad (3.3)$$

Finally, the luminosity is important when describing the intensity of an interaction or of the accumulated amount of data. The rate of a certain process is equal to the luminosity \mathcal{L} times the Lorentz invariant cross section σ , as shown in Eq. 3.4.

$$\text{Rate} = \frac{dN}{dt} = \sigma * \mathcal{L} \quad (3.4)$$

Most cross sections at the Tevatron are given in terms of pico-barns (10^{-36} cm^2) thus the units of luminosity are $\text{pb}^{-1}\text{s}^{-1}$. The time integrated luminosity $\int \mathcal{L} dt$, with units of pb^{-1} , is used when discussing the total number of collected events.

3.4 DØ Detector

The DØ detector [21] is a collection of smaller sub-detectors working in tandem to detect and measure all particles produced from the hard scatter collision. The inner-most detectors near the beam pipe are the tracking detectors, described in Section 3.4.1, which record the paths of charged particles as they enter and leave the detector. The next layer of the detector is the calorimeter, described in Section 3.4.2. The calorimeter measures the energy of the lightest electromagnetically interacting particles, such as the electron and the photon, and strongly interacting particles, such as pions or neutrons. Another sub-detector, called the luminosity monitor, described in Section 3.4.3, is designed to record the presence of an inelastic $p\bar{p}$ collision in the bunch crossing. This information is used in the analysis to normalize backgrounds and expected signal yields. The outer-most layer of the

$D\bar{O}$ detector is the muon detector, which is described in Section 3.4.4. Once the collision has been measured a complex set of trigger decisions, described in Section 3.4.5, must be satisfied before the event is recorded to tape for later analysis.

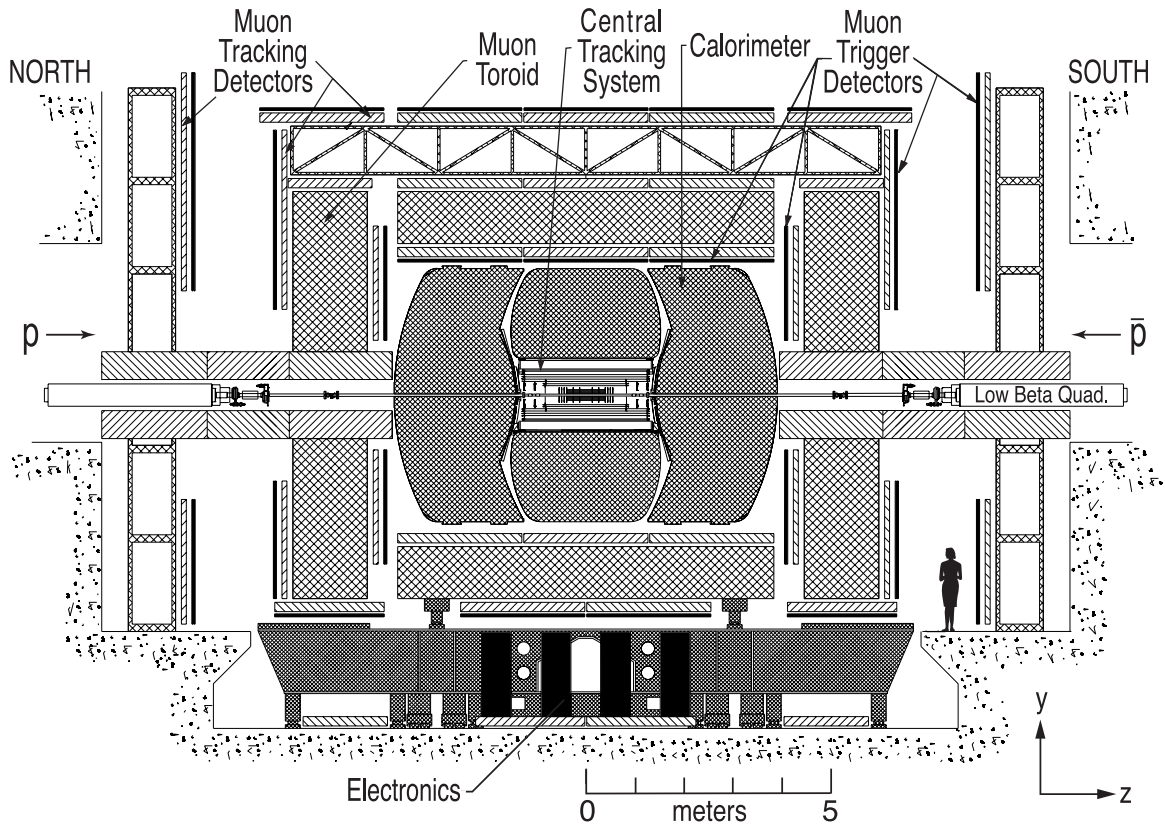


Figure 3.4: Schematic side-view of the $D\bar{O}$ detector [21].

3.4.1 Tracking Detectors

The innermost layer of the $D\bar{O}$ detector is a set of two tracking detectors designed to measure the flight path of charged particles. The two detectors, shown in Fig. 3.5, are the silicon microstrip tracker (SMT) and the central fiber tracker (CFT). The SMT and CFT are located within a 2T magnetic field generated by a superconducting solenoid magnet. The presence of the magnetic field within the tracking detectors will deflect all charged particles allowing a measure of their charge and momentum through the sign and radius

of the induced curvature.

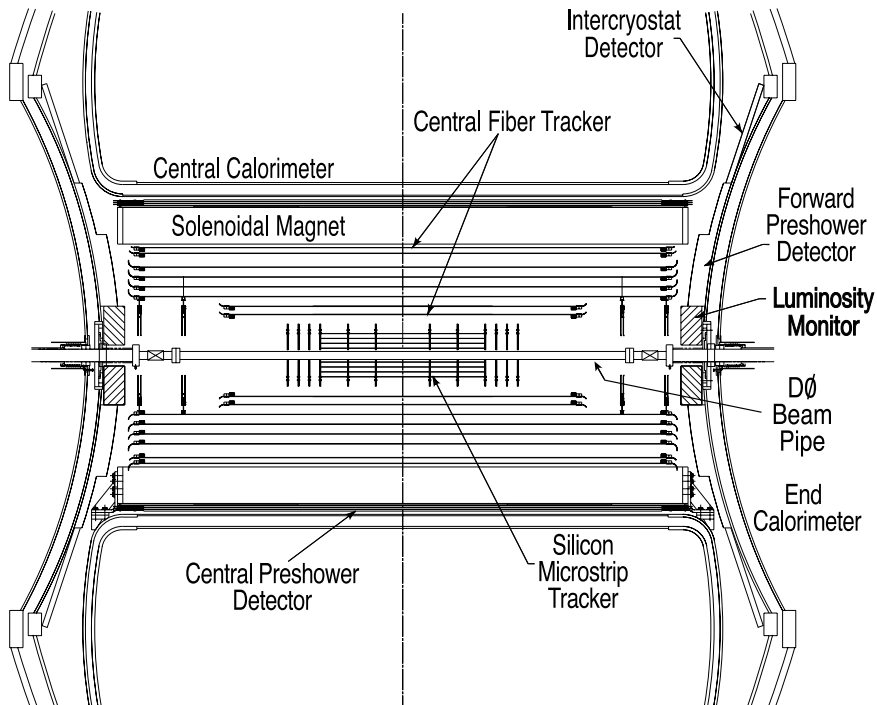


Figure 3.5: Schematic of the two tracking detectors (SMT and CFT) as well as the superconducting solenoid magnet [21].

Silicon Microstrip Tracker

The SMT is located immediately outside the Tevatron beam pipe and is designed to provide high resolution position measurements of charged particles. The SMT is a collection of doped silicon detectors depleted of electric charge by the application of a reverse bias voltage. As a charged particle enters the depleted region it ionizes the silicon creating electron-hole pairs. The result of the applied electric field is to force the charges to drift towards active sensors. The typical drift distance for charges in the silicon is $300\ \mu\text{m}$. A schematic of the SMT is shown in Fig. 3.6.

The geometry of the SMT is dictated by the length of the interaction region¹ and a

¹The typical Gaussian width of the hard scatter interactions is 25 cm centered around $z=0$.

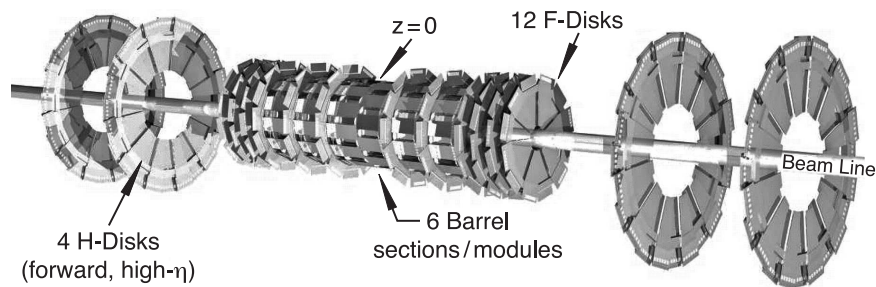


Figure 3.6: Schematic of the silicon microstrip tracker sub-detector [21].

desire to maximize the number of layers a charge particle traverses. To achieve this goal the detector is organized into three structures: the barrel detector, the F-discs, and the H-discs. The barrel detector is a set of six barrels concentric with the beam pipe that each contain four double-sided layers of silicon wafers. The barrels provide coverage for centrally produced charged particles with $|\eta| < 1.1$. The F-discs are also double-sided silicon wafers. These silicon detectors are oriented perpendicular to the beam axis in contrast with the concentric barrels. There are twelve F-discs in the SMT, six in the central region that cap each barrel and six in the forward region. The SMT also has four silicon detectors at high $|z|$ called H-discs, which are oriented perpendicular to the beam axis. In total the SMT has 912 individual readout modules and nearly 800,000 individual readout channels.

Central Fiber Tracker

Immediately outside of the SMT is the central fiber tracker (CFT) which occupies the radial distance of 20 to 52 cm from the beam pipe. The CFT is organized into 8 layers of scintillating fibers which produce light when a charged particle traverses the fibers. Each layer of the CFT consists of two sets of fibers: one that is parallel with the beam axis and one that is rotated 3° with respect to the beam axis. The fibers in the tracker are $835 \mu\text{m}$ in diameter and composed of organic scintillating compounds surrounded by a thin layer of cladding designed to provide total internal reflection inside the fiber. The light produced in the fiber is carried out of the detector by wave guides with typical travel distances between 8 and 11 m. Because the light is only read out at one end of the fiber the other end is

coated with sputtered aluminum which reflects 90% of the light back to the end which is read out. An endview schematic of the CFT layers and their associated waveguides is shown in Fig. 3.7. Light produced in the CFT is recorded on silicon avalanche photon counters called VLPCs (visible light photon counter). The VLPCs operate at 9° K to reduce thermal noise and achieve a quantum efficiency of 75%.

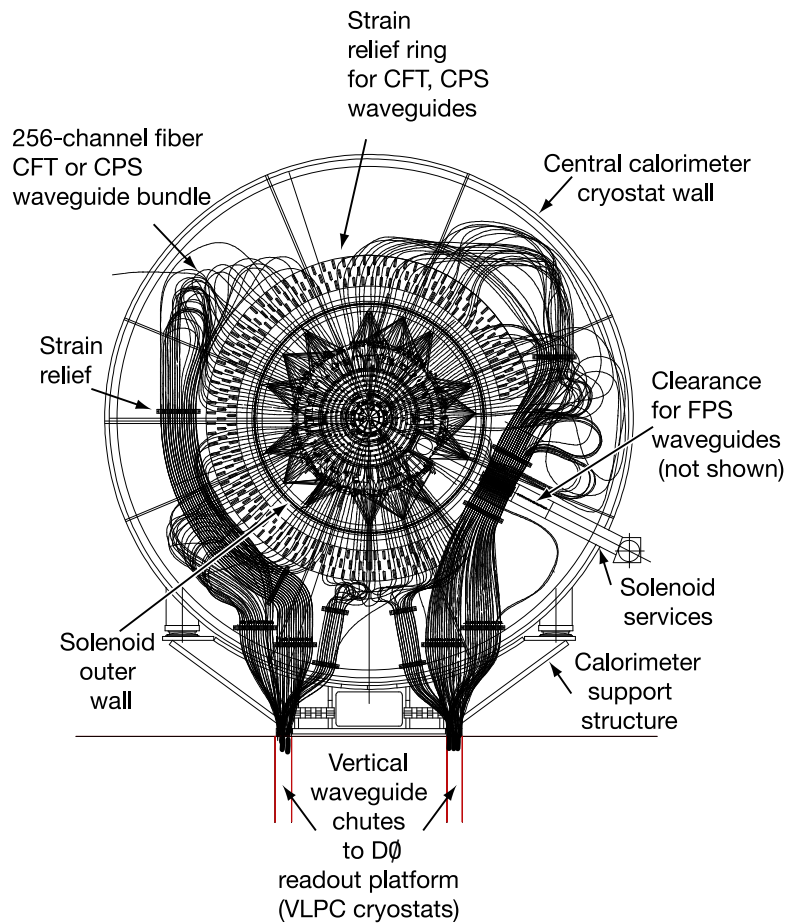


Figure 3.7: Schematic endview of the central fiber tracker with corresponding waveguides [21].

3.4.2 Calorimetry

The next layer of the $D\emptyset$ detector is the calorimeter. The calorimeter is designed to measure the energy of electromagnetically interacting particles such as electrons and photons as well as strongly interacting particles such as pions and neutrons. The $D\emptyset$ calorimeter is divided into three sub-detectors: one central region (CC) and two end-cap regions (EC) as seen in Fig. 3.8. Each region is encased in its own cryostat held at a constant temperature of 90° K. The region between the two cryostats, $0.8 < |\eta| < 1.4$, is called the inner cryostat region (ICR) and contains active scintillator to provide a minimal energy measurement in this region.

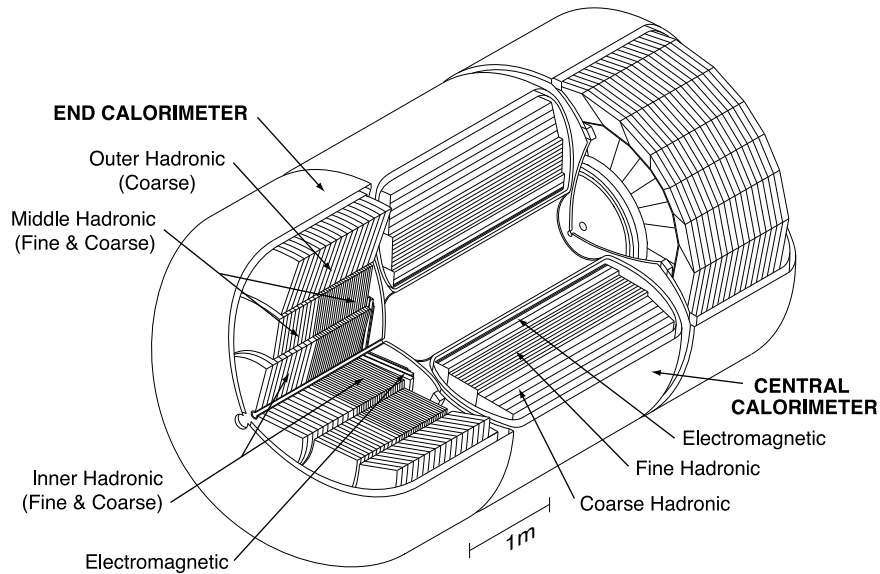


Figure 3.8: 3D view of the $D\emptyset$ calorimeter [21].

Each detector region, except the ICR, measures energy using a similar approach by inducing the incoming particles to produce an electromagnetic shower as they collide with a dense material. As particles from the shower enter the active region they will ionize the material. The ions in the active material move towards a sensor due to an applied bias voltage. The amount of charge collected on the sensor is then proportional to the energy deposited by the ionizing particle. An example of an electromagnetic shower originating

from a photon is shown in Fig. 3.9. The typical ion drift time in the DØ calorimeter is ~ 450 ns.

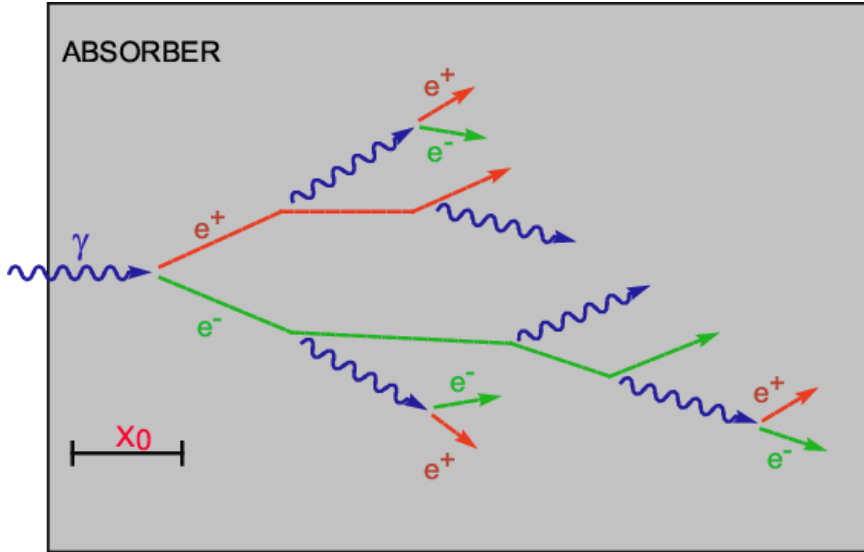


Figure 3.9: Initial stages of an electromagnetic shower caused by a photon interacting with an absorber material. The radiation length x_0 is the typical distance a photon will travel before producing an e^+e^- pair or the distance before an electron will radiate a photon [9].

The DØ calorimeter consists of an inner detector called the EM calorimeter and an outer detector called the hadronic calorimeter. The EM calorimeter is constructed of alternating layers of depleted Uranium, which acts as the shower inducing material, and liquid Argon, which acts as the active medium. The depleted Uranium plates are 3 mm thick in the central region and 4 mm thick in the forward end-cap region while the liquid Argon active region is 2.3 mm thick. An cartoon drawing of this arrangement can be seen in Fig. 3.10. The EM calorimeter has four layers of cells representing nearly 21 radiation lengths. The hadronic calorimeter is actually two detectors: one called the fine hadronic calorimeter which employs 6 mm thick Ur-Ni alloy as the shower inducing material and the coarse hadronic calorimeter which uses 46.5 mm thick plates of copper in the central region and stainless steel in the forward region. The hadronic calorimeter also uses liquid Argon as the active material. The combination of the fine and coarse hadronic calorimeters provides an additional 7 radiation

lengths to the detector. The numerous radiation lengths are important to ensure that a particle deposits nearly all of its energy in the detector.

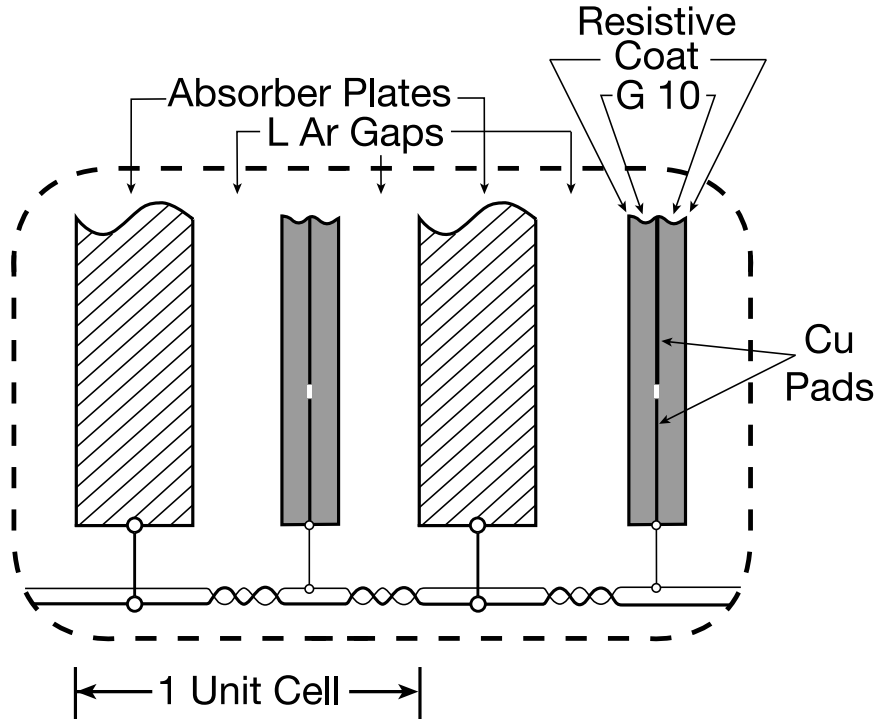


Figure 3.10: Example of a typical calorimeter cell of alternating absorber and active material. Particles traverse the calorimeter cell from left to right in this diagram [21].

The $D\emptyset$ calorimeter also has fine segmentation (i.e. radial size of the cells), which allows for excellent energy and position measurement of particles as they shower in the detector. The segmentation of the EM calorimeter in $\delta\eta \times \delta\phi$ is 0.1×0.1 for all layers except the third layer, where the segmentation is 0.05×0.05 . The fine segmentation in the third layer is because the electromagnetic shower is expected to reach a maximum in this layer. The fine hadronic layers of the calorimeter also have a segmentation of 0.1×0.1 , while the segmentation in the coarse hadronic calorimeter is 0.2×0.2 . An octant of the $D\emptyset$ calorimeter including segmentation can be seen in Fig. 3.11.

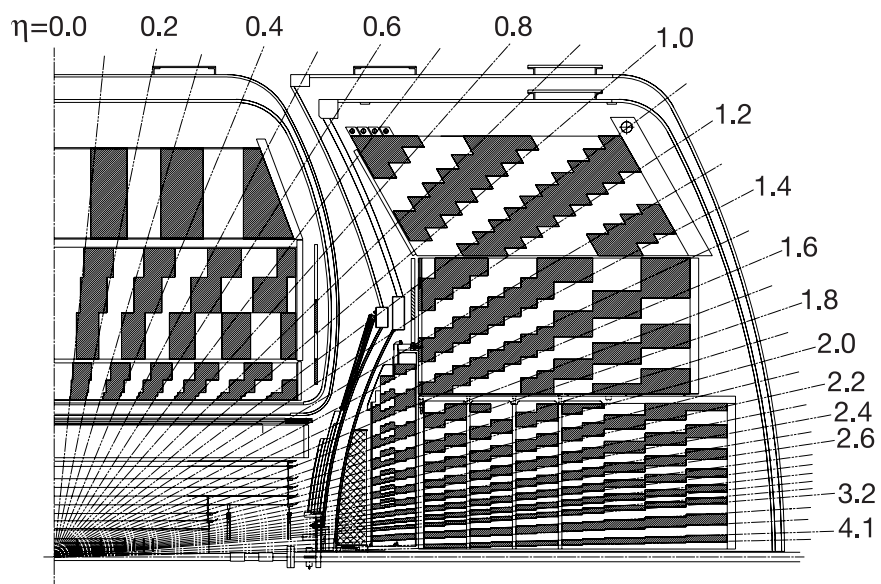


Figure 3.11: Octant of the DØ calorimeter. The fine segmentation of the calorimeter is clearly seen in this diagram [21]. The alternating dark and light blocks represent cells in different calorimeter towers.

3.4.3 Luminosity Monitor

Located directly in front of the end-cap calorimeters, covering a η range between 2.7 and 4.4, is the luminosity monitor, which collects information about inelastic $p\bar{p}$ collisions for each bunch crossing. The luminosity monitor is a set of 24 plastic scintillators which can detect low angle (high η) fragments from the break-up of the protons in the $p\bar{p}$ collision. The scintillators produce light when the charged fragments traverse the detector and that light is recorded by photo-multiplier tubes. A schematic of the luminosity monitor is shown in Fig. 3.12.

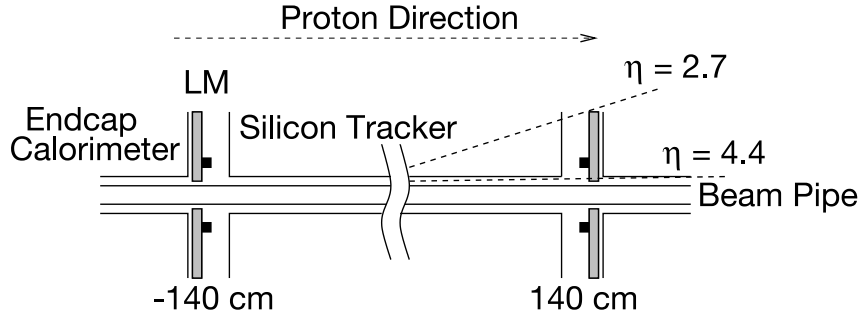


Figure 3.12: Schematic of the DØ luminosity monitor shown in relation to the beam pipe, SMT, and endcap calorimeter [21].

Collecting information about inelastic collisions is vital to properly normalize all data collected at DØ. The luminosity monitor is designed to measure the inelastic $p\bar{p}$ cross section, which is a quantity that is known from measurements by previous experiments. By measuring the inelastic $p\bar{p}$ cross section the total integrated luminosity to which the DØ detector has been exposed to can be measured [60, 61]. A derivation of the luminosity from the measured $p\bar{p}$ inelastic cross section can be found in Appendix C.

Along with providing a luminosity measurement, the detector also acts as a fast vertex finder. By measuring the relative difference of coincidence counts in the North and South detectors the z position of the vertex can be determined from Eq. 3.5, where t_{\pm} are the time measured by the North (+) and South (-) detectors, respectively. The time of flight resolution for the luminosity detector is 0.3 ns.

$$z = \frac{c}{2}(t_+ - t_-) \quad (3.5)$$

3.4.4 Muon Detector

The outer-most layer of the DØ detector is the muon system. A special detector is required to measure muons because they do not deposit much energy in the tracker or calorimeter and thus a confirmation of their presence using these sub-detectors alone is difficult to infer. The muon detector has two active regions called the central region for $|\eta| < 1$ and the forward region for $1 < |\eta| < 2$. The system also employs a 2 T toroid iron magnet to bend the muons from their original paths. The addition of the magnetic field helps to provide a local momentum measurement in the event the momentum can not be determined from the tracking detector. Additional shielding surrounding the beam pipe near the forward muon detector is designed to reduce spurious beam effects which dramatically reduces the amount of radiation to which the detector is exposed. A schematic of the muon system and the beam shielding can be seen in Fig. 3.13.

The muon system at DØ is a three layer detector, both in the central and forward regions, consisting of drift chambers for precise position measurement and scintillator counters for muon identification and fast triggering (Section 3.4.5). The scintillator counters produce light when the muon passes through the detector which is then collected by a photo-multiplier tube. The drift chambers have a central wire held at a large voltage surrounded by an inert gas. As the muon enters the chamber it will ionize the gaseous organic compound mixture and the resulting free charges will drift towards the wire. The position of the muon is found by analyzing the current profile in the wire. In the central region the drift chambers are called PDTs (proportional drift tubes) and are rather large with typical areas of $2.8 \times 5.6 \text{ m}^2$. The forward region uses smaller drift chambers called MDTs (mimi drift tubes), which are a collection of eight cells of size $9.4 \times 9.4 \text{ mm}^2$. The position resolution of the drift chambers is $\sim 1 \text{ mm}$.

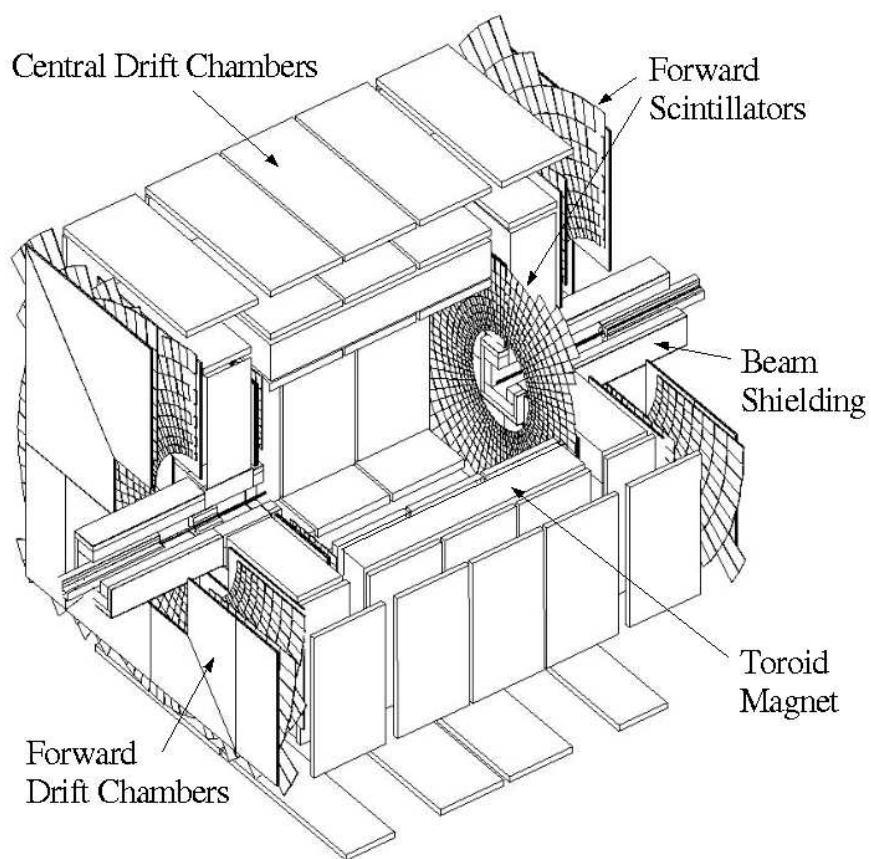


Figure 3.13: 3D view of the DØ muon detector [21].

3.4.5 Trigger and Data Acquisition System

The previous sections in this chapter describe how the $D\bar{O}$ detector collects information from $p\bar{p}$ collisions at the Tevatron, which occur every 396 ns. While $D\bar{O}$ records information about every collision, it does not save every event to tape for two reasons: most collisions at the Tevatron are small angle inelastic collisions which have already been well studied and the total rate of data one can reliably store to tape is limited to $\sim 30\text{MB/s}$. Because $D\bar{O}$ can not save every event, a sophisticated trigger system is employed to reduce the total rate to tape to 50 Hz. This trigger system attempts to select the most “interesting” events, which will be used for an analysis or future calibration of the detector.

The trigger system is comprised of three independent stages called level 1, level 2, and Level 3, which are designed to reduce the total event rate from 1.7 MHz to 50 Hz. A schematic of the combined trigger system is shown in Fig. 3.14. The level 1 system is composed of hardware trigger elements and has the goal of reducing the initial rate of 1.7 MHz to 1.5 kHz. Because the level 1 trigger must act quickly to either accept or reject an event, the tools available for selecting interesting events is limited. At level 1 only calorimeter trigger towers, which are layers of calorimeter cell energies within a $\delta\eta \times \delta\phi = 0.2 \times 0.2$ space, signals in the muon drift chambers or scintillators, and the transverse momentum of charged particle tracks in the central fiber tracker are available for trigger decisions.

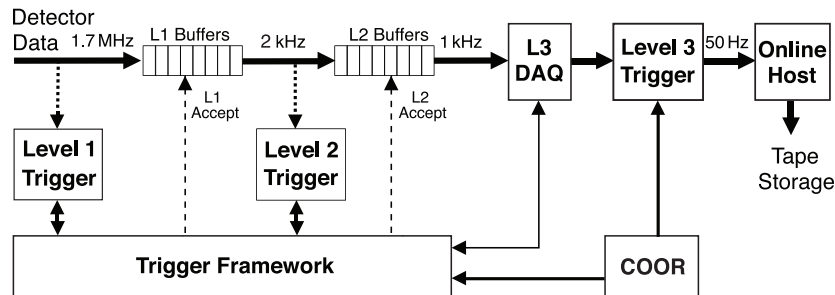


Figure 3.14: Cartoon drawing of the $D\bar{O}$ trigger system [21].

The level 2 trigger acts on all events which pass the level 1 trigger and is designed

to reduce the rate from 1.5kHz to 700Hz. The level 2 trigger uses detector specific pre-processing boards and a global detector board to make trigger decisions. The pre-processors collect data from the level 1 trigger system as well as readout information from the individual detectors. The pre-processors use this information to form physics objects such as electrons, jets, and missing E_T ². A global level 2 pre-processor uses all the information from the sub-detector pre-processors to make trigger decisions based on event-wide kinematics.

The next stage in the trigger selection process is the level 3 trigger, which is a software-based collection of algorithms executed on a collection of computer farm nodes. The goal of the level 3 trigger is to reduce the data rate to tape from 700 Hz to 50 Hz. The level 3 trigger requires the full detector readout to select events, thus all sub-detector data must be transmitted to the farm nodes. A level 3 data acquisition system was designed to transmit data over ethernet cables to the farm nodes. Upon a level 2 trigger accept a controller card in the sub-detector VME crate signals to a single board computer³, located in the VME crate, to begin collecting the crate data and store it in RAM memory located on the SBC. While the data is being collected by the SBCs, a dedicated SBC called the Routing Master is collecting information about the event number as well as the level 1 and level 2 triggers that initially selected the event. The Routing Master communicates with the level 3 computer farm regarding its availability (i.e. if it is busy processing events or waiting for a new event) and assigns each event a unique farm node to which all SBCs must send the event information. This process is repeated for each event which is selected by the level 2 trigger. When the SBC has the full crate data stored in memory and a routing command issued by the Routing Master, the crate data is transmitted via one of two 100 MB/s ethernet cables to the farm nodes.

Each event that is selected by the level 2 trigger ranges in size from 250 to 300 kB resulting in 200-300 MB/s of data being sent to the farm nodes. To handle this enormous data transfer rate, a set of CISCO 2948G ethernet switches concentrate ten 100 MB/s

²Physics objects and event-wide kinematic variables such as missing E_T are fully described in Chapter 4.

³The single board computers used in this DAQ are VMIC 7750 with a 933 MHz Pentium-III processor, 128 MB of RAM, 128 MB of on-board flash memory, and two 100 MB/s ethernet connectors. A few of the CFT crates use 2-1GB/s ethernet connector due to the high event sizes for these crates.

connections into a 1 GB/s optical fiber. The GB fibers are then brought to a CISCO 6509 ethernet switch capable of transmitting data at a rate of 16 GB/s. A schematic of this hardware setup and the data flow are shown in Fig. 3.15.

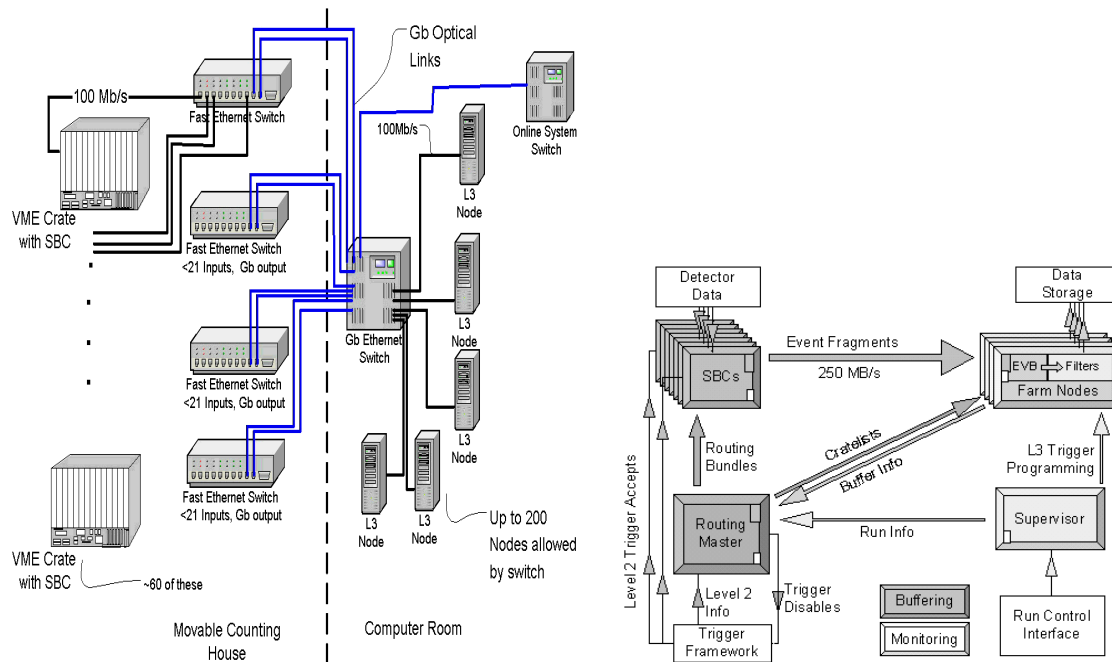


Figure 3.15: Experimental setup of the level 3 trigger and data acquisition system (left) and the flow of data through the system (right).

When the data arrives at a farm node it is processed by a program called the Event Builder. This software package combines event fragments from each sub-detector data and organizes them into a readable format for the level 3 trigger software. If the Event Builder does not receive data from all sub-detector crates within a one second window after receiving the first fragment the event is dropped. As stated earlier the Event Builder transmits the number of events it is currently processing to the Routing Master, allowing this software to choose farm nodes based on availability. Finally, between two and four level 3 trigger processes examine the event to see if it satisfies at least one of the trigger criteria. Events which pass the level 3 trigger are sent over 100 MB/s ethernet for temporary storage on a machine called the Collector. When enough events are accumulated the data is stored

on a machine called the Datalogger and finally to tape storage at the Feynman Computing Center located at Fermilab.

Chapter 4

EVENT RECONSTRUCTION AND SIMULATION

An important step in any high energy physics analysis is to reconstruct the hard scatter collision from the small deposits of energy measured in the detector. This chapter describes how each sub-detector is used to reconstruct a physics object, such as an electron or muon, which can be used to classify the event as signal or background. Section 4.1 of this chapter describes how electrons, muons, and calorimeter jets are reconstructed in data and Monte Carlo simulated events. Reconstruction of Monte Carlo events requires simulating the DØ detector such that each Monte Carlo event reproduces the detector resolution observed in data events. The DØ detector and trigger simulation is described in Sections 4.2 and 4.3, respectively. Finally, to correct for inevitable un-modeled effects in the simulation, correction factors must be applied to the Monte Carlo. The measurement of these factors and how they are applied is given in Section 4.4.

4.1 Object Reconstruction

The following section describes how physics objects are reconstructed using quantities measured in the detector. Section 4.1.1 describes how charged particle tracks are identified through small energy deposits in the central tracking detectors. Once all tracks have been identified the primary interaction vertex can be reconstructed as described in Section 4.1.2. Electrons and muons are identified through a series of quality cuts as described in Sections 4.1.3 and 4.1.4, respectively. Section 4.1.5 explains how jets are identified from showers of electromagnetic and hadronic particles in the calorimeter. Once jets, electrons, and muons have been identified the missing transverse energy can be calculated as the p_T imbalance in the event as described in Section 4.1.6. Finally, identification of heavy flavor jets using a neural network is described in Section 4.1.7.

4.1.1 Tracks

A track represents the three dimensional path of a charged particle as it traverses the detector. In the presence of a magnetic field, such as the case with the inner DØ detectors, all electrically charged particles move in a helical trajectory. Five parameters are needed to fully parameterize the helix and it is the task of the track finding algorithms to measure these parameters for all charged particles.

The first step in constructing a track is to form “hits” where ionizing particles have deposited energy in the tracking detectors. The formation of track hits is described in the *Track Hit Clustering* section below. Once the track hits have been created two algorithms are employed to link them together to create charged particle tracks. The two algorithms are described in the *Histogramming Track Finding Method* and *Alternative Algorithm* sections below. A final set of reconstructed tracks is formed by a global track reconstruction algorithm that combines the tracks found by the two previously mentioned algorithms.

Track Hit Clustering

Building a track begins with forming hits in both the SMT and CFT tracking detectors. A hit in the SMT detector is characterized by the deposition of energy in a silicon strip left by an ionizing particle. If the resulting collected charge is above threshold (to reduce noise hits), a hit is registered. If an adjacent silicon strip also registers a hit the two hits are combined. This process is repeated for any adjacent strip which registers a hit. The center of the SMT hit is given by the charge weighted average of the central position of each silicon strip¹. A hit in the CFT is formed when two fibers in each super layer register scintillation light indicating the presence of a charge particle traversing the fibers. Because the fibers have a relative 3° orientation, the $x - y$ coordinates are calculated as the intersection of two scintillating fibers.

¹Because the SMT detector is immersed in a magnetic field the electron-positron pairs created in the silicon will drift at an angle with respect to electric field lines within the silicon. This angle, known as the Lorentz angle, is corrected for when calculating the center of the SMT hit.

Histogramming Track Finding Method (HTF)

The histogramming track finding (HTF) [69] method is based on the principle that a particle which produces many hits in the transverse plane (x-y) will have a unique curvature and azimuthal angle. This method transforms (x-y) hits in the SMT and CFT and into a new plane defined by the curvature, ρ , and azimuthal angle, ϕ . Hits from the same particle will produce a peak in the $\rho - \phi$ space, whereas random hits will uniformly populate the space. An example of this procedure, known as a Hough transformation, for a 1.5 GeV muon track is shown in Fig. 4.1. A histogram is created of the hits in the new $\rho - \phi$ space and is processed through a two-dimensional Kalman filter, which attempts to remove "noisy" tracks with large track errors as well as incorporate detector geometry and material density. The result of the filter is a set of smoothed tracks whose track parameters have been re-fit with smaller errors. The longitudinal coordinate information is included by creating a new histogram in a space defined by the radial distance to the beam axis and the z coordinate. A second Hough transformation is performed into the (z_0, C) plane, where z_0 is the intersection of the track along the beam axis and C is the track inclination defined as $\frac{dr}{dz}$. The newly formed tracks are extrapolated either inward toward the SMT if the track finding began in the CFT or outward toward the CFT if the track finding began in the inner SMT detector.

Alternative Algorithm Tracking (AA)

The alternative algorithm (AA) [39] track finding method is based on a seed hit in one layer of the detector and building a track by incrementally including more layers of the SMT and CFT detectors. The algorithm takes SMT hits in the innermost layers and adds additional layers if the resulting extrapolated track radius of curvature is greater than 30 cm, which indicates the track must have $p_T > 180$ MeV. All possible combinations that meet these requirements are stored. The algorithm also allows for missing hits in the SMT or CFT if a hit in one of the outer layers is consistent with a previously found track. Also allowed are "CFT-only" tracks built from seeds in the CFT detector that have less than 3 hits in the SMT detector. Allowing tracks to be built in this manner dramatically increases the overall track finding efficiency of the algorithm.

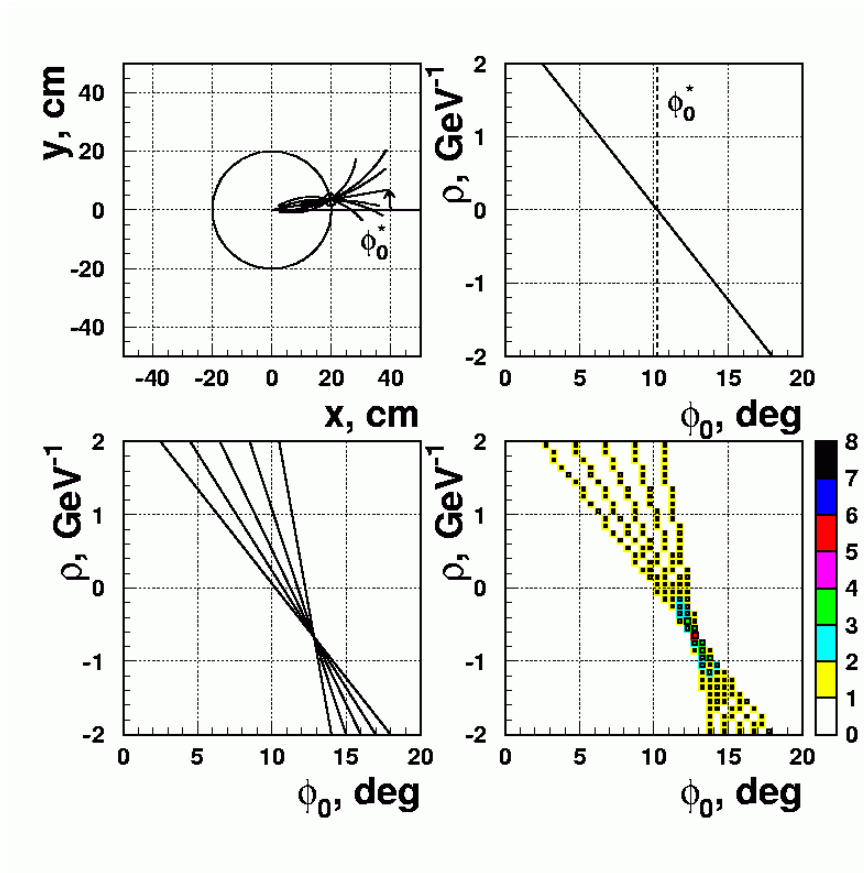


Figure 4.1: This histogramming track finding technique shown for an example of a single 1.5 GeV track of 5 hits. (a) The family of trajectories containing a given hit. (b) The geometric place of all trajectories containing a given hit in parameters space. (c) Curves from different hits intersect at one point corresponding to the track parameters. (d) The point of intersection can be seen as a peak in the (ρ, ϕ) histogram [69].

4.1.2 Primary Interaction Vertex

The primary interaction vertex is defined as the three-dimensional location of the hard scatter interaction. The hard scatter interaction vertex is very important to locate to allow discrimination of physics objects resulting from the $p\bar{p}$ collision and objects created from noise in the detector or other low energy inelastic $p\bar{p}$ collisions.

Primary interaction vertices are found using the adaptive primary vertex algorithm [33]. This algorithm attempts to assign all tracks with $p_T > 0.5$ GeV and at least two SMT hits to a vertex where the extrapolated track paths intersect. The result of this first pass fit to the primary vertex is a χ^2 for each track hypothesis. The algorithm then attempts a second pass fit to the primary vertex except this time each track receives a weight, shown in Eq. 4.1, that includes the χ^2 of the previous track fit.

$$w_i = \frac{1}{1 + e^{(\chi_i^2 - \chi_{\text{cutoff}}^2)/2T}} \quad (4.1)$$

Where the values for χ_{cutoff}^2 and T are 16 and 4, respectively. The vertex fitting procedure is repeated until the difference of weights from the previous iteration for each track is less than 10^{-4} .

The adaptive vertexing algorithm produces a list of possible vertices of which one might be the hard scatter vertex. To determine which vertex is the hard scatter vertex all tracks are assigned a probability to not originate from the hard scatter vertex. This probability, shown in Eq 4.2, is based on the $\log_{10}(p_T)$ ($F(p_T)$) distribution for tracks associated with a minimum bias² interaction as determined from Monte Carlo simulation.

$$P(p_T) = \frac{\int_{\log_{10}(p_T)}^{\infty} F(p'_T) dp'_T}{\int_{\log_{10}(0.5)}^{\infty} F(p'_T) dp'_T} \quad (4.2)$$

The individual track probabilities are combined for each track associated to each vertex found by the adaptive vertex algorithm to form a minimum bias vertex probability. The vertex which has the lowest minimum bias probability is selected as the hard scatter vertex. The distribution of this probability for minimum bias and hard scatter vertices is shown in Fig. 4.2.

²A minimum bias vertex is a vertex from an inelastic $p\bar{p}$ collision.

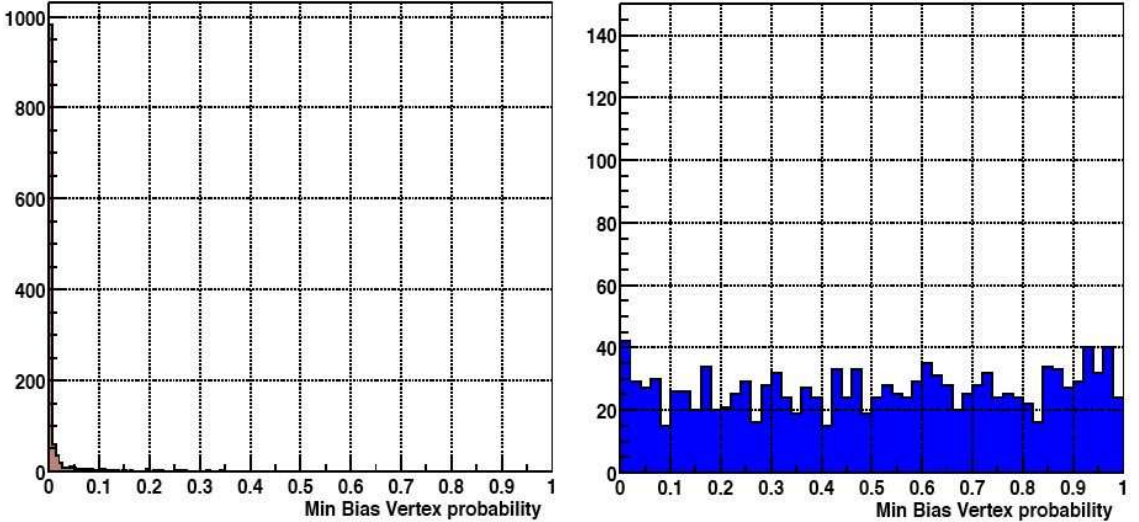


Figure 4.2: Minimum bias probability for the hard scatter vertex (left) and inelastic $p\bar{p}$ vertices (right). The vertex in the event with the lowest minimum bias probability is selected as the hard scatter vertex [33].

4.1.3 Electrons

Electrons in the DØ detector are characterized by narrow electromagnetic showers produced in the electromagnetic calorimeter [57]. Initial electron candidates are first identified by a cluster of calorimeter towers in the electromagnetic calorimeter. Once a tower is found the electron candidate is defined as the towers surrounding the highest E_T tower in a cone of radius 0.4. Since electrons will deposit most of their energy in the inner electromagnetic calorimeter the ratio of the electron candidate energy found in the electromagnetic calorimeter should be greater than 90% of the energy deposited in the electromagnetic calorimeter. The shape of the electromagnetic shower should also be consistent with an electron or photon shower. Electrons are distinct from photons in that they are charged particles thus all electron candidates are required to have a track with $p_T > 5$ GeV pointing in the direction of the electromagnetic cluster. To ensure that the electron is well measured it is also required to be isolated from other electromagnetic clusters. The isolation, shown in Eq. 4.3, is defined in terms of the electromagnetic calorimeter towers with $\Delta R < 0.2$ and $\Delta R < 0.4$ surrounding the electron candidate and is required to be less than 0.15.

$$f_{\text{iso}} = \frac{E_{\text{EM}}(\Delta R < 0.4) - E_{\text{EM}}(\Delta R < 0.2)}{E_{\text{EM}}(\Delta R < 0.4)} \quad (4.3)$$

Finally, to ensure high quality electrons a likelihood discriminant is created using seven variables that will separate electrons from W/Z boson decays (real electrons) from jets with large electromagnetic fractions (fake electrons). Electrons with a likelihood discriminant greater than 0.85 are considered true electrons from a W/Z decay.

4.1.4 Muons

Muons are reconstructed in the DØ detector by requiring hits in the three layers of the muon system from both the scintillators and wire chambers [59]. A muon candidate is required to register at least two wire hits and at least one scintillator hit in the A layer. At least two wire hits in the B and C layers as well as at least one scintillator hit in this region are also required for the muon. From the hits in the three layers it is possible to construct a local momentum measurement due to the curvature induced by the toroid magnet, however, the resolution of this measurement is quite poor. To improve the resolution, the local muon track is required to be matched with a track found by the global track reconstruction algorithm.

To remove muons produced by cosmic rays the muon candidate is required to be temporally coincident with a bunch crossing. After a bunch crossing is registered the muon candidate is required to hit all three layers within 10 ns. To further reduce the cosmic ray background the muon track is required to originate from the primary interaction vertex with a relative longitudinal distance less than 1 cm and a transverse distance of closest approach (DCA) less than 0.2 cm if there are no SMT hits and less than 0.02 cm if there is at least one SMT hit.

Finally, an isolation cut is applied to ensure the muon is the product of a W boson decay and not the result of a heavy flavor decay (e.g. $B \rightarrow \mu\nu_\mu D$). To remove muons from heavy flavor decays the candidate is required to be isolated ($\Delta R(\mu, \text{jet}) > 0.5$) from nearby jets since muons from heavy flavor decays will tend to be found inside or near a jet. To further reject muons from heavy flavor decays, two isolation variables are defined in terms of the muon track p_T and the sum of either calorimeter energy or track momentum surrounding

the muon momentum vector. The two isolation variables, shown in Eq. 4.4 and 4.5 are both required to be less than 0.2.

$$f_{\text{Track Isolation}}(\mu, \text{Tracks}) = \sum_{\text{tracks} \neq \mu, \Delta R < 0.5} p_T(\text{track}) \quad (4.4)$$

$$f_{\text{Calorimeter Isolation}}(\mu, \text{CalTowers}) = \sum_{\text{cal tower } 0.1 < \Delta R < 0.4} E_T(\text{cal tower}) \quad (4.5)$$

4.1.5 Jets

A jet is defined as a narrow cone of strongly interacting particles produced by the hadronization of strongly interacting particles such as quarks or gluons. A jet will shower in the electromagnetic and hadronic calorimeters and its energy is measured by sampling this shower in the many layers of the DØ calorimeter. A proper measurement of the jet energy and direction is needed to determine the original quark or gluon energy and momentum.

The Run II improved legacy cone algorithm [37] is used to reconstruct jets in the DØ calorimeter. This algorithm selects calorimeter towers with transverse energies³ greater than 0.5 GeV as seeds around which the jet is built. The algorithm collects all calorimeter towers in a cone⁴ of radius 0.5 around the seed tower and defines this as the jet candidate if it has $E_T > 1$ GeV. The central axis of the jet is defined by the E_T weighted midpoints of each calorimeter tower. This procedure is repeated throughout the detector until all jets are stable (i.e. the jet axis from one iteration to the next does not change) with a total $E_T > 6$ GeV. The final step of the jet finding algorithm is to remove overlapping jets. A jet is defined as overlapping if it shares energy with another jet. Two overlapping jets are merged if the overlapping energy is more than half of the individual jet energies. If the overlapping jets are not merged, then they are split into two distinct jets whose total E_T and axis are recomputed.

Once the jets have been reconstructed a set of quality criteria are applied to remove fake jets created out of calorimeter noise and remove electromagnetic particles such as electrons

³The transverse energy is the energy of the calorimeter tower weighted by the sine of the polar angle θ of the tower (i.e. $E_T = E \times \sin(\theta)$).

⁴The jet cone is defined in terms of rapidity (y) and azimuthal angle (ϕ).

and photons. To remove jets created by electromagnetic particles a jet is required to have between 5 and 95% of its energy deposited in the hadronic calorimeter. Also, a jet is required to be isolated ($\Delta R > 0.5$) from all electromagnetic clusters in the detector. To remove fake jets created by calorimeter noise the jet is required to have at least 60% of its energy deposited in the fine hadronic calorimeter since this detector has higher energy resolution than the coarse hadronic calorimeter. Jets created by a single “noisy” cell are removed by requiring that more than one calorimeter cell contain at least 90% of the jet energy. Also, to further suppress the effect of a noisy cell the ratio of the most energetic tower to the second most energetic tower must be less than 10.

Jet Energy Scale Correction

In reconstructing physics objects in an event, the goal is to measure the four-momenta of the final state particles from the hard scatter collision. For jets this is quite complicated due to the nearly 4 radiation lengths of material that separate the collision center from the calorimeter. It is the goal of the jet energy scale correction to modify the calorimeter jet energies to the parton energy before any interaction with the DØ detector [4].

The corrected jet energy, which is defined as the energy of a final state parton before interacting with the detector, is given by Eq. 4.6 in terms of five other quantities, which are explained below.

$$E_{\text{jet}}^{\text{corr}} = \frac{E_{\text{jet}}^{\text{uncorr}} - O}{F_{\eta} \times R \times S} \quad (4.6)$$

- $E_{\text{jet}}^{\text{uncorr}}$ is the uncorrected jet energy as determined by the reconstruction algorithm.
- O is the offset correction and represents energy that contributes to the jet that is not associated with the hard scatter collision. Two examples of additional sources of energy are electronics noise and additional minimum bias interactions in the same bunch crossing. The offset correction is measured in minimum bias events by summing the energy of calorimeter towers within a jet cone radius. A plot of the offset energy

correction as a function of the detector pseudorapidity (η^{det})⁵ for several primary vertex multiplicities is shown in Fig. 4.3.

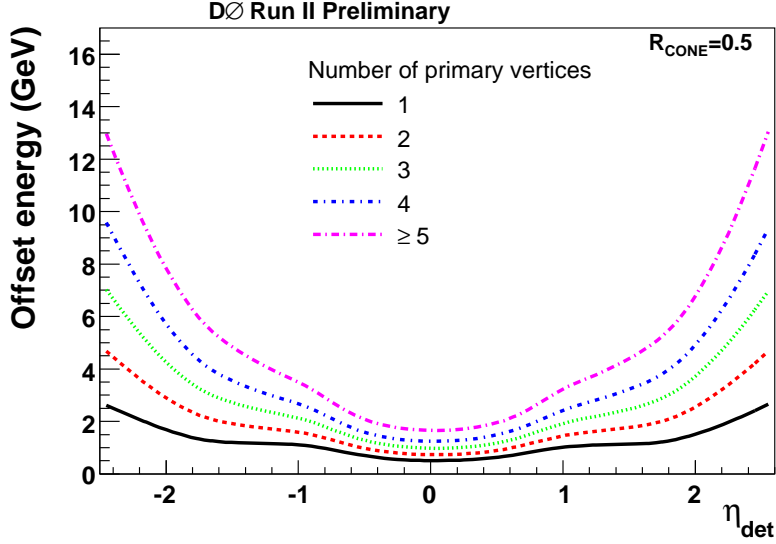


Figure 4.3: Offset energy correction for jets with a cone radius of 0.5 as a function of η^{det} [4].

- F_η is the relative response of the calorimeter in different η regions. This term is designed to cancel the expected non-uniformity of the DØ calorimeter between the central and endcap calorimeter cryostats. The relative response is measured using the missing E_T projection fraction method in back-to-back one photon with one jet events. In this method the photon is considered perfectly well measured, which implies that that any E_T imbalance in the event is an effect of the response. A cartoon of the method is shown in Fig. 4.4.

By measuring the missing E_T and the p_T of the photon and jet the response relative to $\eta = 0$ can be measured in many regions of η^{det} . The relative response with respect to $\eta = 0$ in data is shown in Fig. 4.5.

⁵ η^{det} is the pseudorapidity defined with respect to the detector origin instead of the collision center.

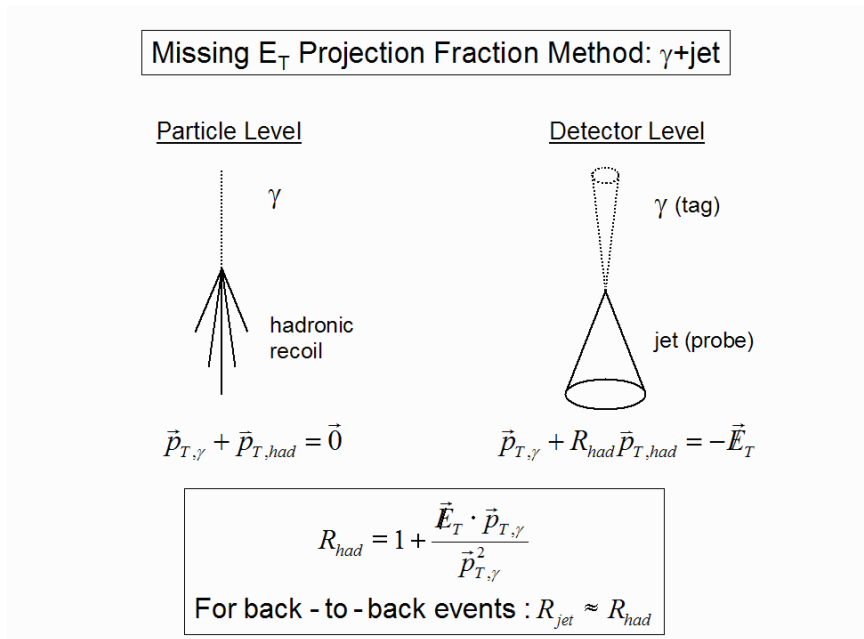


Figure 4.4: Missing E_T (E_T imbalance) projection fraction method cartoon [4].

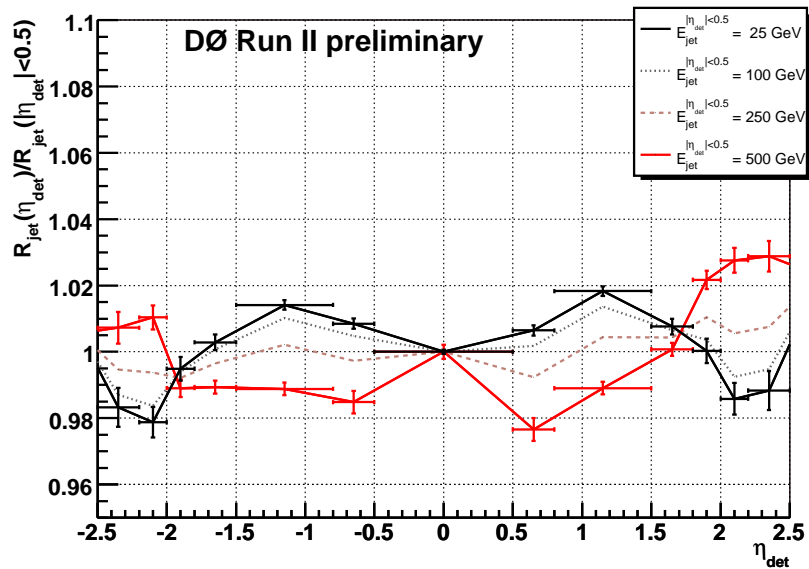


Figure 4.5: The relative energy correction for jets with a cone radius of 0.5 as a function of η^{det} (right) [4].

- R is the absolute energy response of the calorimeter. This term accounts for energy lost in un-instrumented regions of the detector and the lower energy response of the calorimeter to hadrons compared to electrons or photons. The absolute response is also determined using back-to-back photon+jet events and is measured after the relative response in η has been applied. Fig. 4.6 shows the absolute energy response for different η regions to emphasize the uniformity of the calorimeter after applying the relative response term.

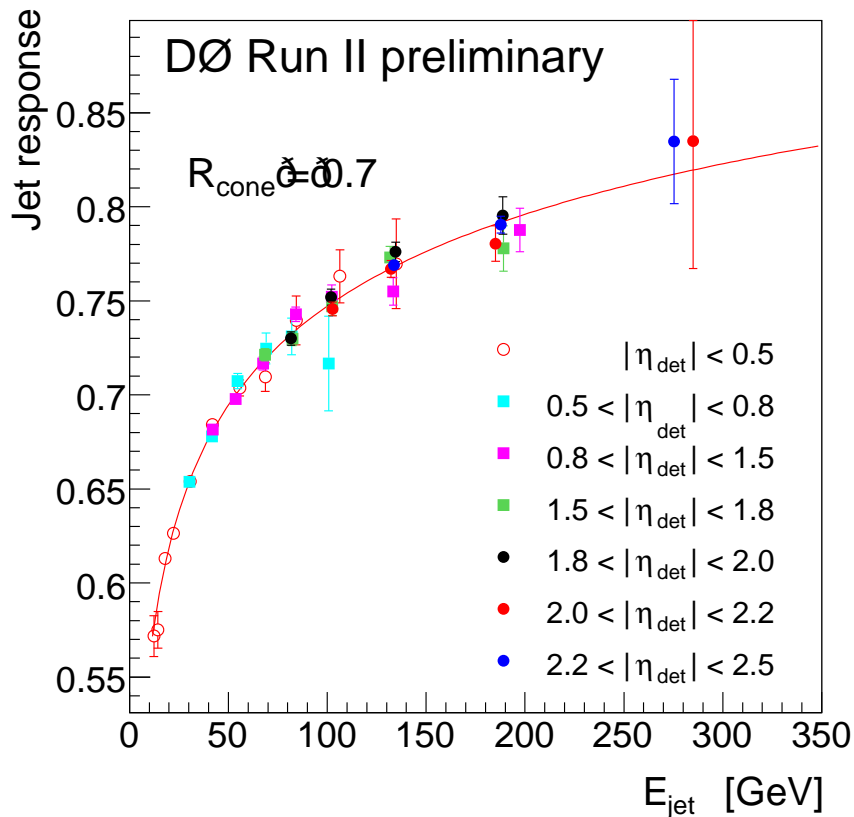


Figure 4.6: Absolute energy response of jets in the calorimeter for several η regions [4].

- S is the showering correction. This term corrects for energy deposited outside the cone radius of the reconstructed jet or additional energy deposited inside the cone radius as a result of spurious particles in the calorimeter. The showering correction is measured

by calculating the total energy deposited inside and outside the jet and taking the ratio of these numbers with the known deposited energy as determined in Monte Carlo events. The calculation in Monte Carlo is done without detector simulation such that the ratio of the two quantities yields the showering correction due to the detector only. Fig. 4.7 shows the showering correction as a function of jet E_T for jets in three different η regions.

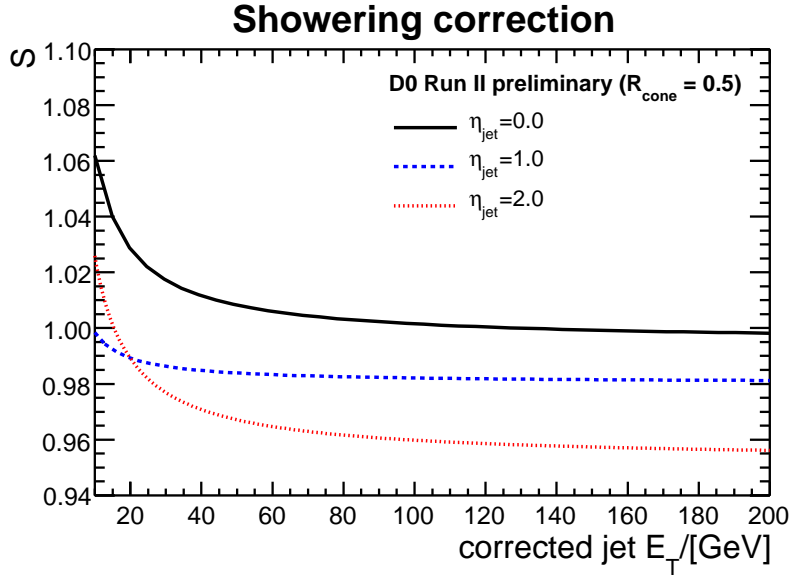


Figure 4.7: Showering correction for jets as a function of E_T for jets in three different η regions [4].

4.1.6 Missing E_T

Missing transverse energy is a useful quantity to calculate because it is highly correlated with the transverse energy of the undetected neutrino. The missing energy is only calculated in the transverse plane (x-y) because there is no net momentum in this plane since the proton-antiproton collision only occurs along the beam axis (z)⁶. The missing E_T (ME_T) is defined as the vector sum of the electromagnetic and fine hadronic calorimeter cell energies as well

⁶The total missing energy of the event can not be calculated because of the unknown boost along the longitudinal direction from the hard scatter process.

as any lepton p_T subtracted from zero such that there is no net transverse momentum in the event. This definition is summarized in Eq. 4.7.

$$\text{ME}_T = - \left[\sum_{\text{cells}} \text{E}_T \right] - p_T(\ell) \quad (4.7)$$

4.1.7 *B*-Jets

B-jets are a subset of all jets found by the jet cone algorithm with the distinction that these jets are formed from the hadronization of a *b* quark. *B*-jets are important to measure because many fundamental particles, such as the top quark, will decay into a *b* quark leaving it as one of the few signatures of its existence. *B*-jets are unique from jets produced from light quarks because the *B* hadron (a bound state of a *b* quark and one or two light quarks) has a much longer lifetime than lighter hadrons. The result of this long lifetime is a displaced decay vertex from the primary interaction vertex. The typical decay length, which is the distance from the decay vertex to the primary vertex, is a few millimeters. The goal of a *B*-jet finding algorithm is to use this property and other kinematically unique characteristics to identify heavy flavor jets from light flavor jets.

The *B*-jet selection algorithm at DØ uses a neural network (NN) to distinguish heavy flavor jets from light flavor jets [80]. The neural network is trained using seven variables that show discrimination between heavy and light flavor jets. The seven variables are shown in Table 4.1. The network was trained with $Z \rightarrow b\bar{b}$ and strongly produced $b\bar{b}$ production as heavy flavor signal-like events and $Z \rightarrow q\bar{q}$ and strongly produced $q\bar{q}$ production as light flavor background-like events. The output of the neural network is a new variable which peaks at 1 for heavy flavor jets and 0 for light flavor jets. A jet is “tagged” as a *B*-jet if the NN value is greater than 0.775. Only jets with at least two tracks with $p_T > 1$ GeV are considered for heavy flavor tagging. Jets which fail this criteria are considered light flavor jets.

Table 4.1: Variables used in the neural networks training. The variables are listed in order of relative importance as determined in the training [80].

Rank	Variable Description
1	Decay length significance ($\frac{L_T}{\delta L_T}$) of the displaced vertex
2	Weighed combination of the input tracks' impact parameter significance ($\frac{IP}{\delta IP}$)
3	Probability that the jet originates from the primary interaction vertex
4	χ^2/N_{dof} of the displaced vertex fit
5	Number of tracks used to reconstruct the displaced vertex
6	Mass of the tracks used to reconstruct the displaced vertex
7	Number of displaced vertices found inside the input jets

4.2 Monte Carlo Generation and Detector Simulation

Generating Monte Carlo events is crucial in a physics analysis to understand the signature a given process will have in the detector. The chain for generating simulated Monte Carlo events at DØ is the following: (1) generate final state four-vectors using Monte Carlo software, (2) simulate the DØ detector response to final state particles, (3) add additional $p\bar{p}$ interactions, and finally (4) reconstruct the event. The DØ trigger simulation is performed separately and described in Section 4.3. The result of the Monte Carlo generation with full detector simulation is a set of events that can be treated as equal to reconstructed data except with a known initial hard scatter physics process.

The first stage of generating Monte Carlo events is to produce and decay particles according to a specified physics process. The hard scatter collision is typically generated by “matrix-element” generators, such as CompHEP or Alpgen, and the decay products are typically handled by particle-specific algorithms. Specifically, the decay of tau leptons is handled by TAUOLA [68] and B hadrons are decayed by EVTGEN [73]. To simulate hadronization and allow for additional strong interaction effects between final state particles, all Monte Carlo events are processed through the Pythia generator.

The DØ detector is simulated using the GEANT software package [62]. GEANT⁷ provides a graphical representation of particles as they traverse the detector and simulates the interaction between particles and material in the detector. All information concerning the detector geometry and material density is modeled with GEANT. Three examples of GEANT’s capabilities are simulating electromagnetic and hadronic showers in the calorimeter, energy loss of electrons in the tracking detector, and bending particle trajectories due to the solenoidal and toroidal magnetic fields.

To properly account for additional inelastic $p\bar{p}$ collisions all Monte Carlo events are provided with a “minimum bias overlay” generated from reconstructed data. A minimum bias event is an event recorded by the detector that was triggered solely by the presence of at least one $p\bar{p}$ interaction. Because the number of minimum bias vertices grows with instantaneous luminosity the minimum bias events are overlaid to match the expected instantaneous luminosity profile of all recorded events. A plot of the average peak instantaneous luminosity versus time is shown in Fig. 4.8.

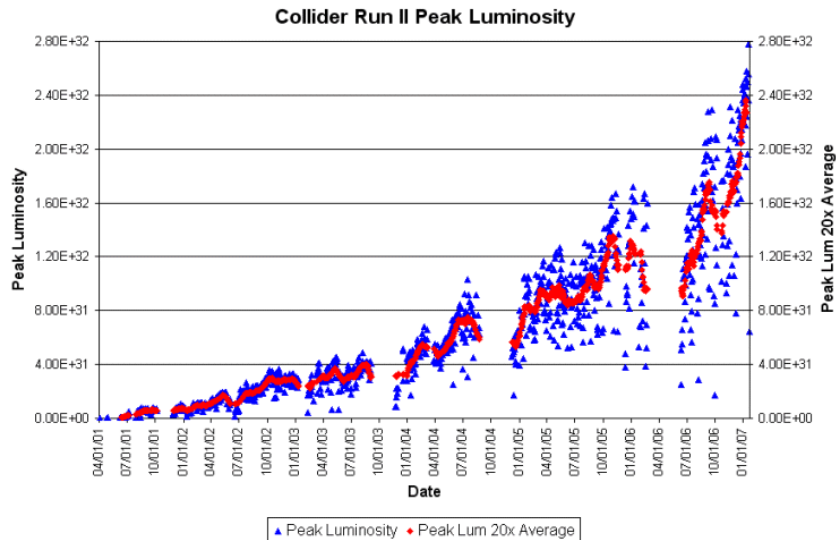


Figure 4.8: Peak instantaneous luminosity as a function of time [10].

⁷GEANT is an acronym formed from "GEometry ANd Tracking".

Reconstruction of Monte Carlo events occurs in the same manner as data events, as described in Section 4.1. It is the goal of the previous three steps of the simulation chain to describe the DØ detector response as accurately as possible such that the reconstruction is blind to the source of the event.

4.3 Trigger Simulation

The DØ trigger system is modeled in a Monte Carlo event by an event-wide probability that the event will pass the trigger selection. The event-wide probability is constructed from the efficiencies with which individual reconstructed objects pass object specific “trigger terms”. Section 4.3.1 derives the event-wide trigger probability in terms of individual trigger term efficiencies and Section 4.3.2 describes the methods used to measure these efficiencies. Triggers used to record single top quark events and their efficiencies are shown in Chapter 5.

4.3.1 Event-Wide Trigger Probability

The probability that a Monte Carlo event \vec{x} is selected by the trigger is defined as a product of the condition probabilities to pass each trigger level given that it passed the previous trigger level as shown in Eq. 4.8.

$$P(\ell_1 \cup (\ell_2 + \text{jets})) = P(\ell_1) + P(\ell_2)P(\text{jets}) - P(\ell_1 \cap \ell_2)P(\text{jets}) \quad (4.8)$$

At a given trigger level the probability for the event to be selected is written as the product of each reconstructed object to be selected by each trigger term as shown in Eq. 4.9. For example, the probability for a muon+2 jet event to pass a μ +jets trigger is the product of the probability for the muon to pass the muon trigger term and the two jets to pass the jet trigger term.

$$P_{\text{Level}}(\vec{x}) = \prod_k^{\text{Terms}} P_{\text{Term},k}(\vec{x}_{\text{Object}}) \quad (4.9)$$

The probability for a reconstructed object to pass a certain trigger level is written as one minus the probability of all the objects not to be selected by the trigger, as shown in Eq. 4.10

$$P_{\text{Term}}(\vec{x}_{\text{Object}}) = 1 - \prod_j^{\text{Nobjs}} (1 - \varepsilon_{\text{Term}}(\vec{x}_{\text{Object},j})) \quad (4.10)$$

where $\varepsilon_{\text{Term}}(\vec{x}_{\text{Object},j})$ is the trigger term efficiency for the reconstructed object.

At $D\bar{O}$ there have been several distinct trigger periods where the trigger used to collect data events has changed. To model this in Monte Carlo an integrated luminosity weighted average of the trigger probabilities for each period is applied to all events. The weighted averaged is shown in Eq. 4.11

$$P(\vec{x}) = \frac{\sum_{\text{version}} [\mathcal{L}_{\text{version}} \times P_{\text{version}}(\vec{x})]}{\sum_{\text{version}} \mathcal{L}_{\text{version}}} \quad (4.11)$$

4.3.2 Trigger Term Efficiency Measurement Methods

Electron and muon trigger term efficiencies are measured in $Z \rightarrow ee$ and $Z \rightarrow \mu\mu$ data events, respectively. The efficiency is measured in a Z boson sample because it provides a clean (i.e. negligible background) sample of leptons with which to measure efficiencies. In the Z sample a “tag and probe” method is used to measure the trigger efficiency where one of the leptons is required to trigger the event such that the other can be used as an unbiased probe to measure the trigger efficiency. The efficiency is defined as the fraction of events for which the probe electron or muon was found to pass the trigger term. To account for detector and reconstruction effects the trigger efficiencies are determined as a function of p_T , η , or ϕ . An example of the L1 muon trigger efficiency and the L3 electron trigger efficiency binned in η and p_T are shown in Fig. 4.9. Jet trigger term efficiencies are measured in muon triggered events. The jet trigger efficiency is defined as the number of jets that pass the jet trigger term divided by the total number of jets. Jet trigger term efficiencies are measured as a function of p_T and η .

4.4 Monte Carlo Corrections

The result of the Monte Carlo generation with a full detector simulation are events that mimic real data events recorded by the $D\bar{O}$ detector. Typically, however, the simulation is not complete for reasons such as missing material in the GEANT simulation or un-

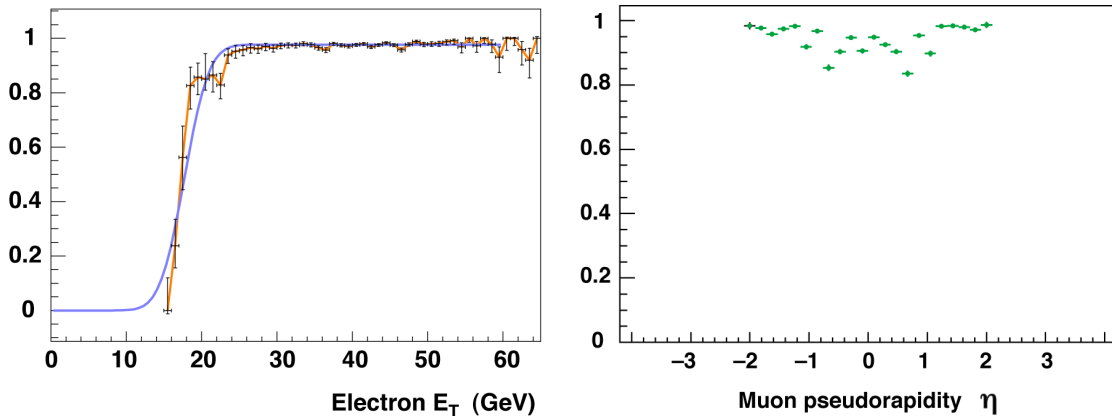


Figure 4.9: An example electron turn-on curve measured as a function of the electron p_T (left) and an example muon turn-on curve measured as a function of η (right). The points are trigger efficiencies derived from data in that bin (with uncertainty bars) [56].

modeled aging effects of the detector. The result of not modeling these effects typically leads to an overestimation of detector resolution in the Monte Carlo. To account for this the reconstructed Monte Carlo objects are typically “smeared” in one variable to ensure similar resolutions as is seen in data events. After the Monte Carlo events are smeared the relative difference between Monte Carlo and data events is measured and used to further correct the Monte Carlo. The following sections describe the smearing and correction factors for all reconstructed objects.

4.4.1 Muons

Muon smearing and correction factors are measured in $Z \rightarrow \mu\mu$ events because it provides a clean and unbiased sample of muons in both data and Monte Carlo. While the presence of a muon is confirmed by hits in the muon system the muon momentum vector is defined by the matched track. The muon track is defined by the charge and radius of curvature, which is proportional to q/p_T , thus the natural quantity to smear is q/p_T . The amount to which the muon track must be smeared is measured by observing the relative shift and width of the Z boson resonance in data and Monte Carlo events. The functional form to which the muon track is smeared is shown in Eq. 4.12.

$$\left(\frac{q}{p_T}\right)' \rightarrow \frac{q}{p_T} + \left(A + \frac{B}{p_T}\right) \times G \quad (4.12)$$

The parameter G is a random number generated from a Gaussian distribution centered at 0 and a width of 1. The parameters A and B are measured for muons with an SMT track hit in two regions ($\eta < 1.6$ and $\eta > 1.6$) and for muons without an SMT hit. Table 4.2 shows the smearing parameters for the three types of muons for two separate run periods.

Table 4.2: Muon smearing parameters for the function $(A + \frac{B}{p_T})$ for two different run periods.

Muon Type	< Dec. 2004		> Dec. 2004	
	A	B	A	B
> 1 SMT Hit ($\eta < 1.6$)	0.00313	-0.0563	0.00308	-0.0370
> 1 SMT Hit ($\eta > 1.6$)	0.00273	-0.0491	0.00458	-0.0550
= 0 SMT Hits	0.00509	-0.0916	0.00424	-0.0509

After the smearing is applied the correction factor for muons is defined as the product of three independent factors, as shown in Eq. 4.13, for reconstruction, track matching, and isolation.

$$f_{\text{Data/MC}}(\mu) = \frac{\varepsilon_{\text{Reco}}^{\text{Data}}(\mu)}{\varepsilon_{\text{Reco}}^{\text{MC}}(\mu)} \times \frac{\varepsilon_{\text{Track|Reco}}^{\text{Data}}(\mu)}{\varepsilon_{\text{Track|Reco}}^{\text{MC}}(\mu)} \times \frac{\varepsilon_{\text{Isolation|Track}}^{\text{Data}}(\mu)}{\varepsilon_{\text{Isolation|Track}}^{\text{MC}}(\mu)} \quad (4.13)$$

The muon reconstruction efficiency for data and the Monte Carlo correction factor are shown in Fig. 4.10. The empty region in the center of the η - ϕ efficiency histogram corresponds to the hole in the bottom of the muon detector. The correction factor is only considered to be a function of η since the reconstruction efficiencies for data and Monte Carlo show the same ϕ dependence. The average reconstruction efficiency in data is 80.2% and the average Monte Carlo correction factor is 0.97.

The muon track match efficiency is measured with respect to reconstructed muons. The efficiency is found to depend on two tracking related quantities, the track η and the longitudinal primary interaction vertex position. The efficiency in data and correction factor

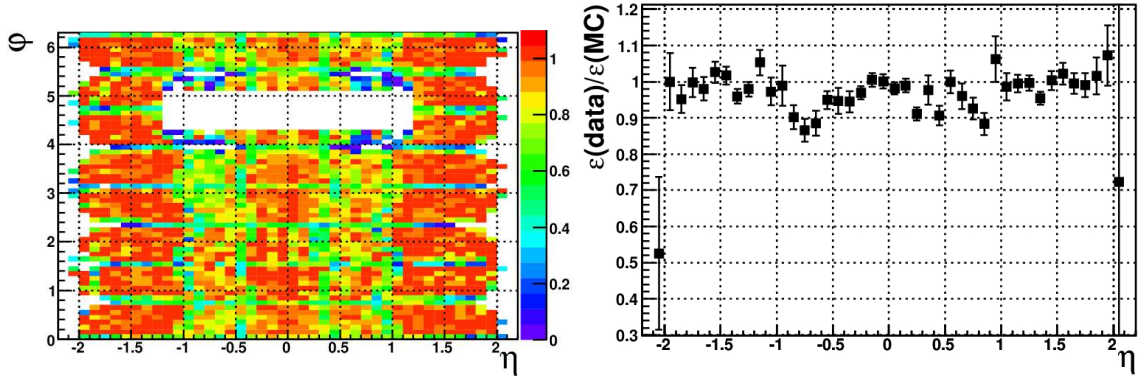


Figure 4.10: Muon reconstruction efficiency as measured in $Z \rightarrow \mu\mu$ data events (left) and the Monte Carlo correction factor as a function of muon η (right) [59].

are shown in Fig. 4.11. The average track match efficiency in data is 91.0% and the average Monte Carlo correction factor is 0.93.

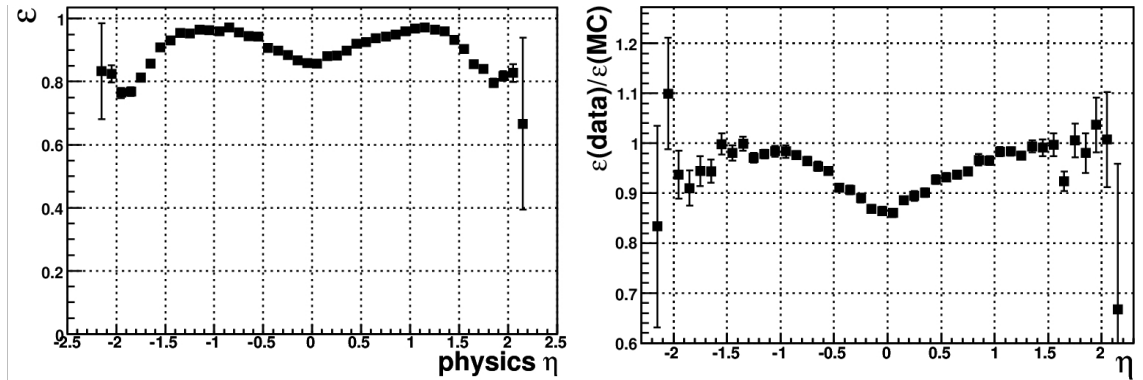


Figure 4.11: Muon track match efficiency as measured in $Z \rightarrow \mu\mu$ data events (left) and the Monte Carlo correction factor as a function of track η (right) [59].

The muon isolation efficiency is measured in $Z \rightarrow \mu\mu$ events for reconstructed muon with a confirmed track match. The isolation efficiency depends most strongly on the number of reconstructed jets in the event since it is more difficult for a muon to be isolated if the jets occupy more space in the detector. Fig. 4.12 shows the isolation efficiency and Monte Carlo correction factor as a function of the jet multiplicity. The Monte Carlo correction factor

for events with two or three jets, such as single top quark events, is 0.98, with an average efficiency of 0.94%.

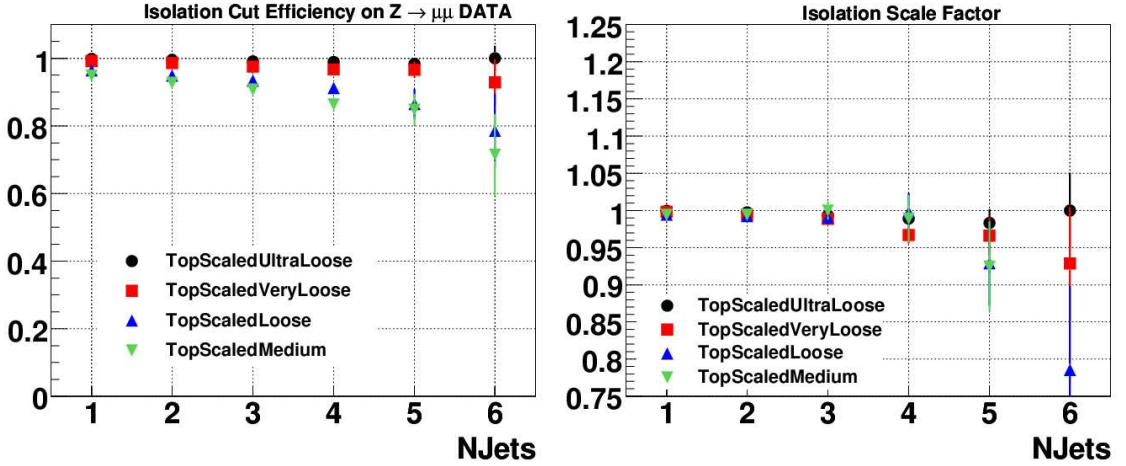


Figure 4.12: Muon isolation efficiency as measured in $Z \rightarrow \mu\mu$ data events for various regions of primary vertex z position (left) and Monte Carlo correction factor as a function of the number of reconstructed jets. The isolation used in the single top quark analysis is labeled TopScaledLoose and corresponds to the blue triangle curve [59].

4.4.2 Electrons

There is no smearing applied to Monte Carlo electrons since the resolution is well-modeled in the Monte Carlo. Electron correction factors are measured in $Z \rightarrow ee$ data and Monte Carlo events. The correction factor for electrons is considered a product of two independent factors: reconstruction and track match plus likelihood cuts, as shown in Eq. 4.14.

$$f_{\text{Data/MC}}(e) = \frac{\varepsilon_{\text{Reco}}^{\text{Data}}(e)}{\varepsilon_{\text{Reco}}^{\text{MC}}(e)} \times \frac{\varepsilon_{\text{TrackMatchLikelihood|Reco}}^{\text{Data}}(e)}{\varepsilon_{\text{TrackMatchLikelihood|Reco}}^{\text{MC}}(e)} \quad (4.14)$$

Electron reconstruction efficiencies as measured in $Z \rightarrow ee$ data and Monte Carlo events and the Monte Carlo correction factor show a slight p_T dependence as seen in Fig. 4.13.

Electron likelihood and track match efficiencies are measured in $Z \rightarrow ee$ data and Monte Carlo events with respect to reconstructed electrons. The efficiency in data and the Monte

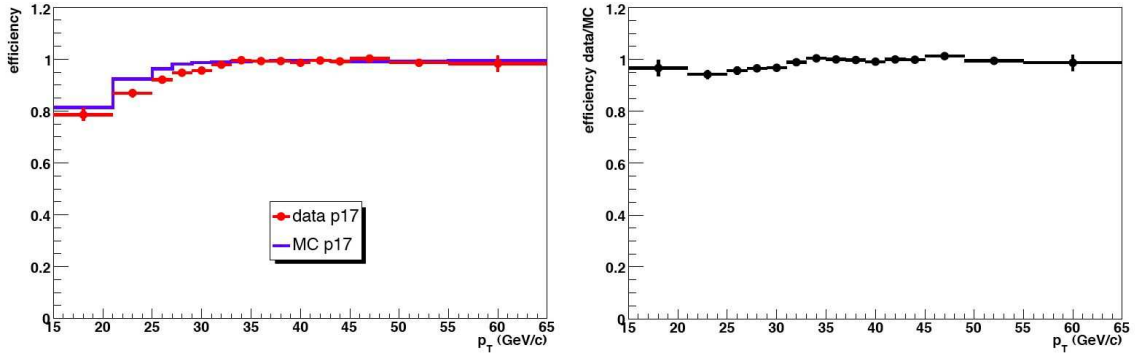


Figure 4.13: Electron reconstruction efficiency as measured in $Z \rightarrow ee$ data (red) and Monte Carlo (blue) events (left) and Monte Carlo correction factor as a function of electron p_T (right) [57].

Carlo correction factor are shown in Fig. 4.14. The single top quark analysis only use electrons out to 1.1 in η^{det} .

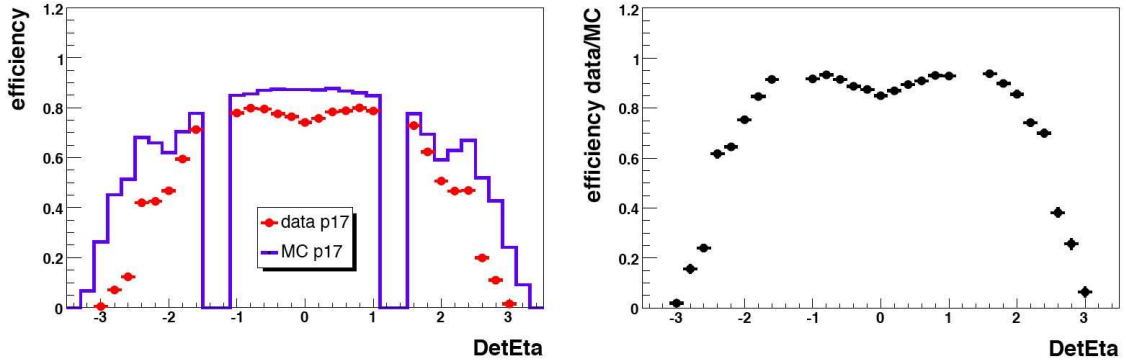


Figure 4.14: Electron reconstruction efficiency as measured in $Z \rightarrow ee$ data (red) and Monte Carlo (blue) events (left) and Monte Carlo correction factor as a function of electron p_T (right) [57].

4.4.3 Primary Interaction Vertex

The primary interaction vertex efficiency is measured using $Z \rightarrow \mu\mu$ data and Monte Carlo events and the correction factor is defined as the ratio of the two efficiencies. The primary

vertex reconstruction efficiency in data is shown in Fig. 4.15. No correction to the Monte Carlo primary vertices is applied.

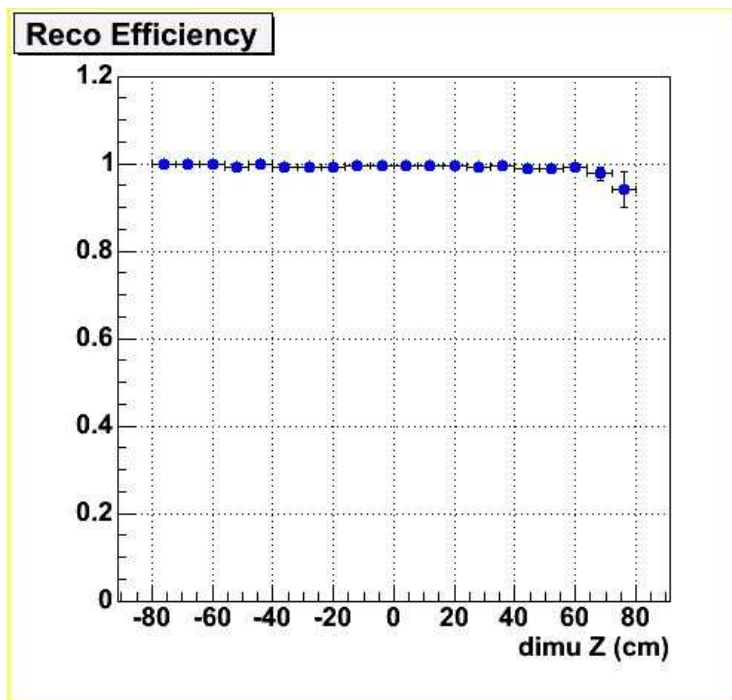


Figure 4.15: Primary vertex reconstruction as measured on $Z \rightarrow ee$ data events. The efficiencies are shown as a function of the longitudinal primary vertex position [33].

4.4.4 Jets

Jets produced in the Monte Carlo simulation exhibit an overestimation of energy resolution, energy scale, and reconstruction efficiency. A procedure called SSR (Smearing, Shifting, and Removing) was designed to properly account for each of these relative differences between data and Monte Carlo [8].

Jet energy resolution, energy scale, and reconstruction efficiency in the data and Monte Carlo are studied in back-to-back photon+jet events. In these events a variable called the transverse momentum imbalance, as shown in Eq. 4.15, is used to study these effects.

$$\Delta S = \frac{p_T^{\text{Jet}} - p_T^\gamma}{p_T^{\text{Jet}}} \quad (4.15)$$

To determine the difference in the jet energy reconstruction efficiency in data and Monte Carlo, the ΔS distribution is determined in several regions of photon p_T and fit to a Gaussian convoluted with a jet reconstruction efficiency function as shown in Eq. 4.16.

$$f(\Delta S) = N \times \left(1 + \text{erf} \left[\frac{\Delta S - \alpha}{\sqrt{2}\beta} \right] \right) \times \exp \left\{ -\frac{(\Delta S - \Delta S_0)^2}{2\sigma^2} \right\} \quad (4.16)$$

Where the constants $\{\alpha, \beta\}$ characterize the jet reconstruction efficiency, ΔS_0 yields information about the relative jet energy scale, and σ characterizes the relative jet energy resolution.

To correct for the difference in jet energy resolution between data and Monte Carlo the Monte Carlo jet p_T is smeared by a Gaussian with a width shown in Eq. 4.17. If the generated jet p_T is less than 15 GeV the jet is removed from the event.

$$\sigma_{\text{smear}} = \sqrt{\sigma_{\text{Data}}^2 - \sigma_{\text{MC}}^2} \quad (4.17)$$

The relative difference between the jet energy scale in data and Monte Carlo was found to be negligible ($\Delta S_0^{\text{data}} \approx \Delta S_0^{\text{MC}}$). The improved ΔS agreement between data and Monte Carlo after smearing and jet removal for two photon p_T ranges can be seen in Fig. 4.16.

4.4.5 *B*-jets

Due to large differences between data and Monte Carlo in tracking related quantities the *B*-tagging algorithms can not be directly applied to Monte Carlo events. Instead a probability for the algorithm to tag a *B*-jet, charm-jet, or a light jet is measured and applied to the Monte Carlo events [80]. These probabilities, called tag-rate functions (TRF), are measured in data and Monte Carlo events and scaled to reproduce the expected *B*-jet, charm-jet and light-jet tagging efficiencies in data. As explained in Section 4.1.7 all jets must have at least two associated tracks with $p_T > 1$ GeV before *B*-tagging can be applied. This requirement is known as jet taggability ($\varepsilon_{\text{Taggability}}$) and the product this quantity with the TRF yields the probability that a jet is *B*-tagged.

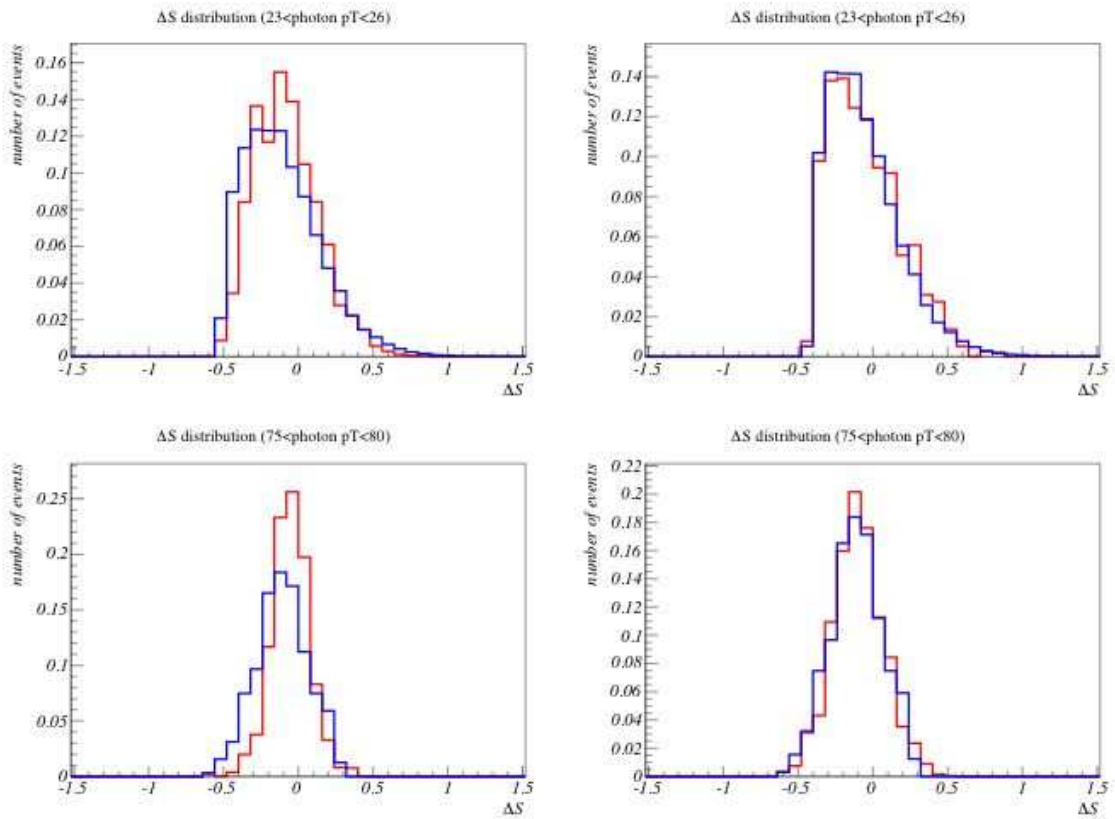


Figure 4.16: p_T imbalance (ΔS) distribution before (left) and after (right) jet smearing and removal are applied for two photon p_T regions: $23 < p_T^\gamma < 26$ (top) and $75 < p_T^\gamma < 80$ (bottom). The data is shown in blue and the Monte Carlo is shown in red [8].

$$P_{\text{tag}}(\vec{x}) = \varepsilon^{\text{Taggability}}(\vec{x}) \times TRF(\vec{x}) \quad (4.18)$$

Using this per-jet tagging probability the probability that one jet is tagged in an event with N jets is shown in Eq. 4.19 and probability that two jets are tagged is shown in Eq. 4.20. These probabilities are applied to the Monte Carlo while the tagging algorithm is applied directly to the data.

$$P_{1\text{-tag}} = \sum_{i=1}^{N_{\text{jets}}} P_{\text{tag},i} \prod_{i \neq j}^{N_{\text{jets}}} (1 - P_{\text{tag},j}) \quad (4.19)$$

$$P_{2\text{-tags}} = \sum_{i=1}^{N_{\text{jets}}} P_{\text{tag},i} \sum_{i \neq j}^{N_{\text{jets}}} P_{\text{tag},j} \prod_{k \neq i \neq j}^{N_{\text{jets}}} (1 - P_{\text{tag},k}) \quad (4.20)$$

The B -jet and light-jet neural network tagging efficiencies in data are measured using a B -tagging algorithm that is relatively uncorrelated with the NN tagger on two different data samples. The first data sample is a relatively loose B -jet enriched sample requiring at least one muon with $p_T > 4$ GeV inside a $\Delta R = 0.7$ cone size jet. The presence of the muon within the jet represents a possible semi-leptonic B decay. The second data sample is highly enriched in B -jets requiring at least two jets where one of the jets is required to have a jet impact parameter probability less than 0.5. The jet impact parameter probability is a measure of the likelihood that the jet originates from the primary interaction vertex. Large values of this quantity imply the jet originated from the hard scatter and low values indicate the jet originated from a displaced vertex. The second B -jet tagging algorithm used is the soft lepton tagger (SLT), which requires a muon to be reconstructed inside a jet. This algorithm is relatively uncorrelated with the NN tagger because it tags based on semi-leptonic B meson decays (e.g. $B \rightarrow D\ell\nu$), while the NN tagger uses information based on the displaced vertex from the B decay. Using the correlation between the taggers, as measured in Monte Carlo, and the correlation between the data samples, a system of eight equations with eight unknowns can be constructed. This system is then solved yielding the B -jet and light-jet tagging efficiencies with uncertainties in data events enriched in semi-leptonic B decays.

The B -jet tagging efficiency for Monte Carlo events with a semi-leptonic B decay is also measured and the ratio of the data to the Monte Carlo efficiency is used as the correction factor to the Monte Carlo. The B -jet tag-rate function for a Monte Carlo event with an inclusive B meson decay is defined as the product of the inclusive B -jet tagging efficiency in Monte Carlo with the correction factor as shown in Eq. 4.21.

$$\text{TRF}_b(p_T, \eta) = \varepsilon_{b \rightarrow \text{INC}}^{\text{MC}} \times \frac{\varepsilon_{b \rightarrow \mu}^{\text{Data}}}{\varepsilon_{b \rightarrow \mu}^{\text{MC}}} \quad (4.21)$$

The charm-jet tagging efficiency is measured using a similar approach with an additional input from the Monte Carlo for the relative inclusive charm-jet to B -jet tagging efficiency. The combined charm-jet TRF is shown in Eq. 4.22

$$\text{TRF}_c(p_T, \eta) = \varepsilon_{b \rightarrow \text{INC}}^{\text{MC}} \times \frac{\varepsilon_{b \rightarrow \mu}^{\text{Data}}}{\varepsilon_{b \rightarrow \mu}^{\text{MC}}} \times \frac{\varepsilon_{c \rightarrow \text{INC}}^{\text{MC}}}{\varepsilon_{b \rightarrow \text{INC}}^{\text{MC}}} \quad (4.22)$$

The tag-rate functions for B -jets and charm-jets as a function of p_T are shown in Fig. 4.17.

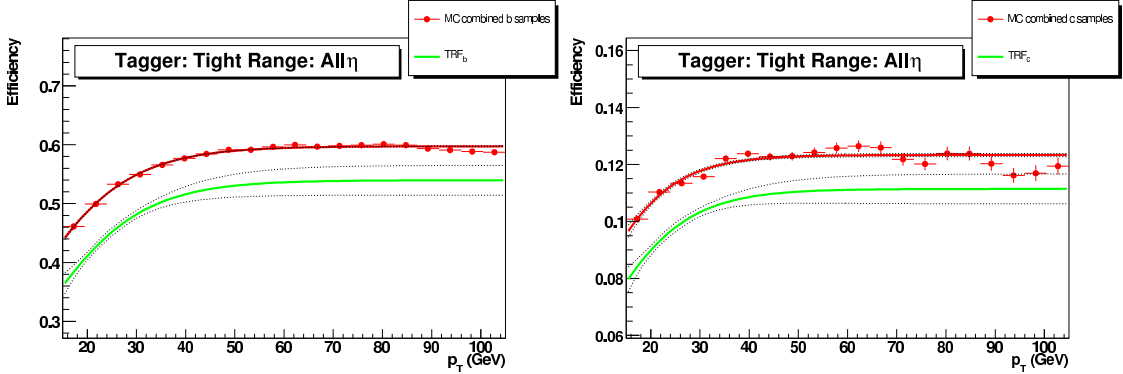


Figure 4.17: Neural network B -jet tagger efficiency (green line) and 1σ error bands (dashed lines) jet p_T and B -jets (left) and charm-jets (right) [80].

The light-jet tagging efficiency, sometimes called the fake tag-rate (FTR), is calculated from the product of the negative tag-rate (NTR) and two Monte Carlo correction factors. The negative tag-rate is the efficiency for which a jet resulting from light flavor partons is mistaken for a B -jet. This typically occurs due to poor track or primary interaction vertex

resolution in the event. A negative tag (NT) is found when the scalar product of the vector defined by the jet axis and the vector defined by the sum of the track vectors is negative. A positive tag is the case when the scalar product is greater than zero. Fig. 4.18 shows the scalar products divided by their error for B -jets and light jets in the Monte Carlo.

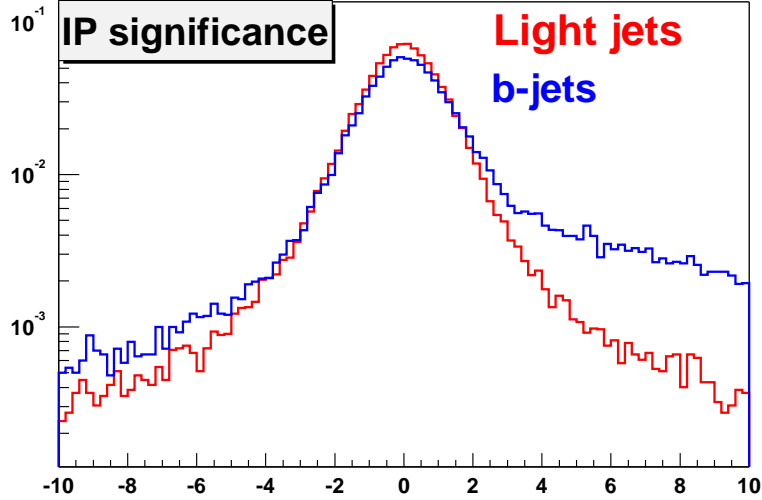


Figure 4.18: The impact parameter significance for B -jets and light jets. The IP significance is defined as the signed scalar product of the jet-axis and vector defined by the tracks of the displaced vertex divided by the error on that measurement [7].

The negative tag-rate is measured in data events with little bias towards heavy-flavor events. The NTR has two corrections which must be applied to remove any effects from heavy-flavor events that also receive a negative tag and a correction factor for the ratio of negative to positive tags for light-jets. The first correction factor is measured on $g \rightarrow b\bar{b}$ and $g \rightarrow c\bar{c}$ Monte Carlo and is defined as the ratio of the number of light-jets with a negative tag to the total number of negative tags. The second correction factor is measured on $g \rightarrow (uds)(uds)$ Monte Carlo and is defined as the ratio of the number of light-jets with a positive tag to the number of light-jets with a negative tag. The combined light-jet fake tag-rate function is shown in Eq. 4.23

$$\text{FTR}(p_T, \eta) = \text{NTR}^{\text{Data}} \times \frac{N_{1 \rightarrow \text{NT}}^{\text{MC}}}{N_{1 \rightarrow \text{NT}}^{\text{MC}} + N_{c \rightarrow \text{NT}}^{\text{MC}} + N_{b \rightarrow \text{NT}}^{\text{MC}}} \times \frac{N_{1 \rightarrow \text{PT}}^{\text{MC}}}{N_{1 \rightarrow \text{NT}}^{\text{MC}}} \quad (4.23)$$

Chapter 5

THE SINGLE TOP QUARK DATASET

This chapter describes the dataset and analysis strategy used in the search for single top quark production. This analysis is a continuation of previous single top quark searches at DØ as summarized in Section 5.1. The dataset used in the latest analysis is divided into independent samples or channels in which the single top quark analysis is performed and later combined when measuring the cross section. The division of analysis channels and the general measurement strategy is described in Section 5.2. The triggers used to select single top-like events at runtime are described in Section 5.3. The integrated luminosity recorded for the dataset is also reported in this section. A set of selection cuts is applied to the data set to remove mis-measured events or events which are unlikely single top quark candidates. In general the cuts are designed to select events with one high p_T lepton from the W boson decay, large missing E_T indicating a neutrino in the final state, and two to four jets. All selection cuts are explained in Section 5.4 with a summary table of expected fraction of s -channel and t -channel remaining after the cuts have been applied.

5.1 Previous Single Top Searches

There have been several searches for single top quark production by the DØ and CDF collaborations. During Run I DØ published two analyses [22, 13] using 90 pb⁻¹ and set limits of $\sigma_{s\text{-channel}} < 17$ pb and $\sigma_{t\text{-channel}} < 22$ pb both at 95% confidence level. The CDF collaboration also published two analyses [29, 28] using 106 pb⁻¹ of Run I data resulting in limits of $\sigma_{s\text{-channel}} < 18$ pb and $\sigma_{t\text{-channel}} < 13$ pb at 95% confidence level.

During Run II both DØ and CDF have performed several searches for single top. DØ has published two analyses [17, 20] using 230 pb⁻¹ and CDF has published one analysis [32]. Both DØ and CDF have released preliminary analyses using 370 pb⁻¹ [46] and 700 pb⁻¹ [50], respectively, with improved limits. Table 5.1 summarizes the limits on both s -channel and

t -channel single top quark production.

Table 5.1: Summary of limits on s -channel, t -channel, and combined $s + t$ -channel single top quark production from the DØ and CDF collaborations.

Analysis	s -channel	t -channel	Combined $s + t$
Tevatron Run I			
DØ with 90 pb ⁻¹	17	22	-
CDF with 106 pb ⁻¹	18	13	14
Tevatron Run II			
DØ with 162 pb ⁻¹	19	25	23
CDF with 162 pb ⁻¹	13.6	10.1	17.8
DØ with 230 pb ⁻¹	6.4	5.0	-
DØ with 370 pb ⁻¹ (prelim.)	5.0	4.4	-
CDF with 700 pb ⁻¹ (prelim.)	3.2	2.9	3.4

The CDF collaboration recently released three analyses using 955 pb⁻¹ of Run II data. One analysis [49] measures the combined s -channel and t -channel cross section of $2.7^{+1.5}_{-1.3}$ pb with a 2.3σ signal significance. The other two analyses [48, 47] do not observe a significant excess of data above background and set limits on the combined $s + t$ -channel production of 2.6 and 2.7 pb⁻¹ at 95% confidence level.

5.2 Analysis Measurement Strategy

The single top quark measurement strategy is to divide the data into many orthogonal samples, perform the analysis in each sample, and combine them during the cross section extraction procedure. The data are divided by lepton flavor, the number of reconstructed jets, and by the number of B -tags. The division by lepton flavor is due to the trigger selection and because events with electrons and muons suffer from different types of backgrounds. The division by the number of reconstructed jets is to ensure proper background modeling by the Monte Carlo for each jet multiplicity. Finally, the division by the number of B -tags

is due to different sensitivities to either s -channel or t -channel events. For instance, events with one B -tag are sensitive to both s -channel and t -channel single top while events with two B -tags are only sensitive to s -channel events. In total there are twelve independent channels corresponding to two lepton channels (electron and muon), three reconstructed jet channels (two, three, and four), and two B -jet channels (one and two tags).

5.3 Triggers for Single Top Quark Events

The Run II dataset used in the single top quark analysis was collected by the DØ detector between August 2002 and December 2005. During this time there have been eight distinct periods in which the triggers used to collect data events have changed. All triggers are described in the following two sections.

5.3.1 Electron Channel Trigger

Electron channel events are selected by triggering on events with at least one electron and at least two jets ¹. The electron trigger used in the single top quark analysis has changed five times during the entire run period. A description of the five triggers used is given below. Table 5.2 summarizes the triggers used to collect electron single top quark events and the total integrated luminosity recorded with each trigger.

- EM15_2JT15
 - Level1: One EM calorimeter tower with $E_T > 10$ GeV and two jet calorimeter towers with $E_T > 5$ GeV.
 - Level2: One EM object with $E_T > 10$ GeV and electromagnetic fraction > 0.85 . Also two jet objects with $E_T > 10$ GeV.
 - Level3: One EM object with $E_T > 15$ GeV and a shower shape consistent an EM object. Also, two jet objects with $E_T > 15$ GeV.
- E1_SHT15_2J20

¹At the trigger level an electron is still considered a jet because it deposits energy in the calorimeter in a similar way to jets.

- Level1: One EM calorimeter tower with $E_T > 11$ GeV.
- Level2: No requirement.
- Level3: One EM object with $E_T > 15$ GeV and a shower shape consistent an EM object. Also, two jet objects with $E_T > 20$ GeV.

- E1_SHT15_2J_J25

- Level1: One EM calorimeter tower with $E_T > 11$ GeV.
- Level1: One EM object with $E_T > 15$ GeV.
- Level2: No requirement.
- Level3: One EM object with $E_T > 15$ GeV and a shower shape consistent an EM object. Also, two jet objects with $E_T > 20$ GeV. One of the jets is also required have $E_T > 25$ GeV.

- E1_SHT15_2J_J30

- Level1: One EM calorimeter tower with $E_T > 11$ GeV.
- Level1: One EM object with $E_T > 15$ GeV.
- Level2: No requirement.
- Level3: One EM object with $E_T > 15$ GeV and a shower shape consistent an EM object. Also, two jet objects with $E_T > 20$ GeV. One of the jets is also required have $E_T > 30$ GeV.

5.3.2 Muon Channel Trigger

Muon channel events are selected by triggering on events with at least one muon and at least one jet. The muon trigger used in the single top quark analysis has changed seven times during the entire run period. A description of the seven triggers used is given below. Table 5.3 summarizes the triggers used to collect muon single top quark events and the total integrated luminosity recorded with each trigger.

Table 5.2: Integrated luminosities by trigger version for the triggers used to record electron single top quark events. The total integrated luminosity is shown in bold.

Trigger Period	Trigger Name	Integrated Luminosity [pb^{-1}]
I	E1_SHT15_2J15	103
II	E1_SHT15_2J20	227
III	E1_SHT15_2J_J25	55
IV	E1_SHT15_2J_J30	294
V	E1_SHT15_2J_J25	234
Total Integrated Luminosity		913

- MU_JT20_L2M0

- Level1: One muon with scintillator and wire hit and one calorimeter tower with $E_T > 5$ GeV.
- Level2: One muon object.
- Level3: One jet object with $E_T > 20$ GeV.

- MU_JT25_L2M0

- Level1: One muon with scintillator and wire hit and one calorimeter tower with $E_T > 5$ GeV.
- Level2: One muon object.
- Level3: One jet object with $E_T > 25$ GeV.

- MUJ2_JT25

- Level1: One muon with scintillator and wire hit and one calorimeter tower with $E_T > 5$ GeV.
- Level2: One muon object and a jet object with $E_T > 8$ GeV.
- Level3: One jet object with $E_T > 25$ GeV.

- MUJ2_JT25_LM3
 - Level1: One muon with scintillator and wire hit and one calorimeter tower with $E_T > 5$ GeV.
 - Level2: One muon object and a jet object with $E_T > 8$ GeV.
 - Level3: One jet object with $E_T > 25$ GeV and a muon object with $p_T > 3$ GeV.

- MUJ2_JT30_LM3
 - Level1: One muon with scintillator and wire hit and one calorimeter tower with $E_T > 5$ GeV.
 - Level2: One muon object and a jet object with $E_T > 8$ GeV.
 - Level3: One jet object with $E_T > 30$ GeV and a muon object with $p_T > 3$ GeV.

- MUJ1_JT25_ILM3
 - Level1: One muon with scintillator and wire hit and one calorimeter tower with $E_T > 5$ GeV.
 - Level2: One muon object and a jet object with $E_T > 8$ GeV.
 - Level3: One jet object with $E_T > 25$ GeV and an isolated muon object with $p_T > 3$ GeV.

- MUJ1_JT35_LM3
 - Level1: One muon with scintillator and wire hit and one calorimeter tower with $E_T > 5$ GeV.
 - Level2: One muon object and a jet object with $E_T > 8$ GeV.
 - Level3: One jet object with $E_T > 35$ GeV and a muon object with $p_T > 3$ GeV.

Table 5.3: Integrated luminosities by trigger version for the triggers used to record muon single top quark events. The total integrated luminosity is shown in bold.

Trigger Period	Trigger Name	Integrated Luminosity [pb^{-1}]
I	MU_JT20_L2M0	109
II	MU_JT25_L2M0	231
III	MUJ2_JT25	31
IV	MUJ2_JT25_LM3	16
V	MUJ2_JT30_LM3	252
VI	MUJ1_JT25_ILM3	21
VII	MUJ1_JT35_LM3	214
Total Integrated Luminosity		871

5.4 Reconstructed Object Selection

The following sections describe the selection cuts applied to the data. The goal of the selection cuts is to remove events which are unlikely single top candidates as well as remove events which may mimic the single top quark event signature, but are created by detector noise or low energy physics processes in the event.

5.4.1 Lepton Selection

Leptons in the event must be consistent with a W decay thus are required to have $p_T > 15(18)$ GeV and $|\eta| < 1.1(2.0)$ for electrons (muons). To remove $Z \rightarrow \ell\ell + \text{jets}$ and $t\bar{t} \rightarrow \ell\ell$ events a veto on additional leptons with $p_T > 15$ GeV is applied. Events with a high p_T muon veto event with an electron and visa versa to ensure orthogonality between search channels. Fig. 5.1 shows the expected muon p_T and η distribution for s -channel and t -channel single top.

5.4.2 Jet Selection

Leading order s -channel and t -channel single top quark events have at most three partons in the final state which will likely yield either two or three jets. To account for higher order

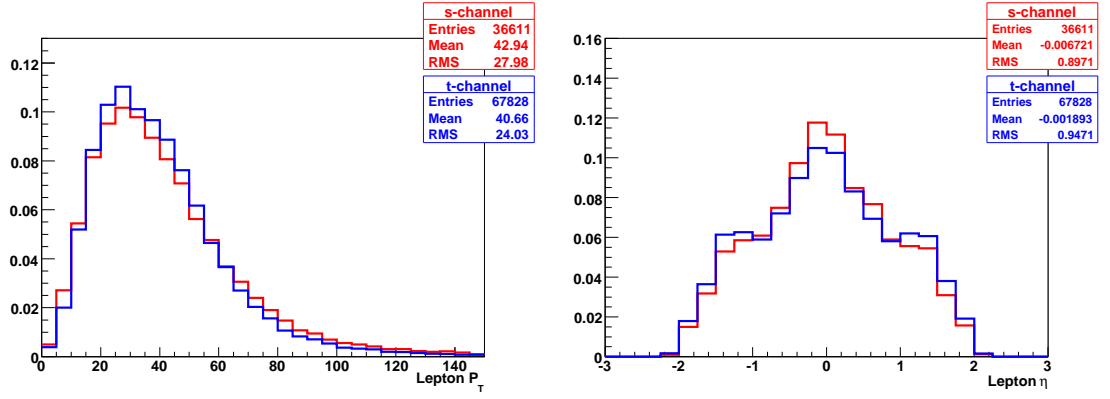


Figure 5.1: Muon p_T (left) and η (right) distributions for s -channel (red) and t -channel (blue) single top. Muons are required to have $p_T > 18$ GeV and $|\eta| < 2$.

radiation effects events are allowed to have between two and four fully corrected jets. The leading jet (highest p_T) must have $p_T > 25$ GeV and $|\eta^{det}| < 2.5$. The second jet (second highest p_T) must have $p_T > 20$ GeV and $|\eta^{det}| < 3.4$. All other jets in the event must have $p_T > 15$ GeV and $|\eta^{det}| < 3.4$. Fig. 5.2 shows the expected leading p_T and η distribution for s -channel and t -channel single top and Fig. 5.3 shows the same distributions for the second leading jet.

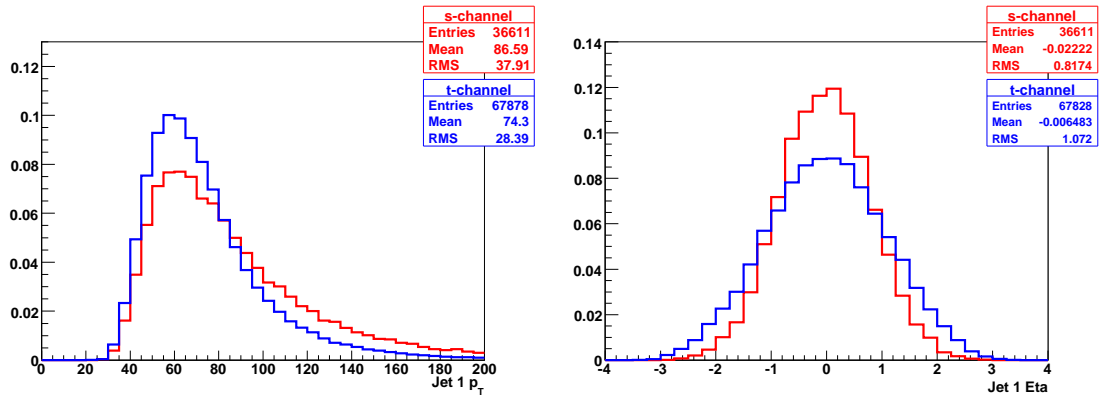


Figure 5.2: Leading jet p_T (left) and η (right) distributions for s -channel (red) and t -channel (blue) single top. The leading jet is required to have $p_T > 25$ GeV and $|\eta| < 2.5$.

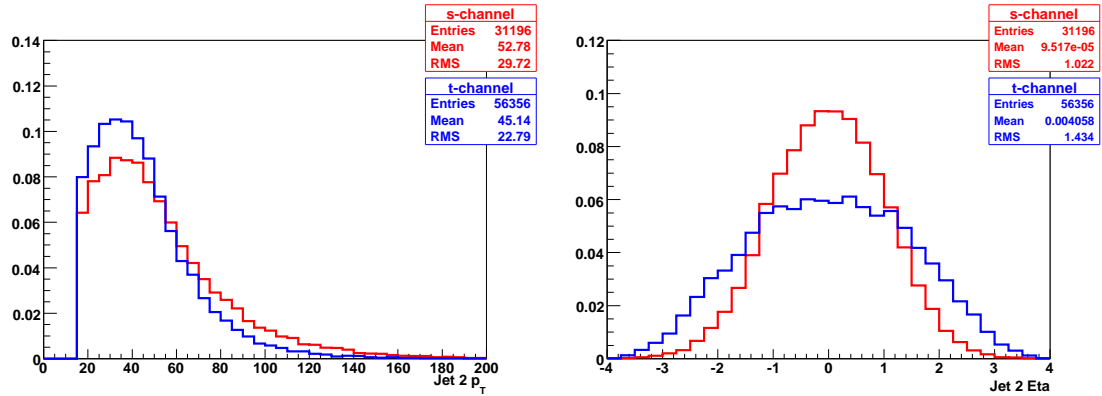


Figure 5.3: Second leading jet p_T (left) and η (right) distributions for s -channel (red) and t -channel (blue) single top. The second leading jet is required to have $p_T > 20$ GeV and $|\eta| < 3.4$

5.4.3 Missing E_T

A large amount of missing transverse energy in an event can indicate the presence of a neutrino in the final state. All events are required to have $ME_T > 15$ GeV. Fig. 5.4 shows the missing E_T distribution for s -channel and t -channel single top.

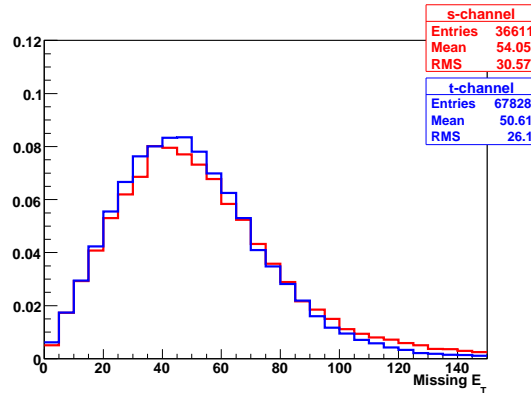


Figure 5.4: Missing E_T distribution for s -channel (red) and t -channel (blue) single top. The missing E_T is required to larger than 15 GeV.

5.4.4 Vertex Selection

All events are required to have one and only one primary interaction vertex as defined in Section 4.1.2. No requirement is placed on additional minimum bias vertices in the event. Fig. 5.5 shows the primary interaction vertex longitudinal location distribution for s -channel and t -channel single top.

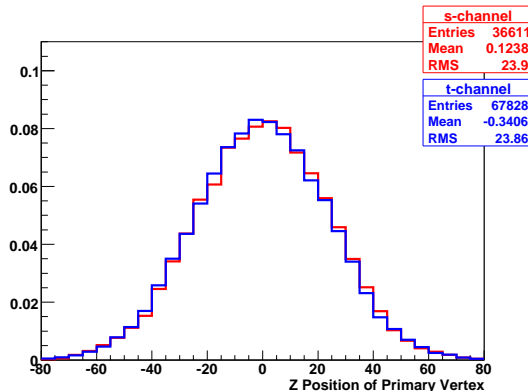


Figure 5.5: Longitudinal location of the primary interaction vertex for s -channel (red) and t -channel (blue) single top. The primary interaction vertex is required to be located within 60 cm of the detector origin.

5.4.5 b -Jet Selection

Both s -channel and t -channel single top quark events have at least one b quark in the final state thus all events are required to have at least one B -tagged jet as identified by the neural network tagging algorithm.

5.4.6 Mis-measured event rejection

There are several selection cuts applied to reduce mis-measured events. First, all events are required to have less than 200 GeV of missing E_T . This cut is applied to remove events where the muon track momentum has been badly measured, which can cause a large imbalance in the missing transverse energy measurement. All events are also allowed at most three “noise” jets. A noise jet is a jet that fails one of the criteria specified in Section 4.1.5 and is

not matched to an electromagnetic cluster. It has been observed that allowing more than three noise jets alters the p_T and η distributions of other jets in the event. The final set of cuts applied to remove unwanted events are “triangle cuts”, which are cuts between the difference in ϕ between an object and the missing E_T versus the missing E_T . An example of triangle cut is shown in Fig. 5.6. Three sets of triangle cuts are applied to the data and Monte Carlo events and shown in the bullets below.

- Electron Triangle Cuts: $|\Delta\phi(e, ME_T)|$ vs. ME_T
 - $0 < |\Delta\phi| < 2$ when $ME_T = 0$ GeV, and $0 < ME_T < 40$ GeV when $|\Delta\phi| = 0$
 - $0 < |\Delta\phi| < 1.5$ when $ME_T = 0$ GeV, and $0 < ME_T < 50$ GeV when $|\Delta\phi| = 0$
 - $2 < |\Delta\phi| < \pi$ when $ME_T = 0$ GeV, and $0 < ME_T < 24$ GeV when $|\Delta\phi| = \pi$
- Muon Triangle Cuts: $|\Delta\phi(\mu, ME_T)|$ vs. ME_T
 - $0 < |\Delta\phi| < 1.1$ when $ME_T = 0$ GeV, and $0 < ME_T < 80$ GeV when $|\Delta\phi| = 0$
 - $0 < |\Delta\phi| < 1.5$ when $ME_T = 0$ GeV, and $0 < ME_T < 50$ GeV when $|\Delta\phi| = 0$
 - $2.5 < |\Delta\phi| < \pi$ when $ME_T = 0$ GeV, and $0 < ME_T < 30$ GeV when $|\Delta\phi| = \pi$
- Leading Jet Triangle Cut: $|\Delta\phi(\text{Jet}_1, ME_T)|$ vs. ME_T
 - $1.5 < |\Delta\phi| < \pi$ when $ME_T = 0$ GeV, and $0 < ME_T < 35$ GeV when $|\Delta\phi| = \pi$

5.4.7 Acceptance for Single Top Quark Events

The signal acceptance is defined as:

$$\mathcal{A} = \frac{1}{N_{\text{initial}}} \sum_i^{N_{\text{selected}}} [\varepsilon_{\text{trigger}} \times \varepsilon_{\text{corrections}} \times \varepsilon_{\text{TRF}}] \quad (5.1)$$

where N_{initial} is the initial number of events in each MC sample, N_{selected} is the number of MC events remaining after selection, $\varepsilon_{\text{trigger}}$ is the trigger weight, $\varepsilon_{\text{corrections}}$ are the Monte Carlo correction factors, and ε_{TRF} is the B -tagging weight. Table 5.4 shows the percentage of each single top quark signal for each jet multiplicity that remain after selection cuts.

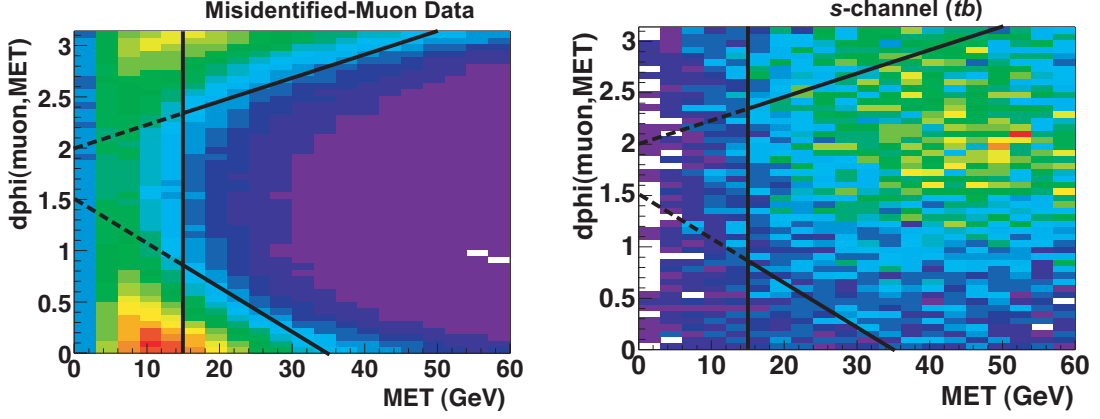


Figure 5.6: Example triangle cut between a muon and the missing E_T for mis-measured events (left) and s -channel single top events (right). The colors indicate the density of events. The brighter colors indicate more densely populated regions. Events which fall inside the triangles are removed from the final data sample. The black line at $ME_T = 15$ GeV indicates the standard missing E_T selection [58].

Table 5.4: Single acceptances after selection cuts, one, and two B -tags. The branching ratio for $W \rightarrow \ell\nu$ is included in the acceptance.

	Electron Channel			Muon Channel		
	2 jets	3 jets	4 jets	2 jets	3 jets	4 jets
Before B tagging						
tb	1.77%	0.83%	0.23%	1.36%	0.69%	0.19%
tqb	1.49%	0.79%	0.25%	1.17%	0.64%	0.20%
One B -tagged jet						
tb	0.82%	0.39%	0.11%	0.64%	0.32%	0.09%
tqb	0.61%	0.34%	0.11%	0.50%	0.28%	0.09%
Two B -tagged jets						
tb	0.29%	0.14%	0.04%	0.24%	0.12%	0.03%
tqb	0.02%	0.05%	0.02%	0.01%	0.04%	0.02%

Chapter 6

BACKGROUND ESTIMATION

Perhaps the most critical aspect of a physics analysis is estimating the background contribution in the data sample. Most physics backgrounds can be modeled using simulated Monte Carlo events and the rest are modeled using reconstructed data events. This chapter describes how all backgrounds are modeled and normalized to their expected contribution in the dataset. Section 6.1 describes the expected backgrounds in the single top quark dataset and how the background event kinematics are modeled. Section 6.2 describes how these backgrounds are normalized to their expected yields in the dataset. Finally, Section 6.3 summarizes all background yields and Section 6.4 compares data with the expected background estimation.

6.1 Background Modeling

As described in Chapter 2 the top quark in single top quark events will decay to a W boson and b quark, where the W boson is only considered to decay to a lepton and neutrino in this analysis¹. With an additional b quark or light quark this makes the signature of single top quark events one high p_T lepton, large missing E_T , and two or more jets. This event signature can be produced by three general types of backgrounds. The largest background which produces this event signature is W or Z boson production in association with two or more jets. Because the kinematics of Z boson production are similar to W boson production, both backgrounds are typically considered as one background called “ W +jets”. An example Feynman diagram for such a process is shown in Fig. 6.1.

Another large background present in the dataset are events origination from top pair production. The top pair production background, referred to as $t\bar{t}$, is defined by the decay of the two W bosons, from the decay of the two top quarks. The first case when one of

¹ $t \rightarrow bW \rightarrow bq\bar{q}'$ decays are removed from the dataset since there is no lepton nor large missing E_T .

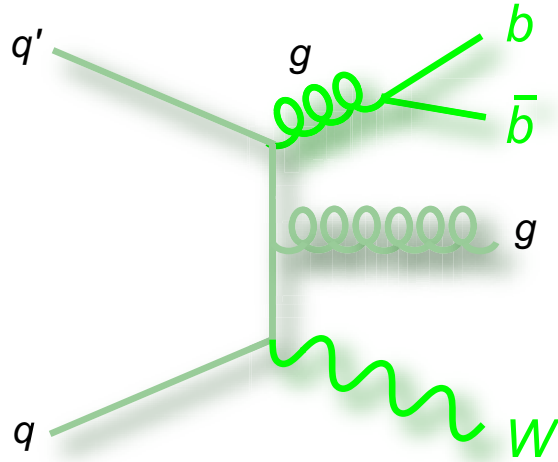


Figure 6.1: Example leading order Feynman diagram for a “ W +jets” event. This particular diagram represents the production of a W boson, and two b quarks and an associated gluon [5].

the W bosons decays to two quarks and other decays to a lepton and neutrino is referred to as “lepton+jets” ($t\bar{t} \rightarrow \ell + jets$) because the final state in the event is one lepton, one neutrino, and four quarks. The other way in which a $t\bar{t}$ event can enter the data sample is when both W bosons decay to leptons and neutrinos. In this case, there are two quarks, two leptons, and two neutrinos. These events are referred to as “dilepton” ($t\bar{t} \rightarrow \ell\ell$) events. An example Feynman diagram for the $t\bar{t} \rightarrow \ell + jets$ process is shown in Fig. 6.2.

The third largest background present in the dataset is multijet events produced by the strong interaction. The background processes responsible for these events in the dataset are quite different for electron events and muon events. In electron events one of the reconstructed jets will have a large electromagnetic fraction causing it to be mis-identified as an electron. In muon events a gluon will decay to a $b\bar{b}$ pair and one of the B mesons will undergo a semi-leptonic decay and produce a muon. In both cases, another jet may not be properly reconstructed leading to a large amount of missing E_T in the event, thus mimicking the single top quark event signature. An example Feynman diagram for a multijet process producing a lepton, missing E_T , and jets is shown in Fig. 6.3.

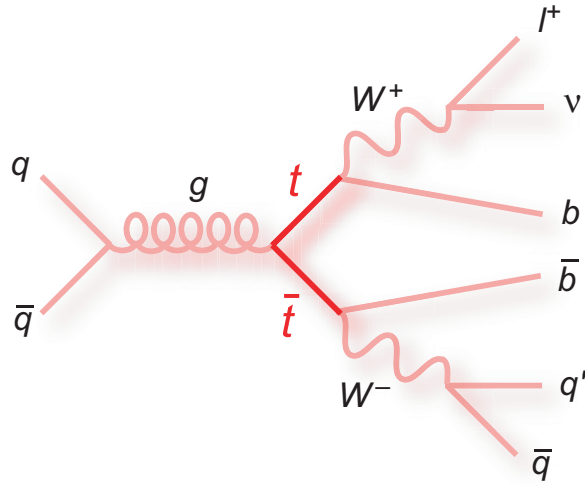


Figure 6.2: Example Feynman diagram for a $t\bar{t} \rightarrow l + \text{jets}$ event [5].

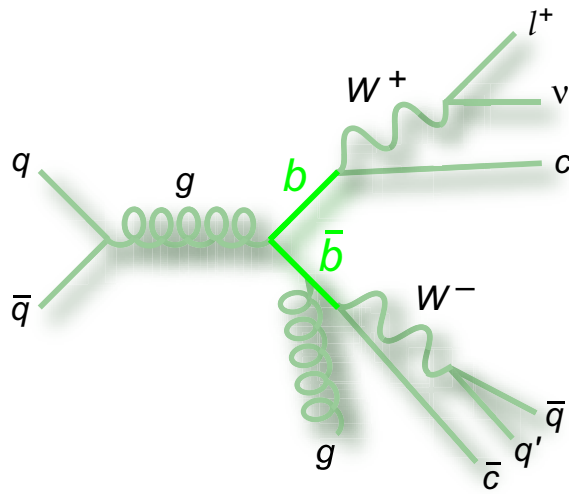


Figure 6.3: Example Feynman diagram for a multijet event [5].

6.1.1 Monte Carlo Modeling of $W + \text{Jets}$ and $t\bar{t}$ Backgrounds

$W + \text{jets}$ and $t\bar{t}$ backgrounds are modeled using the ALPGEN Monte Carlo generator interfaced with Pythia for parton showering [79]. ALPGEN is a leading order matrix element Monte Carlo generator similar to the CompHEP generator used to model single top quark events. All generated events are reconstructed using the simulated DØ detector as described in Chapter 4 and selection cuts are applied as described in Chapter 5. Within ALPGEN, the MLM jet-parton matching scheme [66] is also employed to remove double counted events in a similar manner to the double counting that is encountered when generating single top events. An example of double counting in $W + \text{jets}$ events is given here: $W + \text{light flavor}$ events (e.g Wgg) are generated separately from $W + \text{heavy flavor}$ events (e.g Wbb). When these events are sent through Pythia it is possible that additional gluons will split to heavy flavor quarks (e.g $g \rightarrow b\bar{b}$) leading to double counting of $W + \text{heavy flavor}$ events. The MLM matching scheme is described in more detail below.

MLM Matching Scheme

As stated earlier, the MLM jet-parton matching scheme is designed to remove double counted events. The MLM matching scheme works in the following way:

1. Events are generated with a distinct parton multiplicity. For instance, $W + 2$ light partons (e.g. Wgg) are generated separately from $W + 3$ light partons (e.g. $Wggg$). The same applies to $W + \text{heavy flavor}$ and $t\bar{t}$ events.
2. All generated events are sent to Pythia for parton showering. This procedure will introduce additional quarks and gluons as a product of the shower.
3. Before the final state partons are hadronized, all quarks and gluons are clustered together with a jet algorithm. The algorithm used for this analysis is the UA1 jet cone algorithm [35].
4. Match the generated partons from (1) with the cone jets from (3). Each parton must correspond to one jet and visa versa. A jet is matched if it has $p_T > 15$ GeV and

there is a parton with $\Delta R < 0.7$ from the jet. If a match is found the event is kept, otherwise the process is repeated.

5. Combine all samples together with weights based on the relative cross sections and the relative number of generated events for each process.

The formulas used to combined W +light parton, $W+c\bar{c}$ +light parton, $W+b\bar{b}$ +light parton, $t\bar{t} \rightarrow \ell\ell$ +light parton, and $t\bar{t} \rightarrow \ell + jets$ +light parton events are shown below.

W+Light Parton Sample

The W +light parton sample contains W +light flavor ($udsg$) events as well as $W+c$ +light flavor events. In $W+c$ +light flavor events the c -quark is considered massless. Eq. 6.1 shows the formula used to combine the W +light parton sample and Table 6.1 shows the relative cross sections and weights (k) for each sample. All W +light parton events are generated using CTEQ6L1 PDFs with $Q^2 = m_W^2 + P_T^2(W)$.

$$\begin{aligned}
 W + Nlp &= k_{W+0lp} [W + 0lp]_{\text{excl}} + k_{W+1lp} [W + 1lp]_{\text{excl}} + \\
 &k_{W+2lp} [W + 2lp]_{\text{excl}} + k_{W+3lp} [W + 3lp]_{\text{excl}} + \\
 &k_{W+4lp} [W + 4lp]_{\text{excl}} + k_{W+5lp} [W + 5lp]_{\text{incl}}
 \end{aligned} \tag{6.1}$$

W+c̄+Light Parton Sample

The $W+c\bar{c}$ +light parton sample contains $W+c\bar{c}$ (from gluon splitting) + light flavor partons. In contrast to the W +light parton samples the c -quark in these events are massive. Eq. 6.2 shows the formula used to combine the $W+c\bar{c}$ +light parton sample and Table 6.2 shows the relative cross sections and weights (k) for each sample. All $W+c\bar{c}$ +light parton events are generated using CTEQ6L1 PDFs with $Q^2 = m_W^2 + P_T^2(W)$.

$$W + c\bar{c} + Nlp = k_{W+c\bar{c}+0lp} [W + c\bar{c} + 0lp]_{\text{excl}} + k_{W+c\bar{c}+1lp} [W + c\bar{c} + 1lp]_{\text{excl}} +$$

Table 6.1: Absolute weights for W +light parton ALPGEN Monte Carlo events.

Sample	Type	Cross Section [pb]	Events	Weight (k)
k_{W+0lp}	Exclusive	4574	7844750	2.15
k_{W+1lp}	Exclusive	1273	1053000	0.68
k_{W+2lp}	Exclusive	298.5	1250500	0.34
k_{W+3lp}	Exclusive	70.56	621000	16.4
k_{W+4lp}	Exclusive	15.83	582250	0.07
k_{W+5lp}	Inclusive	11.29	41750	0.13

$$k_{W+c\bar{c}+2lp} [W + c\bar{c} + 2lp]_{\text{excl}} + k_{W+c\bar{c}+3lp} [W + c\bar{c} + 3lp]_{\text{incl}} \quad (6.2)$$

Table 6.2: Absolute weights for $W+c\bar{c}$ +light parton ALPGEN Monte Carlo events.

Sample	Type	Cross Section [pb]	Events	Weight (k)
$k_{W+c\bar{c}+0lp}$	Exclusive	71.15	481572	0.039
$k_{W+c\bar{c}+1lp}$	Exclusive	29.85	336400	0.036
$k_{W+c\bar{c}+2lp}$	Exclusive	10.25	332347	0.016
$k_{W+c\bar{c}+3lp}$	Inclusive	18.39	372248	0.020

$W+b\bar{b}$ +Light Parton Sample

The $W+b\bar{b}$ +light parton sample contains $W+b\bar{b}$ (from gluon splitting) + light flavor partons. Eq. 6.3 shows the formula used to combine the $W+b\bar{b}$ +light parton sample and Table 6.3 shows the relative cross sections and weights (k) for each sample. All $W+b\bar{b}$ +light parton events are generated using CTEQ6L1 PDFs with $Q^2 = m_W^2 + P_T^2(W)$.

$$\begin{aligned}
W + b\bar{b} + Nlp &= k_{W+b\bar{b}+0lp} [W + b\bar{b} + 0lp]_{\text{excl}} + k_{W+b\bar{b}+1lp} [W + b\bar{b} + 1lp]_{\text{excl}} + \\
&k_{W+b\bar{b}+2lp} [W + b\bar{b} + 2lp]_{\text{excl}} + k_{W+b\bar{b}+3lp} [W + b\bar{b} + 3lp]_{\text{incl}} \quad (6.3)
\end{aligned}$$

Table 6.3: Absolute weights for $W+b\bar{b}$ +light parton ALPGEN Monte Carlo events.

Sample	Type	Cross Section [pb]	Events	Weight (k)
$k_{W+b\bar{b}+0lp}$	Exclusive	19.18	738761	0.014
$k_{W+b\bar{b}+1lp}$	Exclusive	7.939	261300	0.011
$k_{W+b\bar{b}+2lp}$	Exclusive	2.636	171411	0.005
$k_{W+b\bar{b}+3lp}$	Inclusive	1.742	163674	0.003

 $t\bar{t} \rightarrow \ell + jets + Light Parton Sample$

The $t\bar{t} \rightarrow \ell + jets + light$ parton sample contains $t\bar{t} \rightarrow \ell + jets + light$ flavor partons. Eq. 6.4 shows the formula used to combine the $t\bar{t} \rightarrow \ell + jets + light$ parton sample and Table 6.4 shows the relative cross sections and weights (k) for each sample. All $t\bar{t} \rightarrow \ell + jets$ events are generated using CTEQ6L1 PDFs with scale $Q^2 = m_t^2 + \sum_{jets} P_T^2$.

$$\begin{aligned}
t\bar{t} \rightarrow \ell + jets + Nlp &= k_{t\bar{t} \rightarrow \ell + jets + 0lp} [t\bar{t} \rightarrow \ell + jets + 0lp]_{\text{excl}} + \\
& k_{t\bar{t} \rightarrow \ell + jets + 1lp} [t\bar{t} \rightarrow \ell + jets + 1lp]_{\text{excl}} + \\
& k_{t\bar{t} \rightarrow \ell + jets + 2lp} [t\bar{t} \rightarrow \ell + jets + 2lp]_{\text{incl}} \quad (6.4)
\end{aligned}$$

Table 6.4: Absolute weights for $t\bar{t} \rightarrow \ell + jets + light$ parton ALPGEN Monte Carlo events.

Sample	Type	Cross Section [pb]	Events	Weight (k)
$k_{t\bar{t} \rightarrow \ell + jets + 0lp}$	Exclusive	1.284	283463	0.048
$k_{t\bar{t} \rightarrow \ell + jets + 1lp}$	Exclusive	0.625	98425	0.032
$k_{t\bar{t} \rightarrow \ell + jets + 2lp}$	Inclusive	0.398	92517	0.020

 $t\bar{t} \rightarrow \ell\ell + Light Parton Sample$

The $t\bar{t} \rightarrow \ell\ell + light$ parton sample contains $t\bar{t} \rightarrow \ell\ell + light$ flavor partons. Eq. 6.5 shows the formula used to combine the $t\bar{t} \rightarrow \ell\ell + light$ parton sample and Table 6.5 shows the

relative cross sections and weights (k) for each sample. All $t\bar{t} \rightarrow \ell\ell$ events are generated using CTEQ6L1 PDFs with scale $Q^2 = m_t^2 + \sum_{\text{jets}} P_T^2$.

$$\begin{aligned}
t\bar{t} \rightarrow \ell\ell + Nlp &= k_{t\bar{t} \rightarrow \ell\ell + 0lp} [t\bar{t} \rightarrow \ell\ell + 0lp]_{\text{excl}} + \\
& k_{t\bar{t} \rightarrow \ell\ell + 1lp} [t\bar{t} \rightarrow \ell\ell + 1lp]_{\text{excl}} + \\
& k_{t\bar{t} \rightarrow \ell\ell + 2lp} [t\bar{t} \rightarrow \ell\ell + 2lp]_{\text{incl}}
\end{aligned} \tag{6.5}$$

Table 6.5: Absolute weights for $t\bar{t} \rightarrow \ell\ell$ +light parton ALPGEN Monte Carlo events.

Sample	Type	Cross Section [pb]	Events	Weight (k)
$k_{t\bar{t} \rightarrow \ell\ell + 0lp}$	Exclusive	0.324	223635	0.0004
$k_{t\bar{t} \rightarrow \ell\ell + 1lp}$	Exclusive	0.151	96386	0.0078
$k_{t\bar{t} \rightarrow \ell\ell + 2lp}$	Inclusive	0.104	148105	0.0051

6.1.2 Data-based Modeling of Multijet Background

In both electron and muon samples the multijet background is a result of muons from heavy flavor decays or jets with a large electromagnetic fraction mimicking a lepton from a W boson decay. The multijet background is modeled using data events that pass all selection cuts except the isolation cut for muons or likelihood cut for electrons. The normalization of this background as well as all Monte Carlo modeled backgrounds is described in Section 6.2

6.2 Background Normalization

6.2.1 $t\bar{t}$ Normalization

All $t\bar{t}$ Monte Carlo events are normalized to the number of events expected from the NLL0 $t\bar{t}$ cross section and branching ratio multiplied by the integrated luminosity as shown in Eq. 6.6.

$$N_{t\bar{t}} = \sigma_{t\bar{t}} \times \text{BR} \times \int \mathcal{L} dt \tag{6.6}$$

The cross sections shown in Tables 6.4 and 6.5 are leading order cross sections from ALPGEN that must be scaled to match the next-to-next-leading log cross section of 6.67 pb as calculated in [72, 42]. Each event is then assigned a weight such that the total number of weighted Monte Carlo events equals $N_{t\bar{t}}$. The event weight is shown in Eq. 6.7.

$$w_i = \frac{N_{t\bar{t}}}{\sum_i^{N_{\text{selected}}} [\varepsilon_{\text{trigger}} \times \varepsilon_{\text{corrections}} \times \varepsilon_{\text{TRF}}]} \quad (6.7)$$

6.2.2 Matrix Method: Normalizing W +jets and Multijet Backgrounds

The W +jets and multijet backgrounds are normalized through a procedure known as the matrix method. This method requires two datasets to determine the mixture of W +jets and multijet backgrounds. The first sample contains a mixture of W +jets and multijet events while the second sample is enriched in W +jets. The sample that contains the mixture of events is called the “loose” sample and is defined in Eq. 6.8 and a subset of that sample which is enriched in W decays and is called the “tight” sample and is defined in Eq. 6.9. In both samples the $t\bar{t}$ background is normalized as described in Section 6.2.1. The tight sample is a subset of the loose sample with the only difference being that tight events have passed the muon isolation selection cut or the electron likelihood cut.

$$N_{\text{loose}} = N_{\text{Multijet}} + N_{W+\text{jets}} + N_{t\bar{t}} \quad (6.8)$$

$$N_{\text{tight}} = \varepsilon_{\text{Multijet}} \times N_{\text{Multijet}} + \varepsilon_{W+\text{jets}} \times [N_{W+\text{jets}} + N_{t\bar{t}}] \quad (6.9)$$

The two parameters, $\varepsilon_{\text{Multijet}}$ and $\varepsilon_{W+\text{jets}}$, represent the efficiency with which multijet and W +jets events satisfy the tight selection requirement given the loose selection requirement. By inverting the system of two equations and by measuring the two ε parameters, the expected number of W +jets and multijet events can be determined. The formula for the expected number of W +jets events is shown in Eq. 6.10 and the formula for the expected number of multijet events is shown in Eq. 6.11. The methods used to measure the efficiency parameters are shown in the appropriately labeled sections below. The number of loose and tight events for each jet multiplicity is shown in Table 6.6 along with the expected number of multijet and W +jets events in the tight sample.

$$N_{W+jets} = \frac{N_{\text{tight}} - \varepsilon_{\text{Multijet}} \times N_{\text{loose}}}{\varepsilon_{W+jets} - \varepsilon_{\text{Multijet}}} - N_{t\bar{t}} \quad (6.10)$$

$$N_{\text{Multijet}} = \frac{\varepsilon_{W+jets} \times N_{\text{loose}} - N_{\text{tight}}}{\varepsilon_{W+jets} - \varepsilon_{\text{Multijet}}} \quad (6.11)$$

Table 6.6: Number of loose and tight data events after all selection cuts (top two rows) along with the expected number W +jets and multijet events in the tight sample (bottom two rows).

	Electron Channel			Muon Channel		
	2 jets	3 jets	4 jets	2 jets	3 jets	4 jets
N_{loose}	15,213	7,118	2,191	7,092	3,054	878
N_{tight}	8,220	3,075	874	6,432	2,590	727
$\varepsilon_{\text{Multijet}} \times N_{\text{Multijet}}$	1,433	860	256	329	223	56
$\varepsilon_{W+jets} \times N_{W+jets}$	6,787	2,215	618	6,105	2,369	669

All W +jets events are then given a weight such that the total number of weighted events equals the expected yields shown in Table 6.6. The W +jets event weight is shown in Eq. 6.12 and the multijet event weight is shown in Eq. 6.13.

$$w_i = \frac{1}{\sum_i^{N_{\text{selected}}} [\varepsilon_{\text{trigger}} \times \varepsilon_{\text{corrections}} \times \varepsilon_{\text{TRF}}]} \times [\varepsilon_{W+jets} \times N_{W+jets}] \quad (6.12)$$

$$w_i = \frac{1}{N_{\text{Data Sample}}} \times [\varepsilon_{\text{Multijet}} \times N_{\text{Multijet}}] \quad (6.13)$$

Multijet Efficiency: $\varepsilon_{\text{Multijet}}$

The efficiency with which multijet events pass the muon isolation or electron likelihood cut is measured on data events that pass all selection cuts except the missing E_T cut. All events are required have missing $E_T < 10$ GeV to eliminate the presence of a $W \rightarrow \ell\nu$ decay. $\varepsilon_{\text{Multijet}}$ is defined as the fraction of events that pass the muon isolation or electron likelihood

cut with missing $E_T < 10$ GeV. Table 6.7 shows the average values of $\varepsilon_{\text{Multijet}}$ in the electron and muon channel.

Table 6.7: Average multijet efficiency: $\varepsilon_{\text{Multijet}}$

	Electron Channel			Muon Channel		
	2 jets	3 jets	4 jets	2 jets	3 jets	4 jets
$\varepsilon_{\text{Multijet}}$	0.19	0.19	0.17	0.36	0.34	0.31

W+jets Efficiency: ε_{W+jets}

The $W+jets$ efficiency is measured in $Z \rightarrow \mu\mu$ and $Z \rightarrow ee$ data events using a tag and probe method as described in Chapter 4. ε_{W+jets} is defined as the fraction of events which pass the muon isolation cut or the electron likelihood cut. The average value of ε_{W+jets} for all jet multiplicities is shown in Table 6.8

Table 6.8: Average $W+jets$ efficiency: ε_{W+jets}

	Electron Channel			Muon Channel		
	2 jets	3 jets	4 jets	2 jets	3 jets	4 jets
ε_{W+jets}	0.87	0.87	0.87	0.99	0.99	0.96

6.2.3 Ratio of W+Heavy Flavor to W+Light Flavor

The $W+jets$ cross sections shown in Tables 6.1, 6.2, and 6.3 are all leading order and are sensitive to next-to-leading order (NLO) corrections. In particular, the NLO corrections for $W + b\bar{b}$ and $W + c\bar{c}$ events are expected to be quite different from $W + lp$ events. The ratio $(Wb\bar{b} + Wc\bar{c})/Wlp$ is measured in data where no jets are B -tagged to avoid a bias from the data sample used in the single top quark analysis. The ratio was also also measured in

the standard data samples, but only as a cross check. Events with one reconstructed jet were included in the α determination. This ratio, called α , is determined after the matrix method normalization of Multijet and W +jets events and is calculated using Eq. 6.14

$$N_{\text{Data}} = \alpha \times (N_{Wb\bar{b}} + N_{Wc\bar{c}}) + N_{Wl\bar{p}} + N_{\text{Multijet}} + N_{t\bar{t}} \quad (6.14)$$

Table 6.9 shows the value of α and the uncertainty in each sample and Fig. 6.4 shows a fit to the eight independent zero B -tag samples. As determined from the fit, α was set to 1.5 and assigned a 30% systematic error. The large systematic uncertainty is designed to cover the known theoretical uncertainties regarding b quark production in $Wb\bar{b}$ and Wbj events between leading order and next-to-leading order [55, 51, 43].

Table 6.9: Scale factor α for the $Wb\bar{b}$ and $Wc\bar{c}$ yields to match the data in each jet bin, for zero B -tags, 1 B -tag, and two B -tags samples. The uncertainties are statistical only.

	1 jet	2 jets	3 jets	4 jets
Electron Channel				
0 B -tags	1.53 ± 0.10	1.48 ± 0.10	1.50 ± 0.20	1.72 ± 0.40
1 B -tag	1.29 ± 0.10	1.58 ± 0.10	1.40 ± 0.20	0.69 ± 0.60
2 B -tags	—	1.71 ± 0.40	2.92 ± 1.20	-2.91 ± 3.50
Muon Channel				
0 B -tags	1.54 ± 0.10	1.50 ± 0.10	1.52 ± 0.10	1.38 ± 0.20
1 B -tag	1.11 ± 0.10	1.52 ± 0.10	1.32 ± 0.20	1.86 ± 0.50
2 B -tags	—	1.40 ± 0.40	2.46 ± 0.90	3.78 ± 2.80

6.3 Background Yields

This section contains tables showing the observed number of data events, the total expected background, and the total number of expected signal events. Tables 6.10, 6.11, and 6.12

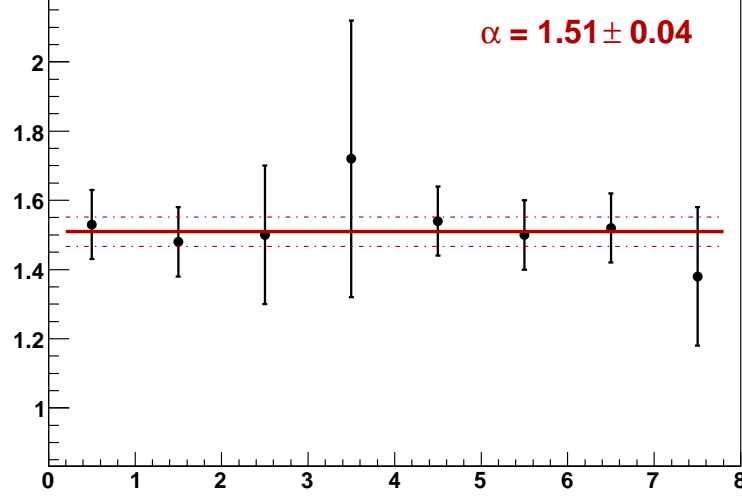
Heavy flavour scale factor α measured in the zero tag bins

Figure 6.4: α values with errors for the eight zero B -tagged jet samples and the linear fit with error to the values [56].

show the number of events for the following cases: before any B -jet requirement, one B -tagged jet, and two B -tagged jets.

Table 6.10: Event yields after selection and before B tagging.

	Electron Channel			Muon Channel		
	2 Jets	3 Jets	4 Jets	2 Jets	3 Jets	4 Jets
Backgrounds						
$t\bar{t}$	61	131	138	41	93	107
W +jets	6,726	2,084	478	6,063	2,275	563
Multijets	1,433	860	256	329	223	58
Expected Signal	41	21	7	30	16	4
Background Sum	8,220	3,075	874	6,434	2,592	727
Data	8,220	3,075	874	6,432	2,590	727

Table 6.11: Event yields after selection and one selected B -jet.

	Electron Channel			Muon Channel		
	2 jets	3 jets	4 jets	2 jets	3 jets	4 jets
Backgrounds						
$t\bar{t}$	27	60	63	19	42	49
W +jets	255	106	28	242	125	35
Multijets	66	48	18	26	24	8
Expected Signal	18	9	3	14	7	2
Background Sum	348	213	110	286	191	93
Data	357	207	97	287	179	100

Table 6.12: Event yields after selection and two selected B -jets.

	Electron Channel			Muon Channel		
	2 jets	3 jets	4 jets	2 jets	3 jets	4 jets
Backgrounds						
$t\bar{t}$	7.2	18.2	23.5	5.6	15.0	19.4
W +jets	17.9	8.0	2.2	17.0	9.8	2.8
Multijets	2.5	3.2	2.7	1.5	1.9	0.4
Expected Signal	2.6	1.9	0.7	2.1	1.6	0.6
Background Sum	27.5	29.4	28.4	24.1	25.7	22.7
Data	30	37	22	23	32	27

6.4 Comparison of Data with Expectation

The following histograms compare data with the sum of the expected background for events before B -tagging, events with one B -tag, and events with two B -tags. Four kinematic variables are shown: leading jet p_T (jet with largest p_T), second jet p_T (jet with second largest p_T), lepton p_T (either electron or muon), and missing E_T . The error bands on the plots represent the combined statistical and systematic error for the data sample. A description and magnitude of each systematic error can be found in Chapter 8. All plots show combined electron and muon events.

All histograms use the same color convention for backgrounds. The convention is shown in Fig. 6.5.

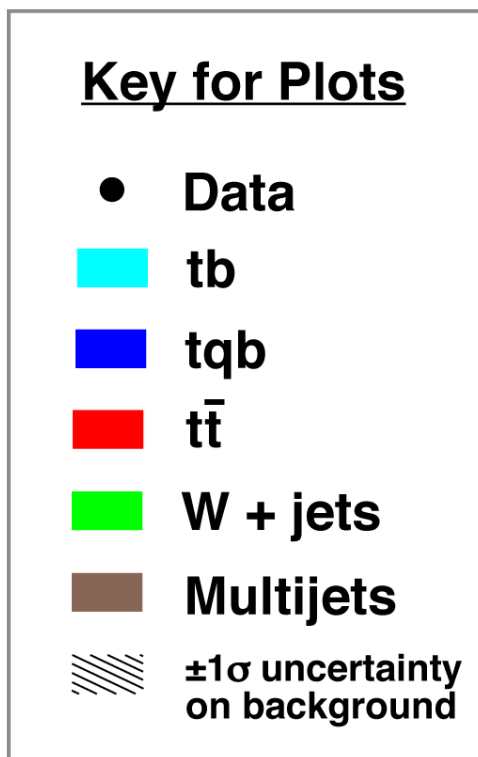


Figure 6.5: Color convention used in all histograms.

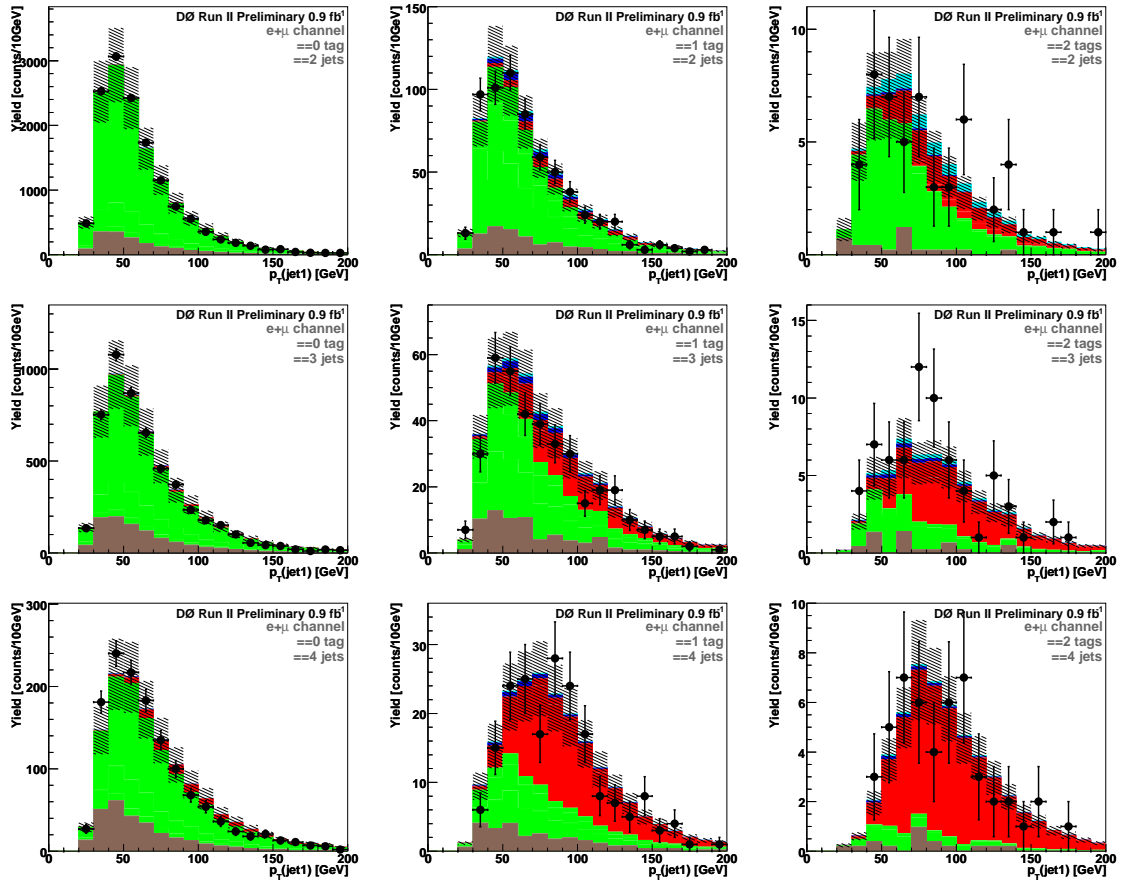
LEADING JET P_T 

Figure 6.6: Leading jet p_T distributions. Upper row: events with 2 jets, Middle row: events with 3 jets, Lower row: events with 4 jets. Left column: events before B -tagging, Middle row: events with one selected B -jet, Right column: events with two selected B -jets [56].

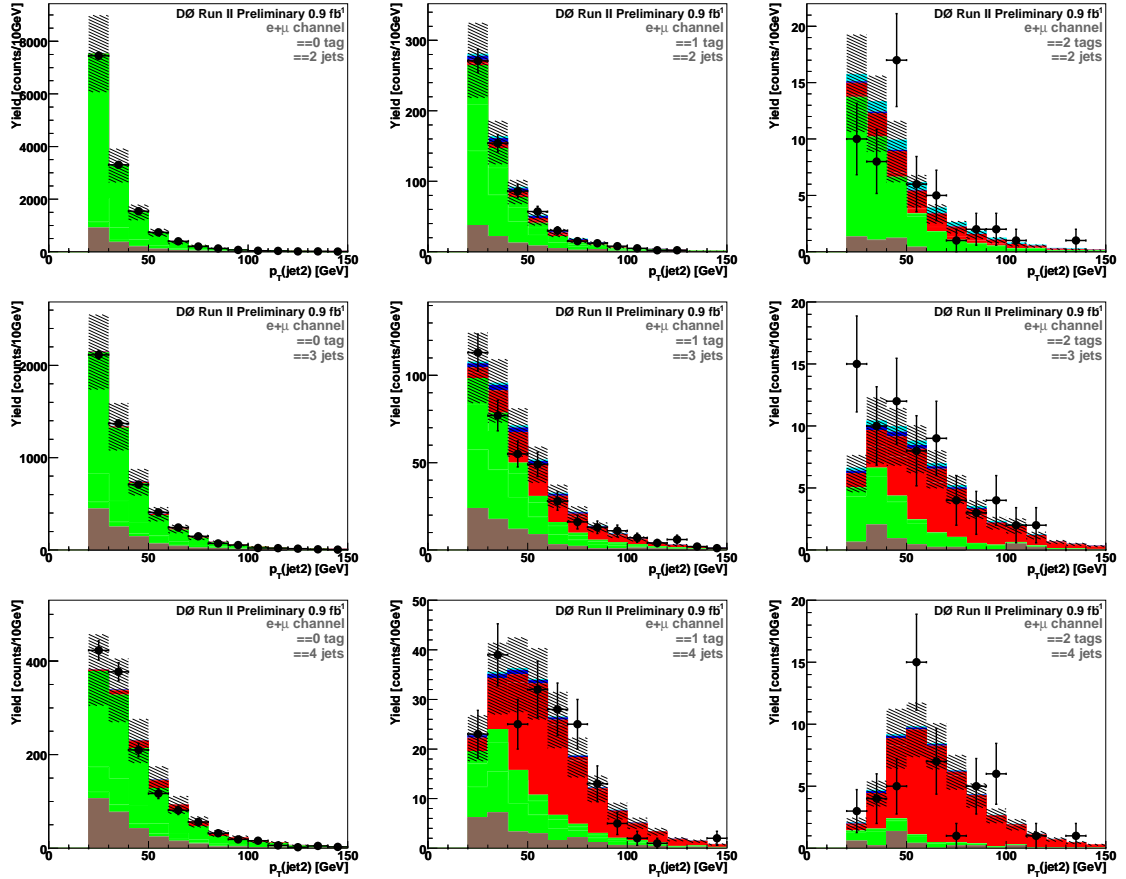
SECOND JET P_T 

Figure 6.7: Second leading jet p_T distributions. Upper row: events with 2 jets, Middle row: events with 3 jets, Lower row: events with 4 jets. Left column: events before B -tagging, Middle row: events with one selected B -jet, Right column: events with two selected B -jets [56].

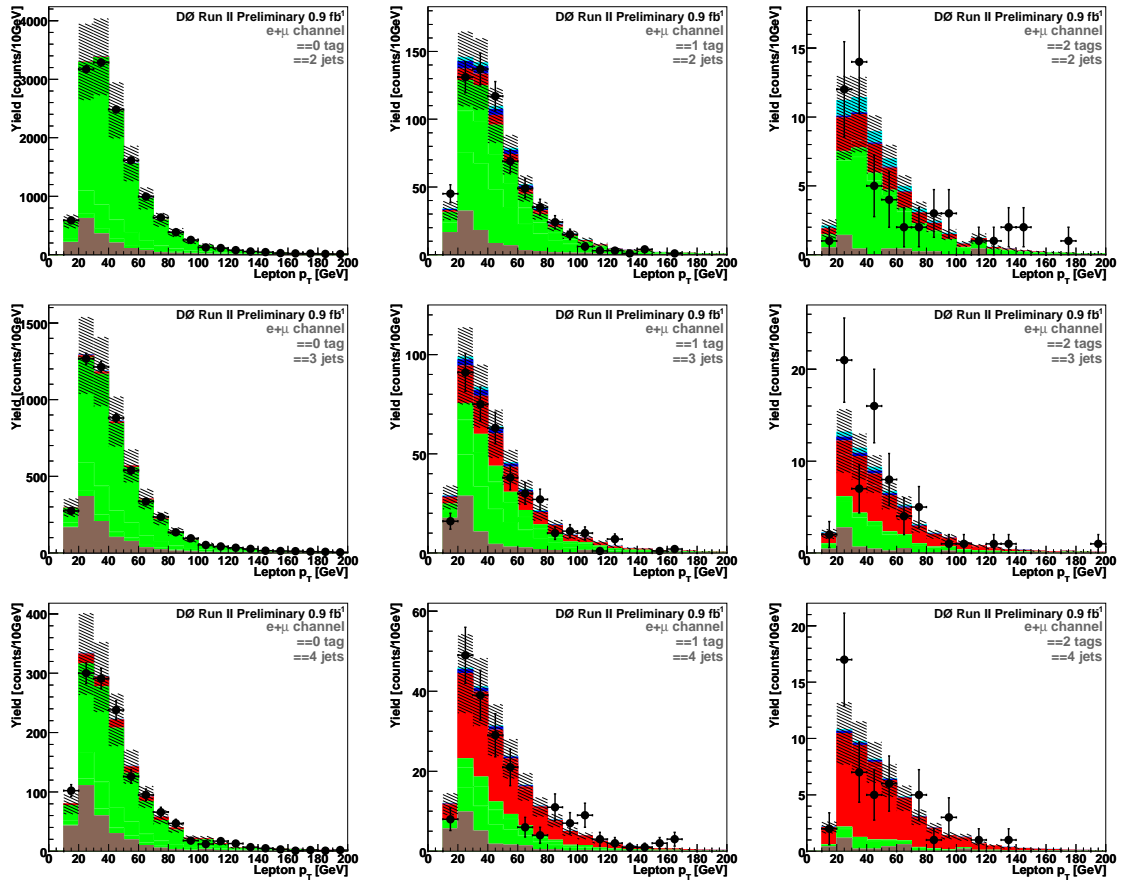
LEPTON P_T 

Figure 6.8: Lepton p_T distributions. Upper row: events with 2 jets, Middle row: events with 3 jets, Lower row: events with 4 jets. Left column: events before B -tagging, Middle row: events with one selected B -jet, Right column: events with two selected B -jets [56].

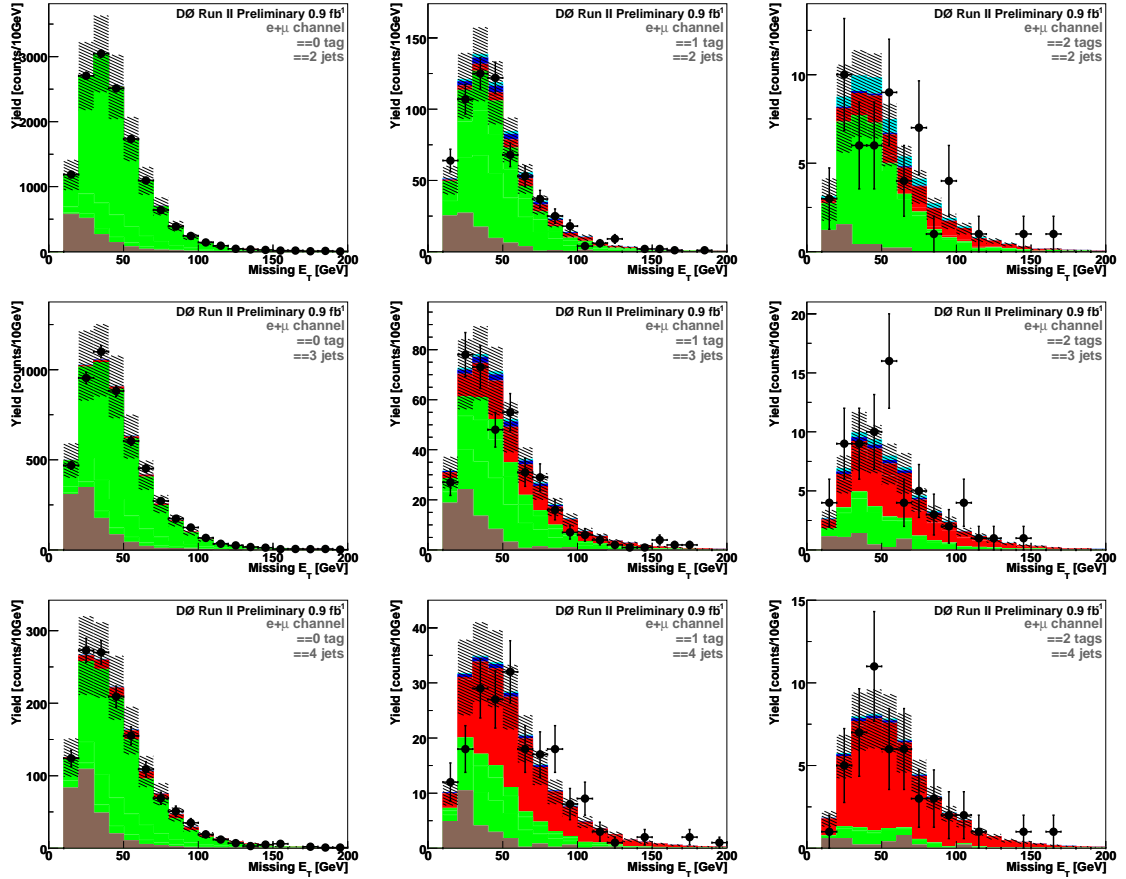
MISSING E_T 

Figure 6.9: Missing E_T distributions. Upper row: events with 2 jets, Middle row: events with 3 jets, Lower row: events with 4 jets. Left column: events before B -tagging, Middle row: events with one selected B -jet, Right column: events with two selected B -jets [56].

Chapter 7

MATRIX ELEMENT ANALYSIS METHOD

This chapter provides the motivation and explanation of a technique known as the matrix element method, which uses probabilities based on leading order matrix elements to extract the single top signal in the dataset. The matrix element method is employed after event selection because the signal to background ratio is $\sim 1 : 20$ thus making an observation of single top impossible. Section 7.1 motivates the matrix element method and explains how it is applied to the single top search. The result of the matrix element method is a set of probabilities for each event to originate from either a signal or background process. The definition and derivation of these probabilities is given in Section 7.2. Section 7.3 shows the expected separation power between signal and background events using the matrix element method. A comparison of data with the background expectation is shown in Section 7.4 for a data sample where the expected signal fraction is negligible. The result of this comparison shows that the data and background estimation agree after applying the matrix element discriminant. Finally, Section 7.5 shows a comparison of data with the expectation for all events.

7.1 Motivation and Introduction to the Matrix Element Method

The measurement of a process with a low rate such as single top quark production requires advanced methods to reduce background rates while keeping signal acceptance high. $D\bar{O}$ has previously published two analyzes using decision trees and neural networks [17, 20] and released preliminary results using a likelihood discriminant method [46]. All three of these methods combine differential distributions, that show discrimination between signal and background events, to form a variable which attempts to maximally separated the signal and background. For example, one famous differential distribution that is quite different in signal and background events is the charge of the lepton from the W boson decay multiplied

by the η of the forward un-tagged jet. This distribution is shown for t -channel single top and $Wb\bar{b}$ production in Fig. 7.1.

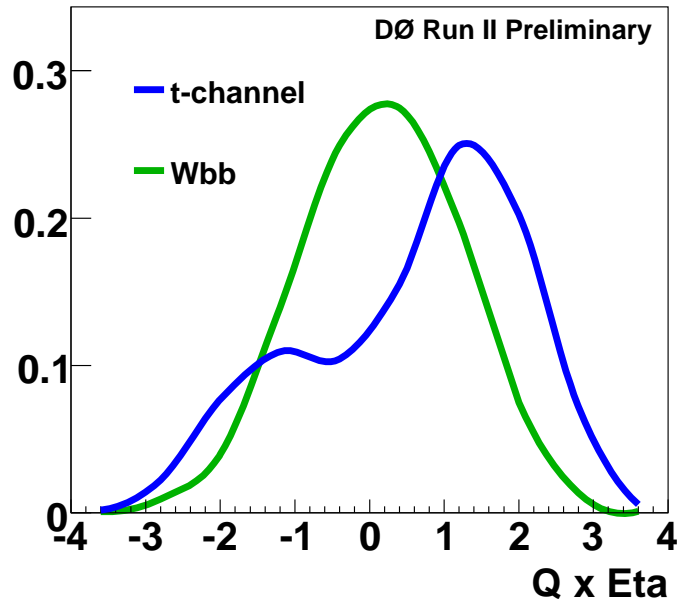


Figure 7.1: Comparison of the lepton charge multiplied by the forward un-tagged jet η ($q_\ell \times \eta$) for t -channel single top (blue) and $Wb\bar{b}$ Monte Carlo events.

While these methods are very powerful they require *a-priori* knowledge of the expected correlations in signal and background events. Searching for these correlations is time consuming and if all correlations are not exploited in the analysis it will lead to sub-optimal separation power.

The matrix element method attempts reproduce all correlations present in both signal and background events by weighting events based on the normalized N -dimensional differential cross section¹ at the detector level for both signal and background processes, as shown in Eq. 7.1.

$$P_{S|B}(\vec{x}) = \frac{1}{\sigma} \frac{d^N \sigma_{S|B}}{dx^N} \quad (7.1)$$

¹ N is the number of independent observables in the event.

The number independent observables (N) in the event depends on the number of observed particles. For example, an event in the single top dataset will have one lepton, large missing E_T and two or three jets² resulting in $3(p_x, p_y, p_z) \times 3(4)$ particles = 9(12) d.o.f for events with two(three) jets. Since the missing E_T is indirectly measured from momentum balance with the lepton and jets it is not an independent quantity and therefore not used in the method.

The normalized differential cross sections for signal and background processes are combined using the *a-posteriori* Bayesian probability density for the signal hypothesis to be true given the measured event \vec{x} as shown in Eq. 7.2

$$D_S(\vec{x}) = P(S|\vec{x}) = \frac{P_S(\vec{x})}{P_S(\vec{x}) + P_B(\vec{x})} \quad (7.2)$$

The remainder of this chapter describes how the differential cross section and normalization are calculated for the signal and background.

7.2 Event Probability Density, $P_{S|B}(\vec{x})$

7.2.1 Differential Cross Section Definition

The differential cross section at the detector level, $\frac{d\sigma}{d\vec{x}}$, is given in Eq. 7.3; it is defined as the integration over the initial and final state particles' phase space weighted by the differential cross section at the parton level convoluted with a conditional probability to observe event \vec{x} given a particular parton-level state (\vec{y}). All quantities in this equation are explained below.

$$\frac{d\sigma}{d\vec{x}} = \sum_{i,j} \int d\vec{y} \left[f_i(q_1, Q^2) dq_1 \times f_j(q_2, Q^2) dq_2 \times \frac{d\sigma_{hs,ij}}{d\vec{y}} \times W(\vec{x}, \vec{y}) \times \Theta_{\text{Parton}}(\vec{y}) \right] \quad (7.3)$$

- $\sum_{i,j}$ is a sum of initial parton flavors in the hard scatter collision. For example, an s -channel collision can occur via $u\bar{d}$, $c\bar{s}$, $d\bar{u}$, or $s\bar{c}$ annihilation.

²Events with four jets are not used in this analysis.

- $f_i(q, Q^2)$ is the parton distribution function for parton i carrying momentum q , evaluated at the factorization scale Q^2 . The scale used for W +jets processes is $Q^2 = M_W^2 + \sum_{jets} (m_i^2 + p_{T,i}^2)$, where m_i are the parton masses and $p_{T,i}$ are the transverse momenta of the partons. The scale used for s -channel events is $Q^2 = m_t^2$ and scale for t -channel events is $Q^2 = (\frac{m_t}{2})^2$. This analysis uses CTEQ6 [81] leading-order parton distribution functions accessed via LHAPDF [40].
- $\frac{d\sigma_{hs,ij}}{d\vec{y}}$ is the differential cross section for the hard scatter collision and is solely a function of the initial and final state four-vectors \vec{y} . This quantity is proportional to the square of the leading order matrix element, as shown in Eq. 7.4:

$$d\sigma_{hs} = \frac{(2\pi)^4}{4\sqrt{(q_1 q_2)^2 - m_1^2 m_2^2}} |\mathcal{M}|^2 d\Phi_n(\vec{y}) \quad (7.4)$$

where the first term is the flux factor, the second term is the matrix element squared, and the third term is the n -body phase space factor, with $n = 4(5)$ for two-jet (three-jet) events, as defined in Eq. 7.5.

$$d\Phi_n(\vec{y}) = \delta^4(P - \sum_{i=1}^n p_i) \prod_{i=1}^n \frac{d^3 p_i}{(2\pi)^3 2E_i} \quad (7.5)$$

Matrix elements in this analysis were obtained from the Madgraph [78] leading-order matrix-element generator. The signal and background matrix elements depend on the the number of reconstructed jets in the event. Events with two jets are integrated using five matrix elements: two signals (s -channel and t -channel) and three backgrounds ($Wb\bar{b}$, Wcg , and Wgg). Events with three jets are integrated using three matrix elements: two signals (s -channel and t -channel and one background ($Wbbg$). The Feynman diagrams for the two and three jet processes are shown in Figs. 7.2.1 and 7.2.1, respectively.

- $W(\vec{x}, \vec{y})$ is called the transfer function, which represents the conditional probability to observe a particular state in the detector (\vec{x}) given the original parton-level state (\vec{y}). The transfer functions are determined using Monte Carlo where the true parton-level

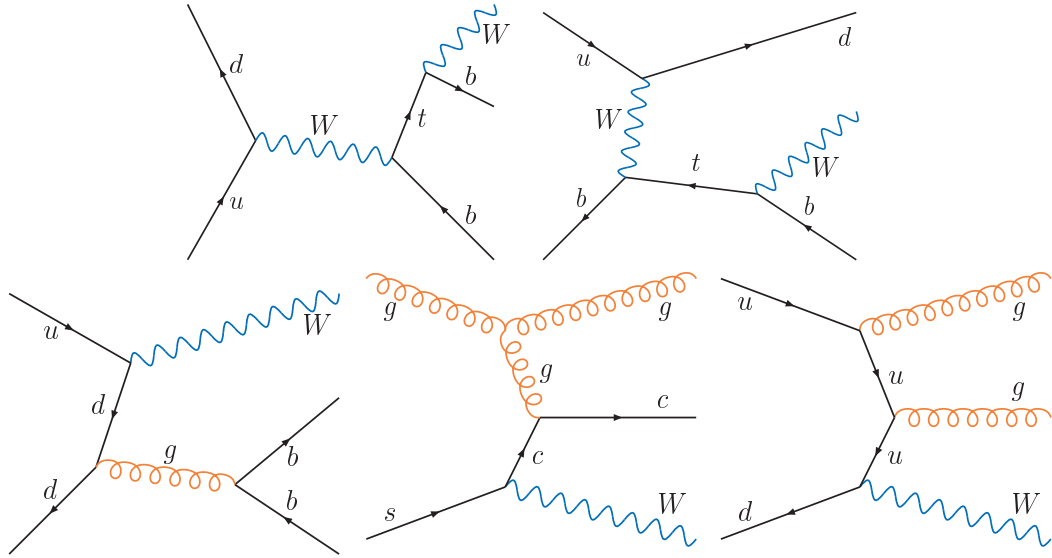


Figure 7.2: Representative Feynman diagrams corresponding to the leading-order matrix elements used for event probability calculation for events with exactly two jets. Upper row are signals: $ud \rightarrow tb$ and $ub \rightarrow td$; lower row are backgrounds: $ud \rightarrow Wbb$, $sg \rightarrow Wcg$, and $ud \rightarrow Wgg$.

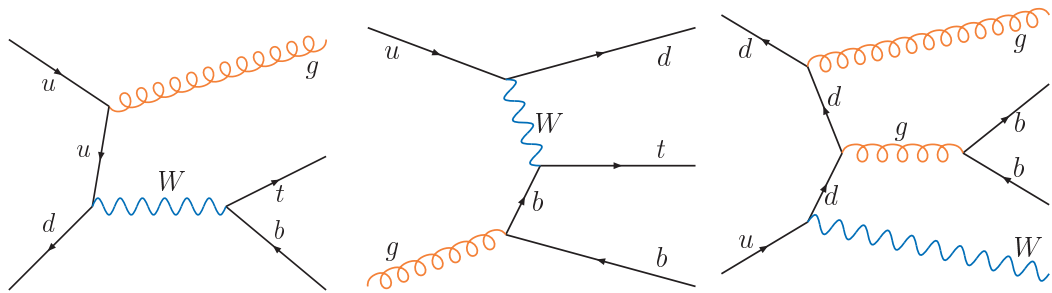


Figure 7.3: Representative Feynman diagrams corresponding to the leading-order matrix elements used for event probability calculation for events with exactly three jets. Left two plots: signals, $ud \rightarrow tbg$, $ug \rightarrow tbd$; right plot: background, $ud \rightarrow Wbbg$.

four-vectors are known. Transfer functions are determined separately for electrons, muons, and jets, and the full event transfer function is defined as a product of each individual object transfer function as shown in Eq. 7.6. The description of the transfer function for each object is given below.

$$W(\vec{x}, \vec{y}) = \prod_{i=1}^n W_{\text{Type}}(\vec{x}_i, \vec{y}_i) \quad (7.6)$$

- Jets - The jet transfer functions are determined for three types of jets: jets originating from a light flavor quark or gluon, jets originating from a b quark that do not contain a muon, and jets originating from a b quark that do contain a muon. A jet is considered to originate from a b quark if there is a B meson with $\Delta R < 0.15$ from the jet axis. Any jet that fails this requirement, but is matched to a light flavor quark or gluon with the same matching criteria is considered a light flavor jet. For all jet types the polar angle θ and azimuthal angle ϕ are assumed to be same for the jet and parton. This assumption has been verified in the Monte Carlo. This leaves the jet and parton energies, E_j and E_p , as the sole factors with which the transfer functions depend. To minimize the effect of statistical fluctuations, the transfer functions are parameterized using the functional form shown in Eq. 7.7. To account for detector effects the transfer functions were also determined in four η^{det} regions ($0 < |\eta| < 0.5$, $0.5 < |\eta| < 1.0$, $1.0 < |\eta| < 1.5$, $1.5 < |\eta| < 3.5$).

$$W_{\text{Jet}}(E_p, E_j) = N \times \left[\exp \left\{ \frac{-(\Delta E - \alpha_1)^2}{2p_2^2} \right\} + \alpha_3 \exp \left\{ \frac{-(\Delta E - \alpha_4)^2}{2p_5^2} \right\} \right] \quad (7.7)$$

$$N = \frac{1}{\sqrt{2\pi}(\alpha_2 + \alpha_3\alpha_5)}$$

Where $\Delta E = E_j - E_p$ and $\alpha_i = a_i + b_i \times E_p$. For each of the three jet types and each of the four detector regions the transfer function parameters are determined by minimizing the logarithm of the likelihood function, shown in Eq. 7.8.

$$L(\vec{\alpha}) = \prod_{i=1}^{N_{\text{Events}}} W(\vec{\alpha}, E_p^i, E_j^i) \quad (7.8)$$

The values of $\vec{\alpha}$ for light jets, B -jets, and B -jets w/ μ can be found in Tables 7.1, 7.2, and 7.3. A plot of ΔE for all jets used to determine the transfer function parameters is shown in Fig. 7.4.

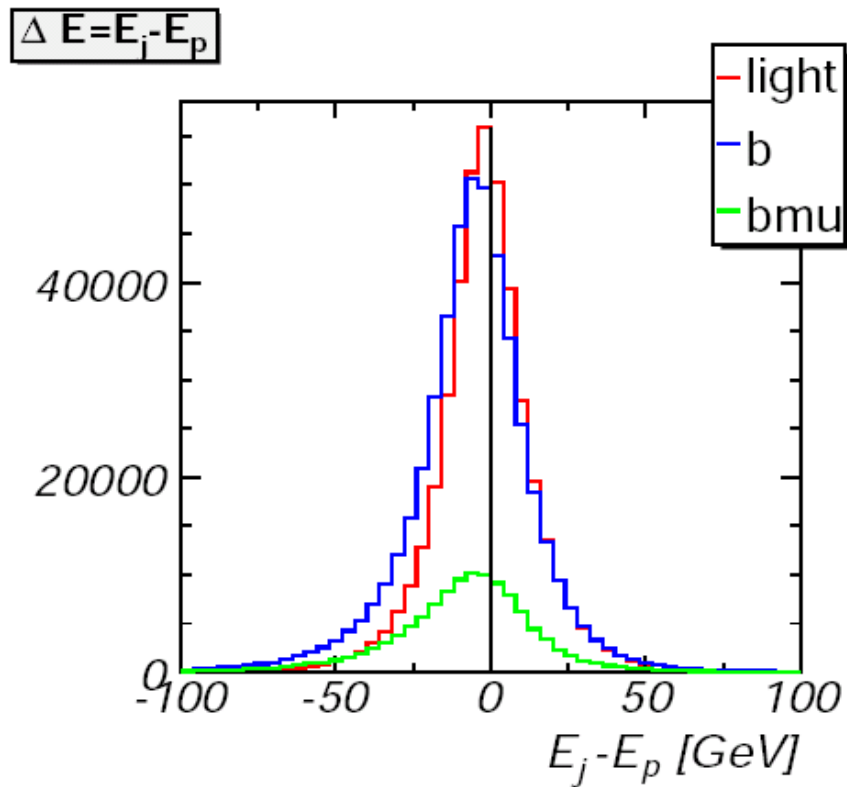


Figure 7.4: Energy difference between a reconstructed jet and its matched parton for three types of jets for all eta regions and all jet energies.

- Electrons - The transfer function for electrons is assumed to be solely a function of the reconstructed energy of the electron, E_e , the parton-level energy of the electron, E_p , and θ , the production angle with respect to the beam axis. The transfer function is parameterized by a Gaussian in the relative energy difference with a width that depends on the reconstructed energy and the production angle.

Table 7.1: Light jet transfer function parameters.

	α_1		α_2		α_3		α_4		α_5	
	a	b	a	b	a	b	a	b	a	b
$0.0 < \eta < 0.5$	-4.17	0.04	4.12	0.11	0.0	0.0013	24.8	-0.19	15.6	0.23
$0.5 < \eta < 1.0$	-2.90	0.03	5.26	0.12	0.0	0.0010	57.3	-0.47	-16.1	0.69
$1.0 < \eta < 1.5$	-0.61	0.02	8.16	0.13	0.0	0.0010	70.7	-0.37	-11.5	0.54
$1.5 < \eta < 3.5$	3.12	-0.06	12.4	0.11	0.0	0.0011	234	-1.53	-22.3	0.49

Table 7.2: B jet transfer function parameters.

	α_1		α_2		α_3		α_4		α_5	
	a	b	a	b	a	b	a	b	a	b
$0.0 < \eta < 0.5$	-5.61	0.01	3.27	0.14	0.0	0.0018	49.9	-0.77	32.7	-0.03
$0.5 < \eta < 1.0$	-4.07	0.01	3.31	0.15	0.0	0.0018	52.1	-0.76	41.1	-0.09
$1.0 < \eta < 1.5$	-1.92	-0.06	6.46	0.15	0.0	0.0011	98.8	-0.74	-17.0	0.64
$1.5 < \eta < 3.5$	-0.87	-0.07	5.84	0.17	0.0	0.0011	-5.84	-0.98	-5.83	0.39

Table 7.3: B w/ μ jet transfer function parameters.

	α_1		α_2		α_3		α_4		α_5	
	a	b	a	b	a	b	a	b	a	b
$0.0 < \eta < 0.5$	-1.38	-0.06	3.65	0.16	0.0	0.0017	55.7	-0.46	91.5	-0.16
$0.5 < \eta < 1.0$	-0.37	-0.07	4.30	0.16	0.0	0.0014	110	-0.93	-4.56	0.66
$1.0 < \eta < 1.5$	2.61	-0.11	5.42	0.17	0.0	0.0015	119	-0.91	-9.31	0.39
$1.5 < \eta < 3.5$	12.9	-0.20	4.17	0.19	0.0	0.0024	215	-1.39	42.3	0.17

This functional form is shown in Eq. 7.9.

$$W(E_e, E_p, \theta) = \frac{1}{2\pi\sigma} \exp \left\{ -\frac{(E_e - \alpha_1 \times E_p - \alpha_2)^2}{2\sigma^2} \right\} \quad (7.9)$$

Where the Gaussian width σ is defined as the product of a parton energy error term, a sampling error term, and a constant error term as shown in Eq. 7.10.

The values of $\vec{\alpha}$ in the electron transfer function are shown in Table 7.4.

$$\begin{aligned} \sigma &= \alpha_3 E_{\text{cen}} \times \text{Sampling}(E_{\text{cen}}, \theta) E_{\text{cen}} \times \alpha_4 \\ E_{\text{cen}} &= \alpha_1 E_p + \alpha_2 \\ \text{Sampling}(E_e, \theta) &= \left[\frac{\alpha_5}{\sqrt{E_e}} + \frac{\alpha_6}{E_e} \right] \exp \left\{ \frac{f(E_e)}{\sin\theta} - f(E_e) \right\} \\ f(E_e) &= \alpha_7 - \frac{\alpha_8}{E_e} - \frac{\alpha_9}{E_e^2}. \end{aligned} \quad (7.10)$$

Table 7.4: Electron transfer function parameters.

E_{cen}		σ		Sampling		$f(E)$		
α_1	α_2	α_3	α_4	α_5	α_6	α_7	α_8	α_9
0.0002	0.324	0.028	0.4	0.164	0.122	1.35	2.09	6.99

- Muons - The muon transfer functions are determined for muons with and without SMT hits and are parameterized using the Gaussian functional form shown in Eq. 7.11.

$$W \left(\left(\frac{q}{p_t} \right)_\mu, \left(\frac{q}{p_t} \right)_p, \eta \right) = \frac{1}{2\pi\sigma} \exp \left\{ -\frac{\left[\Delta \left(\frac{q}{p_t} \right) \right]^2}{2\sigma^2} \right\} \quad (7.11)$$

Where the Gaussian width σ is defined separately for two η regions as shown in Eq. 7.12. The η region dependence is a result of the limited η coverage of the central fiber tracker in the forward region.

$$\sigma = \left\{ \begin{array}{ll} \alpha_1 & : |\eta| \leq 1.4 \\ \sqrt{\alpha_1^2 + [\alpha_2(|\eta| - 1.4)]^2} & : |\eta| > 1.4 \end{array} \right\} \quad (7.12)$$

The parameters α_1 and α_2 in the transfer function parameterization contain a constant term and a term proportional to $\frac{1}{p_T}$. The four parameters are extracted using a maximum likelihood method similar to the method used to determine the jet transfer function. The muon transfer function parameters are shown in Table 7.5.

Table 7.5: Muon transfer function parameters (Eq. 7.11) for muons with and without SMT hits.

Muon Type	α_1		α_2	
	Constant	$\propto \frac{1}{p_T}$	Constant	$\propto \frac{1}{p_T}$
= 0 SMT Hits	2.96×10^{-3}	2.91×10^{-2}	1.95×10^{-2}	-3.04×10^{-2}
≥ 1 SMT Hit	2.07×10^{-3}	2.22×10^{-2}	5.56×10^{-3}	1.19×10^{-1}

- $\Theta_{\text{Parton}}(\vec{y})$ represents the parton level cuts applied to avoid singularities in the matrix element evaluation. All differential cross sections were calculated with the following parton level cuts:
 - Parton isolation: $\Delta R(q_i, q_j) > 0.5$
 - Minimum parton P_T : $P_T(q_i) > 6 \text{ GeV}$
 - Maximum parton pseudorapidity: $|\eta(q_i)| < 3.5$
 - No cuts are applied to the lepton or neutrino
- $\int d\vec{y} dq_1 dq_2$ is an integration over the phase space defined by the final state particles ($d\vec{y}$) and the two initial parton's longitudinal momentum (dq_1, dq_2). The phase space for a lepton, neutrino, and two parton final state event is defined by 14 degrees of

freedom (one momentum (p) and two angles (Ω) for each final state particle plus the two initial parton momenta), as shown in Eq. 7.13.

$$d\vec{y}_{\ell\nu q_1 q_2} = dq_1 dq_2 d|p|_\ell d\Omega_\ell d|p|_\nu d\Omega_\nu d|p|_{q_1} d\Omega_{q_1} d|p|_{q_2} d\Omega_{q_2} \quad (7.13)$$

Events with three partons in the final state have 17 degrees of freedom and has a phase space defined in Eq. 7.14.

$$d\vec{y}_{\ell\nu q_1 q_2 q_3} = dq_1 dq_2 d|p|_\ell d\Omega_\ell d|p|_\nu d\Omega_\nu d|p|_{q_1} d\Omega_{q_1} d|p|_{q_2} d\Omega_{q_2} d|p|_{q_3} d\Omega_{q_3} \quad (7.14)$$

When performing the integration four (six) degrees of freedom are removed for two (three) parton events by assuming equal azimuthal and polar angles (ϕ, θ) for partons and jets as required by the transfer functions. Two more degrees of freedom are removed by assuming well measured lepton angles. Four more degrees of freedom are removed from the integration by energy-momentum conservation, leaving four(five) integration variables for events with two(three) jets. The final integration phase space is then transformed to suit the matrix element being integrated. W +jets matrix element integrations use the phase space defined in Eqs. 7.15 and single top matrix element integrations use the phase space in Eq. 7.16.

$$\begin{aligned} d\vec{y}_{W+\text{jets}-2\text{jets}} &= du_W d|p_{q_1}| d|p_{q_2}| dp_z^{system} \\ d\vec{y}_{W+\text{jets}-3\text{jets}} &= du_W d|p_{q_1}| d|p_{q_2}| d|p_{q_3}| dp_z^{system} \end{aligned} \quad (7.15)$$

$$\begin{aligned} d\vec{y}_{\text{singletop}-2\text{jets}} &= du_t du_W d|p_{q_2}| dp_z^{system} \\ d\vec{y}_{\text{singletop}-3\text{jets}} &= du_t du_W d|p_{q_2}| d|p_{q_3}| dp_z^{system} \end{aligned} \quad (7.16)$$

In Eqs. 7.15 and 7.16, du_W and du_t are used to uniformly sample a Breit-Wigner distribution centered around the W mass and top quark mass, respectively. Because the differential cross section for a W +jets process is sharply peaked when the mass of

the lepton and neutrino system is near the W mass, integrating solely in this region reduces the integration time considerably. The same reasoning applies to the top quark mass and the mass of the lepton, neutrino, and b -quark. The initial parton momentum fractions are transformed into the total system energy and longitudinal momentum. With this choice of integration variables the total energy integral is removed along with the neutrino momentum from energy and momentum conservation. The total longitudinal momentum remains as an integration variable.

When changing integration variables a Jacobian is required to modify the differential cross section. The Jacobians for the W +jets and single top change of variable are shown in Eqs. 7.17 and 7.18.³

$$|J(p_3, \rightarrow u_W)| = \frac{2}{s} \times \Delta S_W \times \left| \frac{[(m_W \Gamma_W)^2 + (m_{34}^2 - m_W^2)^2]}{2(p_3 + p_4)(1 - \hat{p}_3 \cdot \hat{p}_4)} \right| \quad (7.17)$$

$$|J(p_3, p_5 \rightarrow u_W, u_t)| = \frac{2}{s} \times \Delta S_W \times \Delta S_t \times \left| \begin{array}{c} \frac{[(m_t \Gamma_t)^2 + (m_{345}^2 - m_t^2)^2]}{2(p_3 + p_4 + p_5)(1 - \hat{p}_3 \cdot \hat{p}_4)} \\ \frac{[(m_t \Gamma_t)^2 + (m_{345}^2 - m_t^2)^2]}{2(p_3 + p_4 + p_5)(1 - \hat{p}_4 \cdot \hat{p}_5)} \end{array} \right| \left| \begin{array}{c} \frac{[(m_W \Gamma_W)^2 + (m_{34}^2 - m_W^2)^2]}{2(p_3 + p_4)(1 - \hat{p}_3 \cdot \hat{p}_4)} \\ \frac{[(m_W \Gamma_W)^2 + (m_{34}^2 - m_0^2)^2]}{2p_3(\hat{p}_3 \cdot \hat{p}_5 - \hat{p}_4 \cdot \hat{p}_5)} \end{array} \right| \quad (7.18)$$

where ΔS_W and ΔS_t are defined in Eqs. 7.19 and 7.20.

$$\Delta S_W = \left(\frac{1}{m_W \Gamma_W} \right) \left(\tan \left[\frac{s_{\max} - m_W^2}{m_W \Gamma_W} \right] - \tan \left[\frac{s_{\min} - m_W^2}{m_W \Gamma_W} \right] \right) \quad (7.19)$$

$$\Delta S_t = \left(\frac{1}{m_t \Gamma_t} \right) \left(\tan \left[\frac{s_{\max} - m_t^2}{m_t \Gamma_t} \right] - \tan \left[\frac{s_{\min} - m_t^2}{m_t \Gamma_t} \right] \right) \quad (7.20)$$

The multidimensional integrals in this analysis were performed using the GNU Scientific Library version of the VEGAS [74] Monte Carlo integration algorithm.

³In all Jacobian equations the subscript 3 refers to the lepton, 4 refers to the neutrino, and 5,6, and 7, refer to the final state partons. The global factor of $\frac{2}{s}$ is a result of the Jacobian for the $q_1 q_2 \rightarrow E^{\text{tot}} P_z^{\text{tot}}$ change of variables. s_{\max} is the maximum available mass-squared for the collision and s_{\min} is the minimum mass-squared required to create the final state particles.

7.2.2 Probability Normalization Constants

The differential cross section defined in Eq. 7.3 requires a normalization constant to retain a probability density interpretation. The normalization constant σ is defined as the detector level phase space integration ($\int d\vec{x}$) of the differential cross section, as shown in Eq. 7.21.

$$\sigma = \sum_{i,j} \int d\vec{x}d\vec{y} \left[\frac{d\sigma_{i,j}}{d\vec{y}} \times W(\vec{x}, \vec{y}) \times \Theta_{\text{cuts}}(\vec{x}) \right] \quad (7.21)$$

The term $\Theta_{\text{cuts}}(\vec{x})$ is included in the calculation to account for the acceptance after selection cuts. This factor is set to one if the event passes the selection cuts and zero if it fails. All normalization constants were calculated with the following selection cuts:

- Lepton $P_T > 15$ GeV
- Electron (muon) $|\eta| < 1.1(2.0)$
- Missing $E_T > 15$ GeV
- Leading jet $P_T > 25$ GeV
- Leading jet $|\eta| < 2.5$
- Second jet $P_T > 20$ GeV
- Second jet $|\eta| < 3.5$
- Third jet $P_T > 15$ GeV (if three-jet event)
- Third jet $|\eta| < 3.5$ (if three-jet event)

The selection cuts shown above are slightly different from the canonical single top cuts. These cuts are included in the normalization calculation to approximate the relative acceptance difference between signal and background events. The cross sections computed for each signal and background process for two- and three-jet events are summarized in

Table 7.6. In all instances, the statistical uncertainty from the Monte Carlo integration is below 1%.

Table 7.6: Cross section times branching fraction for each analysis channel. All cross sections are given in units of femtobarns (fb).

	2-jet events				3-jet events			
	1 tag		2 tags		1 tag		2 tags	
	Electron	Muon	Electron	Muon	Electron	Muon	Electron	Muon
Signals								
$tb(g)$	8.07	10.4	6.90	8.90	6.02	7.64	5.22	6.66
$tq(b)$	19.6	26.8	0.27	0.38	6.34	8.56	5.40	7.40
Backgrounds								
$Wbb(g)$	29.5	41.9	24.6	34.7	16.5	23.1	14.3	19.9
Wcg	36.4	54.0	0.33	0.61				
Wgg	52.3	74.5	0.33	0.47				

7.2.3 Treatment of Combinatorial Background

The event probability density shown in Eq. 7.3 assumes a known assignment between a jet and parton from the matrix element. In practice this assignment is not known so there must be a sum over all possible assignments. The general treatment of the combinatorial backgrounds for events with two jets is shown in Eq. 7.22 and Eq. 7.23 for three jet events.

$$\begin{aligned}
 d\sigma(\ell, j_1, j_2) &= \alpha_{j_1 \rightarrow p_1} \alpha_{j_2 \rightarrow p_2} d\sigma(\ell, j_1 \rightarrow p_1, j_2 \rightarrow p_2) + \\
 &+ \alpha_{j_2 \rightarrow p_1} \alpha_{j_1 \rightarrow p_2} d\sigma(\ell, j_2 \rightarrow p_1, j_1 \rightarrow p_2)
 \end{aligned}
 \tag{7.22}$$

$$d\sigma(\ell, j_1, j_2, j_3) = \alpha_{j_1 \rightarrow p_1} \alpha_{j_2 \rightarrow p_2} \alpha_{j_3 \rightarrow p_3} d\sigma(\ell, j_1 \rightarrow p_1, j_2 \rightarrow p_2, j_3 \rightarrow p_3)$$

$$\begin{aligned}
& + \alpha_{j_1 \rightarrow p_1} \alpha_{j_3 \rightarrow p_2} \alpha_{j_2 \rightarrow p_3} d\sigma(\ell, j_1 \rightarrow p_1, j_3 \rightarrow p_2, j_2 \rightarrow p_3) \\
& + \alpha_{j_2 \rightarrow p_1} \alpha_{j_1 \rightarrow p_2} \alpha_{j_3 \rightarrow p_3} d\sigma(\ell, j_2 \rightarrow p_1, j_1 \rightarrow p_2, j_3 \rightarrow p_3) \\
& + \alpha_{j_2 \rightarrow p_1} \alpha_{j_3 \rightarrow p_2} \alpha_{j_1 \rightarrow p_3} d\sigma(\ell, j_2 \rightarrow p_1, j_3 \rightarrow p_2, j_1 \rightarrow p_3) \\
& + \alpha_{j_3 \rightarrow p_1} \alpha_{j_1 \rightarrow p_2} \alpha_{j_2 \rightarrow p_3} d\sigma(\ell, j_3 \rightarrow p_1, j_1 \rightarrow p_2, j_2 \rightarrow p_3) \\
& + \alpha_{j_3 \rightarrow p_1} \alpha_{j_2 \rightarrow p_2} \alpha_{j_1 \rightarrow p_3} d\sigma(\ell, j_3 \rightarrow p_1, j_2 \rightarrow p_2, j_1 \rightarrow p_3) \quad (7.23)
\end{aligned}$$

Where the α parameters represent to the probability to assign a parton (p) to a jet (j), also known as a jet-parton match. If there is no knowledge of the correct assignment, these quantities can be made equal and thereby no preference is given to a particular assignment.

This analysis uses information from the neural network B -tagger to weight the different jet-parton combinations depending on whether a given jet is tagged or not and which parton flavor is being assigned to it when summing over the combinatorial background. In this case the α weights are related to the jet tag-rate functions (described in Chapter 4) for the different jet flavors (b , c and light), as shown in Table 7.7.

Table 7.7: Weights for the event differential cross section depending on the B -jet tagging status of the jet and jet-parton assignment.

Parton flavor	b tagged	Not tagged
b	ε_b	$1 - \varepsilon_b$
c	ε_c	$1 - \varepsilon_c$
light	ε_l	$1 - \varepsilon_l$

Example of The Jet-Parton Weight Assignments

Consider a two-jet event where the leading jet, j_1 , is B -tagged and second jet, j_2 , is not tagged. As stated earlier in the text, one of the hypotheses for the background is the Wcg process. The first permutation is to assign the B -tagged jet as the c -quark and the untagged jet as the gluon. In this case the jet-parton weight is equal to the tagging efficiency for a charm-jet ($\varepsilon_c(j_1)$) times one minus the mis-tag rate for a light jet ($1 - \varepsilon_l(j_2)$).

The second permutation assigns the B -tagged leading jet as the gluon and the un-tagged second jet as the charm-quark. In this case the weight is equal to the mis-tag rate for a light-jet ($\varepsilon_l(j_1)$) times one minus the charm-jet tagging efficiency ($1 - \varepsilon_c(j_2)$). The total differential cross for this process is summarized in Eq. 7.24.

$$d\sigma_{Wcg}(\ell, j_1, j_2) = [\varepsilon_c(j_1)(1 - \varepsilon_l(j_2))] \times d\sigma_{Wcg}(\ell, j_1 \rightarrow c, j_2 \rightarrow g) + [(1 - \varepsilon_c(j_2))\varepsilon_l(j_1)] \times d\sigma_{Wcg}(\ell, j_2 \rightarrow c, j_1 \rightarrow g). \quad (7.24)$$

7.3 Single Top Discriminant Performance

7.3.1 Discriminant Definition

The discriminant for the matrix element analysis is constructed from the signal and background probability densities. One discriminant is created using s -channel single top as the signal process and one discriminant is created using t -channel single top as the signal. In both cases the probability density for the background is defined as a weighted sum of probability densities from the background-like processes. For the case of two jet events the background processes are $Wb\bar{b}$, Wcg , and Wgg . For the case of three jet events, the background is defined solely by the $Wbbg$ process. The s -channel and t -channel discriminants for two and three jet events are shown in Eq. 7.25 and 7.26, respectively.

$$D_{tb|tqb}^{2jets}(\vec{x}) = \frac{P_{tb|tqb}(\vec{x})}{P_{tb|tqb}(\vec{x}) + C_{Wbb}P_{Wbb}(\vec{x}) + C_{Wcg}P_{Wcg}(\vec{x}) + C_{Wgg}P_{Wgg}(\vec{x})} \quad (7.25)$$

$$D_{tb|tqb}^{3jets}(\vec{x}) = \frac{P_{tb|tqb}(\vec{x})}{P_{tb|tqb}(\vec{x}) + P_{Wbbg}(\vec{x})} \quad (7.26)$$

Where C_{Wbb} , C_{Wcg} , and C_{Wgg} are the relative fractions that each probability contributes to the total background probability. The background fractions for the two-jet discriminant were found by a grid search to determine the most sensitive set of background fractions⁴. This procedure was performed for single and double tagged events for each lepton channel

⁴The sensitivity was measured using the Bayes ratio for each background fraction set. The Bayes ratio is defined in Chapter 8

to optimize the final discriminant variable. The values of the background fractions are summarized in Table 7.8.

Table 7.8: Background fractions chosen for each analysis channel in two-jet events.

	1 tag		2 tags	
	Electron	Muon	Electron	Muon
C_{Wbb}	0.20	0.40	0.67	1
C_{Wcg}	0.40	0.40	0	0
C_{Wgg}	0.40	0.20	0.33	0

7.3.2 One-Dimensional Discriminants

This section contains overlaid plots of the one-dimensional (1D) s -channel and t -channel discriminants evaluated on signal and background events. The events in the plots come from the combination of the eight analysis channels $\{e,\mu \oplus 1,2 \text{ tags} \oplus 2,3 \text{ jets}\}$. Figures 7.5, 7.6, 7.7 and 7.8 show good discrimination between signal and W +jets and multijet backgrounds. However, the discrimination is poorer between signal and $t\bar{t} \rightarrow \ell\ell$ and $t\bar{t} \rightarrow \ell + jets$ events as shown in Figures 7.9 and 7.10. The lack of discrimination power for $t\bar{t}$ events is due to the fact that the analysis does not yet include a $t\bar{t}$ probability density function in the definition of the discriminant⁵.

⁵The $t\bar{t}$ matrix element takes much longer to integrate because there are six partons in the final state while there are four in the single top and W +jets matrix elements. Adding a $t\bar{t}$ matrix element is envisioned as a future improvement for this analysis.

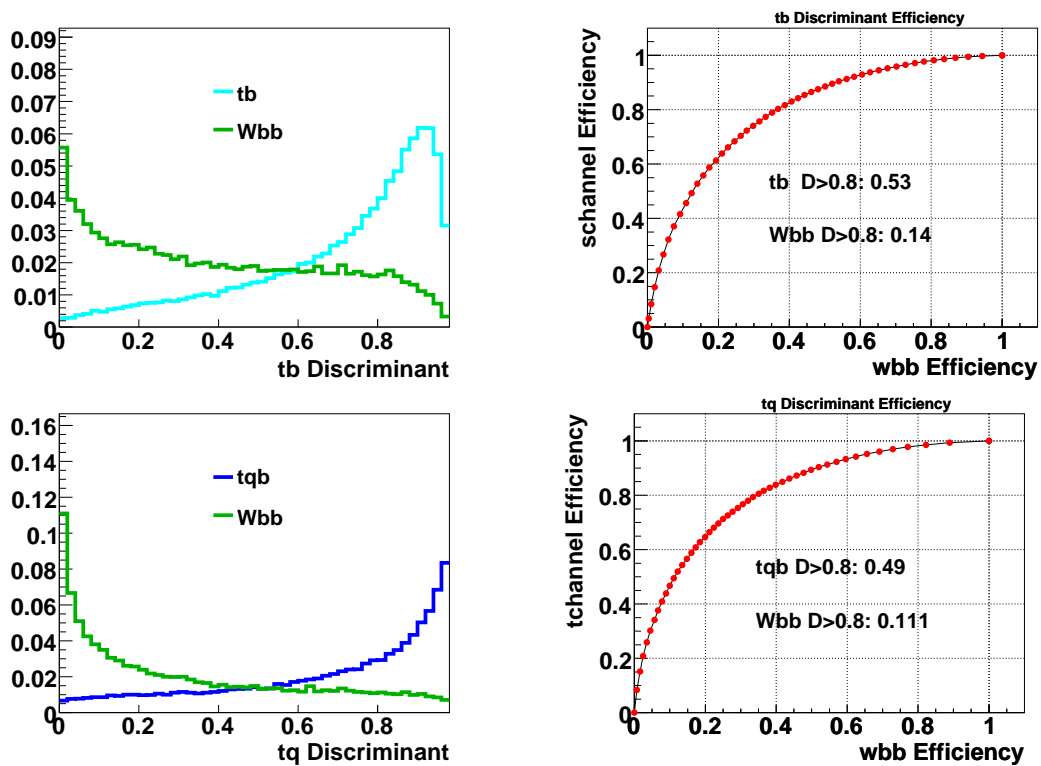


Figure 7.5: Discriminant plots and efficiency curves for: first row, s -channel vs. Wbb and second row, t -channel vs. Wbb . The numbers in the efficiency curves (right column) represent the fraction of signal or background the remains after a discriminant cut of 0.8.

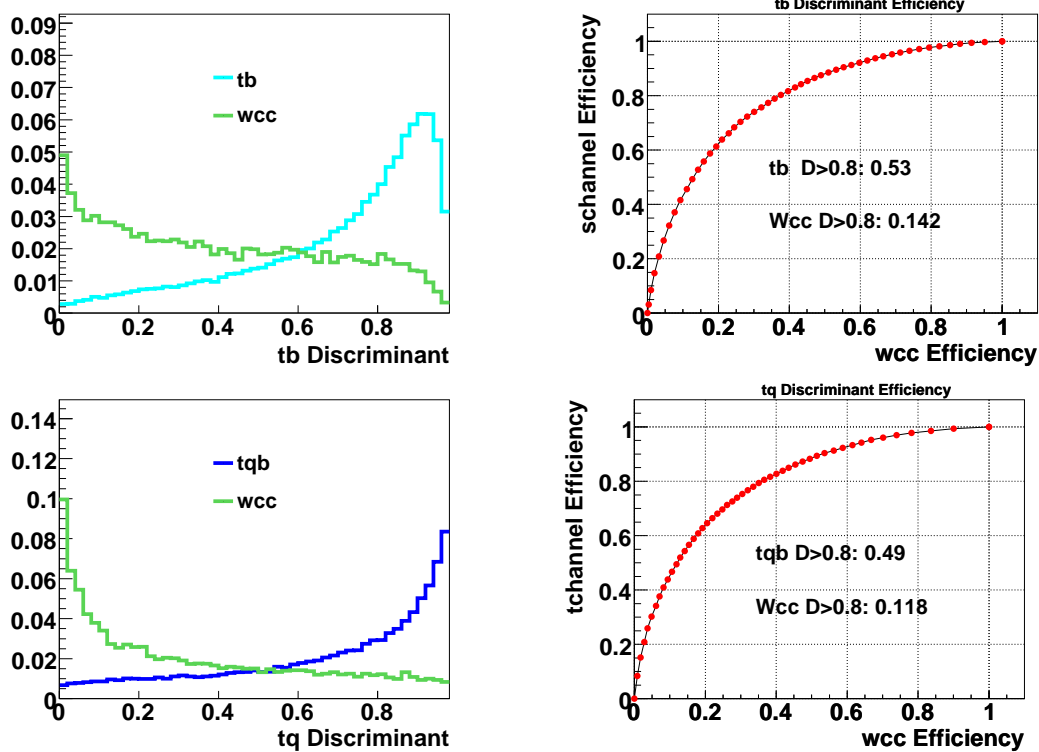


Figure 7.6: Discriminant plots and efficiency curves for: first row, s -channel vs. Wcc and second row, t -channel vs. Wcc . The numbers in the efficiency curves (right column) represent the fraction of signal or background the remains after a discriminant cut of 0.8.

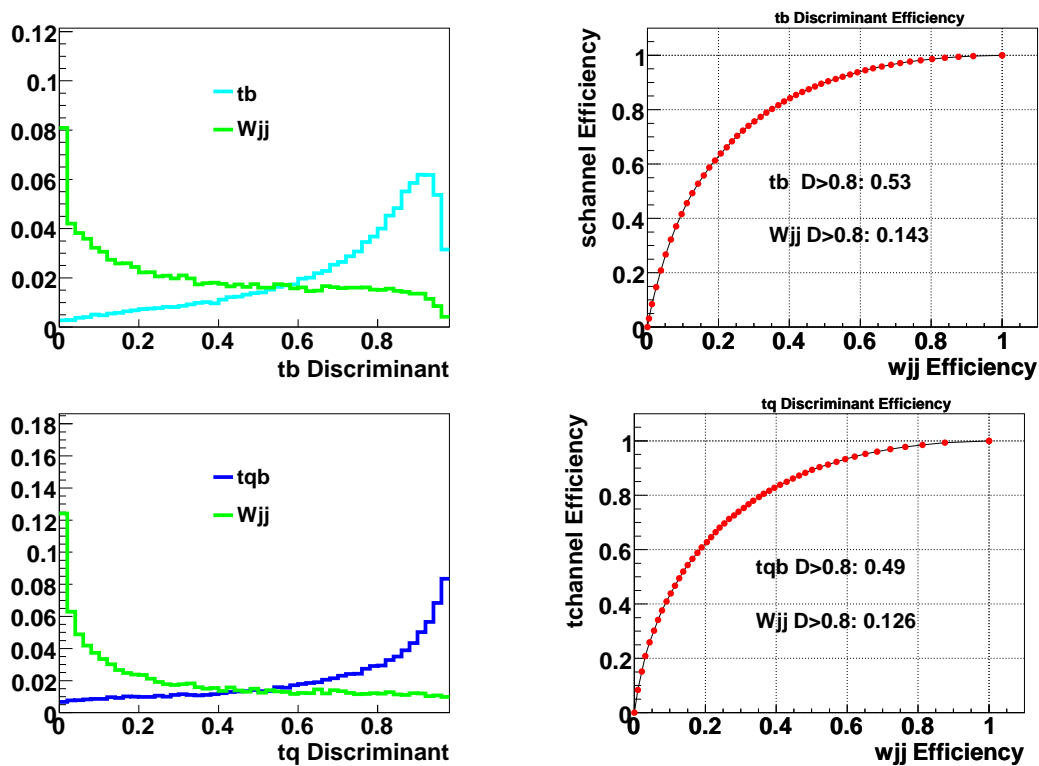


Figure 7.7: Discriminant plots and efficiency curves for: first row, s -channel vs. W_{jj} and second row, t -channel vs. W_{jj} . The numbers in the efficiency curves (right column) represent the fraction of signal or background the remains after a discriminant cut of 0.8.

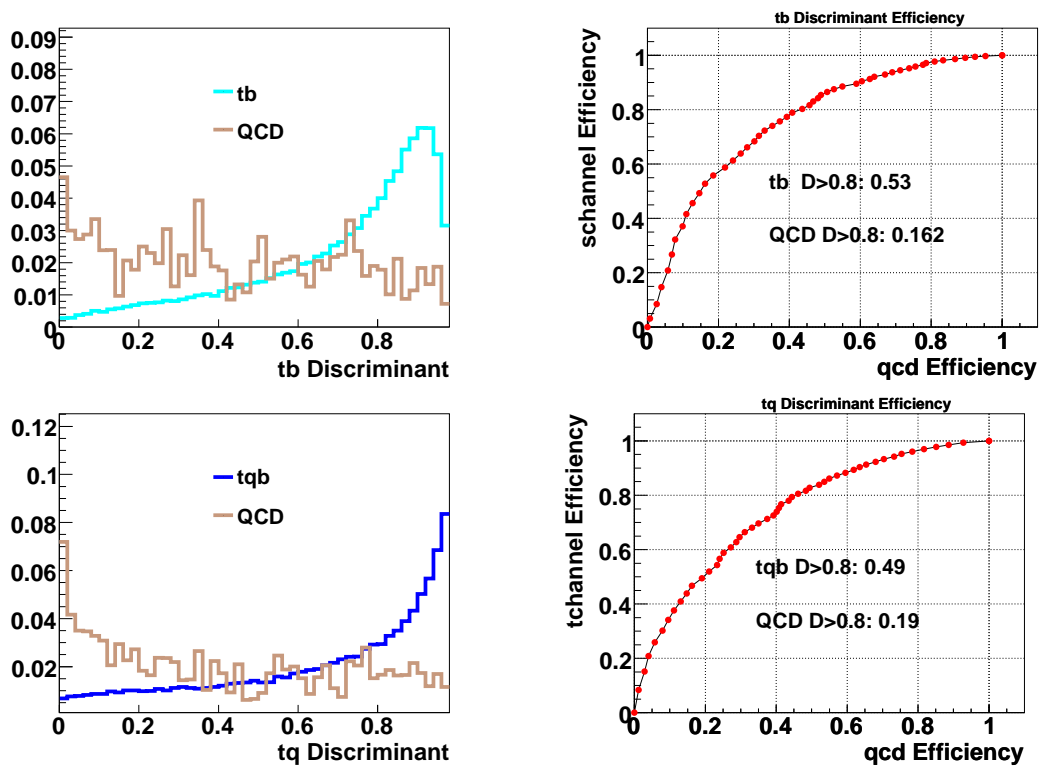


Figure 7.8: Discriminant plots and efficiency curves for: first row, s -channel vs. Multijets and second row, t -channel vs. Multijets. The numbers in the efficiency curves (right column) represent the fraction of signal or background the remains after a discriminant cut of 0.8.

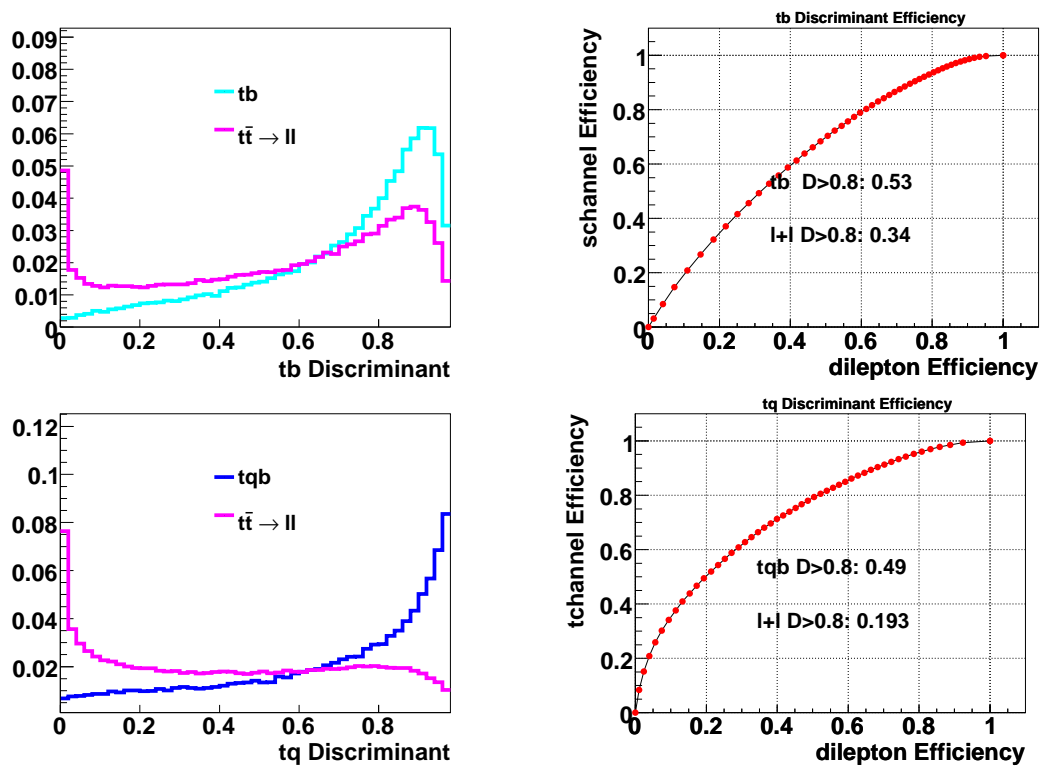


Figure 7.9: Discriminant plots and efficiency curves for: first row, *s*-channel vs. $t\bar{t} \rightarrow \ell\ell$ and second row, *t*-channel vs. $t\bar{t} \rightarrow \ell\ell$. The numbers in the efficiency curves (right column) represent the fraction of signal or background the remains after a discriminant cut of 0.8.

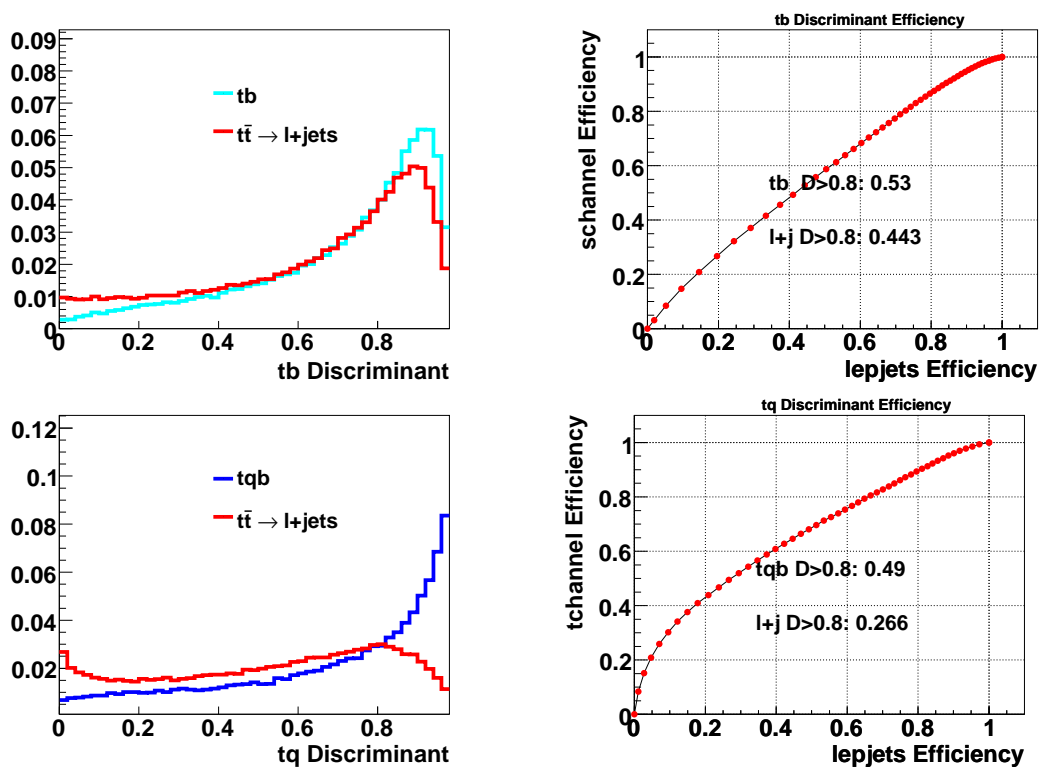


Figure 7.10: Discriminant plots and efficiency curves for: first row, s -channel vs. $t\bar{t} \rightarrow \ell + jets$ and second row, t -channel vs. $t\bar{t} \rightarrow \ell + jets$. The numbers in the efficiency curves (right column) represent the fraction of signal or background the remains after a discriminant cut of 0.8.

7.3.3 Two-Dimensional Discriminants

This analysis uses a two-dimensional (2D) discriminant as the final output where one axis is the s -channel discriminant and the other axis is the t -channel discriminant value for the event. The 2D discriminant is more powerful than either 1D projection because it selects events with both s and t -channel characteristics, which helps to further reduce the W +jets and $t\bar{t}$ background which may have either characteristic but not necessarily both. Fig. 7.11 shows the 2D discriminant for s -channel and t -channel Monte Carlo events. Figures 7.12 and 7.13 show the 2D discriminants for all the backgrounds. The plots are normalized to unit volume.

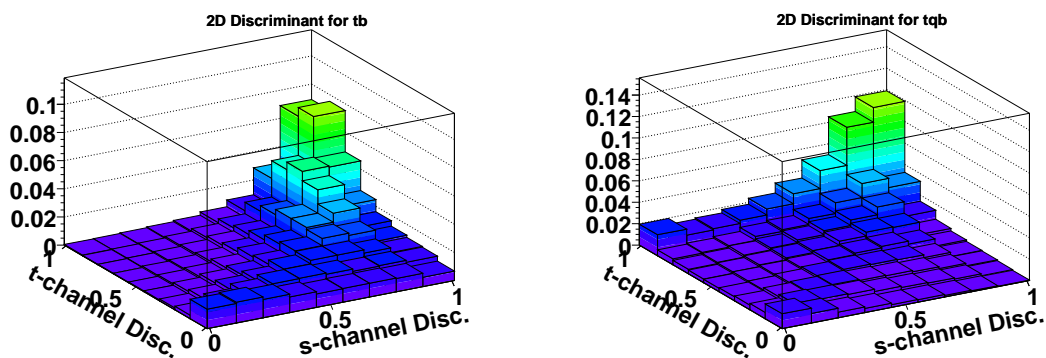


Figure 7.11: 2D-discriminant templates for: left, s -channel, and right, t -channel Monte Carlo events.

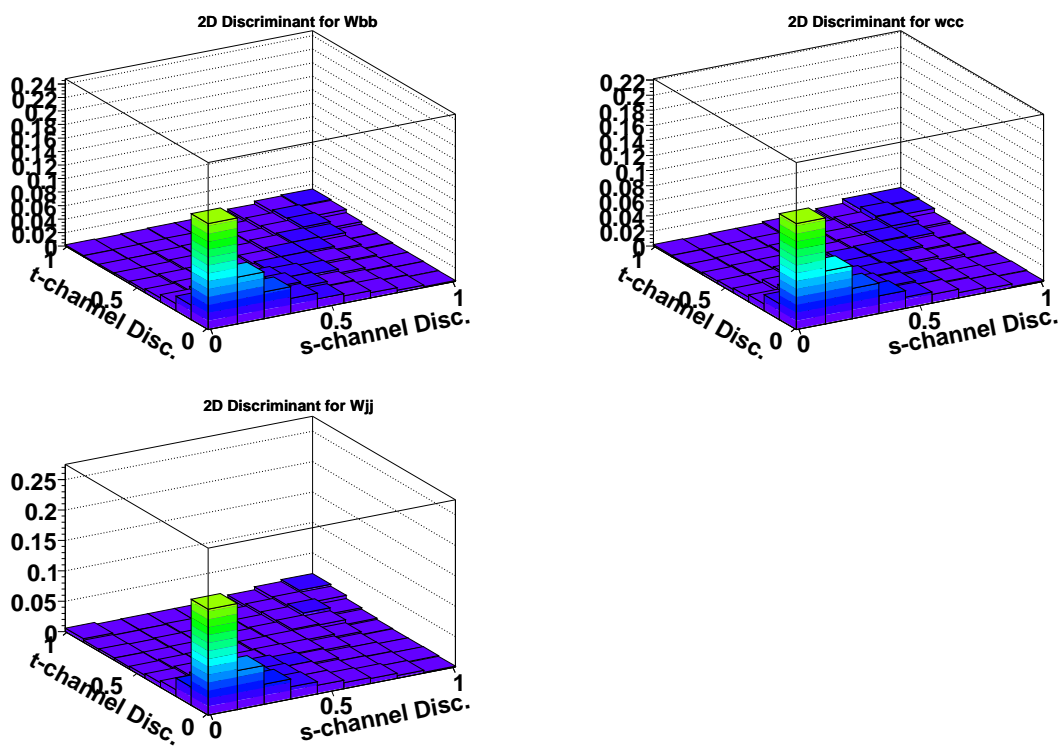


Figure 7.12: 2D-discriminant templates for: top-left, W_{bb} , top-right, W_{cc} , and bottom-left, W_{jj} Monte Carlo events.

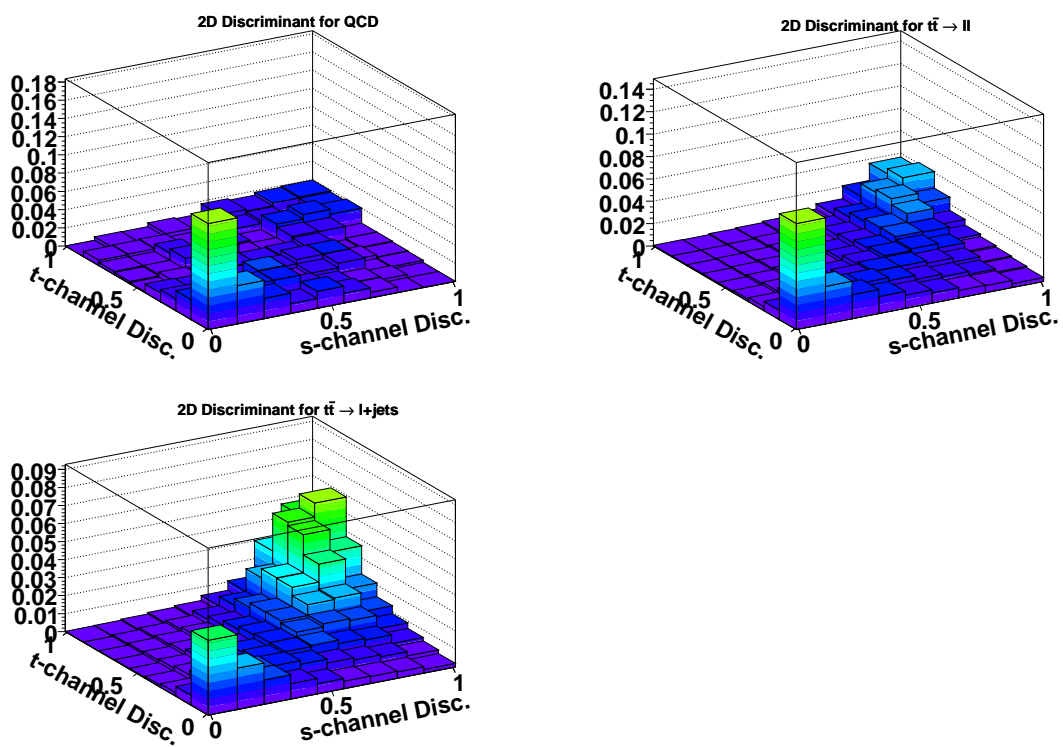


Figure 7.13: 2D-discriminant templates for: top-left, multijets events, top-right, $t\bar{t} \rightarrow ll$, and bottom-right, $t\bar{t} \rightarrow l + jets$ Monte Carlo events.

7.4 Cross-Check Samples

Before a measurement of the single top quark cross section is made, the output of the matrix element analysis is compared between data and background in a region where the signal content is negligible. If the agreement between data and background is good in this sample, there is more confidence that the background is well-modeled in the signal region. In this analysis two background-dominated control samples are defined, and a comparison between the 1D discriminants in data and the background model is performed.

These two control samples are selected by applying the nominal event selection, and requiring an additional cut on the total transverse energy H_T defined as

$$H_T = p_T^{\text{lepton}} + \text{ME}_T + \sum_{\text{jets}} p_T^{\text{jet}} \quad (7.27)$$

The first sample selects events with $H_T < 175$ GeV and the second sample selects events with $H_T > 300$ GeV, respectively. The control samples defined with $H_T < 175$ GeV is referred to as the “soft W +jets” sample and the sample with $H_T > 300$ GeV is referred to as the “hard W +jets” sample. In the case of three-jet events, the “hard W +jets” sample also contains a significant fraction of $t\bar{t}$.

The “soft W +jets” sample selects low momentum W +jets and multijets events and almost no top-quark events. Figures 7.14 and 7.15 compare the s -channel and t -channel discriminants between data and the background model for events with two and three jets respectively.

The “hard W +jets” sample selects mainly $t\bar{t}$ and high momentum W +jets events. Figures 7.16 and 7.17 compare the s -channel and t -channel discriminants between data and the background model for events with two and three jets.

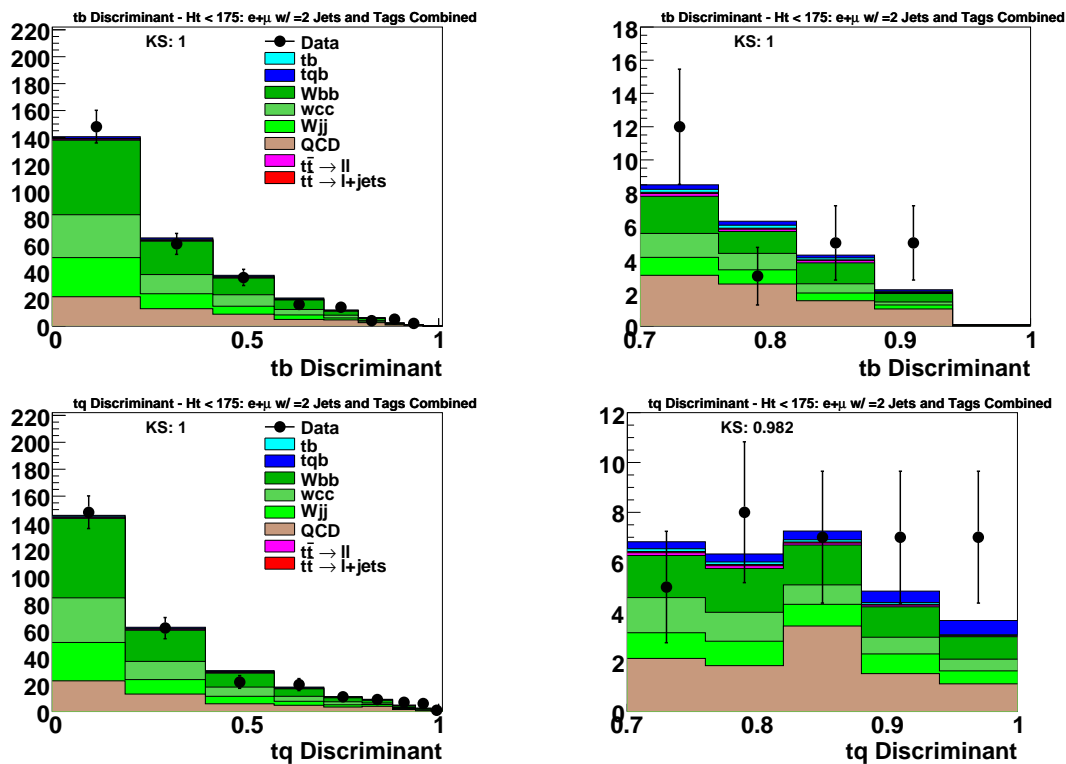


Figure 7.14: “Soft W +jets” cross-check plots in two-jet events for the s -channel discriminant (upper row) and the t -channel discriminant (lower row). The left column shows the full discriminant region while the right column shows the high discriminant region above 0.7.

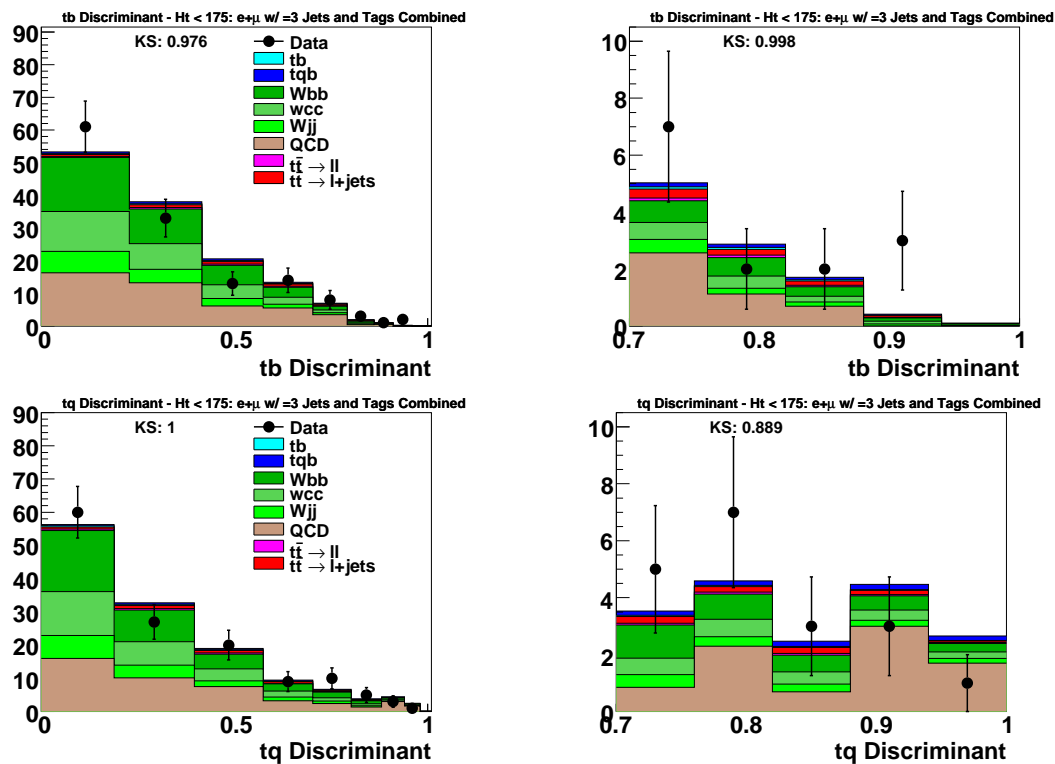


Figure 7.15: “Soft W +jets” cross-check plots in three-jet events for the s -channel discriminant (upper row) and the t -channel discriminant (lower row). The left column shows the full discriminant region while the right column shows the high discriminant region above 0.7.

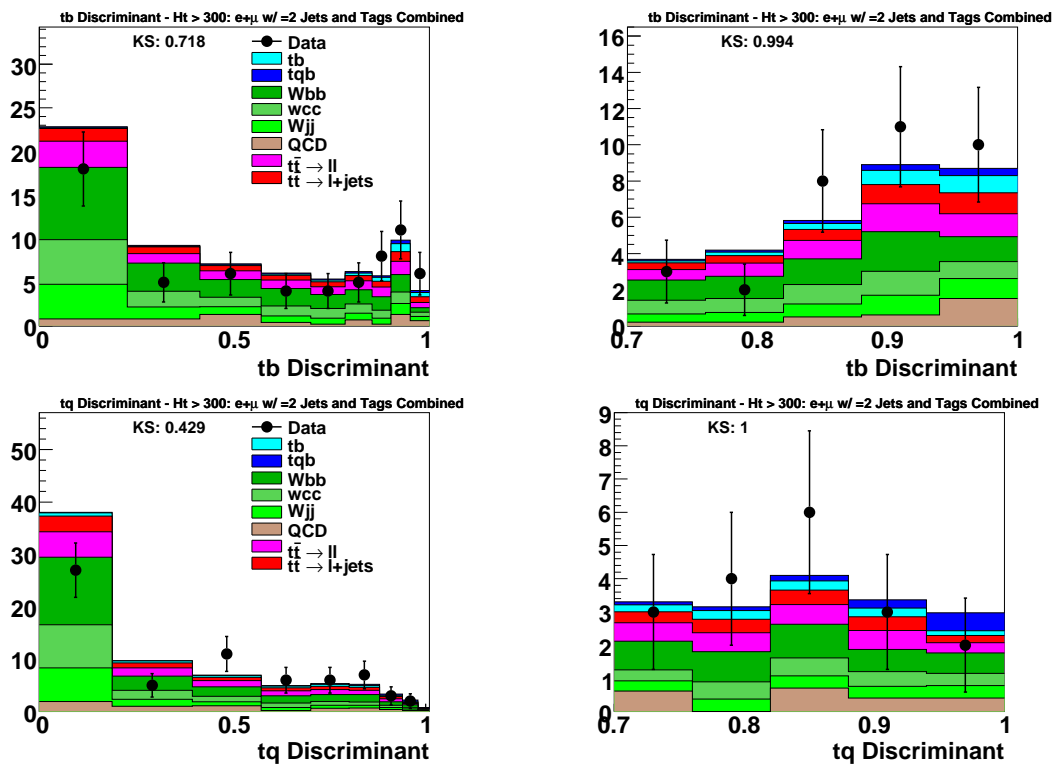


Figure 7.16: "Hard W +jets" cross-check plots in two-jet events for the s -channel discriminant (upper row) and the t -channel discriminant (lower row). The left column shows the full discriminant region while the right column shows the high discriminant region above 0.7.

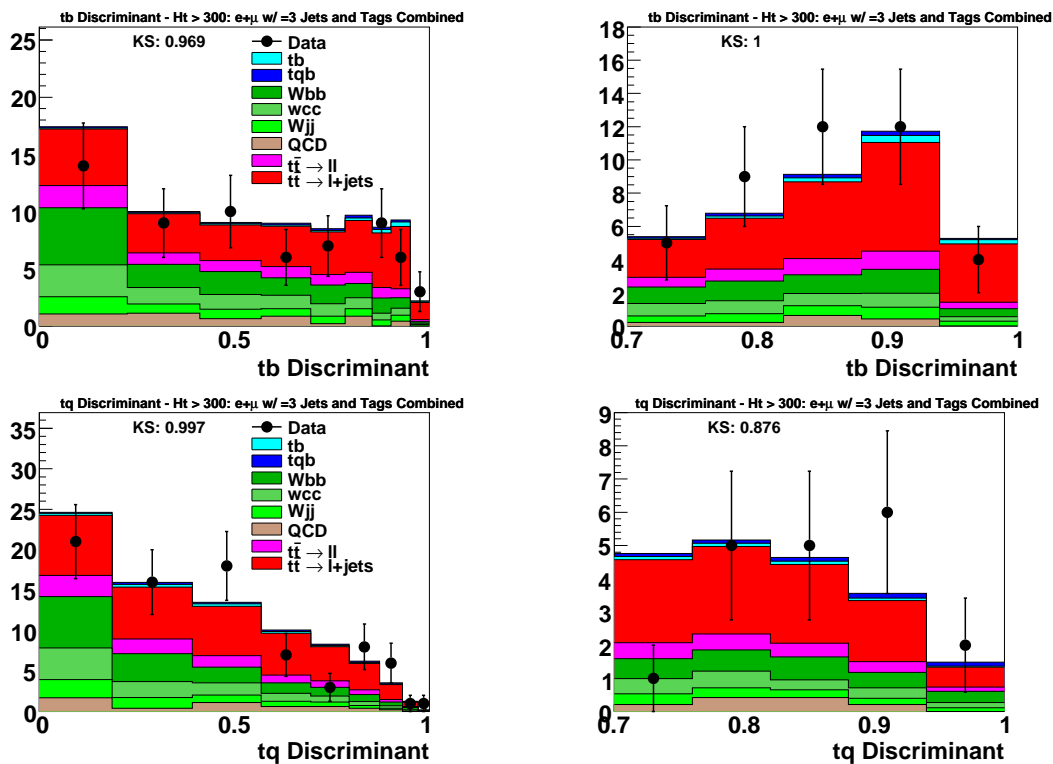


Figure 7.17: “Hard W +jets” cross-check plots in three-jet events for the s -channel discriminant (upper row) and the t -channel discriminant (lower row). The left column shows the full discriminant region while the right column shows the high discriminant region above 0.7.

7.5 Matrix Element Discriminants

This section presents the matrix element discriminants for all events in each analysis channel. Figures 7.18 and 7.19 show the s -channel and t -channel discriminants for the combined e,μ $w/\geq 1$ B -tag events for two-jet and three-jet events where the data distributions may be compared to the background model. The SM prediction for single top quark production has been added to the background sum in the plots. The individual channel plots for the 1D discriminants are shown in Appendix B.

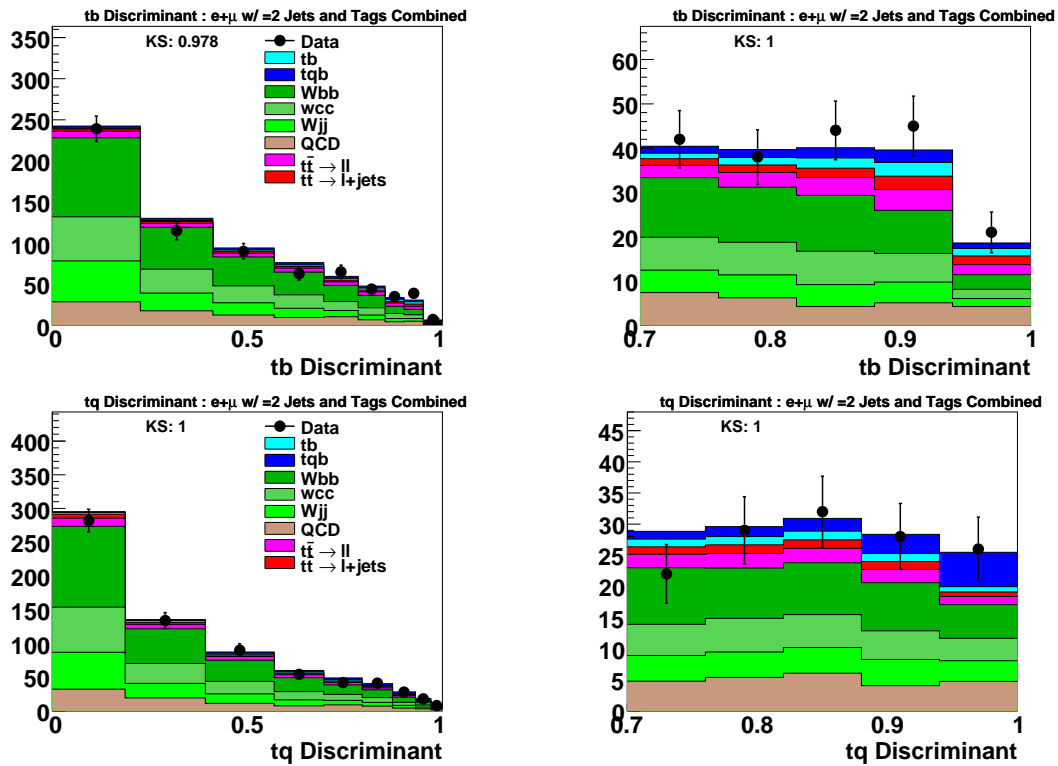


Figure 7.18: Discriminant plots for the $e+\mu$ channel with two jets and ≥ 1 B tag. Upper row: s -channel discriminant; lower row: tq discriminant. Left column: full output range; right column: close-up of the high end of the distributions.

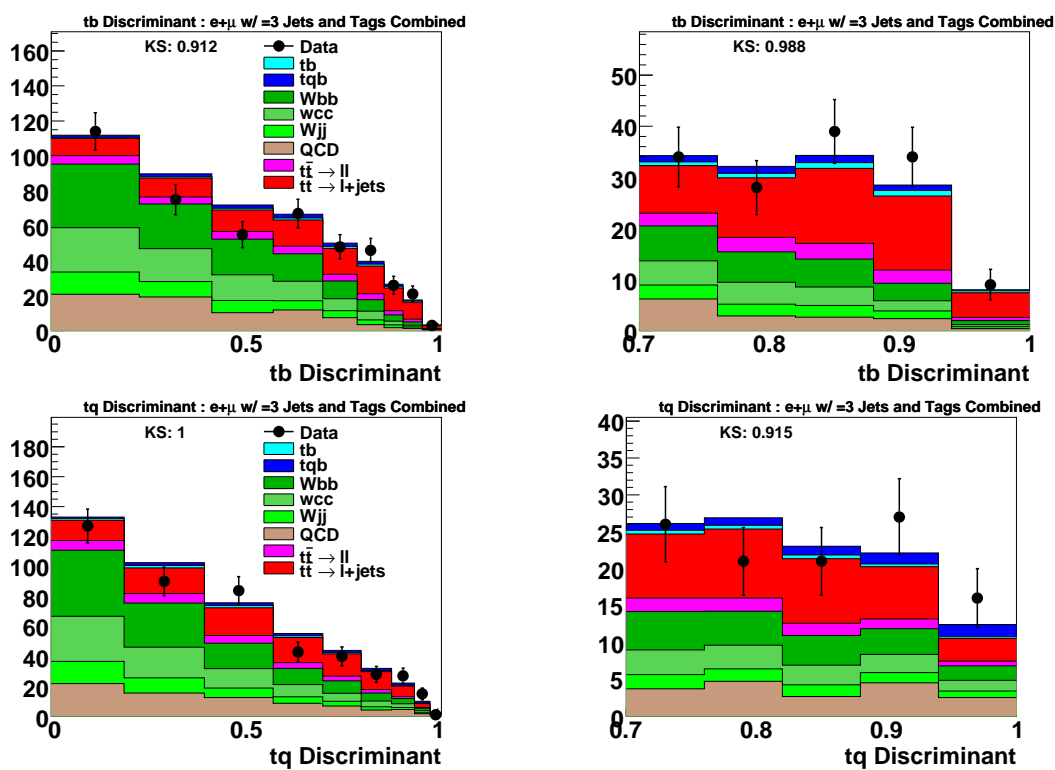


Figure 7.19: Discriminant plots for the $e+\mu$ channel with three jets and ≥ 1 b tag. Upper row: s -channel discriminant; lower row: tq discriminant. Left column: full output range; right column: close-up of the high end of the distributions.

After the matrix element discriminant has been calculated it is possible to select events in data and Monte Carlo to see if they are consistent with single top quark production. For this section, an event is considered very single top quark like if both the s -channel and t -channel discriminants are greater than 0.7. Similarly, an event is considered background like if both discriminants are less than 0.4. Figure 7.20 shows the invariant mass of the lepton, neutrino, and tagged jet before and after the discriminant cut, and Fig. 7.21 shows the lepton-charge times pseudorapidity of the untagged jet. In both cases the background dominated samples show no evidence for top quarks in the event while the signal enhanced samples are re-shaped to look like the expected single top distributions.

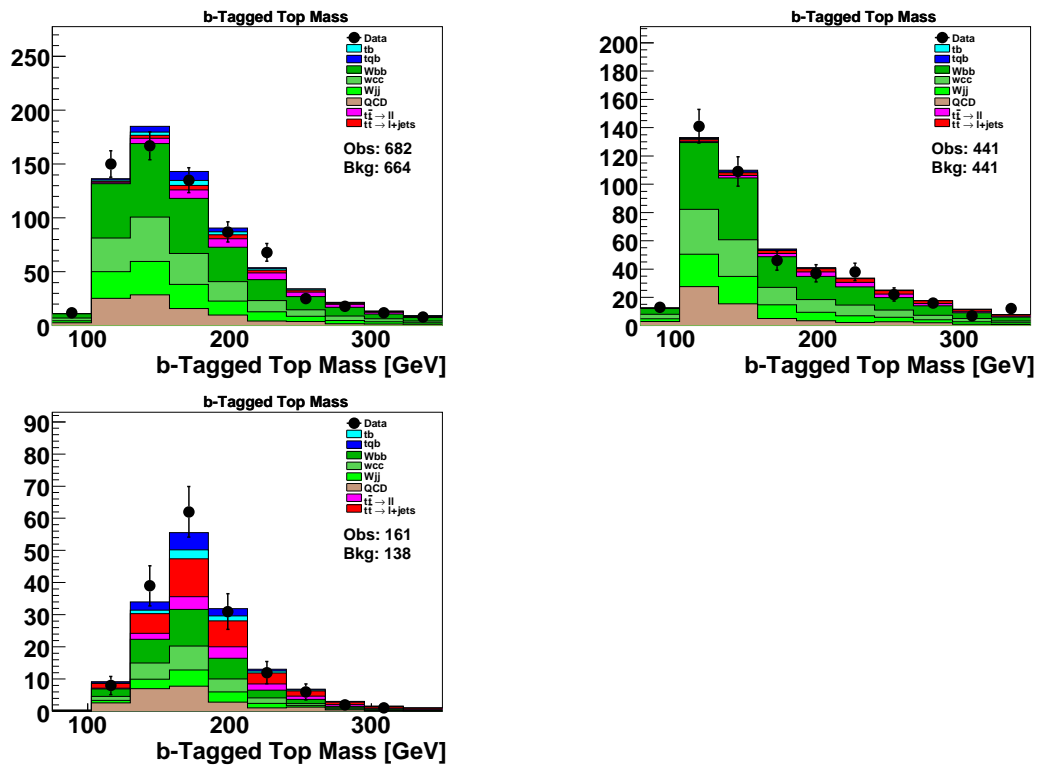


Figure 7.20: Invariant mass of the lepton, neutrino, and tagged jet for all events (upper left plot), for events with $D < 0.4$ (upper right plot), and events with $D > 0.7$ (bottom left plot).

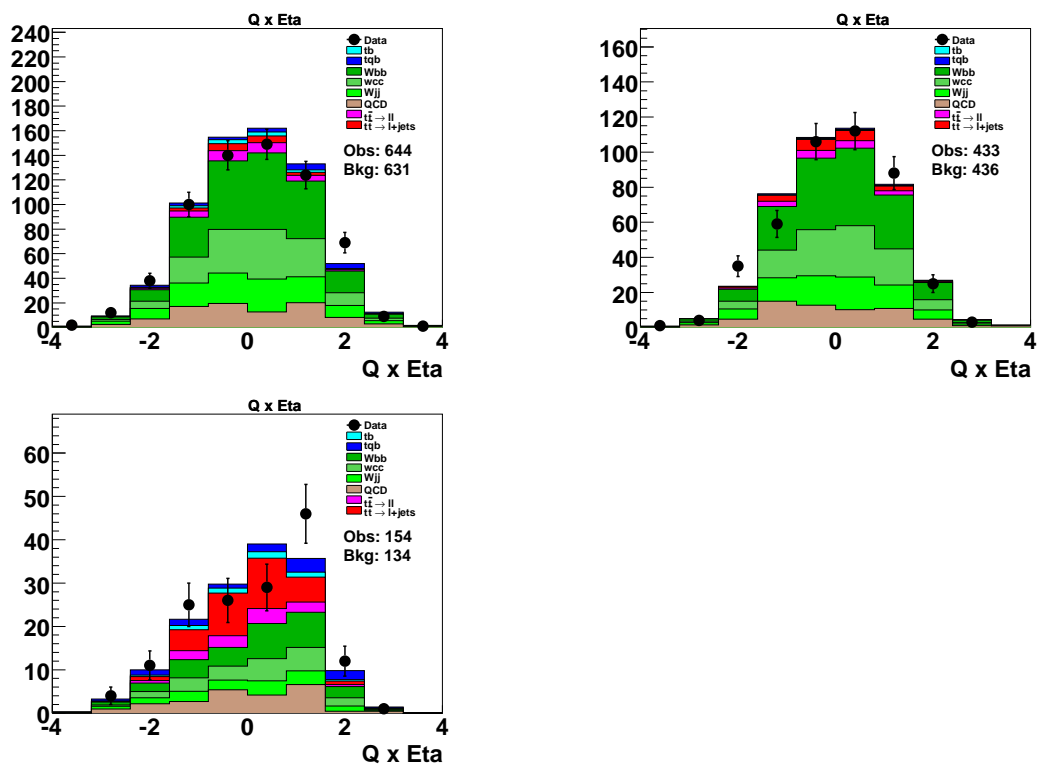


Figure 7.21: Lepton charge multiplied by the pseudorapidity of the untagged jet for all events (upper left plot), for events with $D < 0.4$ (upper right plot), and events with $D > 0.7$ (bottom left plot). The number of observed events is different from the b -tagged top mass plot because this variable is only defined for events with at least one untagged jet.

Chapter 8

CROSS SECTION DETERMINATION METHOD

This chapter summarizes the technique used to measure the single top quark cross section as well as the systematic uncertainties on the expected signal and background yields. Section 8.1 derives the Bayesian posterior density function and shows how it is used to determine the single top quark production cross section. The treatment of systematic uncertainties is also covered in this section. A description of each systematic uncertainty and its effect on the signal acceptance and background yield is presented in Section 8.2. Section 8.3 describes the method designed to measure the stability and linearity of the cross section measurement technique. Finally, the expected sensitivity and cross section resolution for a Standard Model single top signal in the full dataset is presented in Section 8.4.

8.1 Bayesian Posterior Density Function

The single top cross section is measured by creating a Bayesian posterior density function, which yields the probability density for all single top quark production cross sections¹. The posterior is defined as the conditional probability that a process \mathcal{A} is true given that another process \mathcal{B} is also true; it is equal to the conditional probability of process \mathcal{B} given process \mathcal{A} multiplied by the prior probability for process \mathcal{A} ($\pi(\mathcal{A})$) divided by the prior probability for process \mathcal{B} ($\pi(\mathcal{B})$), as shown in Eq. 8.1.

$$P(\mathcal{A}|\mathcal{B}) = \frac{P(\mathcal{B}|\mathcal{A})\pi(\mathcal{A})}{\pi(\mathcal{B})} \quad (8.1)$$

In the single top quark analysis \mathcal{A} is the number of signal and background events and \mathcal{B} is the observed number of events. The conditional probability $P(\mathcal{B}|\mathcal{A})$ is then interpreted as the probability to observe N events given n , where n is the expected number of signal and background events. Numerically this is given as the value of the Poisson probability density

¹The Bayesian posterior density function is sometimes referred to as the posterior in this text.

function for observed number of events given the expectation as seen in Eq. 8.2. This term is also referred to as the likelihood and its application in the single top quark analysis is given latter in this section.

$$P(\mathcal{B}|\mathcal{A}) \equiv \mathcal{L}(N|n) = \frac{n^N e^{-n}}{N!} \quad (8.2)$$

The quantity of interest in this analysis is the signal cross section and not the number of expected signal and background events. To expose the cross section dependence the expected yield n is re-written as

$$n = n_S + n_B = \alpha_S L \sigma_S + \sum_i n_{B,i}, \quad (8.3)$$

where α_S is the signal acceptance, L is the integrated luminosity, σ_S is the signal cross section, and $\sum_i n_{B,i}$ is the sum of background yields.² The likelihood is also re-written as $\mathcal{L}(N|n) = \mathcal{L}(N|\sigma_S, \alpha_S, \vec{n}_B)$ and the prior $\pi(n)$ is re-written as $\pi(\sigma_S, \alpha_S, \vec{n}_B)$.

The prior can be factored into a term dependent on the cross section and a term dependent on the signal acceptance and the background yield as shown in Eq. 8.4.

$$\pi(n) \equiv \pi(\sigma_S, \alpha_S, \vec{n}_B) = \pi(\sigma_S) \times \pi(\alpha_S, \vec{n}_B) \quad (8.4)$$

The likelihood is modified to combined multiple independent channels by replacing the original likelihood by the product of the likelihoods for each channel, as shown in Eq. 8.5.

$$\mathcal{L}(N|\sigma_S, \alpha_S, \vec{n}_B) \rightarrow \prod_i \mathcal{L}(N_i|\sigma_S, \alpha_{S,i}, \vec{n}_{B,i}) \quad (8.5)$$

For the matrix element analysis method the values of N , α , and \vec{n}_B are given in the form of two-dimensional histograms, where one axis corresponds to the s -channel discriminant and the other axis corresponds to the t -channel discriminant. The histograms are filled with matrix element discriminants for the data (N), the signal Monte Carlo ($\alpha_S = n_S/\sigma_S$), and background Monte Carlo (\vec{n}_B). To incorporate the shape information of these quantities,

²For the rest of this section, the luminosity is absorbed by the acceptance term ($\alpha_S \times L \rightarrow \alpha_S$).

the likelihood is further modified for a given channel as the product of the likelihoods for each bin in the two-dimensional histogram, as shown in Eq. 8.6.

$$\mathcal{L}(N|\sigma_S, \alpha_S, \vec{n}_B) \rightarrow \prod_{\text{Bins}\{j\}} \mathcal{L}(N_j|\sigma_S, \alpha_{S,j}, \vec{n}_{B,j}) \quad (8.6)$$

The acceptance and background yield dependence on the posterior are removed by integrating the likelihood and prior with respect to the signal acceptance and each background yield, as shown in Eq. 8.7.

$$P(\sigma|N) = \frac{1}{P(N)} \int \int \mathcal{L}(N|\sigma_S, \alpha'_S, \vec{n}'_B) \times \pi(\sigma_S) \times \pi(\alpha'_S, \vec{n}'_B) d\alpha'_S d\vec{n}'_B \quad (8.7)$$

The term $P(N)$ is the posterior normalization such that the posterior retains a probability density function interpretation (i.e $\int P(\sigma|N)d\sigma = 1$). To ensure that the normalization is finite the prior for the signal cross section $\pi(\sigma_S)$ is cut off at a maximum value, σ_{\max} . The prior is flat in the region of $0 < \sigma < \sigma_{\max}$ and zero beyond this region.³ The value of σ_{\max} is chosen to be large enough such that beyond that limit the likelihood is negligibly small for all α_S and \vec{n}_B .

The prior $\pi(\alpha'_S, \vec{n}'_B)$ is defined separately for the case of no systematics uncertainties and complete systematics. Both cases are described in the following section.

8.1.1 Prior Definition With and Without Systematic Uncertainties

Prior Without Systematics

In the case of no systematic uncertainties the signal acceptance and background yields are perfectly known. This requires the prior to be a product of two delta functions, as shown in Eq. 8.8, and leads to a posterior shown in Eq. 8.9.

$$\pi(\alpha'_S, \vec{n}'_B) = \delta(\alpha'_S - \alpha_S) \times \delta(\vec{n}'_B - \vec{n}_B) \quad (8.8)$$

$$P(\sigma|N) = \frac{\mathcal{L}(N|\sigma_S, \alpha_S, \vec{n}_B) \times \pi(\sigma_S)}{\int \mathcal{L}(N|\sigma'_S, \alpha_S, \vec{n}_B) \times \pi(\sigma'_S) d\sigma'_S} \quad (8.9)$$

³A flat prior represents a minimal bias towards any signal cross section.

Prior With Systematics

In the case of systematic uncertainties the prior is modified to reflect the uncertainty in α_S and \vec{n}_B . For each systematic uncertainty the $\pm 1\sigma$ uncertainty is propagated through the analysis resulting in a $\pm 1\sigma$ uncertainties for the signal acceptance ($\delta\alpha_S$) and the background yield ($\delta\vec{n}_B$). From these values a covariance matrix is created, which accounts for all correlations between systematics (e.g. the uncertainty in the integrated luminosity affects both the signal acceptance and the $t\bar{t}$ normalization). The covariance matrix element $\{i,j\}$ for background or signal i and j is defined as

$$\text{cov}_{i,j} = p_i p_j \sum_{k=1}^m f_{i,k} f_{j,k}, \quad (8.10)$$

where p_i is the signal or background yield for the i^{th} source and $f_{i,k}$ is the fractional uncertainty from the k^{th} systematic component for the i^{th} signal or background. The prior is then calculated as a multivariate Gaussian, as shown in Eq. 8.11.

$$\pi(\alpha'_S, \vec{n}'_B) = \frac{1}{\sqrt{(2\pi)^N |\Sigma|}} \exp \left\{ -\frac{1}{2} (\vec{x} - \mu)^T \Sigma^{-1} (\vec{x} - \mu) \right\} \quad (8.11)$$

where Σ is the covariance matrix, \vec{x} represents $\{\alpha'_S, \vec{n}'_B\}$, and μ represents $\{\alpha_S, \vec{n}_B\}$

The posterior, when systematics are included, is solved using Monte Carlo importance sampling. In this method a set of points in $\{\alpha_S, \vec{n}_B\}$ -space are generated according the prior density defined in Eq. 8.11. The solution to the posterior is given by

$$\int \int \mathcal{L}(N|\sigma_S, \alpha_S, \vec{n}_B) \times \pi(\alpha_S, \vec{n}_B) d\alpha_S d\vec{n}_B = \frac{1}{K} \sum_{i=1}^K \mathcal{L}(N|\sigma_S, \alpha_S, \vec{n}_B) \quad (8.12)$$

A discussion of the systematic uncertainties and their magnitudes can be found in Section 8.2 of this chapter.

8.1.2 Cross Section Extraction

If there is an excess of data events over the expected background yield then it is possible to determine the production cross section for a given process. The cross section is defined as the value which maximizes the posterior, as seen in Fig. 8.1. The solid blue line represents the

cross section (3.9 pb) and the dashed-blue lines represent the $\pm 1\sigma$ uncertainty on the cross section. The uncertainties are calculated by integrating the posterior curve until 33.15% of the area is contained on each side of the cross section. In the case of Fig. 8.1 the $+1\sigma$ error band covers 2.3 pb above the cross section and the -1σ error band covers 2.2 pb below the cross section.

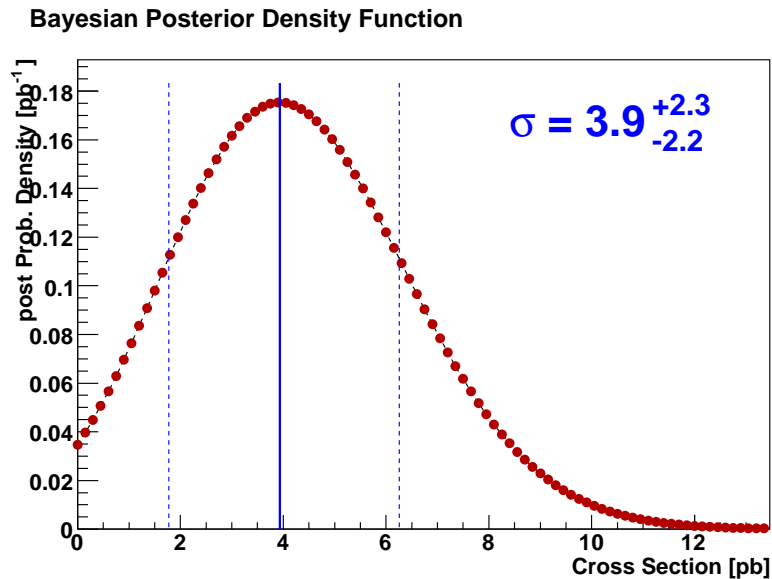


Figure 8.1: Example cross section measurement (solid blue line) with $\pm 1\sigma$ error band (dashed blue lines).

If there is no excess of data above the background, then upper limits on the production cross section can be set. An upper cross section limit, σ_{CL} , at a given confidence level is found by integrating the posterior until an area equal to the confidence level is obtained, as shown in Eq. 8.13. Fig. 8.2 shows the cross section limit for the same posterior shown in Fig. 8.1. The limit is 8.4 pb at 95% CL.

$$\int_0^{\sigma_{CL}} P(\sigma|N) d\sigma = CL \quad (8.13)$$

Finally, a quantity used to optimize the sensitivity of a particular analysis channel is the Bayes ratio. This quantity is an approximation to the Bayes factor which is the likelihood

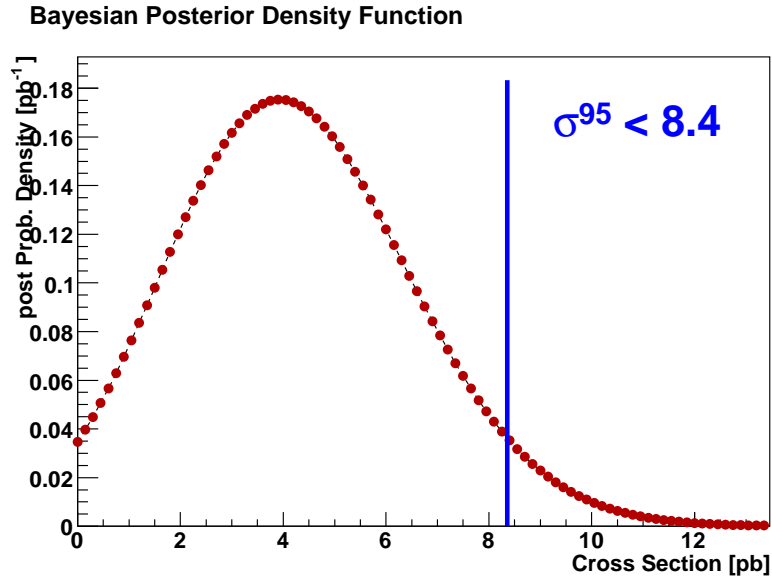


Figure 8.2: Example of the 95% CL upper cross section limit. The value of the upper limit is shown by the blue curve. For this posterior the cross section limit is 8.4 pb.

for the case of signal+background divided by the background only likelihood. The Bayes ratio is defined as the ratio of the posterior at its maximum over the posterior at zero cross section. The larger the Bayes ratio the more sensitive a channel is to measure a cross section different from zero. This is shown graphically in Fig. 8.3 for the same posterior curve used in the previous two figures.

8.1.3 $s + t$ -channel Cross Section Definition

All cross sections presented in this thesis are the combined s -channel plus t -channel cross section. In this case the ratio of s/t -channel cross sections ($0.88/1.98 = 0.44$) is assumed to be consistent with the Standard Model. With an increased dataset a measurement of the individual s -channel and t -channel cross sections will be a future addition to this analysis.

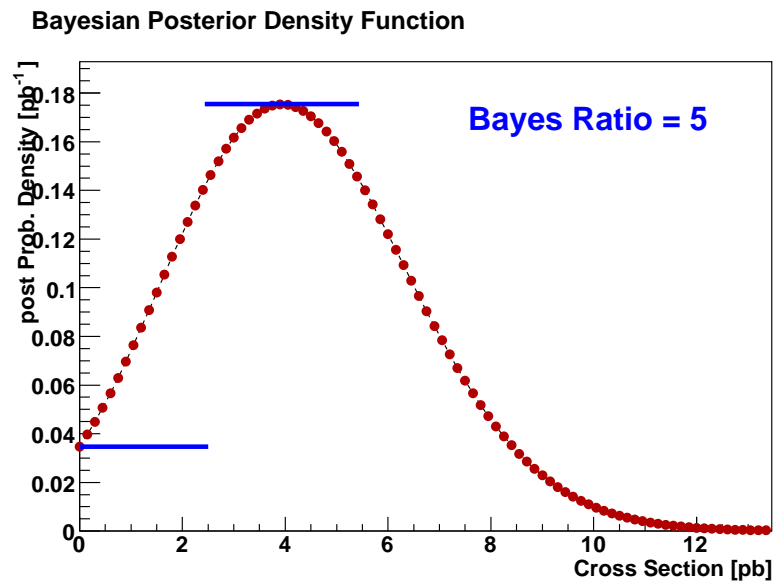


Figure 8.3: Example of the Bayes ratio defined as the maximum of the posterior (top blue line) over the posterior at zero cross section (lower blue line). The Bayes ratio for this curve is 5.0.

8.2 Systematic Uncertainties

This section describes all systematic uncertainties considered in the matrix element analysis. In most cases the uncertainty source applies both to the signal acceptance (α) and the background expectation (n_B). The other systematics are only applied to certain backgrounds as explained in the following text. Two sources of systematic uncertainties (jet energy scale and tag-rate functions) are referred to as “shape changing” systematics, while the rest solely affect the signal or background normalization and are referred to as “flat” systematics. Flat systematics have a uniform uncertainty across all bins of the matrix element discriminant, while shape changing systematics vary bin-to-bin. Table 8.1 summarizes the relative uncertainties due to each systematic source⁴. The effect of each systematic uncertainty on the measured single top cross section can be found in Chapter 9.

Table 8.1: A summary of the relative systematic uncertainties for each of the applied corrections and efficiencies. The uncertainty shown is the error on the correction or the efficiency, before it has been applied to the MC or data samples.

$t\bar{t}$ cross section	18%	Primary vertex	3%
Luminosity	6%	Electron reco * ID	2%
Electron trigger	3%	Electron trackmatch & likelihood	5%
Muon trigger	6%	Muon reco * ID	7%
Jet energy scale	wide range	Muon trackmatch & isolation	2%
Jet efficiency	2%	Electron ε_{W+jets}	2%
Jet fragmentation	5–7%	Muon ε_{W+jets}	2%
Heavy flavor ratio	30%	Electron $\varepsilon_{Multijet}$	3–40%
Tag-rate functions	2–16%	Muon $\varepsilon_{Multijet}$	2–15%

- **Integrated luminosity**

The error on the integrated luminosity used in the analysis is 6.1%. This uncertainty

⁴Appendix E shows the uncertainties for each background yield and signal acceptance for each analysis channel.

comes from the error on the measured inelastic $p\bar{p}$ cross section. The error on the luminosity estimate affects the $t\bar{t}$ background since this background is normalized using the integrated luminosity.

- **Theoretical cross sections**

The $t\bar{t}$ background yield is normalized to the NLO theoretical cross section. The uncertainty of this cross section for a top mass of 175 GeV is 18%. The uncertainty on the cross section is mainly due to the uncertainty from the top mass, but also from the choice of scale and parton distribution function uncertainties.

- **Trigger efficiency**

The uncertainty on the trigger efficiency is determined by varying the trigger term efficiencies at each trigger level by the $\pm 1\sigma$ uncertainties. A total uncertainties of 3% was assigned to the e +jets trigger and 6% to the μ +jets trigger. Fig. 8.4 shows the affect of the $\pm 1\sigma$ shift in the e +jets trigger efficiency on the electron p_T in $t\bar{t} \rightarrow \ell\ell$ Monte Carlo events.

- **Primary vertex selection efficiency**

The longitudinal position of the primary interaction vertex is not well modeled in the Monte Carlo. The maximum deviation between the data and Monte Carlo is 3% thus this number was taken as the systematic uncertainty. This uncertainty accounts for the beam profile along the longitudinal direction [83].

- **Jet reconstruction and identification**

This systematic is due to the difference between the data and Monte Carlo for the η and number of jets distributions. A 2% uncertainty is assigned to this effect.

- **Jet energy scale (JES) and jet energy resolution**

The JES correction is raised and lowered by one standard deviation and the whole analysis is repeated. In the data the JES uncertainty contains the jet energy resolution uncertainty; however, in the Monte Carlo the jet energy resolution uncertainty is not

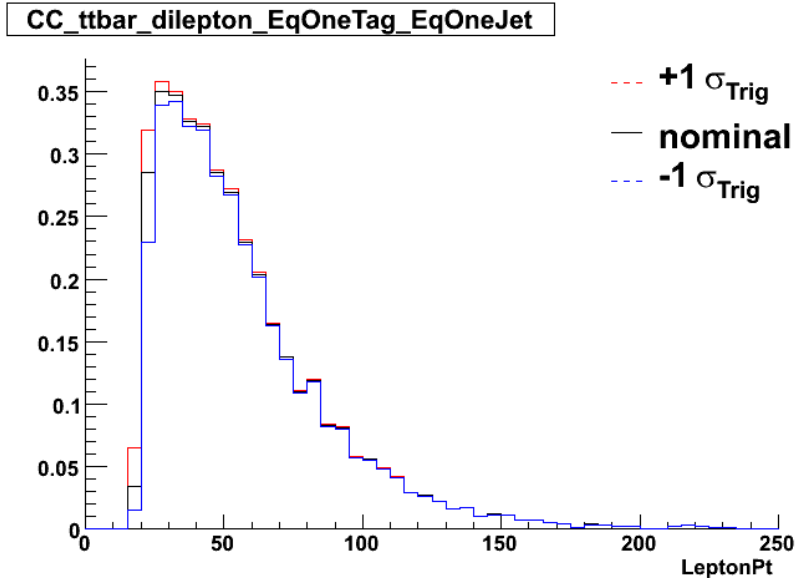


Figure 8.4: Electron p_T in weighted $t\bar{t} \rightarrow \ell\ell$ Monte Carlo events. The three curves represent the estimated yield in each p_T bin for the case of $+1\sigma$ trigger weights (red), nominal trigger weights (black), and -1σ trigger weights (blue).

taken into account in the JES uncertainty. To account for this the Monte Carlo energy smearing is varied by the size of the jet energy resolution in MC. This uncertainty affects the acceptance and the shapes of the distributions. The 1σ error on the JES as a function of jet p_T for central jets is shown in Fig. 8.5. The JES uncertainty is larger for lower p_T and more forward jets.

- **Jet fragmentation**

The uncertainty of the jet fragmentation model is determined by the difference in fragmentation models between the Pythia and Herwig Monte Carlo generators. This uncertainty also covers the uncertainties due to initial and final state radiation. The total uncertainty is 5% for $t\bar{t} \rightarrow \ell\ell$ and single top quark events and 7% for $t\bar{t} \rightarrow \ell + jets$ events.

- **Electron reconstruction and identification efficiency**

This uncertainty derives from the error on the electron reconstruction Monte Carlo

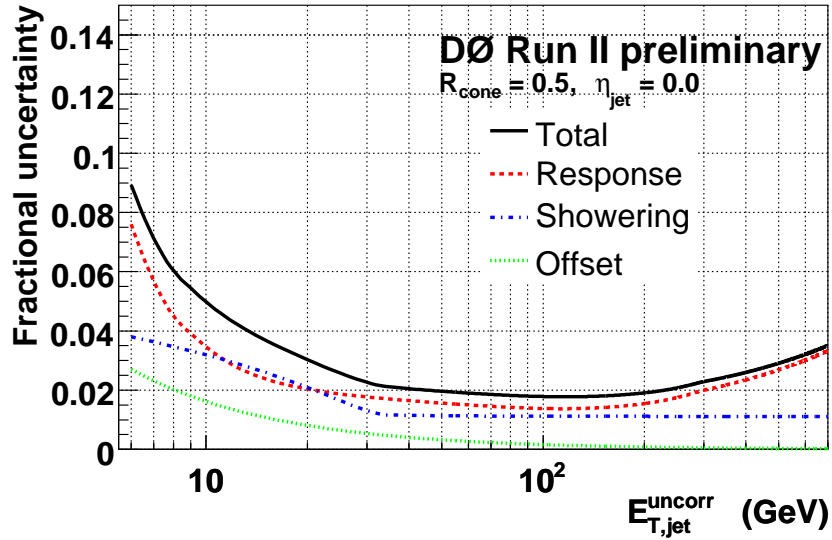


Figure 8.5: 1σ uncertainties from each of the jet energy scale components as a function of jet p_T for jets with $\eta = 0.0$. The total uncertainty is shown by the black line.

correction factor. The uncertainty is determined by varying the correction factor by 1σ in the parameterized bins of p_T and ϕ . The total uncertainty is determined to be 2%.

- **Electron track matching and likelihood efficiency**

This uncertainty derives from the error on the electron track match and likelihood Monte Carlo correction factor. The uncertainty is determined by varying the correction factor by 1σ in the parameterized bins of η and ϕ . The total uncertainty is determined to be 5%.

- **Muon reconstruction and identification efficiency**

This uncertainty derives from the error on the muon reconstruction Monte Carlo correction factor. The uncertainty is determined by varying the correction factor by 1σ in the parameterized bins of η and ϕ . The total uncertainty is determined to be 7%.

- **Muon track matching and isolation**

This uncertainty derives from the error on the muon track match and isolation Monte Carlo correction factor. The uncertainty is determined by varying the correction factor by 1σ in the parameterized bins of η and ϕ for the track match factor and p_T and the number of jets for the isolation factor. The total uncertainty is determined to be 2%.

- **Matrix method normalization**

The normalization of the W+jets and multijet backgrounds is performed using the matrix method and its error is dominated by the error on the efficiency that a lepton not originating from a W decay will pass the electron likelihood or muon isolation cut ($\delta\varepsilon_{\text{Multijet}}$). The statistics of the normalized samples also contributes to the total uncertainty. The average values and errors for $\varepsilon_{\text{Multijet}}$ for both electron and muon events is shown in Table 8.2.

Table 8.2: $\varepsilon_{\text{Multijet}}$ for electrons as a function of the trigger period and jet multiplicity, and $\varepsilon_{\text{Multijet}}$ for muons averaged over η . The definition of the trigger periods is found in Chapter 5.

Jets	Electron $\varepsilon_{\text{Multijet}}$ For Five Trigger Periods (%)					Muon $\varepsilon_{\text{Multijet}}$ (%)
	I	II	III	IV	IV	I
2	12.8 ± 1.0	19.2 ± 1.0	18.8 ± 2.2	19.4 ± 1.1	22.0 ± 1.2	35.8 ± 3.2
3	13.6 ± 1.5	19.5 ± 1.6	19.8 ± 3.4	19.2 ± 1.6	19.4 ± 1.7	34.2 ± 4.5

- **Ratio of $Wb\bar{b} + Wc\bar{c}$ to Wjj Events**

There is a 30% systematic error due to the uncertainty on this ratio. The error is much larger than the fit to the events in the zero tag sample to account for theoretical shape-dependent errors that are not modeled in the Monte Carlo. The largest of these theoretical errors is the shape change to the b -quark p_T between NLO and LO Wbb events. The error on this ratio is folded into the overall matrix method normalization uncertainty when determining the acceptance and background yield uncertainties.

- **Monte Carlo tag-rate functions**

The uncertainty associated with the tag-rate functions is evaluated by shifting the TRFs by $\pm 1\sigma$ and evaluating the change in the signal acceptance and background yield. The tag-rate function uncertainties are dominated by the assumed fraction of heavy flavor in the multijet samples used to determine the fake tagging rate in data and the decreased statistics in each bin due the parameterization in p_T and η . The tag rate functions for B -jets and charm-jets and the 1σ error bands are shown in Fig. 8.6. The total uncertainty depends heavily on the number of B -tagged jets in the event.

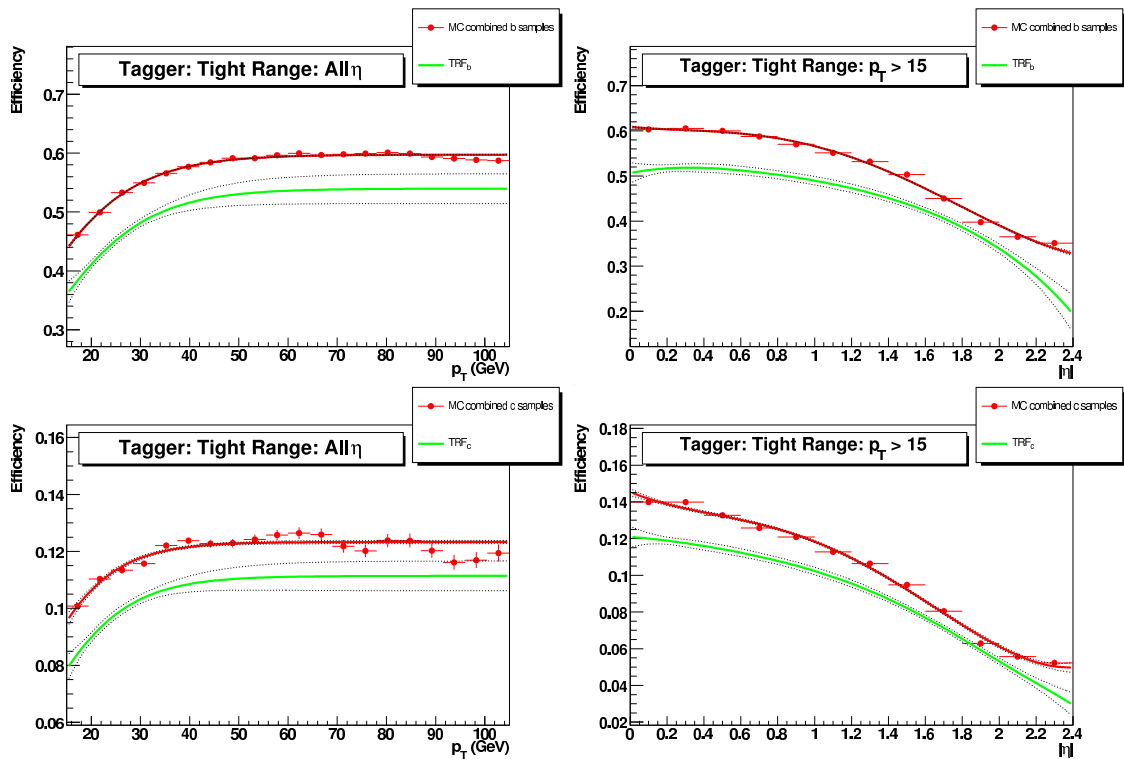


Figure 8.6: Neural network B -jet tagger efficiency (green line) and 1σ error bands (dashed lines) jet p_T and η for B -jets (upper row) and charm-jets (lower row). The red lines represent the efficiency of the B -tagging algorithm when applied directly to the Monte Carlo.

8.3 Ensemble Testing

Ensemble tests are performed to ensure there is no bias in the measured cross section. An ensemble is a group of pseudo-datasets created with a known fraction of signal and background events. Since the fractions are known the linearity of the measured cross section can be tested against the known cross section.

The ensembles are generated from a large set of weighted signal and background events. For each analysis channel the total background yield, as shown in Chapter 6, is used as the expected value of a Poisson distribution and a new background yield is generated from this distribution. The uncertainty in the yield due to systematics is included when generating a new background and signal yield as explained in Appendix D. This procedure will on average produce the expected background compositeness (e.g. ratio of W_{bb} to W_{jj} events). The cross section is then determined for all pseudo-datasets in the ensemble.

Five ensembles were generated with the following $s+t$ -channel input signal cross sections:

- $\sigma_{s+t} = 2$ pb.
- $\sigma_{s+t} = 2.9$ pb. (Expected Standard Model cross section)
- $\sigma_{s+t} = 4$ pb.
- $\sigma_{s+t} = 6$ pb.
- $\sigma_{s+t} = 8$ pb.

2,000 datasets were generated in each ensemble. A histogram of the measured cross sections for each of these ensembles is shown in Fig. 8.7. A plot of the mean of these histograms versus the input cross section is shown in Fig. 8.8. A linear fit to the data points yields a good χ^2/dof of 0.13/3, a slope consistent with 1 of 1.03 ± 0.03 , and an offset of 0.32 ± 0.09 .

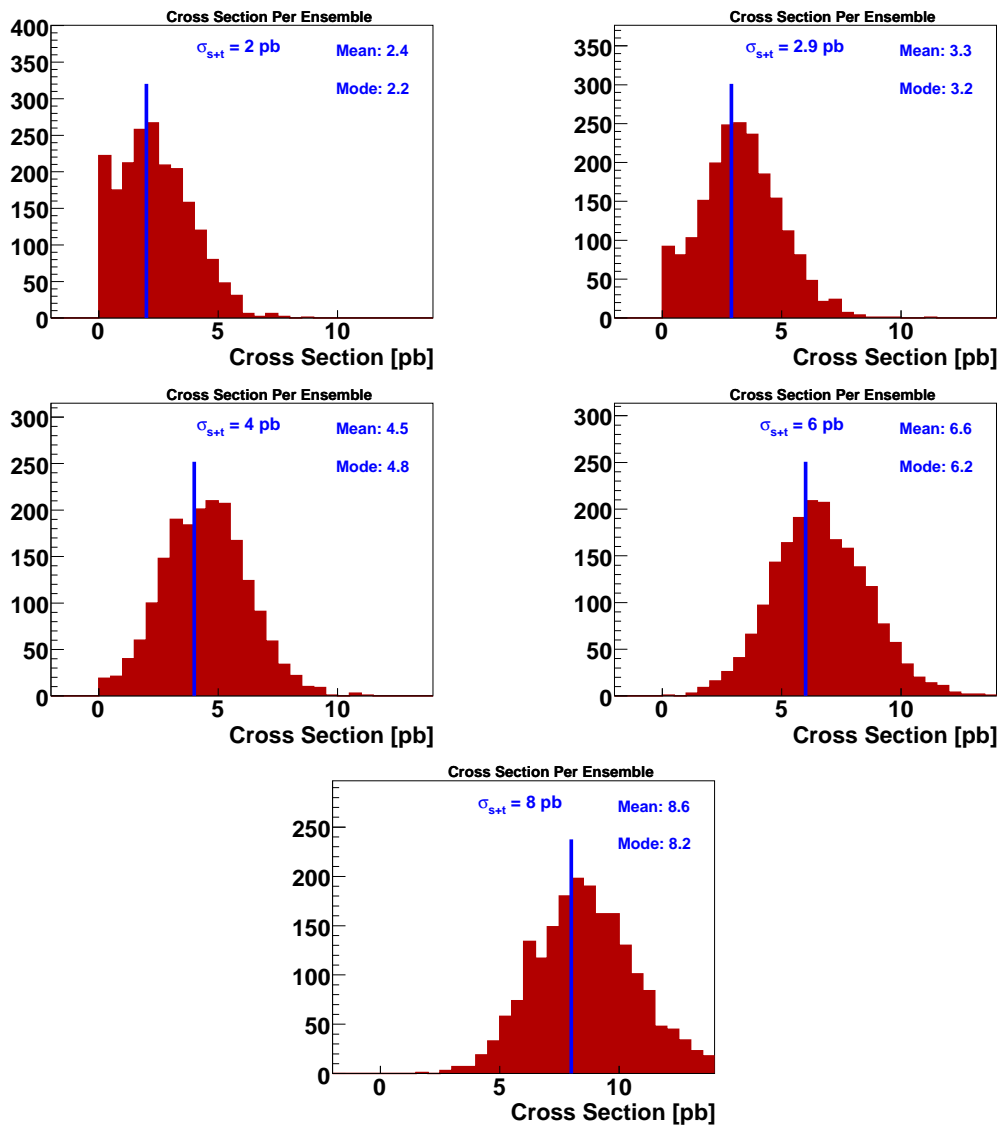


Figure 8.7: Observed cross section for a set of 2,000 pseudo-datasets for the five ensembles: $\sigma_{s+t} = 2.0$ pb (upper left), $\sigma_{s+t} = 2.9$ pb (upper right), $\sigma_{s+t} = 4.0$ pb (middle left), $\sigma_{s+t} = 6.0$ pb (middle right), and $\sigma_{s+t} = 8.0$ pb (bottom middle)

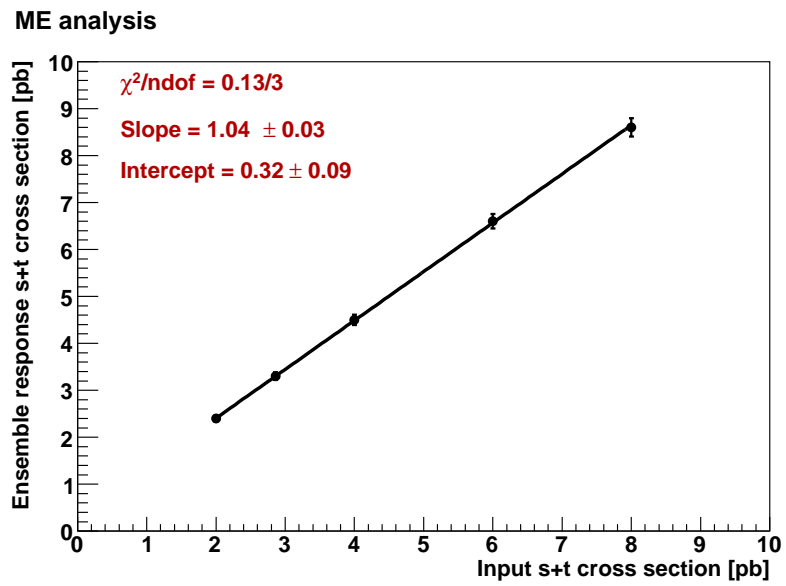


Figure 8.8: Response of the five generated ensemble sets versus input cross section. The response is measured as the mean value of the histogram for each ensemble.

8.4 Expected Results

This section presents the expected performance of the analysis given a Standard Model single top signal. To test the expected sensitivity the number of data events is set equal to the number of signal and background events in each bin of the Likelihood (i.e. the excess of data over background in each bin is equal, by construction, to the number of events expected from a signal with $\sigma = 2.9$ pb). This test is performed for each analysis channel and various combinations of the channels. Figs. 8.9 and 8.10 show the resulting $tb+ tqb^5$ posterior for the combined $e+\mu \geq 1$ B -tag channel in two-jet and three-jet events. Figure 8.11 shows the $tb+ tqb$ posterior for the combination of all channels. The figures on the left correspond to the case of only statistical uncertainties, whereas the figures on the right include statistical and systematic uncertainties.

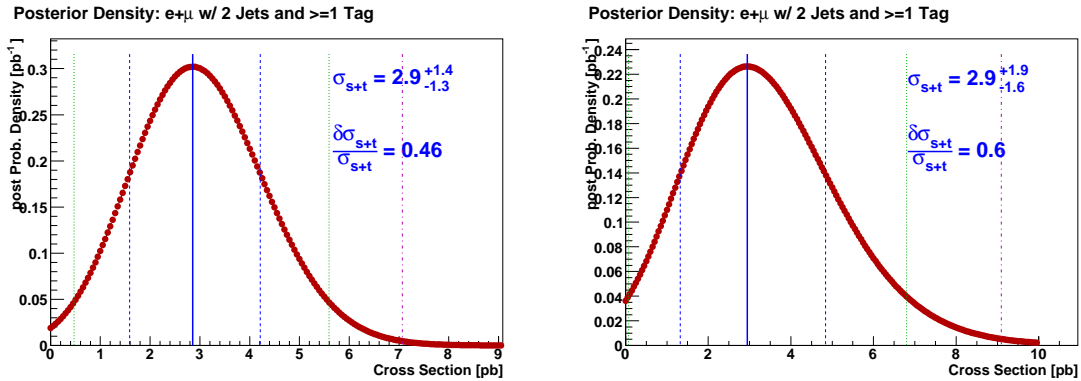


Figure 8.9: Expected 1D posterior plots for the combined $e+\mu \geq 1$ B -tag channel in two-jet events, with statistical uncertainties only (left plot) and including also systematic uncertainties (right plot).

Table 8.3 shows the expected cross sections for various combinations of analysis channels. The expected result for each combination is consistent with the standard model cross section. Table 8.4 summarizes the relative uncertainty on the expected $tb+ tqb$ cross section measurement, defined as half the width of the $tb+ tqb$ posterior, divided by the cross section

⁵ $tb + tqb$ is used to denote the combined s -channel plus t -channel cross section measurement

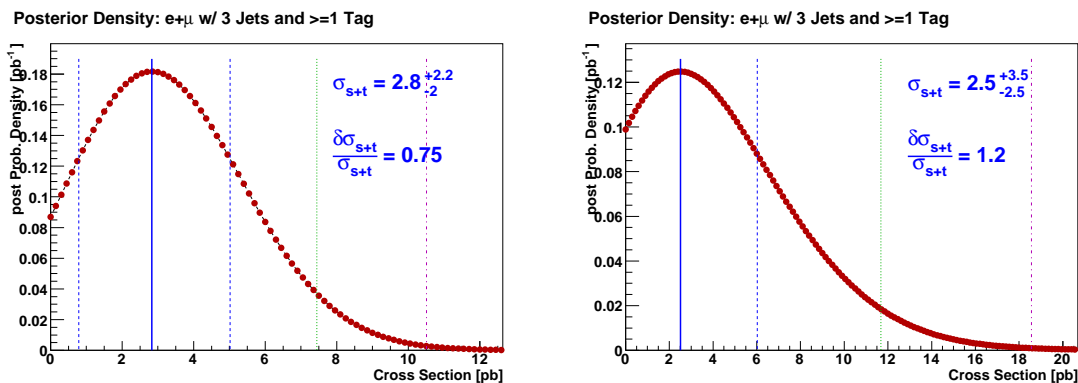


Figure 8.10: Expected 1D posterior plots for the combined $e+\mu \geq 1$ b -tag channel in three-jet events, with statistical uncertainties only (left plot) and including also systematic uncertainties (right plot).

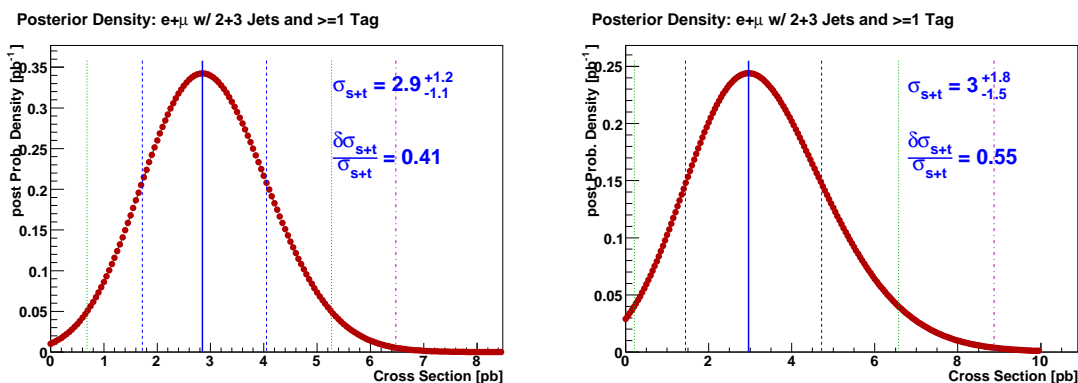


Figure 8.11: Expected 1D posterior plots for the combination of all channels, with statistical uncertainties only (left plot) and including also systematic uncertainties (right plot).

value at the posterior peak.

Table 8.3: Expected $tb+tb$ cross sections, without and with systematic uncertainties, for many combinations of the analysis channels. The final expected result of this analysis are shown in the lower right hand corner in bold type.

	1,2tags + 2,3jets		$e,\mu + 2,3$ jets		$e,\mu + 1,2$ tags		All channels
	e -chan	μ -chan	1 tag	2 tags	2 jets	3 jets	
Statistics only	$2.8^{+1.5}_{-1.4}$	$2.8^{+1.8}_{-1.7}$	$2.9^{+1.3}_{-1.2}$	$2.8^{+2.5}_{-2.2}$	$2.9^{+1.4}_{-1.3}$	$2.8^{+2.2}_{-2.1}$	$2.9^{+1.2}_{-1.1}$
With systematics	$3.0^{+2.2}_{-1.8}$	$3.1^{+2.5}_{-2.1}$	$2.9^{+1.8}_{-1.6}$	$2.7^{+3.4}_{-2.7}$	$2.9^{+1.9}_{-1.6}$	$2.5^{+3.5}_{-2.5}$	$3.0^{+1.8}_{-1.5}$

Table 8.4: Relative uncertainties on the expected $tb+tb$ cross section, without and with systematic uncertainties, for many combinations of the analysis channels. The best value from all channels combined, with systematics, is shown in bold type.

	1,2tags + 2,3jets		$e,\mu + 2,3$ jets		$e,\mu + 1,2$ tags		All channels
	e -chan	μ -chan	1 tag	2 tags	2 jets	3 jets	
Statistics only	52%	60%	45%	83%	46%	75%	41%
With systematics	67%	75%	59%	115%	60%	121%	55%

Chapter 9

RESULTS WITH DATA

The chapter presents the single top quark production cross section measured in nearly 1 fb^{-1} of Tevatron RunII data. The cross section and the observed resolution is presented in Section 9.1. To measure the expected and observed significance pseudo-datasets with no signal contribution are created and the fraction of datasets with a measured cross section above the observed cross section is calculated. This value is the probability of a background-only fluctuation and can be converted to a Gaussian equivalent signal significance. This result is presented in Section 9.2.

9.1 Measured Cross Section

Figure 9.1 shows the observed $tb+tb$ posterior without and with systematic uncertainties for all channels combined.

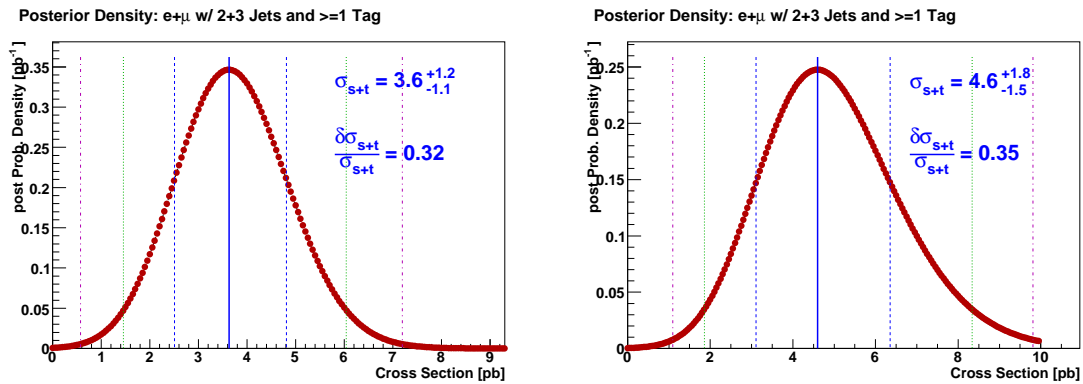


Figure 9.1: Measured 1D posterior plots for the combined $e+\mu \geq 1$ B -tag channel with statistical uncertainties only (left plot) and with systematic uncertainties as well (right plot).

Table 9.1 shows the measured cross sections from various combinations of analysis channels. The averaged relative uncertainties on the measured cross sections are shown in

Table 9.2.

Table 9.1: Measured $tb+ tqb$ cross sections, without and with systematic uncertainties, for many combinations of the analysis channels. The final result of this analysis is shown in the lower right hand corner in bold type.

	1,2tags + 2,3jets		$e,\mu + 2,3jets$		$e,\mu + 1,2tags$		All channels
	e -chan	μ -chan	1 tag	2 tags	2 jets	3 jets	
Statistics only	$3.0^{+1.5}_{-1.4}$	$4.5^{+1.8}_{-1.7}$	$2.8^{+1.2}_{-1.2}$	$7.9^{+3.3}_{-3.0}$	$3.5^{+1.4}_{-1.3}$	$3.9^{+2.3}_{-2.2}$	$3.6^{+1.2}_{-1.1}$
With systematics	$3.1^{+2.2}_{-1.8}$	$7.4^{+3.0}_{-2.5}$	$4.5^{+2.0}_{-1.7}$	$6.8^{+4.7}_{-3.8}$	$4.7^{+2.0}_{-1.7}$	$4.9^{+3.7}_{-3.1}$	$4.6^{+1.8}_{-1.5}$

Table 9.2: Relative uncertainties on the measured $tb+ tqb$ cross section, without and with systematic uncertainties, for many combinations of the analysis channels. The best value from all channels combined, with systematics, is shown in bold type.

	1,2tags + 2,3jets		$e,\mu + 2,3jets$		$e,\mu + 1,2tags$		All channels
	e -chan	μ -chan	1 tag	2 tags	2 jets	3 jets	
Statistics only	50%	39%	44%	40%	37%	57%	32%
With systematics	64%	38%	41%	62%	39%	70%	35%

The combined result with full systematics is

$$\sigma(p\bar{p} \rightarrow tb + tqb + X) = 4.6^{+1.8}_{-1.5} \text{ pb.}$$

A breakdown of the uncertainties on the $tb+ tqb$ cross section measurement is given in Table 9.3. The systematic uncertainties were calculated using an ensemble containing 200 datasets generated with an input single top cross section of 4.6 pb. The cross section of each dataset was measured and the average posterior width (average of upper and lower 1σ uncertainties) was calculated over all datasets for each source of systematic uncertainty independently. The systematic uncertainty for each source was estimated by subtracting in quadrature from the average posterior width obtained with a particular source of systematic, the average posterior width without systematic uncertainties. The total expected systematic

uncertainty is estimated by adding in quadrature all the individual expected systematic uncertainties. The statistical uncertainty of the measurement is estimated by subtracting in quadrature the total expected systematic uncertainty from the actual total uncertainty.

Table 9.3: Contribution of each systematic uncertainty to the total systematic uncertainty on the $tb+tb$ cross section.

Systematics components		
Luminosity		0.69 pb
$t\bar{t}$ cross section		0.74 pb
Matrix method		0.84 pb
Trigger		0.48 pb
Primary vertex		0.31 pb
Lepton ID		0.50 pb
Jet ID		0.18 pb
Jet fragmentation		0.63 pb
Jet energy scale		0.57 pb
Tag-rate functions		0.60 pb
Combined systematics	+1.34	-1.02 pb
Statistics	+1.19	-1.13 pb
Total uncertainty	+1.79	-1.50 pb

Figure 9.2 shows the cross sections measured for combined the $tb+tb$ production in each independent analysis channel, and the combined result.

9.2 Signal Significance and Standard Model Compatibility

The measured significance is defined as the fraction ensembles generated with zero input cross section that result in a measured cross section above the observed cross section of 4.6 pb. This quantity, known as the p -value, represents the probability that the background alone could fluctuate to mimic the single top quark signal. For the case of Standard Model

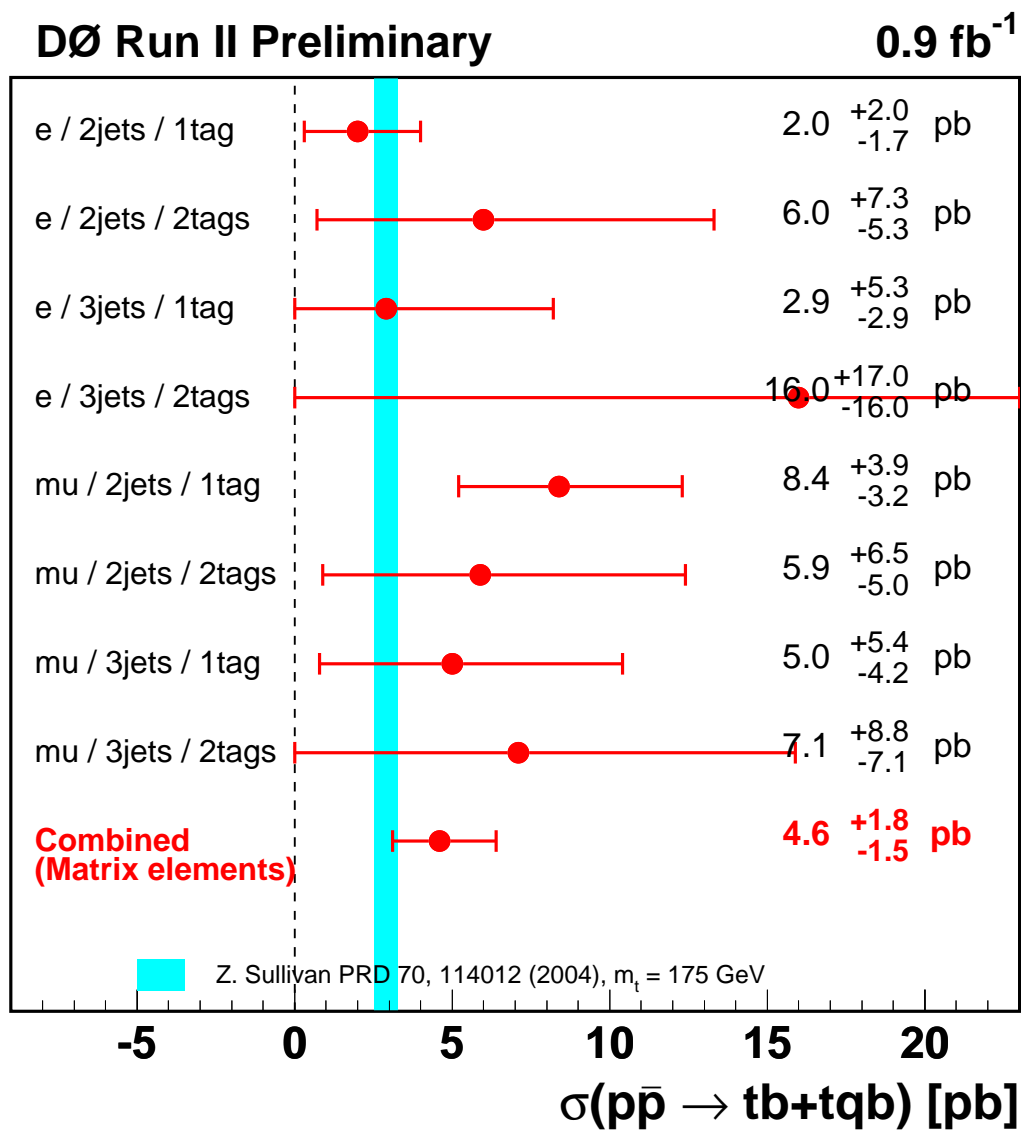


Figure 9.2: Summary plot of the measured single top quark cross sections showing the individual measurements and their combination.

single top the expected p -value is 3.7%, which is equivalent to a 1.8σ Gaussian significance of a deviation from a background fluctuation. The measured p -value of 0.21% is equivalent to a 2.9σ significance indicating evidence for single top quark production in the dataset.

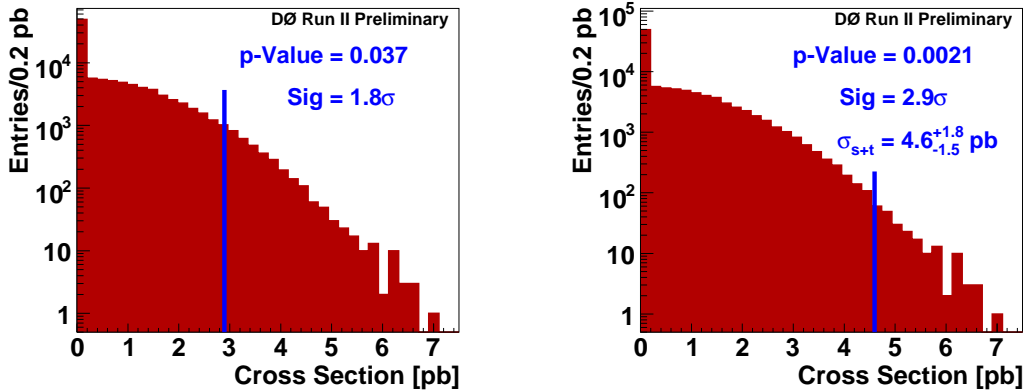


Figure 9.3: Distribution of expected (left) and measured (right) cross sections from a zero-signal ensemble with full systematics included. The probability that the background alone could have a measured cross section above 4.6 pb or above is 0.21% leading to a Gaussian equivalent signal significance of 2.9σ .

The probability of a Standard Model signal to have a measured cross section above 4.6 pb can be estimated using the Standard Model ensemble dataset (i.e. $\sigma_{s+t} = 2.9$ pb). Fig. 9.4 shows the measured cross section for 2,000 Standard Model pseudo-datasets. From this histogram there is a 20.5% probability that a Standard Model signal could be measured at or above 4.6 pb.

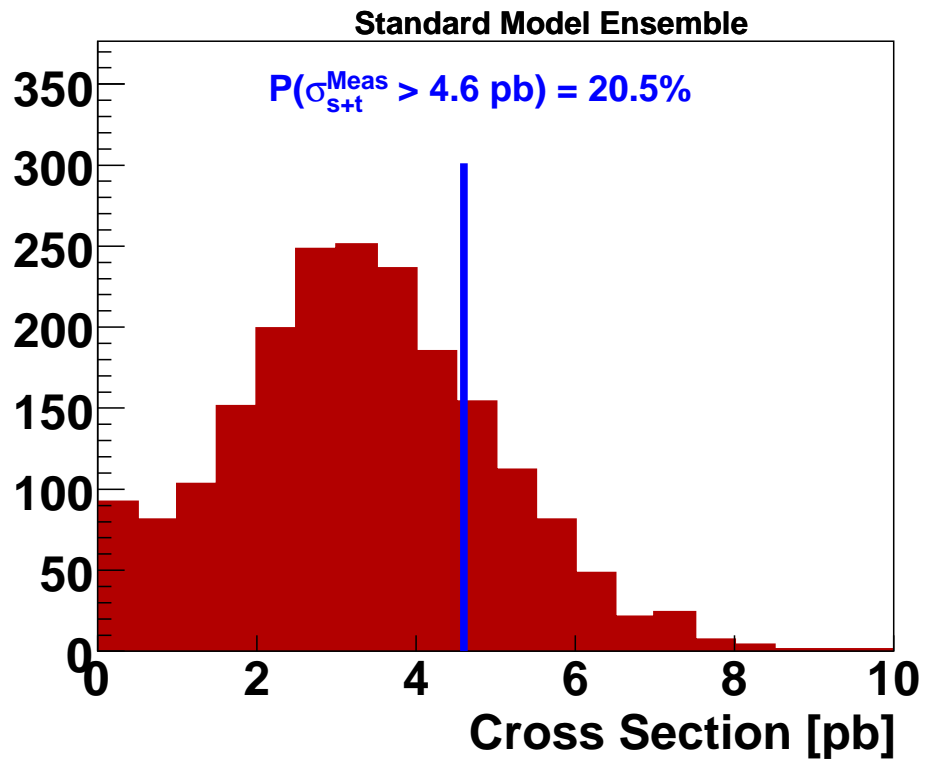


Figure 9.4: Distribution of measured cross sections from a Standard Model ensemble with full systematics included. The probability that a Standard Model signal could have a measured cross section of 4.6 pb or above is 20.5%.

Chapter 10

CONCLUSION AND DISCUSSION

This thesis presents evidence for electroweak single top quark production at the Tevatron. An analysis of nearly 1 fb^{-1} of Run II data using the matrix element method to select single top quark-like events measures the combined $s + t$ -channel production cross section to be

$$\sigma(p\bar{p} \rightarrow tb + tqb + X) = 4.6_{-1.5}^{+1.8} \text{ pb},$$

where the probability of a background fluctuation is 0.21%, which corresponds to a Gaussian equivalent signal significance of 2.9σ . This analysis is one of three single top searches performed by the $D\bar{O}$ collaboration. The first analysis using boosted decision trees measures a combined $s + t$ cross section of $4.9 \pm 1.4 \text{ pb}$ with a signal significance of 3.4σ , while the second analysis uses Bayesian neural networks and measures a cross section of $5.0 \pm 1.9 \text{ pb}$ at 2.4σ signal significance. The results of these three analyses were recently accepted for publication by Physical Review Letters [18]. More recently the three results were combined using the BLUE (Best Linear Unbiased Estimator) [75] method; this resulted in a measured cross section of $4.8 \pm 1.3 \text{ pb}$ with 3.5σ signal significance [54]. The cross sections from the three analyses as well as the combination are shown in Fig. 10.1, where they are also compared with two next-to-leading order single top cross section calculations.

Several improvements to the matrix element analysis presented in this thesis are currently underway. First is the addition of a $t\bar{t}$ matrix element in the discriminant definition. This should dramatically enhance the signal significance in events with three jets where the $t\bar{t}$ background contribution is substantial. The second improvement is the use of the muon charge from a semi-leptonic B decay to weight the jet-parton assignment of jets to b and \bar{b} quarks, while the third is the addition of the neural network B -tagging algorithm in the discriminant definition. Events with jets that are very B -jet like will receive a higher weight from background processes involving b quarks (e.g. $Wb\bar{b}$) while the remaining events will receive a higher weight from processes involving light quarks (e.g. Wgg and Wcg).

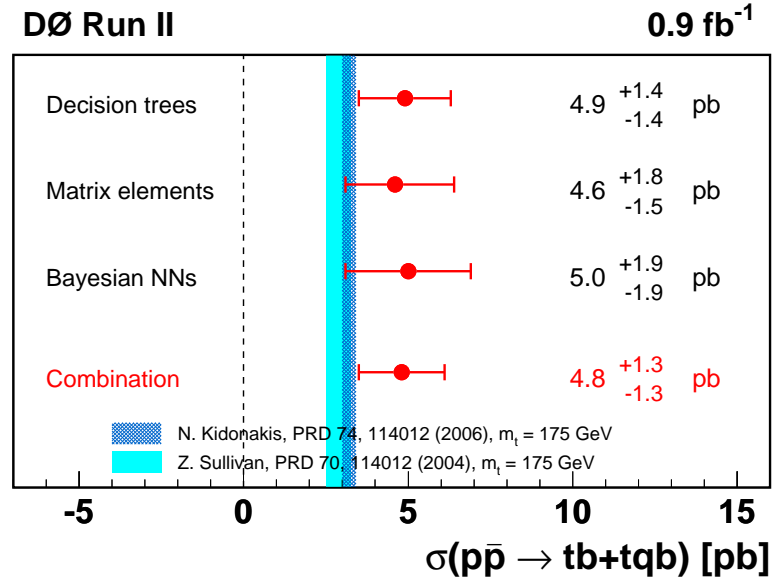


Figure 10.1: Results from the three single top quark analyses and the combined analysis compared with two NLO cross section calculations [54].

DØ has already recorded more than 2 fb^{-1} of Run II data. With this increased dataset several important measurements are possible. The first is an individual measurement of the s -channel and t -channel cross sections. Each production process is sensitive to different new physics models making a determination of the cross section for each channel an important test for physics beyond the Standard Model. Another important measurement using this dataset is a precise determination of $|V_{tb}|$. The current uncertainty on the combined single top cross section is $\sim 30\%$, which leads to an uncertainty on $|V_{tb}|$ of $\sim 20\%$. With this increased dataset the expected error on $|V_{tb}|$ will decrease to 15% .

A precise measurement of the single top quark production cross section is also important because single top events are one of the largest backgrounds for Higgs production. At the Tevatron one of the most sensitive channels for a low mass Higgs is W -associated Higgs production (WH). The WH production cross section for $m_H = 115$ GeV is nearly one-tenth of the single top cross section. Using the full Run II dataset and employing advanced

multivariate analysis techniques such as the method described in this thesis, DØ hopes to find evidence for the Higgs boson before the start of the Large Hadron Collider era.

The analysis presented in this thesis has shown that with a detailed understanding of the detector apparatus, an advanced multivariate technique to reduce backgrounds, and a sophisticated statistical analysis of the dataset, the measurement of a process which occurs in 1 out of every 10 billion collisions at the Tevatron is possible. With an increased dataset of $3 - 4 \text{ fb}^{-1}$ a 5σ observation of single top production will be possible, thereby providing a stringent test of the Standard Model and possibly establishing the presence of new physics.

BIBLIOGRAPHY

- [1] <http://www-bd.fnal.gov/public/antiproton.html>.
- [2] <http://www-bd.fnal.gov/public/proton.html>.
- [3] <http://www-bd.fnal.gov/public/tevatron.html>.
- [4] http://www-d0.fnal.gov/phys_id/jes/public/plots_v7.1.
- [5] <http://www-d0.fnal.gov/run2physics/top/index.html>.
- [6] <http://www-d0.fnal.gov/run2physics/top/public/fall06/singletop/>.
- [7] <http://www-d0.hef.kun.nl//fullagenda.php?ida=a03632&fid=35>.
- [8] <http://www-d0.hef.kun.nl//fullagenda.php?ida=a052073&fid=64>.
- [9] <http://www.aanda.org/index.php>.
- [10] <http://www.fnal.gov/pub/now/tevlum.html>.
- [11] <http://www.fuw.edu.pl/dobaczew/maub-42w/node12.html>.
- [12] S. Abachi et al. Observation of the top quark. *Phys. Rev. Lett.*, 74:2632–2637, 1995.
- [13] V. M. Abazov et al. Search for single top quark production at $d\bar{o}$ using neural networks. *Phys. Lett.*, B517:282–294, 2001.
- [14] V. M. Abazov et al. Measurement of the t anti- t production cross section in p anti- p collisions at $s^{*(1/2)} = 1.96$ -tev in dilepton final states. *Phys. Lett.*, B626:55–64, 2005.
- [15] V. M. Abazov et al. Measurement of the t anti- t production cross section in p anti- p collisions at $s^{*(1/2)} = 1.96$ -tev using kinematic characteristics of lepton + jets events. *Phys. Lett.*, B626:45–54, 2005.
- [16] V. M. Abazov et al. Measurement of the t anti- t production cross section in p anti- p collisions at $s^{*(1/2)} = 1.96$ -tev using lepton + jets events with lifetime b -tagging. *Phys. Lett.*, B626:35–44, 2005.

- [17] V. M. Abazov et al. Search for single top quark production in p anti-p collisions at $\sqrt{s} = 1.96$ -tev. *Phys. Lett.*, B622:265–276, 2005.
- [18] V. M. Abazov et al. Evidence for production of single top quarks and first direct measurement of σ_{vtb} . 2006.
- [19] V. M. Abazov et al. Measurement of the $t\bar{t}$ production cross section in $p\bar{p}$ collisions at $\sqrt{s} = 1.96$ -tev using secondary vertex b tagging. *Phys. Rev.*, D74:112004, 2006.
- [20] V. M. Abazov et al. Multivariate searches for single top quark production with the d0 detector. 2006.
- [21] V. M. Abazov et al. The upgraded d0 detector. *Nucl. Instrum. Meth.*, A565:463–537, 2006.
- [22] B. Abbott et al. Search for electroweak production of single top quarks in $p\bar{p}$ collisions. *Phys. Rev.*, D63:031101, 2001.
- [23] F. Abe et al. Observation of top quark production in $\bar{p}p$ collisions. *Phys. Rev. Lett.*, 74:2626–2631, 1995.
- [24] A. Abulencia et al. Measurement of the t anti-t production cross section in p anti-p collisions at $\sqrt{s} = 1.96$ -tev using missing $e(t) + \text{jets}$ events with secondary vertex b-tagging. *Phys. Rev. Lett.*, 96:202002, 2006.
- [25] A. Abulencia et al. Measurement of the $t\bar{t}$ production cross section in $p\bar{p}$ collisions at $\sqrt{s} = 1.96$ -tev in the all hadronic decay mode. *Phys. Rev.*, D74:072005, 2006.
- [26] A. Abulencia et al. Measurement of the $t\bar{t}$ production cross section in $p\bar{p}$ collisions at $\sqrt{s} = 1.96$ -tev using lepton + jets events with jet probability b^- tagging. *Phys. Rev.*, D74:072006, 2006.
- [27] A. Abulencia et al. Measurement of the $t\bar{t}$ production cross section in p anti-p collisions at $\sqrt{s} = 1.96$ -tev. *Phys. Rev. Lett.*, 97:082004, 2006.
- [28] D. Acosta et al. Search for single top quark production in $p\bar{p}$ collisions at $\sqrt{s} = 1.8$ -tev. *Phys. Rev.*, D65:091102, 2002.
- [29] D. Acosta et al. Optimized search for single top quark production at the fermilab tevatron. *Phys. Rev.*, D69:052003, 2004.
- [30] D. Acosta et al. Measurement of the cross section for $t\bar{t}$ production in $p\bar{p}$ collisions using the kinematics of lepton + jets events. *Phys. Rev.*, D72:052003, 2005.

- [31] D. Acosta et al. Measurement of the $t\bar{t}$ production cross section in $p\bar{p}$ collisions at $\sqrt{s} = 1.96$ tev using lepton plus jets events with semileptonic b decays to muons. *Phys. Rev.*, D72:032002, 2005.
- [32] D. Acosta et al. Search for electroweak single top quark production in $p\bar{p}$ collisions at $\sqrt{s} = 1.96$ tev. *Phys. Rev.*, D71:012005, 2005.
- [33] Chris Tully Ariel Schwartzman. Primary vertex reconstruction by means of adaptive vertex fitting. d0 note number: 004918.
- [34] William A. Bardeen, Christopher T. Hill, and Manfred Lindner. Minimal dynamical symmetry breaking of the standard model. *Phys. Rev. D*, 41(5):1647–1660, Mar 1990.
- [35] R. Michael Barnett, Howard E. Haber, and G. L. Kane. Implications of a systematic study of the cern monojets for supersymmetry. *Phys. Rev. Lett.*, 54(18):1983–1986, May 1985.
- [36] Ikaros I. Y. Bigi, Yuri L. Dokshitzer, Valery A. Khoze, Johann H. Kuhn, and Peter M. Zerwas. Production and decay properties of ultraheavy quarks. *Phys. Lett.*, B181:157, 1986.
- [37] Gerald C. Blazey et al. Run ii jet physics. 2000.
- [38] E. Boos, V. Bunichev, L. Dudko, V. Savrin, and A. Sherstnev. A simulation method of the electroweak top quark production events in the nlo approximation. a monte-carlo generator “singletop”. *SINP MSU 2005-16/78; accepted for publication in Physics of Atomic Nuclei*, 2005.
- [39] Guennadi Borissov. Ordering a chaos or... technical details of aa tracking. all DØ meeting 2/28/03.
- [40] D Bourilkov, R C Group, and M R Whalley. Lhapdf: Pdf use from the tevatron to the lhc. 2006.
- [41] E. Brubaker et al. Combination of cdf and d0 results on the mass of the top quark. 2006.
- [42] M. Cacciari, S. Frixione, M. L. Mangano, P. Nason, and G. Ridolfi. The t-tbar cross-section at 1.8 and 1.96 tev: a study of the systematics due to parton densities and scale dependence. *JHEP*, 0404:068, 2004.
- [43] J. Campbell, R. K. Ellis, F. Maltoni, and S. Willenbrock. Production of a w boson and two jets with one b-quark tag. *Phys. Rev.*, D75:054015, 2007.

- [44] Qing-Hong Cao, Reinhard Schwienhorst, Jorge A. Benitez, Raymond Brock, and C. P. Yuan. Next-to-leading order corrections to single top quark production and decay at the tevatron. ii: t-channel process. *Phys. Rev.*, D72:094027, 2005.
- [45] Qing-Hong Cao, Reinhard Schwienhorst, and C. P. Yuan. Next-to-leading order corrections to single top quark production and decay at tevatron. i: s-channel process. *Phys. Rev.*, D71:054023, 2005.
- [46] B. Clément and D. Gelé. Search for single top quark production using likelihood discriminants. DØ note 4825 (2005).
- [47] The CDF Collaboration. Multivariate likelihood search for single-top-quark production with 1 fb^{-1} . cdf conference note 8585, (2006).
- [48] The CDF Collaboration. Search for electroweak single-top-quark production using neural networks with 955 pb^{-1} of cdf runii data. cdf conference note 8677, (2007).
- [49] The CDF Collaboration. Search for single top quark production in 955 pb^{-1} using the matrix element technique. cdf conference note 8588, (2006).
- [50] The CDF Collaboration. Single top quark search with 0.7 fb^{-1} . cdf conference note 8185, (2006).
- [51] F. F. Cordero, L. Reina, and D. Wackerroth. NLO QCD corrections to W boson production with a massive b-quark jet pair at the Fermilab Tevatron $p\bar{p}$ collider. *Phys. Rev. D*, 74(3):034007+, August 2006.
- [52] S. Cortese and R. Petronzio. The single top production channel at tevatron energies. *Phys. Lett.*, B253:494–498, 1991.
- [53] R. O. Duda and P. E. Hart. Use of the hough transformation to detect lines and curves in pictures. *Comm. ACM*, 15:1115, 1972.
- [54] The DØ Collaboration. Combining results from three single top quark cross section measurements using the blue method. d0 conference note number 5342.
- [55] R. K. Ellis and Siniša Veseli. Strong radiative corrections to $wbb[\overline{v}]$ production in $pp[\overline{v}]$ collisions. *Phys. Rev. D*, 60(1):011501, Jun 1999.
- [56] E. Aguilo et al. Search for single top quark production in 1 fb^{-1} of data. d0 note number: 005285.
- [57] J. Hays et. al. Single electron efficiencies in p17 data and monte-carlo. d0 note number: 005025.

- [58] M. Agelou et al. Search for single top quark production at dzero in run ii. d0 note number: 004398.
- [59] T. Gadfort et. al. Muon identification certification for p17 data. d0 note number: 005157.
- [60] B. Casey *et al.* Determination of the effective inelastic $p\bar{p}$ cross section for the DØ luminosity measurement using upgraded readout electronics. DØ note 4958 (2005).
- [61] G. Snow *et al.* Adjustments to the measured integrated luminosity in run iia. DØ note 5139 (2006).
- [62] Womersley J. Fisyak Y. D0gstar d0 geant simulation of the total apparatus response (<http://d0sgio.fnal.gov/d0upgrad>. d0 note number: 003191.
- [63] Andrew C. Haas. A search for neutral higgs bosons at high tan beta in multi-jet events from p anti-p collisions at $s^{*1/2} = 1960$ -gev. FERMILAB-THESIS-2004-26.
- [64] B. W. Harris, E. Laenen, L. Phaf, Z. Sullivan, and S. Weinzierl. The fully differential single top quark cross section in next-to-leading order qcd. *Phys. Rev.*, D66:054024, 2002.
- [65] A. P. Heinson, A. S. Belyaev, and E. E. Boos. Single top quarks at the fermilab tevatron. *Phys. Rev. D*, 56(5):3114–3128, Sep 1997.
- [66] Stefan Hoche et al. Matching parton showers and matrix elements. 2006.
- [67] Shabnam Jabeen. Search for the single top quarks produced in s-channel via electroweak interactions at $s = 1.96$ at the tevatron. FERMILAB-THESIS-2006-24.
- [68] S. Jadach, Z. Ws, R. Decker, and J. H. Kühn. The τ decay library TAUOLA, version 2.4. *Computer Physics Communications*, 76:361–380, August 1993.
- [69] Alexander Khanov. Htf: histogramming method for finding tracks. the algorithm description. d0 note number: 3778.
- [70] Nikolaos Kidonakis. Single top production at the tevatron: Threshold resummation and finite-order soft gluon corrections. *Phys. Rev.*, D74:114012, 2006.
- [71] Nikolaos Kidonakis and Ramona Vogt. Next-to-next-to-leading order soft-gluon corrections in top quark hadroproduction. *Phys. Rev.*, D68:114014, 2003.
- [72] Nikolaos Kidonakis and Ramona Vogt. Top quark production at the tevatron at nnlo. *Eur. Phys. J.*, C33:S466–S468, 2004.

- [73] D. J. Lange. The EvtGen particle decay simulation package. *Nuclear Instruments and Methods in Physics Research A*, 462:152–155, April 2001.
- [74] G. Peter Lepage. Vegas: An adaptive multidimensional integration program. CLNS-80/447.
- [75] L. Lyons, D. Gibaut, and P. Clifford. How to combine correlated estimates of a single physical quantity. *Nuclear Instruments and Methods in Physics Research A*, 270:110–117, July 1988.
- [76] Louis Lyons, Alex J. Martin, and David H. Saxon. On the determination of the b lifetime by combining the results of different experiments. *Phys. Rev. D*, 41(3):982–985, Feb 1990.
- [77] Gregory Mahlon. Spin polarization in single top events. 1998.
- [78] Fabio Maltoni and Tim Stelzer. MadEvent: Automatic event generation with MadGraph. *JHEP*, 02:027, 2003.
- [79] Michelangelo L. Mangano, Mauro Moretti, Fulvio Piccinini, Roberto Pittau, and Antonio D. Polosa. Alpgen, a generator for hard multiparton processes in hadronic collisions. *JHEP*, 07:001, 2003.
- [80] Tim Scanlon Miruna Anastasoae, Stephen Robinson. Performance of the nn b-tagging tool on p17 data. d0 note number: 005213.
- [81] J. Pumplin, A. Belyaev, J. Huston, D. Stump, and W. K. Tung. Parton distributions and the strong coupling: Cteq6ab pdfs. *JHEP*, 02:032, 2006.
- [82] J. Pumplin et al. New generation of parton distributions with uncertainties from global qcd analysis. *JHEP*, 07:012, 2002.
- [83] H. Schellman. The longitudinal shape of the luminous region at DØ. DØ note 5142 (2006).
- [84] Torbjorn Sjostrand, Leif Lonnblad, and Stephen Mrenna. Pythia 6.2: Physics and manual. 2001.
- [85] Martin C. Smith and S. Willenbrock. Qcd and yukawa corrections to single-top-quark production via $q\bar{q} \rightarrow t\bar{b}$. *Phys. Rev.*, D54:6696–6702, 1996.
- [86] Bernd Stelzer. Search for electroweak single top quark production in 1.96- tev proton antiproton collisions. FERMILAB-THESIS-2005-79.

- [87] T. Stelzer, Z. Sullivan, and S. Willenbrock. Single-top-quark production via w-gluon fusion at next-to-leading order. *Phys. Rev.*, D56:5919–5927, 1997.
- [88] Zack Sullivan. Understanding single-top-quark production and jets at hadron colliders. *Phys. Rev.*, D70:114012, 2004.
- [89] Tim M. P. Tait and C.-P. Yuan. Single top quark production as a window to physics beyond the standard model. *Phys. Rev. D*, 63(1):014018, Dec 2000.
- [90] Scott S. D. Willenbrock and Duane A. Dicus. Production of heavy quarks from w gluon fusion. *Phys. Rev.*, D34:155, 1986.
- [91] W. M. Yao et al. Review of particle physics. *J. Phys.*, G33:1–1232, 2006.
- [92] C. P. Yuan. A new method to detect a heavy top quark at the tevatron. *Phys. Rev.*, D41:42, 1990.

Appendix A

DIFFERENTIAL CROSS SECTION DERIVATION

A.1 Probability Calculation*A.1.1 Differential Cross Section at the Parton Level*

The matrix element analysis technique reconstructs each event to the final state four-vectors to evaluate the signal and background leading order matrix element. The following sections derive the signal and background probabilities starting from the final state at the parton level and then relating these objects to the physical quantities measured in the detector. The following also assumes a lepton, neutrino, and two quarks in the final state.

The probability density for a process to occur at a hadron-hadron collider is given as an integral of the hard-scatter differential cross section over all possible ways of producing the process from the quarks and gluons inside the hadron. This probability density, shown below, is a convolution of the hard scatter differential cross section with a parton distribution function for each of the two partons from the hadrons with an integral over all possible momentum fractions x_i, x_j from each initial parton.

$$\mathcal{P}(\vec{y}) = \frac{1}{\sigma} \sum_{i,j} \int f_i(q_1, Q^2) dq_1 \times f_j(q_2, Q^2) dq_2 \times d\sigma_{hs,ij}(\vec{y}) \quad (\text{A.1})$$

where the normalization constant σ is defined as integral of the differential cross section over the initial- and final-state phase spac:

$$\sigma = \int \sum_{i,j} \int f_i(q_1, Q^2) dq_1 \times f_j(q_2, Q^2) dq_2 \times \frac{\partial \sigma_{hs,ij}(\vec{y})}{\partial \vec{y}} d\vec{y} \quad (\text{A.2})$$

and finally, the hard-scatter differential cross section is defined as the product of the final state phase space factor, the square of the matrix element amplitude and an overall flux factor:

$$d\sigma_{hs} = \frac{(2\pi)^4}{4} \frac{|\mathcal{M}|^2}{\sqrt{(q_1 q_2)^2 - m_1^2 m_2^2}} \frac{d^3 p_1}{(2\pi)^3 2E_1} \frac{d^3 p_2}{(2\pi)^3 2E_2} \frac{d^3 p_\ell}{(2\pi)^3 2E_\ell} \frac{d^3 p_\nu}{(2\pi)^3 2E_\nu} \delta^4(q_1 q_2; p_1, p_2, p_\ell, p_\nu) \quad (\text{A.3})$$

A.1.2 Evaluating the Hard Scatter Differential Cross Section

The following section evaluates the differential cross section shown in Eq. A.2 given a set of initial and final state four-vectors.

The first assumption made is that all collisions occur along the beam axis with no net transverse momentum. This means the initial state four vectors can be written as

$$q_1 = (E_{beam}x_1, 0, 0, E_{beam}x_1) \quad (\text{A.4})$$

$$q_2 = (E_{beam}x_2, 0, 0, -E_{beam}x_2) \quad (\text{A.5})$$

The next assumption is that all particle masses are known and are negligible compared to their energies and thus can be ignored for this calculation. The flux factor (shown below) in the hard scatter cross section can now be written in terms in the two momentum fractions of the incoming partons:

$$\frac{1}{\sqrt{(q_1q_2)^2 - m_1^2m_2^2}} \rightarrow \frac{1}{\sqrt{(q_1q_2)^2}} \rightarrow \frac{1}{2E_{beam}x_1x_2} \quad (\text{A.6})$$

For the remainder of the note, the following notation will be used to distinguish quarks, leptons, and neutrinos: p_ℓ is the momentum of the lepton, $p_{1,2}$ is the momentum of the first and second final state partons, and p_ν is the neutrino momentum. Because the phase space is written in terms of rectangular coordinates, the next step towards the final differential cross section equation is to redefine the phase space factors in terms of spherical coordinates. This is done for all final state particles except the neutrino for reasons that will be clear later in the document.

$$d\Phi_4 = \frac{d^3p_1}{(2\pi)^3 2E_1} \frac{d^3p_2}{(2\pi)^3 2E_2} \frac{d^3p_\ell}{(2\pi)^3 2E_\ell} \frac{d^3p_\nu}{(2\pi)^3 2E_\nu} \delta^4 \rightarrow \quad (\text{A.7})$$

$$\frac{1}{16(2\pi)^{12}} \frac{|p_1|^2 d|p_1| d\Omega_1}{E_1} \frac{|p_2|^2 d|p_2| d\Omega_2}{E_2} \frac{|p_\ell|^2 d|p_\ell| d\Omega_\ell}{E_\ell} \frac{d_\nu^x d_\nu^y d_\nu^z}{E_\nu} \delta^4 \quad (\text{A.8})$$

To summarize, the full hard scatter differential cross section is now

$$d\sigma_{hs} = \frac{1}{128(2\pi)^8 E_{beam}} \frac{|\mathcal{M}|^2}{2x_1x_2} \frac{|p_1|^2 d|p_1| d\Omega_1}{E_1} \frac{|p_2|^2 d|p_2| d\Omega_2}{E_2} \frac{|p_\ell|^2 d|p_\ell| d\Omega_\ell}{E_\ell} \frac{d_\nu^x d_\nu^y d_\nu^z}{E_\nu} \delta^4 \quad (\text{A.9})$$

A.1.3 Evaluating the Hadron-Hadron Differential Cross Section

The next step to writing the full hadron-hadron differential cross section is to rewrite Eq. A.9 such that any integration over the phase space will remove the four-dimensional delta function required for energy and momentum conservation. The delta function is currently written such that it will vanish only over integrations of total p_x, p_y, p_z , and E . Because there was an original assumption of no net transverse momentum in the collision, the total p_x and p_y can be solved for the neutrino transverse momentum.

$$\sum_i P_i^x = p_1^x + p_2^x + p_\ell^x + p_\nu^x = 0 \rightarrow p_\nu^x = -p_1^x - p_2^x - p_\ell^x \quad (\text{A.10})$$

$$\sum_i P_i^y = p_1^y + p_2^y + p_\ell^y + p_\nu^y = 0 \rightarrow p_\nu^y = -p_1^y - p_2^y - p_\ell^y \quad (\text{A.11})$$

The total p_z and requirement can be rewritten in terms of the initial parton's momentum fraction and the other final state partons' z momenta and thus solve for the neutrino p_z :

$$\begin{aligned} \sum_i P_i^z = p_1^z + p_2^z + p_\ell^z + p_\nu^z - E_{beam}x_1 + E_{beam}x_2 = 0 \rightarrow \\ p_\nu^z = -E_{beam}(x_1 - x_2) - p_1^z - p_2^z - p_\ell^z \end{aligned} \quad (\text{A.12})$$

Finally, the total energy delta function implies the following:

$$E_{beam}x_1 + E_{beam}x_2 = E_1 + E_2 + E_\ell + E_\nu \quad (\text{A.13})$$

At this point, is it useful to rewrite the full differential cross section at the parton level:

$$\begin{aligned} d\sigma(\vec{y}) = \sum_{i,j} \int f_i(x_1, Q^2) dx_1 \times f_j(x_2, Q^2) dx_2 \times \frac{1}{128(2\pi)^8 E_{beam}} \frac{|\mathcal{M}|^2}{2x_1x_2} \times \\ \frac{|p_1|^2 d|p_1| d\Omega_1}{E_1} \frac{|p_2|^2 d|p_2| d\Omega_2}{E_2} \frac{|p_\ell|^2 d|p_\ell| d\Omega_\ell}{E_\ell} \frac{d_\nu^x d_\nu^y d_\nu^z}{E_\nu} \times \\ \delta(p_\nu^x + p_1^x + p_2^x + p_\ell^x) \times \\ \delta(p_\nu^y + p_1^y + p_2^y + p_\ell^y) \times \\ \delta(p_\nu^z + E_{beam}(x_1 - x_2) + p_1^z + p_2^z + p_\ell^z) \times \\ \delta(E_{beam}x_1 + E_{beam}x_2 - E_1 - E_2 - E_\ell - E_\nu) \end{aligned} \quad (\text{A.14})$$

The next step is to rewrite the integrational variables, x_1 and x_2 , in terms of the total energy and total p_z :

$$x_1 = \frac{E_{tot} + p_{tot}^z}{2E_{beam}} \quad (\text{A.15})$$

$$x_2 = \frac{E_{tot} - p_{tot}^z}{2E_{beam}} \quad (\text{A.16})$$

Now, the integration over x_1 and x_2 can be rewritten in terms of E_{tot} and p_z :

$$dx_1 dx_2 = \frac{1}{J(x_1, x_2; E_{tot}, p_{tot}^z)} dE_{tot} dp_{tot}^z \quad (\text{A.17})$$

$$J(x_1, x_2; E_{tot}, p_{tot}^z) = 2E_{beam}^2 \quad (\text{A.18})$$

At this point the integration over the total energy and p_z will constrain the two incoming partons' momentum fractions through Eq. A.15 and A.16.

The full differential cross section at the parton level can now be written as

$$d\sigma(\vec{y}) = \sum_{i,j} \int f_i(x_1, Q^2) \times f_j(x_2, Q^2) \times \frac{1}{128(2\pi)^8 E_{beam}} \frac{|\mathcal{M}|^2}{2x_1 x_2} \times \frac{|p_1|^2 d|p_1| d\Omega_1}{E_1} \frac{|p_2|^2 d|p_2| d\Omega_2}{E_2} \frac{|p_\ell|^2 d|p_\ell| d\Omega_\ell}{E_\ell} \frac{d_\nu^x d_\nu^y d_\nu^z}{E_\nu} \times \int \frac{1}{2E_{beam}^2} dp_{tot}^z \quad (\text{A.19})$$

where the implicit integration over the four dimensional delta function yields the following formulas for the neutrino four vector and the incoming partons' momentum fraction in terms of the remaining differential variables.

$$p_\nu^x = -p_1^x - p_2^x - p_\ell^x \quad (\text{A.20})$$

$$p_\nu^y = -p_1^y - p_2^y - p_\ell^y \quad (\text{A.21})$$

$$p_\nu^z = -p_{tot}^z - p_1^z - p_2^z - p_\ell^z \quad (\text{A.22})$$

$$x_1 = \frac{E_1 + E_2 + E_\ell + E_\nu + p_{tot}^z}{2E_{beam}} \quad (\text{A.23})$$

$$x_2 = \frac{E_1 + E_2 + E_\ell + E_\nu - p_{tot}^z}{2E_{beam}} \quad (\text{A.24})$$

A.1.4 Relating Reconstructed Objects to Partons

The previous sections have calculated the differential cross section for a hadron-hadron collision producing a lepton, neutrino, and two partons in the final state. These particles are not exactly what is measured in the detector and thus it is necessary to relate quantities. To do this, the differential cross section is convoluted with a function, $W(\vec{x}, \vec{y})$, which is

the probability of producing a final state, \vec{y} , and observed state, \vec{x} , in the detector. The resulting differential cross section is then integrated over the final state phase space, $d\vec{y}$:

$$\frac{\partial\sigma'(\vec{x})}{\partial\vec{x}} = \int \frac{\partial\sigma(\vec{y})}{\partial\vec{y}} W(\vec{x}, \vec{y}) d\vec{y} \quad (\text{A.25})$$

where the function $W(\vec{x}, \vec{y})$ is assumed to be factorizable for each measured object:

$$W(\vec{x}, \vec{y}) = \prod_i W_i(\vec{x}_i, \vec{y}_i) \quad (\text{A.26})$$

Jets

The transfer function for jets measured in the calorimeter is assumed to only be a function of the relative energy difference between the two objects and all angles are assumed to be well measured:

$$W_{jet}(\vec{x}_{jet}, \vec{y}_{parton}) = W(E_{jet} - E_{parton}) \times \delta(\Omega_{jet} - \Omega_{parton}) \quad (\text{A.27})$$

where $W(E_{jet} - E_{parton})$ is parametrized using the following functional form:

$$W(E_{jet} - E_{parton}) = \frac{e^{-\frac{(E_{jet} - E_{parton} - p_1)^2}{2p_2^2}} + p_3 e^{-\frac{(E_{jet} - E_{parton} - p_4)^2}{2p_2^5}}}{2\pi(p_2 + p_3 p_5)} \quad (\text{A.28})$$

where $p_i = \alpha_i + \beta_i \times E_{parton}$. The five α and five β parameters are determined by minimizing a likelihood formed by measuring the parton energy in Monte Carlo and the matched jet energy also in Monte Carlo. The parameters used for this analysis were determined in several regions of the calorimeter to account for the resolution differences in the detector.

Electrons

The transfer function for electrons is assumed to be solely a function of the reconstructed energy of the electron, E_{reco} , the parton energy of the electron, E_{parton} , and θ , the production angle with respect to the beam axis:

$$W_{electron}(\vec{x}_{reco}, \vec{y}_{parton}) = W(E_{reco}, E_{parton}, \theta) \times \delta(\Omega_{reco} - \Omega_{parton}) \quad (\text{A.29})$$

where $W(E_{reco}, E_{parton}, \theta)$ is parametrized using the following functional form:

$$W(E_{reco}, E_{parton}, \theta) = \frac{1}{2\pi\sigma} \exp\left[-\frac{(E_{reco} - E_{center})^2}{2\sigma^2}\right] \quad (\text{A.30})$$

$$E_{center} = 1.0002E_{parton} + 0.324 \text{ GeV}/c^2 \quad (\text{A.31})$$

$$\sigma = 0.028E_{center} \oplus \text{Sampling}(E_{center}, \eta)E_{center} \oplus 0.4 \quad (\text{A.32})$$

$$\text{Sampling}(E, \theta) = \left[\frac{0.164}{\sqrt{E}} + \frac{0.122}{E} \right] \exp\left[\frac{\text{p1}(E)}{\sin\theta} - \text{p1}(E) \right] \quad (\text{A.33})$$

$$\text{p1}(E) = 1.35193 - \frac{2.09564}{E} - \frac{6.98578}{E^2}. \quad (\text{A.34})$$

Muons

The transfer function for muons is assumed to be a function of

$$\Delta\left(\frac{q}{p_t}\right) = \left(\frac{q}{p_t}\right)_{reco} - \left(\frac{q}{p_t}\right)_{parton} \quad (\text{A.35})$$

and of η_{CFT} ,

$$W_{muon}(\vec{x}_{reco}, \vec{y}_{parton}) = W\left(\Delta\left(\frac{q}{p_t}\right), \eta_{\text{CFT}}\right) \times \delta(\Omega_{reco} - \Omega_{parton}) \quad (\text{A.36})$$

where $W\left(\Delta\left(\frac{q}{p_t}\right), \eta_{\text{CFT}}\right)$ is parametrized using a single Gaussian:

$$W\left(\Delta\left(\frac{q}{p_t}\right), \eta_{\text{CFT}}\right) = \frac{1}{2\pi\sigma} \exp\left\{-\frac{\left[\Delta\left(\frac{q}{p_t}\right)\right]^2}{2\sigma^2}\right\} \quad (\text{A.37})$$

$$\sigma = \begin{cases} \sigma_o & : |\eta_{\text{CFT}}| \leq \eta_o \\ \sqrt{\sigma_o^2 + [c(|\eta_{\text{CFT}}| - \eta_o)]^2} & : |\eta_{\text{CFT}}| > \eta_o \end{cases} \quad (\text{A.38})$$

There are three fitted parameters in the above equations: σ_o , c , and η_o , each of which is actually fitted by two sub-parameters:

$$par = par(0) + par(1) \cdot 1/p_t. \quad (\text{A.39})$$

Furthermore, these parameters are derived for four classes of events: those that were from before or after the 2004 shutdown, when the magnetic field strength changed, and in each run range, those that have an SMT hit and those that do not.

As a simplification, we assume $q_{reco} = q_{parton}$, that is, we do not consider charge misidentification

A.1.5 Full Differential Cross Section and Normalization

The full differential cross section at the detector object level can now be written as

$$\begin{aligned} \frac{\partial \sigma'(\vec{x})}{\partial \vec{x}} &= \int dp_{tot}^z dq_1 dq_2 dp_\ell \sum_{i,j} f_i(q_1, Q^2) \times f_j(q_2, Q^2) \\ &\times \frac{1}{256(2\pi)^8 E_{beam}^3} \frac{|\mathcal{M}|^2}{2x_1 x_2} \times \frac{p_1^2}{E_1} \frac{p_2^2}{E_2} \frac{p_\ell^2}{E_\ell} \frac{1}{E_\nu} \times W_{Lepton} W_{Jet1} W_{Jet2} \end{aligned} \quad (\text{A.40})$$

The final step to evaluating the probability density is to properly normalize the differential cross section in Eq. A.40. This is done by integration of the differential cross section over all possible states in the detector. Since the event selection cuts will change the number events due to acceptance losses, this must be accounted for in the overall normalization (cross section) calculation. The total cross section is then written as

$$\begin{aligned} \sigma &= \int \frac{\partial \sigma'(\vec{x})}{\partial \vec{x}} d\vec{x} = \int d\vec{x} dp_{tot}^z dq_1 dq_2 dp_\ell \sum_{i,j} f_i(q_1, Q^2) \times f_j(q_2, Q^2) \\ &\times \frac{1}{256(2\pi)^8 E_{beam}^3} \frac{|\mathcal{M}|^2}{2x_1 x_2} \times \frac{p_1^2}{E_1} \frac{p_2^2}{E_2} \frac{p_\ell^2}{E_\ell} \frac{1}{E_\nu} \times W_{Lepton} W_{Jet1} W_{Jet2} \times \Theta_{Cuts}(\vec{x}) \end{aligned} \quad (\text{A.41})$$

A.2 Integration Variable Remapping

A.2.1 Introduction

This section will layout the jacobian needed for the 10 \rightarrow 10 remapping of variables for the parton level cross section. The base variables used are shown below.

- p_3 : Absolute momentum of the lepton
- p_5 : Absolute momentum of the first quark
- p_6 : Absolute momentum of the second quark
- p_{tot}^z : Total p_z of the system
- $\cos(\theta_3)$: Cosine(θ) of the lepton
- ϕ_3 : ϕ of the lepton

- $\cos(\theta_5)$: Cosine(θ) of the first quark
- ϕ_5 : ϕ of the first quark
- $\cos(\theta_6)$: Cosine(θ) of the second quark
- ϕ_6 : ϕ of the second quark

Other variables that are useful for the integration are

- m_{34} : Mass of the lepton and neutrino (W mass)
- m_{345} : Mass of the lepton, neutrino, and first quark (top mass)
- m_{56} : Mass of the first and second quark ($b\bar{b}$ mass)

Since some of these variables are sharp peaks (W and top masses), it is much better to sample from the expected distribution rather than make requirements of the invariant masses. The W and top masses are expected to follow a Breit-Wigner distribution shown below.

$$\sigma(M_{34}) = \frac{1}{\pi} \left[\frac{\gamma}{(M_{34} - M_W)^2 + \gamma^2} \right] \quad (\text{A.42})$$

where M_{34} is the mass of the lepton and neutrino. Similarly, the top mass has the following expected distribution.

$$\sigma(M_{345}) = \frac{1}{\pi} \left[\frac{\gamma}{(M_{345} - M_{top})^2 + \Gamma^2} \right] \quad (\text{A.43})$$

where M_{345} is the mass of the lepton, neutrino, and first quark.

A.2.2 Sampling from a Breit-Wigner mass distribution

Sampling from a Breit-Wigner distribution is done by selecting a random point between 0 and 1 from the cumulative distribution function of the BW function. The cumulative distribution function, or cdf, for the Breit-Wigner distribution is shown below.

$$\int \sigma(m; m_0; \Gamma) = F(m; m_0, \Gamma) = \frac{1}{\pi} \tan^{-1} \left[\frac{m - m_0}{\Gamma} \right] + \frac{1}{2} \quad (\text{A.44})$$

The value of F is taken as a random number between 0 and 1. After selecting a value of F, the next step is to solve for m. As a function of F, defined as u for the following, the mass is

$$m = m_0 + \Gamma \tan \left[\pi \left(u - \frac{1}{2} \right) \right] \quad (\text{A.45})$$

A.2.3 Sampling from a Breit-Wigner S_{cm} distribution

In the previous example, a distribution was sampled using a random number uniformly distributed from 0 to 1. In, this example, a new random number is used that is uniformly samples from 0 to 1, but the maximum and minimum values of the variable are taken into account in the Jacobian.

The distribution of the variable S_{cm} is the following

$$s = m_0^2 + m_0 \Gamma \tan [m_0 \Gamma r] \quad (\text{A.46})$$

where r is defined in terms of the random variable, u, that is uniformly distributed between 0 and 1.

$$r = (r_{max} - r_{min}) \times u + r_{min} \quad (\text{A.47})$$

where r_{max} and r_{min} are defined in terms of the variable s_{cm} .

$$r = \frac{1}{m_0 \Gamma} \tan \left[\frac{s - m_0^2}{m_0 \Gamma} \right] \quad (\text{A.48})$$

$$r_{min} = \frac{1}{m_0 \Gamma} \tan \left[\frac{s_{min} - m_0^2}{m_0 \Gamma} \right] \quad (\text{A.49})$$

$$r_{max} = \frac{1}{m_0 \Gamma} \tan \left[\frac{s_{max} - m_0^2}{m_0 \Gamma} \right] \quad (\text{A.50})$$

A.2.4 *Jacobian for random sampling of a Breit-Wigner distribution around the W mass squared, s_{34}*

The first case to consider is the Breit-Wigner sampling around the W mass S_{34} distribution and replace the integration variable, p_3 or the lepton momentum.

$$|J(p_3, u)| = \left| \frac{\partial p_3}{\partial u} \right| \quad (\text{A.51})$$

Because u is redined in terms of the variable r , we can rewrite A.51 in terms of r instead of u .

$$|J(p_3, u)| = \left| \frac{\partial p_3}{\partial u} \right| = \left| \frac{\partial p_3}{\partial r} \times \frac{\partial r}{\partial u} \right| \quad (\text{A.52})$$

And since the variable r is sampling the S_{34} distribution it makes sense to define the Jacobian in terms of this variable instead of p_3 .

$$|J(p_3, u)| = \left| \frac{\partial p_3}{\partial r} \times \frac{\partial r}{\partial u} \right| = \left| \frac{\partial p_3}{\partial s_{34}} \times \frac{\partial s_{34}}{\partial r} \times \frac{\partial r}{\partial u} \right| = \left| \frac{\frac{\partial s_{34}}{\partial r} \times \frac{\partial r}{\partial u}}{\frac{\partial s_{34}}{\partial p_3}} \right| \quad (\text{A.53})$$

Equation A.53 has three components: $\frac{\partial s_{34}}{\partial r}$, $\frac{\partial r}{\partial u}$, and $\frac{\partial s_{34}}{\partial p_3}$. From equation A.47, the partial derivative of r with respect to u is

$$\frac{\partial r}{\partial u} = r_{max} - r_{min} = \Delta r \quad (\text{A.54})$$

Next, the partial of s_{34} with respect to r can be determined from equation A.46.

$$\frac{\partial s_{34}}{\partial r} = (m_W \Gamma_W)^2 \sec^2 [m_W \Gamma_W r] \quad (\text{A.55})$$

Inserting the value of $r(s)$ as defined in equation A.48, equation A.55 can be re-written as

$$\frac{\partial s_{34}}{\partial r} = (m_W \Gamma_W)^2 \sec^2 [m_W \Gamma_W r] = (m_W \Gamma_W)^2 \sec^2 \left[\arctan \left[\frac{s_{34} - m_W^2}{m_W \Gamma_W} \right] \right] \quad (\text{A.56})$$

Equation A.56 is solved by defining a right triangle where

$$\begin{aligned}\tan(\theta) &= \frac{s_{34} - m_W^2}{m_W \Gamma_W} \\ \cos(\theta) &= \frac{1}{\sqrt{1 + \left[\frac{s_{34} - m_W^2}{m_W \Gamma_W} \right]^2}}\end{aligned}\quad (\text{A.57})$$

Using these definitions, equation A.56 is finally defined as

$$\frac{\partial s_{34}}{\partial r} = (m_W \Gamma_W)^2 \sec^2 \left[\arctan \left[\frac{s_{34} - m_W^2}{m_W \Gamma_W} \right] \right] = (m_W \Gamma_W)^2 + (s_{34} - m_W^2)^2 \quad (\text{A.58})$$

Finally, we need the partial derivative of s_{34} with respect to p_3 . First, we define s_{34}

$$s_{34} = m_3^2 + m_4^2 + 2E_3 E_4 - 2p_3^x p_4^x - 2p_3^y p_4^y - 2p_3^z p_4^z \quad (\text{A.59})$$

Since the neutino four-vector is defined in terms of all the other particles in the event, we need to rewrite equation A.59 to expose all the dependences on p_3 . For the following, it is assumed that the lepton and neutrino are massless meaning $E_3 = p_3$.

$$\begin{aligned}s_{34} &= 2p_3 \sqrt{(-p_3^x - p_5^x - p_6^x)^2 + (-p_3^y - p_5^y - p_6^y)^2 + (p_{tot}^z - p_3^z - p_5^z - p_6^z)^2} \\ &\quad - 2p_3^x (-p_3^x - p_5^x - p_6^x) - 2p_3^y (-p_3^y - p_5^y - p_6^y) - 2p_3^z (p_{tot}^z - p_3^z - p_5^z - p_6^z)\end{aligned}\quad (\text{A.60})$$

After combining like terms, we can evaluate the partial derivative of s_{34} with respect to p_3 that yields the relatively simple formula

$$\frac{\partial s_{34}}{\partial p_3} = 2(p_3 + p_4)(1 - \hat{p}_3 \cdot \hat{p}_4) \quad (\text{A.61})$$

Finally, we can rewrite the Jacobian defined in A.53 as

$$|J(p_3, u)| = \left| \frac{\frac{\partial s_{34}}{\partial r} \times \frac{\partial r}{\partial u}}{\frac{\partial s_{34}}{\partial p_3}} \right| = \frac{\Delta R \times [(m_W \Gamma_W)^2 + (s_{34} - m_W^2)^2]}{2(p_3 + p_4)(1 - \hat{p}_3 \cdot \hat{p}_4)} \quad (\text{A.62})$$

In some cases, it is also common to replace the first quark momentum integration with the Breit-Wigner sampling variable. In that case, we need to evaluate

$$|J(p_5, u)| = \left| \frac{\frac{\partial s_{34}}{\partial r} \times \frac{\partial r}{\partial u}}{\frac{\partial s_{34}}{\partial p_5}} \right| \quad (\text{A.63})$$

For this substitution, we only need to evaluate the partial derivative of s_{34} with respect to p_5 . Assuming a massless quark, the result is

$$\frac{\partial s_{34}}{\partial p_5} = 2p_3(\hat{p}_3 \cdot \hat{p}_5 - \hat{p}_4 \cdot \hat{p}_5) \quad (\text{A.64})$$

Combining equation A.64 with A.63 yields

$$|J(p_5, u)| = \left| \frac{\frac{\partial s_{34}}{\partial r} \times \frac{\partial r}{\partial u}}{\frac{\partial s_{34}}{\partial p_5}} \right| = \frac{\Delta R \times [(m_W \Gamma_W)^2 + (s_{34} - m_W^2)^2]}{2p_3(\hat{p}_3 \cdot \hat{p}_5 - \hat{p}_4 \cdot \hat{p}_5)} \quad (\text{A.65})$$

A.2.5 Jacobian for random sampling of a Breit-Wigner distribution around the top mass squared, s_{345}

The next case to consider is the Breit-Wigner sampling around the top mass squared S_{345} distribution and replace the integration variable, p_3 or the lepton momentum. As before, we need need to calculate the following

$$|J(p_3, u)| = \left| \frac{\partial p_3}{\partial r} \times \frac{\partial r}{\partial u} \right| = \left| \frac{\partial p_3}{\partial s_{345}} \times \frac{\partial s_{345}}{\partial r} \times \frac{\partial r}{\partial u} \right| = \left| \frac{\frac{\partial s_{345}}{\partial r} \times \frac{\partial r}{\partial u}}{\frac{\partial s_{345}}{\partial p_3}} \right| \quad (\text{A.66})$$

Equation A.66 has three components: $\frac{\partial s_{345}}{\partial r}$, $\frac{\partial r}{\partial u}$, and $\frac{\partial s_{345}}{\partial p_3}$. We know $\frac{\partial r}{\partial u}$ from equation A.54 where r_{min} and r_{max} are defined by the s_{345} system instead of the s_{34} system. We also know $\frac{\partial s_{345}}{\partial r}$ from A.58 where we replace s_{34} with s_{345} .

$$\frac{\partial s_{345}}{\partial r} = (m_t \Gamma_t)^2 + (s_{345} - m_t^2)^2 \quad (\text{A.67})$$

We do need the partial derivative of s_{345} with respect to p_3 . First, we define s_{345}

$$s_{345} = m_3^2 + m_4^2 + m_5^2 + 2E_3E_4 + 2E_3E_5 + 2E_4E_5 - 2p_3^x p_4^x - 2p_3^x p_5^x - 2p_4^x p_5^x - 2p_3^y p_4^y - 2p_3^y p_5^y - 2p_4^y p_5^y - 2p_3^z p_4^z - 2p_3^z p_5^z - 2p_4^z p_5^z \quad (\text{A.68})$$

As before, the neutrino four-vector is defined in terms of all the other particles in the event so we need to rewrite equation A.68 to expose all the dependences on p_3 . For the following, it is assumed that the lepton, neutrino, and quark are massless meaning $E_3 = p_3$.

$$\begin{aligned}
s_{345} = & 2p_3 \sqrt{(-p_3^x - p_5^x - p_6^x)^2 + (-p_3^y - p_5^y - p_6^y)^2 + (p_{tot}^z - p_3^z - p_5^z - p_6^z)^2} + \\
& 2p_3 p_5 + 2 \sqrt{(-p_3^x - p_5^x - p_6^x)^2 + (-p_3^y - p_5^y - p_6^y)^2 + (p_{tot}^z - p_3^z - p_5^z - p_6^z)^2} p_5 - \\
& 2p_3^x (-p_3^x - p_5^x - p_6^x) - 2p_3^x p_5^x - 2(-p_3^x - p_5^x - p_6^x) p_5^x - \\
& 2p_3^y (-p_3^y - p_5^y - p_6^y) - 2p_3^y p_5^y - 2(-p_3^y - p_5^y - p_6^y) p_5^y - \\
& 2p_3^z (-p_3^z - p_5^z - p_6^z) - 2p_3^z p_5^z - 2(-p_3^z - p_5^z - p_6^z) p_5^z \quad (\text{A.69})
\end{aligned}$$

After combining like terms, we can evaluate the partial derivative of s_{345} with respect to p_3 as

$$\frac{\partial s_{345}}{\partial p_3} = 2(p_3 + p_4 + p_5)(1 - \hat{p}_3 \cdot \hat{p}_4) \quad (\text{A.70})$$

Finally, we can rewrite the Jacobian defined in A.66 as

$$|J(p_3, u)| = \left| \frac{\frac{\partial s_{345}}{\partial r} \times \frac{\partial r}{\partial u}}{\frac{\partial s_{345}}{\partial p_3}} \right| = \frac{\Delta R \times [(m_t \Gamma_t)^2 + (s_{345} - m_t^2)^2]}{2(p_3 + p_4 + p_5)(1 - \hat{p}_3 \cdot \hat{p}_4)} \quad (\text{A.71})$$

Instead of replacing the lepton momentum integration variable, it is also common to replace the first quark momentum integration variable, p_5 . In that case, we need to evaluate the following Jacobian.

$$|J(p_5, u)| = \left| \frac{\partial p_5}{\partial r} \times \frac{\partial r}{\partial u} \right| = \left| \frac{\partial p_5}{\partial s_{345}} \times \frac{\partial s_{345}}{\partial r} \times \frac{\partial r}{\partial u} \right| = \left| \frac{\frac{\partial s_{345}}{\partial r} \times \frac{\partial r}{\partial u}}{\frac{\partial s_{345}}{\partial p_5}} \right| \quad (\text{A.72})$$

The only difference is that partial derivative of s_{345} with respect to p_5 instead of p_3 . However, since s_{345} is invariant under a change of p_3 and p_5 the partial derivatives must be equal. Thus,

$$|J(p_5, u)| = \left| \frac{\frac{\partial s_{345}}{\partial r} \times \frac{\partial r}{\partial u}}{\frac{\partial s_{345}}{\partial p_5}} \right| = \frac{\Delta R \times [(m_t \Gamma_t)^2 + (s_{345} - m_t^2)^2]}{2(p_3 + p_4 + p_5)(1 - \hat{p}_4 \cdot \hat{p}_5)} \quad (\text{A.73})$$

A.2.6 *Jacobian for random sampling of two Breit-Wigner distributions around the top mass squared, s_{345} and W mass squared, s_{34}*

The next situation is to sample from a Breit-Wigner around the top mass squared and the W mass squared, or s_{345} and s_{34} . It is common to replace the lepton momentum and first quark momentum integration variables with the two new variables. Since we are replacing two variables, we need to evaluate the following Jacobian

$$|J(p_3, p_5; u_1, u_2)| = \begin{vmatrix} \frac{\partial p_3}{\partial u_1} & \frac{\partial p_3}{\partial u_2} \\ \frac{\partial p_5}{\partial u_1} & \frac{\partial p_5}{\partial u_2} \end{vmatrix} \quad (\text{A.74})$$

where u_1 and u_2 are the sampling variables around the top mass squared and W mass squared, respectively.

We have already computed the partial derivatives for each of these cases in the previous two sections, thus the result is

$$|J(p_3, p_5; u_1, u_2)| = \begin{vmatrix} \frac{\partial p_3}{\partial u_1} & \frac{\partial p_3}{\partial u_2} \\ \frac{\partial p_5}{\partial u_1} & \frac{\partial p_5}{\partial u_2} \end{vmatrix} = \begin{vmatrix} \frac{\frac{\partial s_{345}}{\partial r} \times \frac{\partial r}{\partial u}}{\frac{\partial s_{345}}{\partial p_3}} & \frac{\frac{\partial s_{345}}{\partial r} \times \frac{\partial r}{\partial u}}{\frac{\partial s_{345}}{\partial p_5}} \\ \frac{\frac{\partial s_{34}}{\partial r} \times \frac{\partial r}{\partial u}}{\frac{\partial s_{34}}{\partial p_3}} & \frac{\frac{\partial s_{34}}{\partial r} \times \frac{\partial r}{\partial u}}{\frac{\partial s_{34}}{\partial p_5}} \end{vmatrix} = \begin{vmatrix} \frac{\Delta R_{345} \times [(m_t \Gamma_t)^2 + (s_{345} - m_t^2)^2]}{2(p_3 + p_4 + p_5)(1 - \hat{p}_3 \cdot \hat{p}_4)} & \frac{\Delta R_{34} \times [(m_W \Gamma_W)^2 + (s_{34} - m_W^2)^2]}{2(p_3 + p_4)(1 - \hat{p}_3 \cdot \hat{p}_4)} \\ \frac{\Delta R_{345} \times [(m_t \Gamma_t)^2 + (s_{345} - m_t^2)^2]}{2(p_3 + p_4 + p_5)(1 - \hat{p}_4 \cdot \hat{p}_5)} & \frac{\Delta R_{34} \times [(m_W \Gamma_W)^2 + (s_{34} - m_0^2)^2]}{2p_3(\hat{p}_3 \cdot \hat{p}_5 - \hat{p}_4 \cdot \hat{p}_5)} \end{vmatrix} \quad (\text{A.75})$$

A.2.7 *Sampling from a Polynomial S_{cm} distribution*

*** This is where I am taking a function from Aurelio and I can't seem to derive it on my own ***

The distribution of the variable S_{cm} according to a polynomial power distribution is

$$s = m_0^2 + [(1 - \alpha)r]^{\frac{-1}{\alpha-1}} \quad (\text{A.76})$$

where r is defined in terms of the random variable, u, that is uniformly distributed between 0 and 1.

$$r = (r_{max} - r_{min}) \times u + r_{min} \quad (\text{A.77})$$

where r_{max} and r_{min} are defined in terms of the variable s_{cm} .

$$r = \frac{1}{1-\alpha} \times [s - m_0^2]^{1-\alpha} \quad (\text{A.78})$$

$$r_{min} = \frac{1}{1-\alpha} \times [s_{min} - m_0^2]^{1-\alpha} \quad (\text{A.79})$$

$$r_{max} = \frac{1}{1-\alpha} \times [s_{max} - m_0^2]^{1-\alpha} \quad (\text{A.80})$$

where alpha can not equal 1.

A.2.8 Jacobian for random sampling of a polynomial distribution starting at m_{pole}

The first case to consider is sampling around a falling polynomial distribution for the mass squared of two quarks in the event, s_{56} . We need to define the Jacobian with respect p_5 or p_6 . Since s_{56} is invariant under an interchange of particle 5 and 6, the Jacobian will be the same for each momentum integration. The following assume p_5 will be replaced with the variable, u , which is sampled from a polynomial distribution.

$$|J(p_5, u)| = \left| \frac{\partial p_5}{\partial u} \right| \quad (\text{A.81})$$

Because u is defined in terms of the variable r , we can rewrite A.81 in terms of r instead of u .

$$|J(p_5, u)| = \left| \frac{\partial p_5}{\partial u} \right| = \left| \frac{\partial p_5}{\partial r} \times \frac{\partial r}{\partial u} \right| \quad (\text{A.82})$$

And since the variable r is sampling the S_{56} distribution it makes sense to define the Jacobian in terms of this variable instead of p_5 .

$$|J(p_5, u)| = \left| \frac{\partial p_5}{\partial r} \times \frac{\partial r}{\partial u} \right| = \left| \frac{\partial p_5}{\partial s_{56}} \times \frac{\partial s_{56}}{\partial r} \times \frac{\partial r}{\partial u} \right| = \left| \frac{\frac{\partial s_{56}}{\partial r} \times \frac{\partial r}{\partial u}}{\frac{\partial s_{56}}{\partial p_5}} \right| \quad (\text{A.83})$$

Equation A.83 has three components: $\frac{\partial s_{56}}{\partial r}$, $\frac{\partial r}{\partial u}$, and $\frac{\partial s_{56}}{\partial p_5}$. From equation A.77, the partial derivative of r with respect to u is

$$\frac{\partial r}{\partial u} = r_{max} - r_{min} = \Delta R_{56} \quad (\text{A.84})$$

Next, the partial of s_{56} with respect to r can be determined from equation A.76.

$$\frac{\partial s_{56}}{\partial r} = [r(1 - \alpha)]^{\frac{\alpha}{1-\alpha}} \quad (\text{A.85})$$

Inserting the value of $r(s)$ as defined in equation A.78, equation A.85 can be re-written as

$$\frac{\partial s_{56}}{\partial r} = [s_{56} - m_0^2]^\alpha \quad (\text{A.86})$$

Finally, we need the partial derivative of s_{56} with respect to p_5 . First, we define s_{56}

$$s_{56} = m_5^2 + m_6^2 + 2E_5E_6 - 2p_5^x p_6^x - 2p_5^y p_6^y - 2p_5^z p_6^z \quad (\text{A.87})$$

we can evaluate the partial derivative of s_{56} with respect to p_5 .

$$\frac{\partial s_{56}}{\partial p_5} = 2p_6(1 - \hat{p}_5 \cdot \hat{p}_6) \quad (\text{A.88})$$

Finally, we can rewrite the Jacobian defined in A.83 as

$$|J(p_5, u)| = \left| \frac{\frac{\partial s_{56}}{\partial r} \times \frac{\partial r}{\partial u}}{\frac{\partial s_{56}}{\partial p_5}} \right| = \frac{\Delta R_{56} \times [s_{56} - m_0^2]^\alpha}{2p_6(1 - \hat{p}_5 \cdot \hat{p}_6)} \quad (\text{A.89})$$

and

$$|J(p_6, u)| = \left| \frac{\frac{\partial s_{56}}{\partial r} \times \frac{\partial r}{\partial u}}{\frac{\partial s_{56}}{\partial p_6}} \right| = \frac{\Delta R_{56} \times [s_{56} - m_0^2]^\alpha}{2p_5(1 - \hat{p}_5 \cdot \hat{p}_6)} \quad (\text{A.90})$$

Appendix B

DISCRIMINANT OUTPUT PLOTS

MATRIX ELEMENT OUTPUTS FOR THE ELECTRON CHANNEL WITH TWO
JETS AND ONE B-TAG

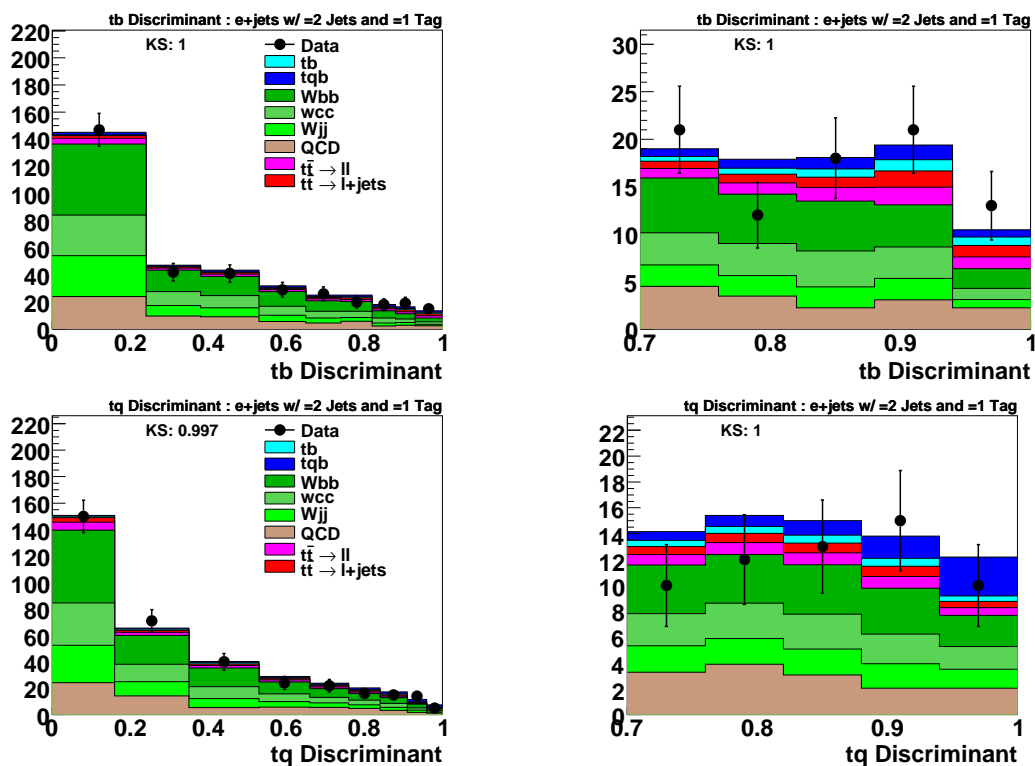


Figure B.1: Discriminant plots for the electron channel with one b tag and two jets. Upper row: tb discriminant, lower row: tq discriminant. Left column, full discriminant range, right column, close-up of the high end of the distribution.

MATRIX ELEMENT OUTPUTS FOR THE ELECTRON CHANNEL WITH TWO
JETS AND TWO B-TAGS

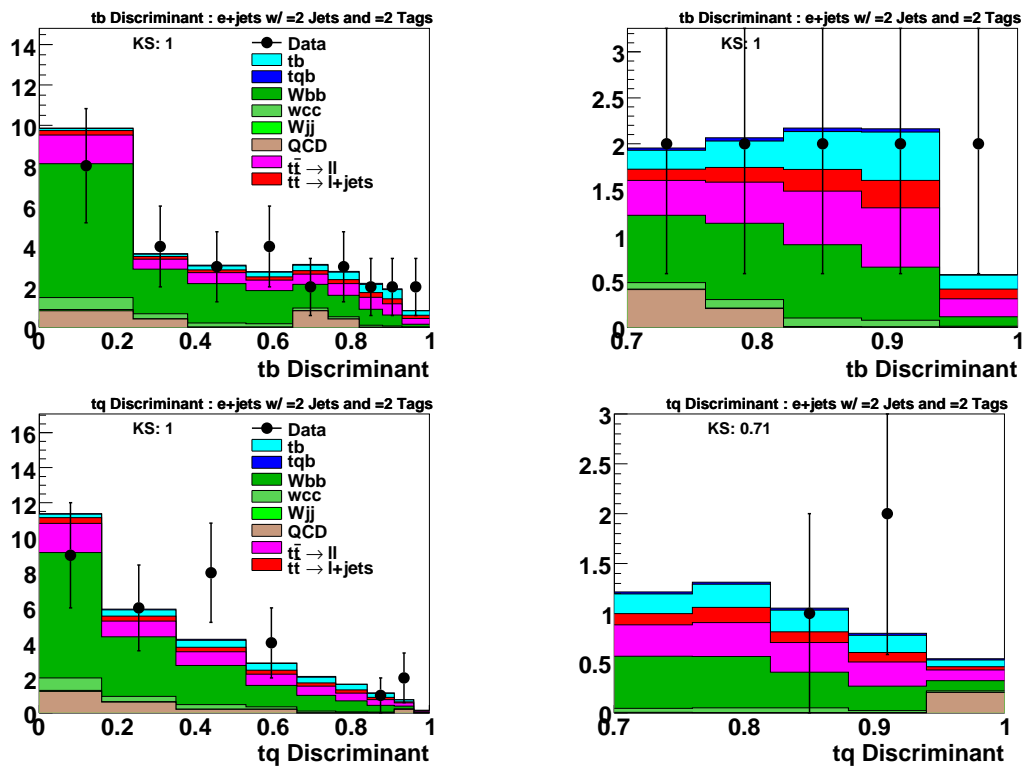


Figure B.2: Discriminant plots for the electron channel with two b tags and two jets. Upper row: tb discriminant, lower row: tq discriminant. Left column, full discriminant range, right column, close-up of the high end of the distribution.

MATRIX ELEMENT OUTPUTS FOR THE MUON CHANNEL WITH TWO JETS
AND ONE B-TAG

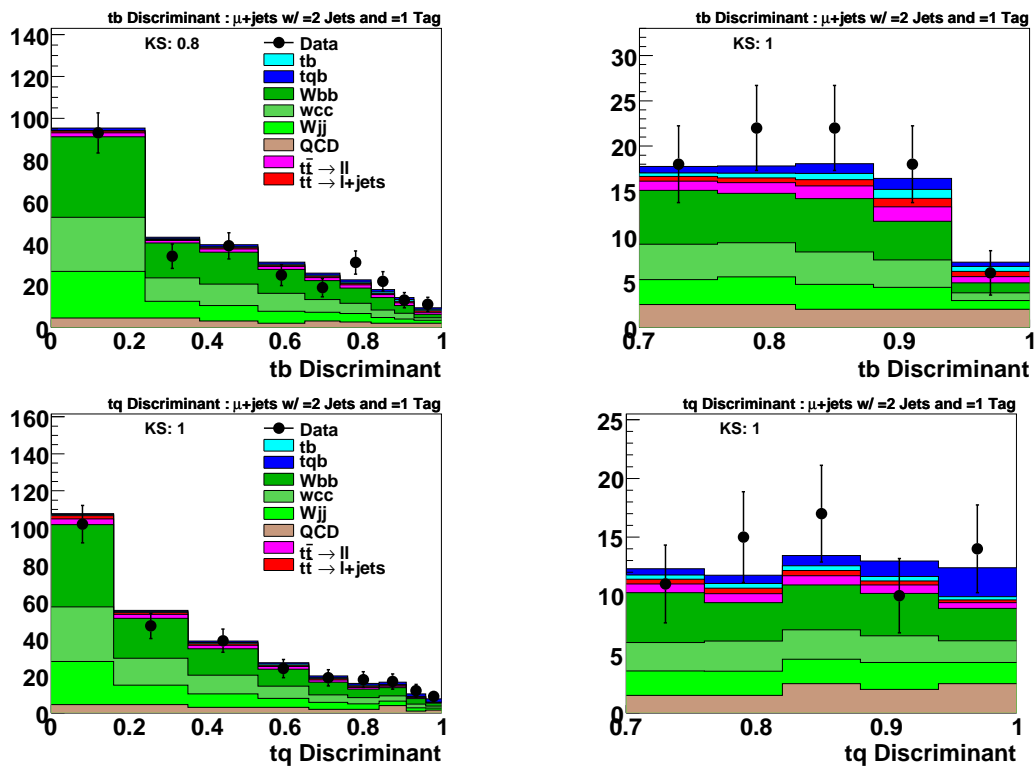


Figure B.3: Discriminant plots for the muon channel with one b tag and two jets. Upper row: tb discriminant, lower row: tq discriminant. Left column, full discriminant range, right column, close-up of the high end of the distribution.

MATRIX ELEMENT OUTPUTS FOR THE MUON CHANNEL WITH TWO JETS
AND TWO B-TAGS

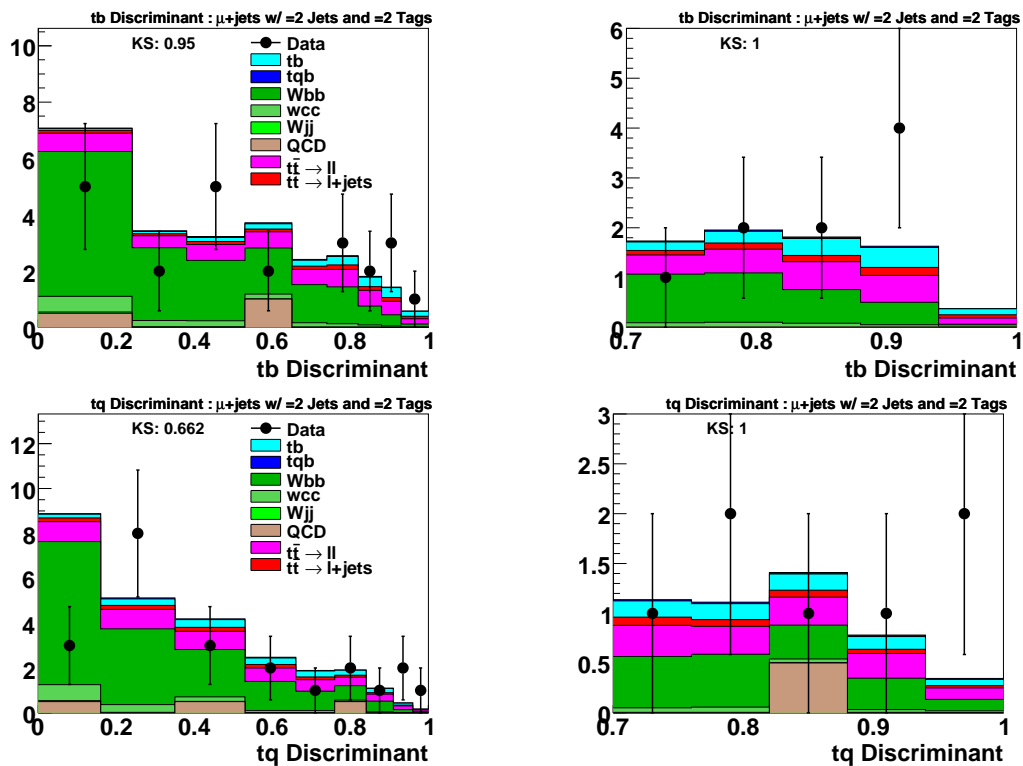


Figure B.4: Discriminant plots for the muon channel with two b tags and two jets. Upper row: tb discriminant, lower row: tq discriminant. Left column, full discriminant range, right column, close-up of the high end of the distribution.

MATRIX ELEMENT OUTPUTS FOR THE ELECTRON CHANNEL WITH THREE
JETS AND ONE B-TAG

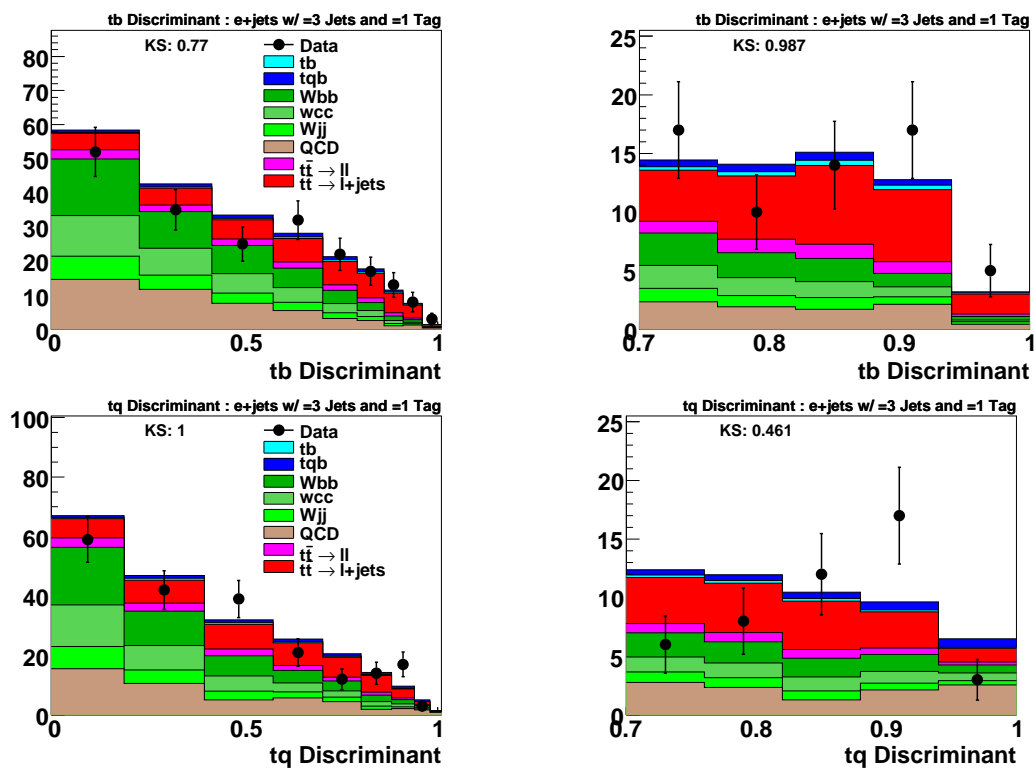


Figure B.5: Discriminant plots for the electron channel with one b tag and three jets. Upper row: tb discriminant, lower row: tq discriminant. Left column, full discriminant range, right column, close-up of the high end of the distribution.

MATRIX ELEMENT OUTPUTS FOR THE ELECTRON CHANNEL WITH THREE
JETS AND TWO B-TAGS

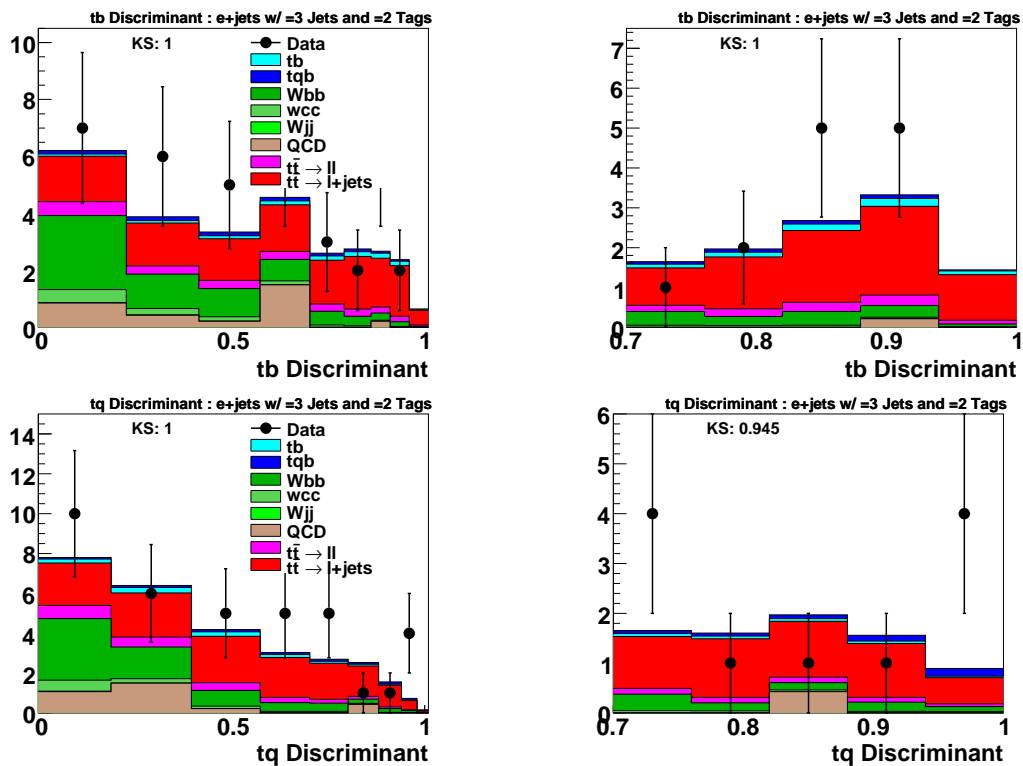


Figure B.6: Discriminant plots for the electron channel with two b tags and three jets. Upper row: tb discriminant, lower row: tq discriminant. Left column, full discriminant range, right column, close-up of the high end of the distribution.

MATRIX ELEMENT OUTPUTS FOR THE MUON CHANNEL WITH THREE JETS
AND ONE B-TAG

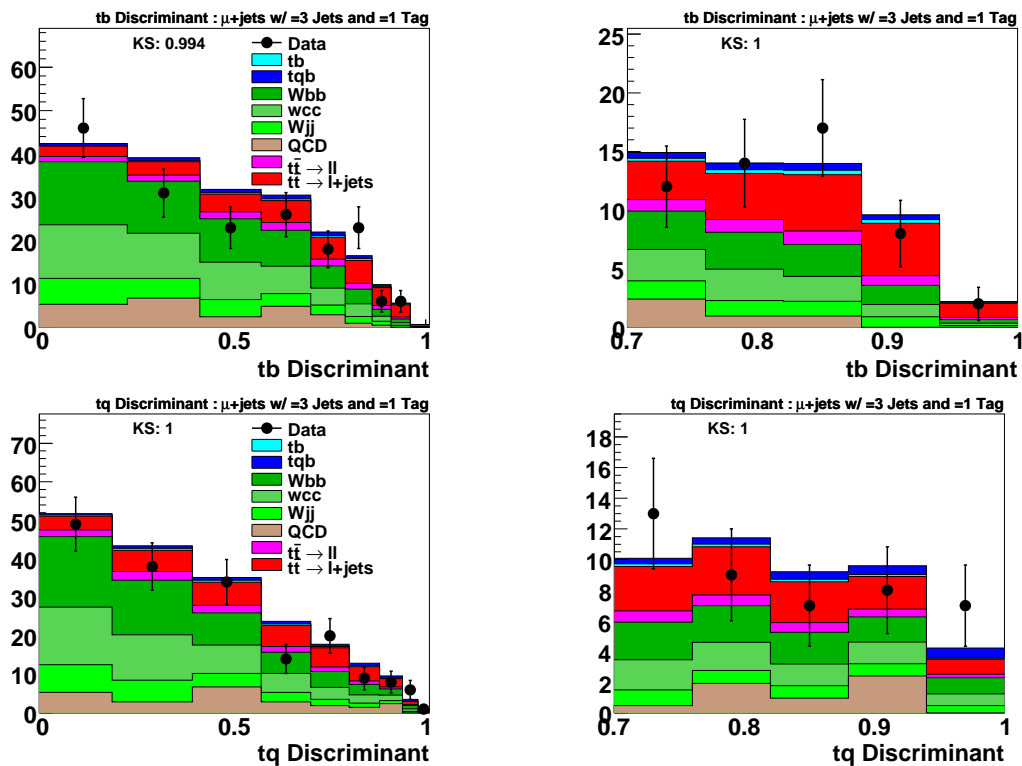


Figure B.7: Discriminant plots for the muon channel with one b tag and three jets. Upper row: tb discriminant, lower row: tq discriminant. Left column, full discriminant range, right column, close-up of the high end of the distribution.

MATRIX ELEMENT OUTPUTS FOR THE MUON CHANNEL WITH THREE JETS
AND TWO B-TAGS

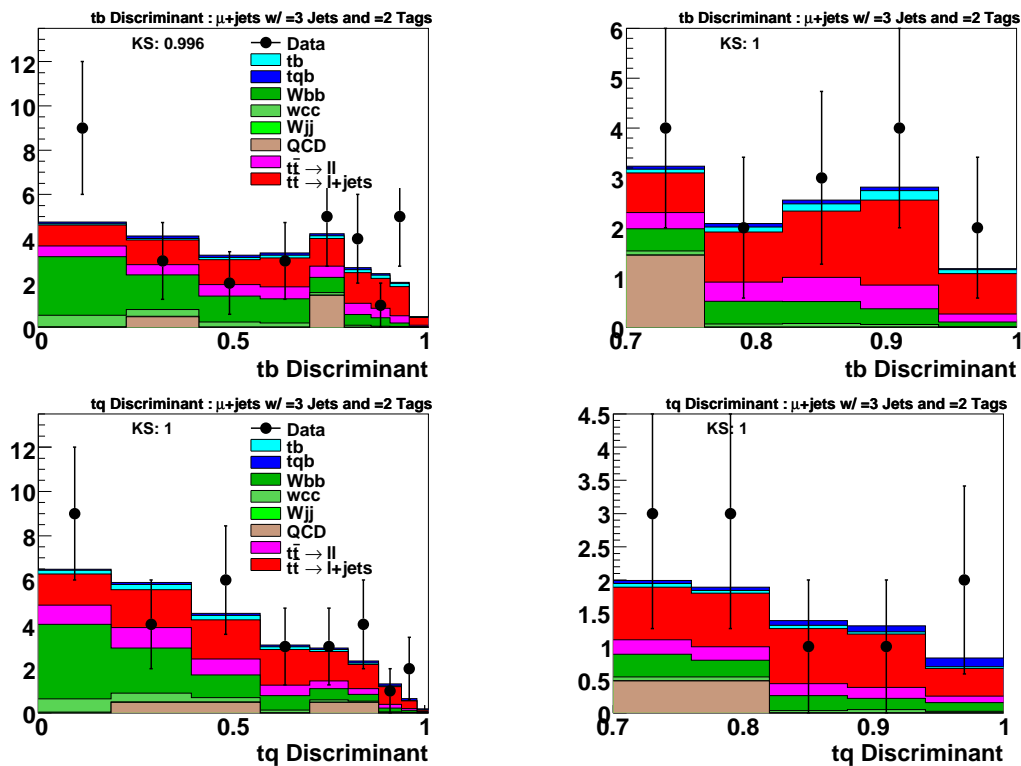


Figure B.8: Discriminant plots for the muon channel with two b tags and three jets. Upper row: tb discriminant, lower row: tq discriminant. Left column, full discriminant range, right column, close-up of the high end of the distribution.

Appendix C

LUMINOSITY CALCULATION

The probability of n interactions per bunch crossing is (because a collision is a random process, the distribution will follow Poisson statistics.

$$P = \frac{\mu^N}{N!} \times e^{-\mu} \quad (\text{C.1})$$

The probability of at least one bunch crossing is

$$P = 1 - e^{-\mu} \quad (\text{C.2})$$

The average number of bunch crossings, μ , is defined as

$$\mu = \frac{\mathcal{L} \times \sigma_{\text{eff}}}{f_{\text{beam}}} \quad (\text{C.3})$$

Thus, the luminosity can be written as

$$\mathcal{L} = -\frac{f_{\text{beam}}}{\sigma_{\text{eff}}} \ln(1 - P(n > 0)) \quad (\text{C.4})$$

By recording the number of bunch crossings without an inelastic collision, the luminosity can be calculated.

Appendix D

ENSEMBLE GENERATION TECHNIQUE

We can generate multiple pseudo-datasets containing only background events and run them through the analysis exactly as if they were the real data events, and obtain a cross section from each one of them. The p-value can then be calculated as the number of these ensembles that yield a result equal to the observed or higher, divided by the total number of ensembles.

To generate these ensembles, we use background events from our model and treat the fluctuations of each background source separately. We draw random events from each background source separately, as indicated by the allowed variation due to systematic and statistical uncertainties. The event weights are taken into account such that events with a higher weight will be more likely to be picked. The variance of the background events is large: we start from 1.34M electron events and 1.28M muon events, then only consider the two thirds of these that have not been used in the discriminant training. The nominal background yields are 755 electron events and 643 muon events. Thus, each ensemble is generated picking around 700 events from around 850,000. The source of background most affected by oversampling is multijets, since some channels contain very few events that will be picked repeatedly. Given that the multijet background is very small and the statistical errors dominate, this does not introduce a large bias.

The ensemble generation includes a flat (i.e., normalization only, not shape changing) 20% error for the $t\bar{t}$ yield ($N_{t\bar{t}}$), which represents approximately the overall yield uncertainty from all systematic effects combined (see Appendix 6). The shift in the $t\bar{t}$ yield:

$$N'_{t\bar{t}} = N_{t\bar{t}} \times \text{Gaussian}(\text{mean} = 1, \text{width} = 0.2)$$

is the same for electrons and muons. The treatment of the W +jets and multijet backgrounds accounts for the normalization to data from the matrix method and for the effect of b -tagging. The error from the matrix method normalization of W +jets and multijet events is

incorporated in the ensemble generation by letting each sample (multijets, $Wc\bar{c}$, $Wb\bar{b}$ and Wjj) fluctuate with a different random number r sampled from a Gaussian distribution:

$$r_{\text{QCD}} = \text{Gaussian}(1, 0.2)$$

$$r_{Wjj} = \text{Gaussian}(1, 0.2)$$

$$r_{Wbb} = \text{Gaussian}(1, 0.2)$$

$$r_{Wcc} = \text{Gaussian}(1, 0.2)$$

The background sum of W +jets and multijets yields N_{WQCD} is fluctuated to become N'_{WQCD} :

$$N_{\text{WQCD}} = N_{\text{QCD}} + N_{Wjj} + N_{Wbb} + N_{Wcc}$$

$$N'_{\text{WQCD}} = r_{\text{QCD}} \times N_{\text{QCD}} + r_{Wjj} \times N_{Wjj} + r_{Wbb} \times N_{Wbb} + r_{Wcc} \times N_{Wcc}$$

These two expressions fix the normalization to data. What is changed here is the composition of each of the subcomponents. Once the correlation between multijets and W +jets is taken care of, we also need to take into account the effect of b -tagging. We split the summed samples of W +jets and multijets into 1-tag and 2-tags sets. The average uncertainty on these samples is 5% and 12% respectively (see Appendix 6), so we form a scale factor $S_{\text{WQCD}}^{\text{tag}}$ that incorporates the different rates for tagging single- and double-tagged events in these samples:

$$r_{1\text{tag}} = \text{Gaussian}(1, 0.05)$$

$$r_{2\text{tag}} = \text{Gaussian}(1, 0.12)$$

$$S_{\text{WQCD}}^{\text{tag}} = \frac{r_{1\text{tag}} \times N_{\text{WQCD}}^{1\text{tag}} + r_{2\text{tag}} \times N_{\text{WQCD}}^{2\text{tag}}}{N_{\text{WQCD}}^{1\text{tag}} + N_{\text{WQCD}}^{2\text{tag}}}$$

Finally, the multijets and W +jets event yields are fluctuated to:

$$N'_i = r_i \times \frac{N_{\text{WQCD}}}{N'_{\text{WQCD}}} \times S_{\text{tag}}^{\text{WQCD}} \times N_i ; i = \text{QCD}, Wjj, Wbb, Wcc$$

Once each background source has been fluctuated, we randomly pick events based on a Poisson distribution of the new systematics-shifted total background sum:

$$N'_{\text{Data}} = N'_{\text{QCD}} + N'_{Wjj} + N'_{Wbb} + N'_{Wcc} + N'_{t\bar{t}}$$

Appendix E

ANALYSIS CHANNEL SYSTEMATICS UNCERTAINTIES

Tables E.1–E.8 show the systematic uncertainties on the signal and background samples for the single-tagged and two double-tagged analyses.

UNCERTAINTIES FOR ELECTRON TWO-JET SINGLE-TAGGED ANALYSIS

	<u>Single-Tagged Electron Channel Percentage Errors</u>							
	tb	tqb	$t\bar{l}j$	$t\bar{l}l$	Wbb	Wcc	Wjj	Mis-ID e
<u>Components for Normalization</u>								
Luminosity	(6.1)	(6.1)	6.1	6.1	—	—	—	—
Cross section	(16.0)	(15.0)	18.0	18.0	—	—	—	—
Branching fraction	(1.0)	(1.0)	1.0	1.0	—	—	—	—
Matrix method	—	—	—	—	18.2	18.2	18.2	18.2
Primary vertex	2.4	2.4	2.4	2.4	—	—	—	—
Electron ID	5.5	5.5	5.5	5.5	—	—	—	—
Jet ID	1.5	1.5	1.5	1.5	—	—	—	—
Jet fragmentation	5.0	5.0	7.0	5.0	—	—	—	—
Trigger	3.0	3.0	3.0	3.0	—	—	—	—
<u>Components for Normalization and Shape</u>								
Jet energy scale	1.4	0.3	9.9	1.7	—	—	—	—
Flavor-dependent TRFs	2.1	5.9	4.6	2.4	4.4	6.3	7.4	—
<u>Statistics</u>	0.7	0.7	1.3	0.8	0.9	0.9	0.4	5.6
<u>Combined</u>								
Acceptance uncertainty	10.8	12.1	—	—	—	—	—	—
Yield uncertainty	19.3	19.3	24.1	21.1	18.8	19.3	19.7	19.1

Table E.1: Electron channel uncertainties, requiring exactly one tag and exactly two jets.

UNCERTAINTIES FOR ELECTRON THREE-JET SINGLE-TAGGED ANALYSIS

	<u>Single-Tagged Electron Channel Percentage Errors</u>							
	tb	tqb	$t\bar{l}j$	$t\bar{l}l$	Wbb	Wcc	Wjj	Mis-ID e
<u>Components for Normalization</u>								
Luminosity	(6.1)	(6.1)	6.1	6.1	—	—	—	—
Cross section	(16.0)	(15.0)	18.0	18.0	—	—	—	—
Branching fraction	(1.0)	(1.0)	1.0	1.0	—	—	—	—
Matrix method	—	—	—	—	16.8	16.8	16.8	16.8
Primary vertex	2.4	2.4	2.4	2.4	—	—	—	—
Electron ID	5.5	5.5	5.5	5.5	—	—	—	—
Jet ID	1.5	1.5	1.5	1.5	—	—	—	—
Jet fragmentation	5.0	5.0	7.0	5.0	—	—	—	—
Trigger	3.0	3.0	3.0	3.0	—	—	—	—
<u>Components for Normalization and Shape</u>								
Jet energy scale	5.3	5.8	4.1	3.2	—	—	—	—
Flavor-dependent TRFs	2.1	4.5	2.9	2.1	4.4	6.2	7.6	—
<u>Statistics</u>	1.0	1.0	0.5	0.5	1.0	1.0	0.5	6.7
<u>Combined</u>								
Acceptance uncertainty	12.0	12.9	—	—	—	—	—	—
Yield uncertainty	20.0	19.8	22.0	21.2	17.4	18.0	18.5	18.1

Table E.2: Electron channel uncertainties, requiring exactly one tag and exactly three jets.

UNCERTAINTIES FOR MUON TWO-JET SINGLE-TAGGED ANALYSES

	<u>Single-Tagged Muon Channel Percentage Errors</u>							
	tb	tqb	$t\bar{l}j$	$t\bar{l}l$	Wbb	Wcc	Wjj	Mis-ID e
<u>Components for Normalization</u>								
Luminosity	(6.1)	(6.1)	6.1	6.1	—	—	—	—
Cross section	(16.0)	(15.0)	18.0	18.0	—	—	—	—
Branching fraction	(1.0)	(1.0)	1.0	1.0	—	—	—	—
Matrix method	—	—	—	—	20.7	20.7	20.7	20.7
Primary vertex	3.0	3.0	3.0	3.0	—	—	—	—
Muon ID	7.4	7.4	7.4	7.4	—	—	—	—
Jet ID	1.5	1.5	1.5	1.5	—	—	—	—
Jet fragmentation	5.0	5.0	7.0	5.0	—	—	—	—
Trigger	6.0	6.0	6.0	6.0	—	—	—	—
<u>Components for Normalization and Shape</u>								
Jet energy scale	5.3	6.1	20.1	6.8	—	—	—	—
Flavor-dependent TRFs	1.8	5.9	4.5	2.0	4.4	6.3	7.5	—
<u>Statistics</u>	9.0	0.7	1.0	1.0	0.8	0.8	0.4	14.0
<u>Combined</u>								
Acceptance uncertainty	16.7	15.4	—	—	—	—	—	—
Yield uncertainty	23.1	21.5	30.7	23.2	21.2	21.7	22.0	25.0

Table E.3: Muon channel uncertainties, requiring exactly one tag and exactly two jets.

UNCERTAINTIES FOR MUON THREE-JET SINGLE-TAGGED ANALYSES

	<u>Single-Tagged Muon Channel Percentage Errors</u>							
	tb	tqb	$t\bar{l}j$	$t\bar{l}l$	Wbb	Wcc	Wjj	Mis-ID e
<u>Components for Normalization</u>								
Luminosity	(6.1)	(6.1)	6.1	6.1	—	—	—	—
Cross section	(16.0)	(15.0)	18.0	18.0	—	—	—	—
Branching fraction	(1.0)	(1.0)	1.0	1.0	—	—	—	—
Matrix method	—	—	—	—	20.8	20.8	20.8	20.8
Primary vertex	3.0	3.0	3.0	3.0	—	—	—	—
Muon ID	7.4	7.4	7.4	7.4	—	—	—	—
Jet ID	1.5	1.5	1.5	1.5	—	—	—	—
Jet fragmentation	5.0	5.0	7.0	5.0	—	—	—	—
Trigger	6.0	6.0	6.0	6.0	—	—	—	—
<u>Components for Normalization and Shape</u>								
Jet energy scale	9.3	9.0	10.8	7.6	—	—	—	—
Flavor-dependent TRFs	1.8	4.4	2.6	1.9	4.3	6.2	7.6	—
<u>Statistics</u>	2.0	2.0	0.8	0.7	1.0	1.0	0.7	14.3
<u>Combined</u>								
Acceptance uncertainty	16.1	16.5	—	—	—	—	—	—
Yield uncertainty	22.7	22.3	25.2	23.5	21.2	21.7	22.1	25.2

Table E.4: Muon channel uncertainties, requiring exactly one tag and exactly three jets.

UNCERTAINTIES FOR ELECTRON TWO-JET DOUBLE-TAGGED ANALYSES

	<u>Double-Tagged Electron Channel Percentage Errors</u>							
	tb	tqb	$t\bar{l}j$	$t\bar{l}l$	Wbb	Wcc	Wjj	Mis-ID e
<u>Components for Normalization</u>								
Luminosity	(6.1)	(6.1)	6.1	6.1	—	—	—	—
Cross section	(16.0)	(15.0)	18.0	18.0	—	—	—	—
Branching fraction	(1.0)	(1.0)	1.0	1.0	—	—	—	—
Matrix method	—	—	—	—	26.5	26.5	26.5	26.5
Primary vertex	2.4	2.4	2.4	2.4	—	—	—	—
Electron ID	5.5	5.5	5.5	5.5	—	—	—	—
Jet ID	1.5	1.5	1.5	1.5	—	—	—	—
Jet fragmentation	5.0	5.0	7.0	5.0	—	—	—	—
Trigger	3.0	3.0	3.0	3.0	—	—	—	—
<u>Components for Normalization and Shape</u>								
Jet energy scale	0.8	4.1	8.0	1.8	—	—	—	—
Flavor-dependent TRFs	12.9	12.9	13.5	13.0	12.2	13.6	16.1	—
<u>Statistics</u>	0.7	0.7	1.3	0.8	0.9	0.9	0.4	28.9
<u>Combined</u>								
Acceptance uncertainty	16.7	17.2	—	—	—	—	—	—
Yield uncertainty	23.1	22.8	26.6	24.6	29.1	29.8	31.0	39.2

Table E.5: Electron channel uncertainties, requiring exactly two tags and exactly two jets.

UNCERTAINTIES FOR ELECTRON THREE-JET DOUBLE-TAGGED ANALYSES

	<u>Double-Tagged Electron Channel Percentage Errors</u>							
	tb	tqb	$t\bar{l}j$	$t\bar{l}l$	Wbb	Wcc	Wjj	Mis-ID e
<u>Components for Normalization</u>								
Luminosity	(6.1)	(6.1)	6.1	6.1	—	—	—	—
Cross section	(16.0)	(15.0)	18.0	18.0	—	—	—	—
Branching fraction	(1.0)	(1.0)	1.0	1.0	—	—	—	—
Matrix method	—	—	—	—	22.1	22.1	22.1	22.1
Primary vertex	2.4	2.4	2.4	2.4	—	—	—	—
Electron ID	5.5	5.5	5.5	5.5	—	—	—	—
Jet ID	1.5	1.5	1.5	1.5	—	—	—	—
Jet fragmentation	5.0	5.0	7.0	5.0	—	—	—	—
Trigger	3.0	3.0	3.0	3.0	—	—	—	—
<u>Components for Normalization and Shape</u>								
Jet energy scale	4.8	4.0	3.5	2.9	—	—	—	—
Flavor-dependent TRFs	12.7	12.4	12.6	12.8	12.0	13.3	16.4	—
<u>Statistics</u>	1.0	1.0	0.7	0.7	1.0	1.0	0.5	25.8
<u>Combined</u>								
Acceptance uncertainty	17.2	16.8	—	—	—	—	—	—
Yield uncertainty	23.5	22.5	25.1	24.6	25.2	25.8	27.5	34.0

Table E.6: Electron channel uncertainties, requiring exactly two tags and exactly three jets.

UNCERTAINTIES FOR MUON TWO-JET DOUBLE-TAGGED ANALYSES

	<u>Double-Tagged Muon Channel Percentage Errors</u>							
	tb	tqb	$t\bar{l}j$	$t\bar{l}l$	Wbb	Wcc	Wjj	Mis-ID e
<u>Components for Normalization</u>								
Luminosity	(6.1)	(6.1)	6.1	6.1	—	—	—	—
Cross section	(16.0)	(15.0)	18.0	18.0	—	—	—	—
Branching fraction	(1.0)	(1.0)	1.0	1.0	—	—	—	—
Matrix method	—	—	—	—	27.6	27.6	27.6	27.6
Primary vertex	3.0	3.0	3.0	3.0	—	—	—	—
Muon ID	7.4	7.4	7.4	7.4	—	—	—	—
Jet ID	1.5	1.5	1.5	1.5	—	—	—	—
Jet fragmentation	5.0	5.0	7.0	5.0	—	—	—	—
Trigger	6.0	6.0	6.0	6.0	—	—	—	—
<u>Components for Normalization and Shape</u>								
Jet energy scale	5.2	9.1	19.7	6.9	—	—	—	—
Flavor-dependent TRFs	12.9	12.8	13.4	12.9	12.2	13.5	16.1	—
<u>Statistics</u>	1.3	0.9	0.7	0.7	1.0	1.0	0.5	57.7
<u>Combined</u>								
Acceptance uncertainty	19.0	20.3	—	—	—	—	—	—
Yield uncertainty	24.8	25.2	32.9	26.5	30.2	30.7	31.9	64.0

Table E.7: Muon channel uncertainties, requiring exactly two tags and exactly two jets.

UNCERTAINTIES FOR MUON THREE-JET DOUBLE-TAGGED ANALYSES

	<u>Double-Tagged Muon Channel Percentage Errors</u>							
	tb	tqb	$t\bar{l}j$	$t\bar{l}l$	Wbb	Wcc	Wjj	Mis-ID e
<u>Components for Normalization</u>								
Luminosity	(6.1)	(6.1)	6.1	6.1	—	—	—	—
Cross section	(16.0)	(15.0)	18.0	18.0	—	—	—	—
Branching fraction	(1.0)	(1.0)	1.0	1.0	—	—	—	—
Matrix method	—	—	—	—	25.0	25.0	25.0	25.0
Primary vertex	3.0	3.0	3.0	3.0	—	—	—	—
Muon ID	7.4	7.4	7.4	7.4	—	—	—	—
Jet ID	1.5	1.5	1.5	1.5	—	—	—	—
Jet fragmentation	5.0	5.0	7.0	5.0	—	—	—	—
Trigger	6.0	6.0	6.0	6.0	—	—	—	—
<u>Components for Normalization and Shape</u>								
Jet energy scale	10.2	7.6	10.1	7.8	—	—	—	—
Flavor-dependent TRFs	12.6	12.3	12.4	12.7	12.0	13.1	16.4	—
<u>Statistics</u>	2.0	2.0	0.8	0.6	1.0	1.0	0.6	50.0
<u>Combined</u>								
Acceptance uncertainty	20.8	19.4	—	—	—	—	—	—
Yield uncertainty	26.3	24.5	27.7	26.7	27.7	28.2	29.9	55.9

Table E.8: Muon channel uncertainties, requiring exactly two tags and exactly three jets.

VITA

Thomas Gadfort was born in Copenhagen, Denmark, in 1979. He graduated from Oak Ridge High School in Oak Ridge, Tennessee in 1997. At The University of Tennessee he earned a B.A. in College Scholars with an emphasis in Physics and Mathematics in 2001. After receiving a M.S. in Physics from the University of Washington in 2003, he moved to Chicago, IL, to perform research at Fermilab. He has graduated with a Ph.D. in Physics from the University of Washington in 2007, and looks forward to continuing research in High-Energy Physics.